Síntesis, caracterización y estudio en superficie de nanoimanes moleculares

Tesis Doctoral
2005

Jordi Gómez Segura
Dtor. Daniel Ruiz Molina

Institut de Ciència de Materials de Barcelona (ICMAB-CSIC)

Universitat Autònoma de Barcelona UAB

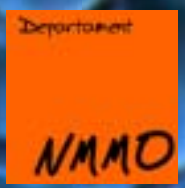

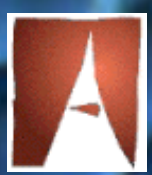

DANIEL RUIZ MOLINA, Investigador Titular y Doctor del CSIC en el *Institut de Ciència de Materials* de Barcelona,

CERTIFICA

Que Jordi Gómez Segura, Licenciado en Ciencias Químicas, ha realizado bajo su supervisión, la Tesis Doctoral titulada *Síntesis, caracterización y estudio en superficie de nanoimanes moleculares*, cuyo trabajo queda reflejado en el desarrollo de esta memoria para optar al título de Doctor en Ciencias Químicas.

Y para que así conste, firma el presente certificado.

Dr. Daniel Ruiz Molina

Bellaterra, 30 de Junio de 2005

“A veces no se ve nada en la superficie
pero por debajo todo está ardiendo”

Y. B. Mangunwijaya

Mi agradecimiento de antemano a aquellas personas que dediquen su esfuerzo a evaluar el contenido científico del manuscrito.

En mi formación científica, a todas aquellas personas coautoras de los artículos adjuntos en la Tesis. Al grupo de investigación por mi convivencia particular durante el periodo comprendido entre el 2002-2005. Concretamente, a mi Director de Tesis por su especial contribución y a los responsables del grupo en el Laboratorio de Materiales Orgánicos al ofrecerme una oportunidad científica de inicio.

Al proyecto europeo Nanomagiqc y a su beca predoctoral vinculada por su ayuda económica.

Durante el transcurso de estos años no debo olvidar en absoluto de la acogida, así como de la convivencia con otros grupos de trabajo en los distintos centros europeos que he visitado, especialmente el National Physical Laboratory de Londres, el Consiglio Nazionale delle la Ricerche en Bolonia, el Instituto de Ciencia de Materiales de Aragón y finalmente, el Institut Max Von Laue-Paul Langevin de Grenoble.

A quienes han depositado su confianza en mí y aquellos que recibieron mi amistad y seguro nunca olvidaré.

Finalmente, a mi familia por su apoyo incondicional.

Índice

Introducción

1. Introducción

La continua miniaturización de los sistemas de almacenamiento de información magnéticos así como el rápido desarrollo de ordenadores de alta velocidad han implicado un creciente interés en la obtención y estudio de materiales magnéticos a escala submicrométrica. Hasta hace unos años, estos materiales se obtenían por fragmentación *(aproximación descendente)*, que se basa en una reducción en el tamaño del material macroscópico hasta alcanzar las dimensiones deseadas *(Fig. 1)*. Sin embargo, entre los inconvenientes, los materiales magnéticos resultantes presentaban una elevada distribución de tamaños de partícula, anisotropía y forma asociadas. Como consecuencia, resulta una elevada distribución de alturas de barrera energética, las cuales están asociadas a la inversión de la orientación de los espines dentro de los dominios magnéticos. Dicha situación, además de poco práctica, supone que la observación de fenómenos cuánticos, tales como la relajación de la magnetización por efecto túnel, se vean enmascarados. No obstante, dichas limitaciones se han visto superadas con el uso de técnicas litográficas, permitiendo la obtención de sistemas magnéticos monodispersos de dimensiones nanoscópicas con un elevado control. Sin embargo, las limitaciones experimentales para continuar disminuyendo el tamaño de los dominios magnéticos, ya sea debido a fenómenos tales como el superparamagnetismo, o bien los elevados costes que suelen conllevar estas técnicas, suponen un impedimento para su implantación real al día de hoy.

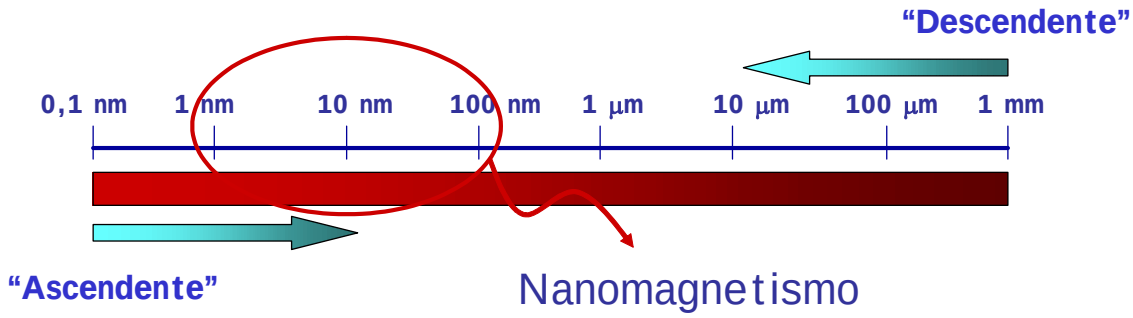

Fig. 1. Aproximaciones básicas, ascendente y descendente, para la obtención de materiales nanoestructurados.

Una alternativa complementaria desarrollada en los últimos años es el uso de métodos sintéticos (*aproximación ascendente)* para la obtención de imanes moleculares, donde cada molécula o complejo polinuclear se comporta como un dominio magnético *(ver Fig. 1)*. A priori, para que un material molecular mostrara magnetización espontánea por debajo de una temperatura crítica, era necesario una red 3-D de centros magnéticos interactivos. Sin embargo, en los últimos años se han descrito diversos ejemplos de complejos metálicos polinucleares *(0-D)* que presentan propiedades características de las partículas magnéticas, como son las señales fuera de fase en la susceptibilidad ac *(corriente alterna)* o bien la histéresis en las curvas de magnetización. Dichas propiedades se ha comprobado que tienen su origen asociado a cada una de las moléculas y no a interacciones de largo alcance. De acuerdo con la comunidad internacional, a dicha familia de moléculas se les ha denominado *Imanes Unimoleculares*.[1]

Las ventajas de los imanes unimoleculares son considerables: I) se sintetizan mediante técnicas químicas que permiten su diseño y obtención en grandes cantidades y a precios relativamente asequibles; II) presentan una elevada solubilidad en los disolventes más comunes, lo que facilita su manipulación; III) la presencia de tamaños perfectamente definidos, tal y como se atribuye a las dimensiones de las moléculas, permite evitar la presencia de una distribución de alturas en la barrera energética y IV) desde un punto de vista teórico, la interpretación de las propiedades magnéticas de estas moléculas supone una transición continua entre las propiedades magnéticas asociadas a pequeños objetos, donde los mecanismos cuánticos son necesarios para su interpretación, y los objetos macroscópicos, cuya fenomenología magnética puede ser comprendida a través de la física clásica.[2-5] Por todo ello, una vez establecidas y comprendidas las leyes básicas que rigen su comportamiento, estos imanes unimoleculares son unos excelentes candidatos como futuros dispositivos moleculares, por ejemplo, en sistemas de almacenamiento de información magnética de alta densidad donde cada molécula se asocia a un *bit* de información.

2. Imanes unimoleculares

El número de complejos metálicos polinucleares descritos en la literatura hasta la fecha es enorme. No obstante, sólo un número limitado de ellos exhibe las características de un imán unimolecular. Un ejemplo significativo corresponde al compuesto $[Mn_9^{II}(\mu\text{-}CN)_{30}Mo_6^{V}]$ *(1)* mostrado en la Figura 2. El complejo **1** tiene uno de los estados fundamentales de espín más elevado de todos los descritos hasta la fecha *(S=51/2)*, aunque no exhibe el comportamiento de imán unimolecular.[6] Para que un complejo determinado presente comportamiento de imán unimolecular no sólo es necesario poseer centros paramagnéticos de capa electrónica abierta, cuya interacción pueda dar lugar a estados fundamentales de alto espín *(S)*, se requiere además combinar una marcada anisotropía magnética negativa en la molécula *(i.e., la magnitud del parámetro de desdoblamiento a campo cero, D)*. La combinación de ambos factores es la que conlleva a la existencia de una barrera energética $(U=S^2|D|)$ que separa los microestados m_{+S} de los m_{-S}, y por consiguiente, a la observación de relajaciones lentas de la magnetización.

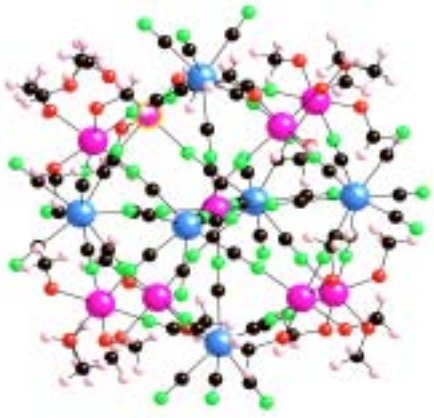

Fig. 2. Representación de la estructura con núcleo central $[Mn_9^{II}(\mu\text{-}CN)_{30}Mo_6^{V}]$ *(1)* de topología octaédrica.

La anisotropía magnética tiene su origen en la existencia de átomos metálicos con electrones desapareados cuya distribución no se localiza de forma equivalente en todas las direcciones del espacio *(i.e., distribución anisótropa)*, que depende directamente de la geometría molecular. Cualquier especie que posea simetría axial y plano

magnéticamente isótropo perpendicular al eje de simetría posee desdoblamiento a campo cero *(ZFS)*, que se caracteriza a través del parámetro de distorsión D. Por el contrario, no existe desdoblamiento si la distribución de electrones es esférica. Además, por convenio, D es positivo para una distribución de espín estabilizada a través del aplanamiento en una dirección o compresión a lo largo de un eje, mientras que adquiere un valor negativo si la distribución electrónica implica una elongación en una dirección o alargamiento de un eje. Por ejemplo, para metales de transición con simetría octaédrica *(O_h)* únicamente los estados de tipo T triplemente degenerados *(d_{xy}, d_{xz}, d_{yz})* dan lugar a momento orbital magnético, mientras que los estados fundamentales de tipo E, doblemente degenerados *($d_{x^2-y^2}$, d_{z^2})*, no poseen ninguna contribución orbital a la anisotropía. Si la degeneración orbital se ve alterada por las distorsiones de Jahn-Teller, se origina una anisotropía magnética debido a la movilidad electrónica hacia una dirección preferencial de la molécula.

Históricamente, el complejo de valencia mixta *($4Mn^{IV}$·$8Mn^{III}$)* Mn_{12} acetato, $[Mn_{12}O_{12}(O_2CCH_3)_{16}(H_2O)_4]$ *(2)*, no sólo fue el primer complejo polinuclear en demostrarse su comportamiento como imán unimolecular, sino que también ha sido uno de los más estudiados hasta la fecha. Su gran interés se basa en poseer un elevado estado fundamental de espín *(S=10)* además de marcada anisotropía magnética *(D<0)*, dando lugar a una de las barreras energéticas *(U)* más altas conocidas *(ca. 66K)*, y por consiguiente, a fenómenos de relajación lenta de la magnetización. Además, presenta una química relativamente sencilla, lo que ha permitido la obtención de numerosos derivados que varían tanto en el grado de oxidación como en la naturaleza de los ligandos. Hasta el momento, entre las modificaciones químicas descritas se incluyen la substitución de los grupos acetato puente por otros carboxilatos *(i.e., reacciones de substitución de ligandos)* y substituciones parciales de iones Mn^{III} periféricos por Fe^{III} [7], o Cr^{III} [8]. Los aniones carboxilato pueden a su vez ser intercambiados por oxoaniones[9-13] tales como NO_3^-, RSO_3^- y $R_2PO_2^-$, mientras que la geometría de coordinación octaédrica de los iones Mn^{III} puede ser convertida parcialmente a pirámide de base cuadrada en presencia de ligandos fosfonato adecuados.[14] Desde su descubrimiento, otros complejos metálicos basados en metales de transición *(Mn,[15] Ni,[16] Co,[17] Fe[18,19] y mezclas[20])* han sido sintetizados y caracterizados. Sin embargo, la preparación de complejos homometálicos de Mn_x *(Mn_2,[21] Mn_4,[22-28] Mn_6,[29] Mn_9,[30] Mn_{16},[31] Mn_{18},[32] Mn_{22},[33] Mn_{25},[34] Mn_{30},[35] Mn_{84},[36])* o bien derivados de la familia del Mn_{12} corresponden a la mayor fuente de obtención de imanes unimoleculares *(Fig. 3)*. En toda la serie de complejos homometálicos de Mn_x la presencia de iones Mn^{III} distorsionados por efecto Jahn-Teller son la principal fuente de anisotropía molecular, que es la proyección de las anisotropías individuales de cada ion Mn^{III} en el eje anisótropo molecular *(z)* al orientar de forma casi paralela los ejes de elongación axial del entorno octaédrico distorsionado.

Por otro lado, son varias las rutas preparativas utilizadas hasta la fecha para la obtención de dichos complejos. Entre ellas destacan: I) el uso de ligandos tipo quelato flexibles.[22-28] Estos pueden adoptar una variedad amplia de posibles modos de coordinación a través de más de un centro metálico, generando especies polinucleares con nuevas topologías estructurales.[37] II) agregación de complejos polinucleares de baja nuclearidad para originar complejos de una mayor nuclearidad, tal y como sucede en la bien estudiada formación de complejos de Mn_6 a partir de complejos de Mn_3, y III) mecanismos de agregación reductiva[38] a partir de una fuente de Mn^{II} y MnO_4^- que originan especies de valencia mixta tipo *(Mn^{IV}/Mn^{III})*[39] o *(Mn^{III}/Mn^{II}).*[26,27] Este último método ha sido utilizado con éxito en la síntesis de Mn_6,[29,40] Mn_{12},[1] Mn_{16} o incluso

Mn_{84}. A modo de ejemplo, en la Figura 3 se muestran el complejo Mn_{18} y Mn_{84}, sintetizados recientemente, y ambos con comportamiento de imán unimolecular. El complejo de Mn_{18} se obtuvo mediante un ligando flexible como el heph mostrado en la figura, con una barrera efectiva para la inversión de la magnetización de 21.3 K, mientras que el Mn_{84} se obtuvo mediante agregación reductiva a partir de Mn_{12} acetato, con una barrera energética efectiva de 18 K.

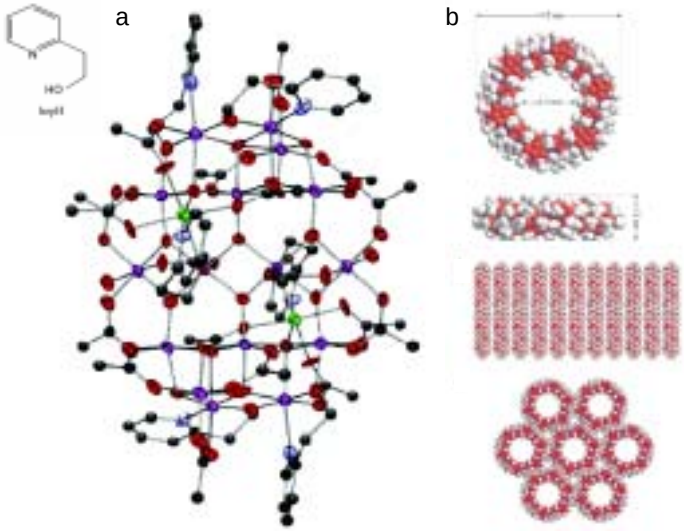

Fig. 3. Dos ejemplos correspondientes a imanes unimoleculares: a) Mn_{18} obtenido a partir de la síntesis en presencia de ligandos quelato flexibles *(heph)*; b) Mn_{84} obtenido mediante agregación reductiva.

Para finalizar esta sección, hay que destacar que el imán unimolecular con la barrera de interconversión más elevada fue descrito recientemente y no corresponde a la familia de complejos de Mn_x sino sorprendentemente a un complejo mononuclear de Tb. Efectivamente, estudios realizados sobre complejos mononucleares a partir de lantánidos[41] muestran fenómenos de relajación lenta de la magnetización a temperaturas entorno a los 20-30 K, gracias sobre todo a una elevada anisotropía magnética basada en el acoplamiento espín-órbita característico de los iones pesados. De esta manera, se abre una vía alternativa al estudio actual en imanes unimoleculares basados en metales de transición.

3. Imanes unimoleculares $[Mn_{12}O_{12}(O_2CR)_{16}(H_2O)_4]$ ó Mn_{12}

Entre la extensa familia de imanes unimoleculares mencionados, los trabajos de esta Tesis Doctoral se han centrado en la familia de complejos de Mn_{12} que presentan fórmula general $[Mn_{12}O_{12}(O_2CR)_{16}(H_2O)_4]$. A continuación se describen brevemente sus características estructurales y magnéticas.

Estructura.

Los complejos de Mn_{12} poseen un núcleo metálico con doce átomos de manganeso tipo $[Mn_{12}(\mu_3\text{-}O)_{12}]$. Dentro de esta estructura podemos distinguir dos zonas bien diferenciadas. Por un lado una estructura tipo cubano $[Mn^{IV}{}_4O_4]^{8+}$ *(marcada en verde en la Figura 4)* con cuatro átomos de Mn^{IV} *($S_{(MnIV)}$=3/2)*, que interaccionan ferromagnéticamente para dar lugar a un teórico estado fundamental $S_{(4MnIV)}$=6 dentro

de la subunidad. A su vez, la cavidad tipo cubano está rodeada a través de iones puente μ_3-O^{2-} por un anillo externo *(marcado en lila en la Figura 4)* compuesta de 8 iones Mn^{III} *($S_{(MnIII)}$=2),* todos ellos acoplados ferromagnéticamente entre sí para dar lugar a un estado fundamental teórico de $S_{(8MnIII)}$=16. Finalmente, las interacciones de carácter antiferromagnético entre el núcleo de $[Mn^{IV}{}_4O_4]^{8+}$ y el anillo de Mn^{III} no compensan los momentos magnéticos individuales dando lugar a baja temperatura a un estado fundamental con espín neto total S_T:

$$S_T = S_{(8MnIII)} - S_{(4MnIV)} = 16\text{-}6=10$$

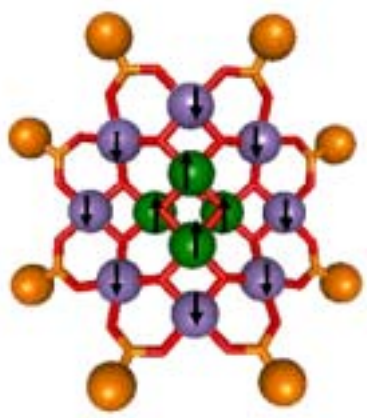

Fig. 4. Representación esquemática del núcleo metálico del Mn_{12} mostrando el plano perpendicular al eje axial molecular. Los iones Mn^{IV} *(en verde)* interaccionan antiferromagnéticamente con los iones Mn^{III} *(en lila)* a través de ligandos μ_3-O^{2-}.

Si bien la estructura nuclear del complejo **2**, Mn_{12} acetato, posee una simetría S_4, otros complejos de Mn_{12} muestran un núcleo $[Mn_{12}(\mu_3\text{-}O)_{12}]$ similar con diferencias en la posición de las cuatro aguas de coordinación. Como consecuencia, los ligandos carboxilato se reorganizan en la esfera de coordinación dando lugar a variaciones estructurales del núcleo central. Sin embargo, todos los complejos presentan dos grupos distintos formados por $4Mn^{III}$. En el grupo I cada Mn^{III} se enlaza a un ion Mn^{IV} mediante dos ligandos puente μ_3-O^{2-} mientras que en el grupo II cada Mn^{III} se enlaza a dos iones Mn^{IV} mediante dos ligandos puente μ_3-O^{2-}. Las aguas de coordinación sólo se coordinan a los iones Mn^{III} del grupo II en posiciones axiales. De esta manera, es posible identificar once isómeros geométricos diferentes como resultado de la reorganización de los 4 ligandos H_2O en las posiciones axiales de los iones Mn^{III}. De los once posibles isómeros se han detectado diferentes estructuras mediante espectroscopia de rayos-X *(Fig. 5)*.

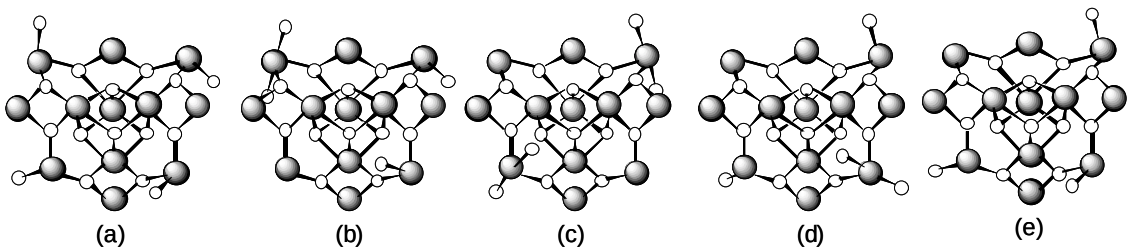

Fig. 5. Isómeros geométricos del Mn_{12} encontrados en moléculas caracterizadas estructuralmente: (a) (1:1:1:1), (b) (1:1:2), (c) (2:2), (d) (1:2:1), y (e) (1:1:1).

Propiedades magnéticas. Las distorsiones de Jahn-Teller de los iones Mn^{III} y su disposición elongada a lo largo del denominado "eje fácil" *(D<O; E=0)* generan anisotropía magnética. El estado fundamental de espín total del sistema *(S_T=10)* y la marcada magnetoanisotropía negativa conlleva a la aparición del fenómeno de desdoblamiento a campo cero y a la formación de una barrera energética entre los microestados ±10 *(Fig. 6)*. Al aplicar un campo magnético externo elevado que conduzca a la saturación de la muestra, y posteriormente a ser eliminado, la barrera energética origina que el compuesto vuelva a su estado fundamental con velocidades de relajación lentas. A temperaturas suficientemente bajas, dicha barrera, que impide a los espines reorientarse rápidamente, origina unos tiempos de relajación de hasta dos meses de duración. Por ello se observa la aparición de picos en las medidas de susceptibilidad alterna fuera de fase, así como la presencia de histéresis en las curvas de magnetización. Todas estas peculiaridades están asociadas a las propiedades de las moléculas y no a la existencia de interacciones intermoleculares, tal y como se ha demostrado experimentalmente. Para verificarlo, normalmente se llevan a cabo medidas magnéticas a partir de disoluciones congeladas. De esta manera, en disolución, se descarta la posible organización de moléculas en dominios mientras que la necesidad de congelar la disolución se basa en minimizar al máximo la rotación de las moléculas al aplicar el campo magnético externo *(H)*.

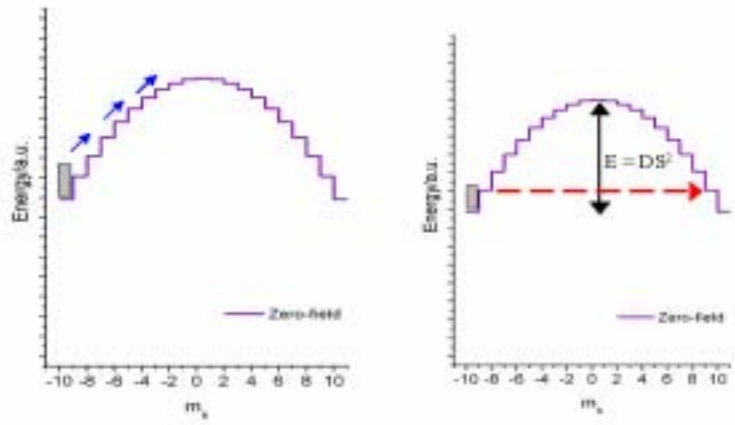

Fig. 6. Microestados energéticos para un estado fundamental de espín S=10 sujeto a desdoblamiento axial *(z)* a campo cero $-DS_z^2$. Fenómeno de relajación de la magnetización por activación térmica *(iz.)* y efecto túnel *(der.)*.

Para una molécula paramagnética, la inversión de la dirección de la magnetización *(M)* varía de forma muy rápida *($\leq 10^{-9}$s)*. Si se aplica un campo magnético oscilante ac de pequeña magnitud *(1-5G)* a frecuencia determinada *(ν)*, es posible estudiar los fenómenos dinámicos correspondientes a la relajación de la magnetización *(i.e., momento magnético)*. Si el vector de la magnetización puede relajarse lo suficientemente rápido, la susceptibilidad magnética medida *($\chi = \delta M/\delta H$)* variará en fase con el campo magnético. Esta componente en fase de la magnetización *(χ_M')* equivale a la susceptibilidad medida dc. Sin embargo, si la barrera que debe superar la magnetización, durante el proceso de relajación, es significativa en comparación a la

activación térmica *(kT)*, la susceptibilidad en fase disminuirá dando lugar a la aparición de una componente fuera de fase (χ_M'') *(Fig. 7)*. Por lo que respecta a la susceptibilidad magnética fuera de fase, la medida de la temperatura y frecuencia a la que se alcanza el máximo de susceptibilidad permite extraer información acerca de la temperatura de bloqueo *(T_B)* por encima de la cual el sistema se comporta como un superparamagneto.[42-51]

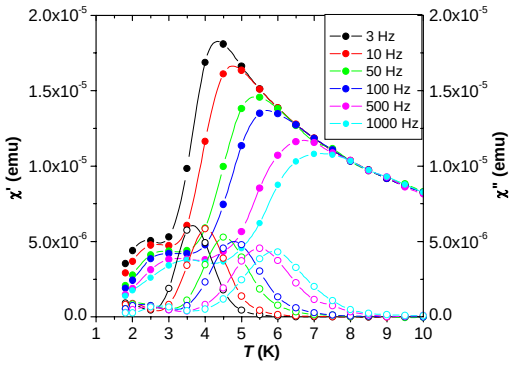

Fig. 7. Susceptibilidad magnética ac en función de la temperatura a distintas frecuencias entre 3 y 1000 Hz, con campos magnéticos externos aplicados de H_{ac}=3.8 Oe y H_{dc}=0 Oe. Los puntos representados en color sólido y vacíos corresponden a las componentes en fase (χ_M') y fuera de fase (χ_M''), respectivamente.

En la Figura 8 también se representa la magnetización frente al campo magnético aplicado (*cíclico)* a temperaturas en que la activación térmica es mínima. Además de los fenómenos de histéresis característicos de los dominios magnéticos, las curvas de histéresis correspondientes muestran de forma regular, a campos resonantes H_r *($H=nH_r$)*, incrementos en la velocidad de relajación de la magnetización cuando las energías de los microestados en ambos lados del pozo de potencial coinciden.[52-60] Estos fenómenos se han atribuido a la existencia de fenómenos de resonancia por efecto túnel. Por consiguiente, el enorme interés de estas moléculas no radica tan solo en su aplicación como dispositivos de almacenamiento de información sino también, desde un punto de vista teórico, como excelentes ejemplos para estudiar fenómenos cuánticos. Desde un punto de vista teórico, una de las más fascinantes predicciones de la Mecánica Cuántica es que el estado de un sistema físico puede ser descrito mediante una superposición de diferentes estados clásicos separados por una barrera de energía. A medida que el tamaño de los sistemas aumenta, la manifestación cuántica por efecto túnel disminuye exponencialmente, resultando la coherencia cuántica entre los estados energéticos fácilmente destruida por la interacción del sistema con su entorno, es decir con los grados de libertad microscópicos *(fonones, espines nucleares, etc.)*.

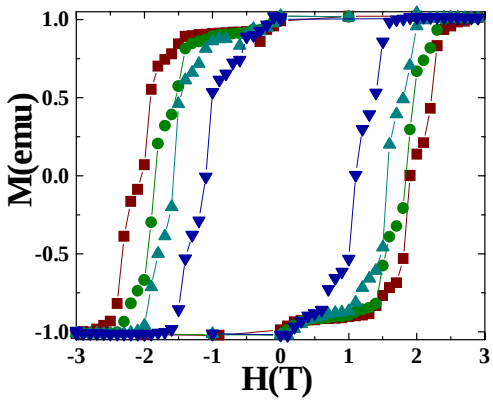

Fig. 8. Curvas de histéresis mostrando la dependencia de la magnetización *(M)* frente al campo magnético externo *(H)* a distintas temperaturas. El aumento de la velocidad de relajación cada 0.5 T se atribuye a fenómenos de relajación por efecto túnel a través de la barrera energética.

El estudio de la coherencia cuántica a escala nanométrica es de interés fundamental para determinar cómo tiene lugar la transición entre la descripción clásica y cuántica de la naturaleza. Los sistemas que se pretenden sintetizar y estudiar en este proyecto son los mejores candidatos para tal tipo de estudio. Tales sistemas poseen un elevado estado fundamental de espín y una gran anisotropía magnética. Por consiguiente, a bajas temperaturas, estos imanes pueden ser considerados como sistemas físicos ideales compuestos de dos niveles de energía en los cuales se puede conseguir un alto grado de coherencia cuántica. Resumiendo podemos asegurar que entender el comportamiento magnético de estas moléculas es importante para eliminar el vacío que existe entre el conocimiento clásico y cuántico de la naturaleza.

Finalmente, hay que destacar que en muchos de los Mn_{12} sintetizados hasta la fecha se ha observado la presencia no sólo de uno sino como mínimo de dos mecanismos de relajación diferentes.[61] La presencia de ambos mecanismos se ha comprobado por la aparición de señales adicionales, a temperaturas inferiores *(2-3 K)*, en las medidas de susceptibilidad ac, así como la observación de fenómenos de relajación rápida en las curvas de magnetización. La presencia del pico de baja temperatura correspondiente a un máximo en la curva de susceptibilidad fuera de fase *(especie de baja temperatura o de relajación rápida)* se ha atribuido a la pérdida de simetría relativa a las distorsiones de Jahn-Teller en el núcleo metálico *(Fig. 9)*. Así pues, se ha podido correlacionar de forma experimental, la observación del pico fuera de fase a bajas temperaturas, es decir, la existencia de dos mecanismos de relajación magnética, cuando la estructura molecular posee una de las distorsiones de Jahn-Teller en el entorno octaédrico de los Mn^{III}. Para que ello ocurra, no es necesario ni tan siquiera variar la naturaleza del ligando externo, sino que un mismo compuesto puede presentar dichas variaciones según el entorno de cristalización *(fase cristalina, presencia de disolventes, etc.)*.

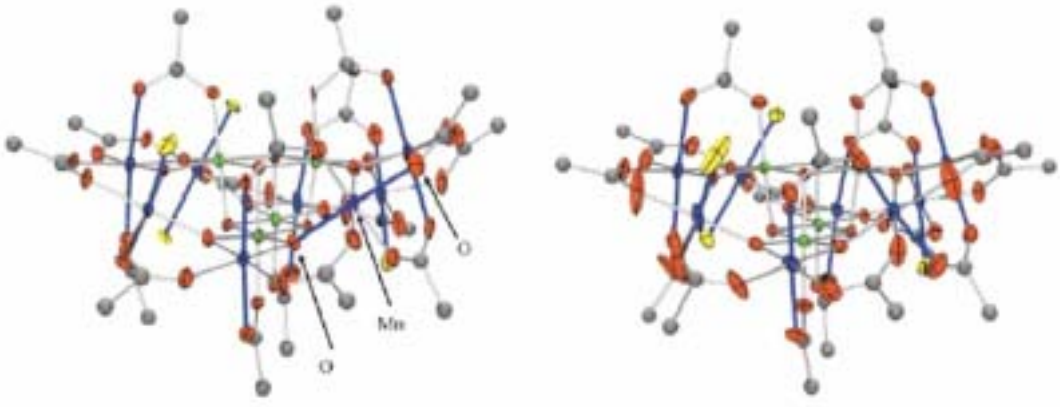

Fig. 9. Distorsiones de Jahn-Teller en el entorno octaédrico del Mn^{III}. Los ejes de máxima elongación *(en azul)* se encuentran dispuestos de forma más o menos paralela al eje axial *(iz.)* correspondiente a la especie de baja temperatura o relajación rápida. La disposición casi perpendicular del eje O-Mn-O *(der.)* da origen a la especie de alta temperatura o relajación lenta.

4. Contexto de la Tesis

Tal y como se ha expuesto anteriormente, el descubrimiento del comportamiento como imán unimolecular en ciertos complejos polinucleares supuso una revolución dentro del campo del magnetismo molecular. Dicho interés tuvo su origen no sólo ante las enormes expectativas que se abren para su futuro uso en dispositivos moleculares o sistemas de almacenamiento de información magnética de alta densidad, sino también porque sus tamaños nanoscópicos y monodispersos han permitido observar nuevas fenomenologías y determinar la existencia de fenómenos cuánticos como el efecto túnel de espín, los cuales son de gran valía para conocer mejor el comportamiento magnético en la transición del mundo macroscópico al mundo nanoscópico. Sin embargo, a pesar de dicho interés, este campo es lo suficientemente reciente y al mismo tiempo complejo para que todavía queden un elevado número de preguntas, limitaciones y retos por afrontar. Así, científicos de todo el mundo, tanto químicos como físicos, han centrado su atención y trabajo en tres campos básicos de los imanes unimoleculares, que son:

1) **Síntesis**. Estos trabajos se dirigen a la obtención de nuevos imanes unimoleculares que presenten unas temperaturas de bloqueo cada vez mayores, con el objetivo de acercarse en la medida de lo posible a temperaturas próximas a la temperatura ambiente. Dentro de este campo, cabe destacar científicos como los Profesores G. Christou y D. N. Hendrickson en los E.E.U.U, los Profesores R. Wimpenny, A. Powell y J. Ribas en Europa y los Profesores Ishikawa y T. Kuroda-Sowa en Japón. La mayor dificultad que se encuentran en el camino es la dificultad de diseñar y obtener de forma racional agregados polinucleares donde se puedan controlar a voluntad tanto el tamaño *(número de centros paramagnéticos)*, la naturaleza de las interacciones magnéticas así como la anisotropía resultante.

2) **Estudios magnéticos**. El segundo campo donde un gran número de grupos de investigación, sobre todo físicos, se ha involucrado es el estudio detallado de las inusuales propiedades magnéticas y otros fenómenos cuánticos que exhiben estos compuestos. Dentro de este campo, caben destacar grupos como el de los Profesores J. Tejada, W. Wernsdorfer, D. Gatteschi, B. Barbara y F. Luis en Europa, los Prof. S. Hill, E.Chudnovsky y M. Sarachik en los E.E.U.U.

3) **Estructuración y/o deposición en superficies**. El tercer campo donde un creciente número de grupos están centrando su atención, especialmente en los últimos años, es en el desarrollo de técnicas que permitan la deposición controlada de los imanes unimoleculares en superficies así como su caracterización. Dichos estudios son fundamentales antes de que cualquier dispositivo basado en imanes unimoleculares sea una realidad. Como científicos activos dentro de este campo hay que destacar los Profesores E. Coronado, D. Gatteschi y M. Drillon en Europa y la Profesora K. Dunbar en los E.E.U.U.

Los trabajos que han conducido a la redacción de la presente Tesis se afrontarán como una aproximación científica diversificada con incursiones en cada uno de los tres campos anteriormente mencionados. Dentro de la síntesis de nuevos compuestos, el objetivo se centró en la funcionalización de los complejos de Mn_{12} con ligandos ópticos o electroquímicamente activos *(capítulo 1)*. La segunda parte del trabajo fue entender

cómo puede variar el comportamiento de imán unimolecular en la traslación del mundo macroscópico ó 3-D al mundo nanoscópico ó 2-D. Para ello se estudió de forma sistemática la obtención de partículas cuyas dimensiones oscilen entre las dimensiones microscópicas a unas dimensiones nanoscópicas, así como la influencia de otros parámetros de red en la relajación magnética *(Capítulo 2)*. Finalmente, se abordó la estructuración de los imanes unimoleculares desde una escala microscópica en sistemas poliméricos *(Capítulo 3)* hasta la escala nanoscópica mediante la deposición controlada de los sistemas moleculares en diversas superficies *(Capítulo 3)*.

Cuando se comenzaron los trabajos que han conducido a la redacción de la Tesis, en el grupo de investigación ya se poseía una amplia experiencia en el campo del Magnetismo Molecular, y especialmente en el campo de los imanes unimoleculares. Sin embargo, dada la diversidad de los trabajos en las distintas áreas de conocimiento, además de un mayor esfuerzo, ello también suponía la necesidad de colaborar con otros grupos expertos en temas como los fenómenos de relajación magnética, procesado de nanopartículas y el uso de técnicas neutrónicas y de microscopia. Cabe destacar que todos los trabajos anteriormente mencionados fueron pioneros en el momento de comenzarlos a estudiar. Por ejemplo, en los inicios de la presente Tesis tan sólo había un trabajo germinal de deposición de Mn_{12} en superficies realizado en el grupo del Prof. Coronado con la técnica de Langmuir-Blodgett. De forma similar, la funcionalización de imanes unimoleculares con ligandos multifuncionales o el escalado del tamaño de partícula eran completamente innovadores.

5. Referencias

1. G. Christou, D. Gatteschi, D.N. Hendrickson, R. Sessoli, *MRS Bull.*, **2000**, *25*, 66.
2. D. Gatteschi, A. Caneschi, L. Pardi, R. Sessoli, *Science*, **1994**, *265*, 1054.
3. P.C.E. Stamp, *Nature*, **1996**, *383*, 125.
4. E.M. Chudnovsky, *Science*, **1996**, *274*, 838.
5. B. Barbara, L. Gunther, *Phys. World*, **1999**, *12*, 35.
6. J. Larionova, M. Gross, M. Pilkington, H. Andres, H. Stoeckli-Evans, H. Güdel, S. Decurtins, *Angew. Chem., Int. Ed.*, **2000**, *39*, 1605.
7. A. R. Schake, H.L. Tsai, N.D. Vires, K. Folting, D.N. Hendrickson, G. Christou, *J. Chem. Soc., Chem. Commun.*, **1992**, 181.
8. J.Y. Li, H. Xu, J.Z. Zou, Z. Xu, X.Z. You, K.B. Yu, *Polyedron*, **1996**, *15*, 3325.
9. P. Artus, C. Boskovic, J. Yoo, W.E. Streib, L.C. Brune, D.N. Hendrickson, C. Christou, *Inorg. Chem.*, **2001**, *40*, 4199.
10. C. Boskovic, M. Pink, J.C. Huffman, D.N. Hendrickson, G. Christou, *J. Am. Chem. Soc.*, **2001**, *123*, 9914.
11. T. Kuroda-Sowa, S. Fukuda, S. Miyoshi, M. Maekawa, M. Munakata, H. Miyasaka, M. Yamashita, *Chem. Lett.*, **2002**, 682.
12. N.E. Chakov, W. Wernsdorfer, K.A. Abboud, D.N. Hendrickson, G. Christou, *Dalton Trans.*, **2003**, 2243.
13. T. Kuroda-Sowa, T. Handa, T. Kotera, M. Maekawa, M. Munakata, H. Miyasaka, M. Yamashita, *Chem. Lett.*, **2004**, *33*, 540.
14. G.-Q. Bian, T. Kuroda-Sowa, H. Konaka, M. Hatano, M. Maekawa, M. Munakata, H. Miyasaka, M. Yamashita, *Inorg. Chem.*, **2004**, *43*, 4790.
15. C. Boskovic, W. Wernsdorfer, K. Folting, J.C. Huffman, D.N. Hendrickson, G. Christou, *Inorg. Chem.*, **2002**, *41*, 5107.
16. C. Cadiou, M. Murrie, C. Paulsen, V. Villar, W. Wernsdorfer, R.E.P. Winpenny, *Chem. Commun.*, **2001**, *24*, 2666.
17. E.C. Yang, D.N. Hendrickson, W. Wernsdorfer, M. Nakano, G. Christou, *J. Appl. Phys.*, **2002**, *91*, 7382.
18. C. Sangregorio, T. Ohm, C. Paulsen, R. Sessoli, D. Gatteschi, *Phys. Rev. Lett.*, **1997**, *78*, 4645.
19. A.L. Barra, A. Caneschi, A. Cornia, F.F. De Biani, D.Gatteschi, C. Sangregorio, R. Sessoli, L. Sorace, *J. Am. Chem. Soc.*, **1999**, *121*, 5302.
20. J.J. Sokol, A.G. Hee, J.R. Long, *J. Am. Chem. Soc.*, **2002**, *124*, 7656.
21. H. Miyasaka, R. Clérac, W. Wernsdorfer, L. Lecren, C. Bonhomme, K. Sugiura, M.A. Yamashita, *Angew. Chem., Int. Ed.*, **2004**, *43*, 2801.
22. S.M.J. Aubin, M.W. Wemple, D.M. Adams, H.-L. Tsai, G. Christou, D.N. Hendrickson, *J. Am. Chem. Soc.*, **1996**, *118*, 7746.
23. S.M.Aubin, N.R. Gilley, L. Pardi, J. Krzystek, M.W. Wemple, L.C. Brunel, M.B. Marple, G. Christou, D.N. Hendrickson, *J. Am. Chem. Soc.*, **1998**, *120*, 4991.
24. E.K. Brechin, J. Yoo, J.C. Huffman, D.N. Hendrickson, G. Christou, *Chem. Commun.*, **1999**, 783.
25. J. Yoo, E.K. Brechin, A. Yamaguchi, M. Nakano, J.C. Huffman, A.L. Maniero, L.-C. Brunel, K. Awaga, H. Ishimoto, G. Christou, D.N. Hendrickson, *Inorg. Chem.*, **2000**, *39*, 3615.
26. J. Yoo, A. Yamaguchi, M. Nakano, J. Krzystek, W.E. Streib, L.-C. Brunel, H. Ishimoto, G. Christou, D.N. Hendrickson, *Inorg. Chem.*, **2001**, *40*, 4604.
27. E. Yang, N. Harden, W. Wernsdorfer, L. Zakharov, E.K. Brechin, A.L. Rheingold, G. Christou, D.N. Hendrickson, *Polyhedron*, **2003**, *22*, 1857.
28. L.M. Wittick, K.S. Murray, B. Moubaraki, S.R. Batten, L. Spiccia, K.J. Berry, *J. Chem. Soc., Dalton Trans.*, **2004**, *7*, 1003.
29. C.J. Milios, C.P. Raptopoulou, A. Terzis, F. Lloret, R. Vicente, S. P. Perlepes, A. Escuer, *Angew. Chem., Int. Ed.*, **2003,** *43*, 210.
30. E.K. Brechin, S. Soler, J. Davidson, D.N. Hendrickson, S. Parsons, G. Christou, *Chem. Commun.*, **2002**, 2252.
31. D.J. Price, S.R. Batten, B. Moubaraki, K.S. Murray, *Chem. Commun.*, **2002**, 762.
32. E.K. Brechin, E.C. Sañudo, W. Wernsdorfer, C. Boskovic, J. Yoo, D.N. Hendrickson, A. Yamaguchi, H. Ishimoto, T.E. Concolino, A.L. Rheingold, G. Christou, *Inorg. Chem.*, **2005**, *44*, 502.

33. M. Murugesu, J. Raftery, W. Wernsdorfer, G. Christou, E.K. Brechin, *Inorg. Chem.*, **2004**, *43*, 4203.
34. M. Murugesu, M. Habrych, W. Wernsdorfer, K.A. Abboud, G. Christou, *J. Am. Chem. Soc.*, **2004**, *126*, 4766.
35. M. Soler, E. Rumberger, K. Folting, D.N. Hendrickson, G. Christou, *Polyhedron*, **2001**, *20*, 1365.
36. A.J. Tasiopoulos, A. Vinslava, W. Wernsdorfer, K.A. Abboud, G. Christou, *Angew. Chem., Int. Ed.*, **2004**, *43*, 2117.
37. E.M. Rumberger, L.N. Zakharov, A.L. Rheingold, D.N. Hendrickson, *Inorg. Chem.*, **2004**, *43*, 6531.
38. P. King, W. Wernsdorfer, K.A. Abboud, G. Christou, *Inorg. Chem.*, **2004**, *43*, 7315.
39. M.A. Bolcar, S.M.J. Aubin, K. Folting, D.N. Hendrickson, G. Christou, *Chem. Commun.*, **1997**, 1485.
40. S. Mukhopadhyay, B.A. Gandhi, M. L. Kirk, W. H. Armstrong, *Inorg. Chem.*, **2003**, *42*, 8171.
41. N. Ishikawa, M. Sugita, N. Tanaka, T. Ishikawa, S. Koshihara, Y. Kaizu, *Inorg. Chem.*, **2004**, *43*, 5498.
42. R. Sessoli, H.-L. Tsai, A.R. Schake, S. Wang, J.B. Vincent, K. Folting. D. Gatteschi, D.N. Hendrickson, *J. Am. Chem. Soc.*, **1993**, *115*, 1804.
43. C. Sangregorio, T. Ohm, C. Paulsen, R. Sessoli, D. Gatteschi, *Phys. Rev. Lett.*, **1997**, *78*, 4645.
44. A.L. Barra, A. Caneschi, A. Cornia, F.F. De Biani, D. Gatteschi, C. Sangregorio, R. Sessoli, L. Sorace, *J. Am. Chem. Soc.*, **1999**, *121*, 5302.
45. C. Cadiou, M. Murrie, C. Paulsen, V. Villar, W. Wernsdorfer, R.E.P. Winpenny, *Chem. Commun.*, **2001**, 2666.
46. C. Boskovic, W. Wernsdorfer, K. Folting, J.C. Huffman, D.N. Hendrickson, G. Christou, *Inorg. Chem.*, **2002**, *41*, 5107.
47. E.C. Yang, D.N. Hendrickson, W. Wernsdorfer, M. Nakano, G. Christou, *J. Appl. Phys.*, **2002**, *91*, 7382.
48. J.J. Sokol, A.G. Hee, J.R. Long, *J. Am. Chem. Soc.*, **2002**, *124*, 7656.
49. D. Gatteschi, R. Sessoli, *Angew. Chem., Int. Ed.*, **2003**, *42*, 268.
50. E.-C. Yang, N. Harden, W. Wernsdorfer, L. Zakharov, E.K. Brechin, A.L. Rheingold, G. Christou, D.N. Hendrickson, *Polyhedron*, **2003**, *22*, 1857.
51. E.-C. Yang, W. Wernsdorfer, S. Hill, R.S. Edwards, M. Nakano, S. Maccagnano, L.N. Zakharov, A.L. Rheingold, G. Christou, D.N. Hendrickson, *Polyhedron*, **2003**, *22*, 1727.
52. J.M. Hernandez, X.X. Zhang, F. Luis, J. Bartolomé, J. Tejada, R. Ziolo, *Europhys. Lett.*, **1996**, *76*, 3830.
53. J.R. Friedman, M.P. Sarachik, J. Tejada, R. Ziolo, *Phys. Rev. Lett.*, **1996**, *76*, 3830.
54. J.M. Hernández, X.X. Zhang, F. Luis, J. Tejada, J.R. Friedman, M.P. Sarachik, R. Ziolo, *Phys. Rev. B*, **1997**, *55*, 5858.
55. F. Luis, J. Bartolomé, J.F. Fernández, J. Tejada, J.M. Hernández, X.X. Zhang, R. Ziolo, *Phys. Rev. B*, **1997**, *55*, 11448.
56. J.R. Friedman, M.P. Sarachik, J.M. Hernández, X.X. Zhang, J. Tejada, E. Molins, R. Ziolo, *J. Appl. Phys.*, **1997**, *81*, 3978.
57. E.M. Chudnovsky, J. Tejada, *Macroscopic Quantum Tunneling of the Magnetic Moment*, Cambridge University Press, Cambridge, **1998**.
58. J. Tejada, J.M. Hernández, E. del Barco, *J. Magn. Magn. Mater.*, **1999**, *196-197*, 552.
59. F. Luis, J.M. Hernández, J. Bartolomé, J. Tejada, *Nanotechnology*, **1999**, *10*, 86.
60. D. Gatteschi, R. Sessoli, *Angew. Chem., Int. Ed.*, **2003**, *42*, 268.
61. D. Ruiz, Z. Sun, B. Albela, K. Folting, J. Ribas, G. Christou, D.N. Hendrickson, *Angew. Chem., Int. Ed.*, **1998**, *37*, 300.

Objetivos

Los objetivos de la presente Tesis Doctoral, ***Síntesis, caracterización y estudio en superficie de imanes unimoleculares***, son la preparación de nuevos dispositivos unimoleculares de dimensiones nanoscópicas para desarrollar el estudio y compresión del origen de los fenómenos de relajación magnética observados. Para ello, se prepararán y procesarán nuevos imanes unimoleculares basados en la familia de complejos metalorgánicos de Mn_{12} convenientemente funcionalizados en base a los siguientes estudios a desarrollar:

- Síntesis y caracterización de imanes unimoleculares. Reacciones de substitución en presencia de ligandos multifuncionales.

- Estabilidades térmicas asociadas a la estructura nuclear metálica en función de la naturaleza físico-química de los ligandos orgánicos.

- Sinergismo de propiedades magneto-ópticas a través de ligandos orgánicos de naturaleza quiral.

- Ordenamiento magnético a bajas temperaturas a través de técnicas de dispersión de neutrones en presencia de ligandos deuterados.

- Fenómenos de relajación magnética a nivel macroscópico en materiales micro/nanocristalinos o monocristales.

- Influencia de variables tales como el tamaño y entorno químico en los mecanismos de relajación magnética.

- Desarrollo de técnicas de microestructuración en superficie.

- Caracterización magnética en superficie de imanes unimoleculares en régimen paramagnético a temperatura ambiente.

Finalmente, se desarrollarán nuevos estudios sistemáticos basados en nuevas técnicas de deposición en superficie que permitan localizar de forma controlada dominios moleculares magnéticos como acceso potencial a sistemas de almacenamiento de información de alta densidad. Desde la síntesis, caracterización y cristalización convencionales a nivel macroscópico, introduciremos el procesado del material obtenido a través de técnicas de micronización, y finalmente concluiremos con su escalado submicrométrico en superficie.

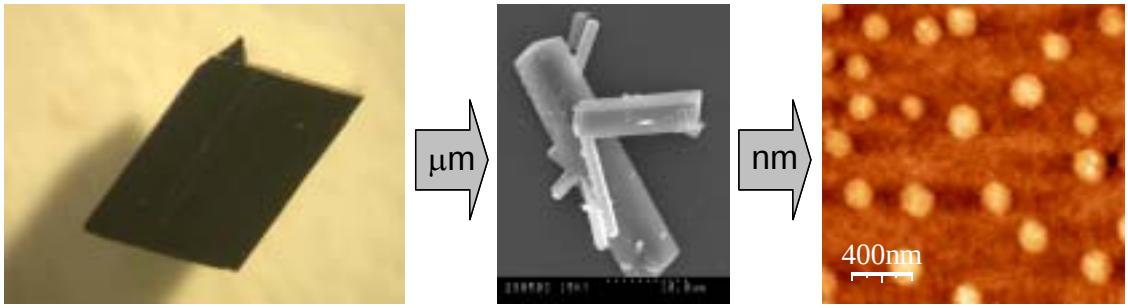

Discusión y resultados

Capítulo 1

Síntesis y caracterización de nuevos Mn_{12} multifuncionales

1.1. Introducción

Los complejos de Mn_{12} poseen un núcleo metálico $[Mn_{12}(\mu_3\text{-}O)_{12}]$ formado por una estructura tipo cubano $[Mn^{IV}{}_4O_4]^{8+}$ *(S=6)* que interacciona a través de iones puente $\mu_3\text{-}O_2^-$ con un anillo externo de 8 iones Mn^{III} *(S=16)*. A baja temperatura, las interacciones antiferromagnéticas entre ambas unidades no compensan los momentos magnéticos individuales dando lugar a un estado fundamental de espín S=10. Este corazón metálico está cohesionado por la presencia de 16 ligandos carboxilato en la periferia que pueden ser intercambiados mediante una simple reacción de substitución sin que se pierdan las propiedades características de imán unimolecular. A modo de ejemplo, en la Figura 1.1 se muestran las estructuras de tres de los Mn_{12} que se han descrito hasta la fecha en la literatura. Tal y como se puede ver, además de variar la naturaleza de dichos ligandos, también varía de forma significativa el tamaño, pudiendo oscilar desde unas dimensiones ligeramente inferiores a los dos nanómetros hasta casi cuatro nanómetros.

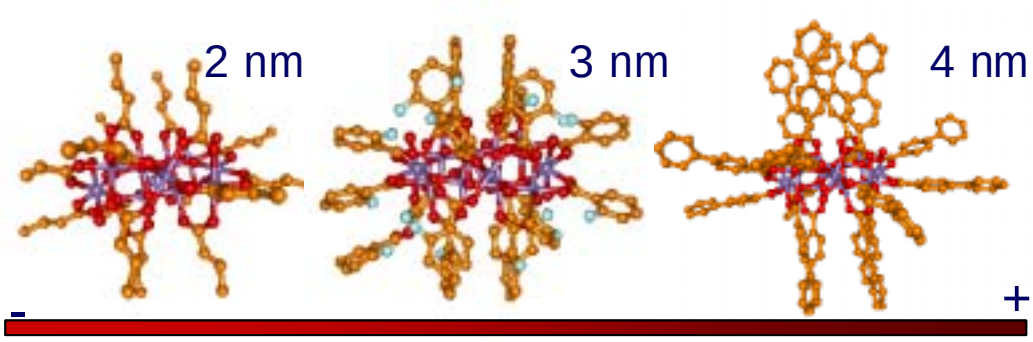

Fig. 1.1. Modificación del tamaño en complejos de Mn_{12} mediante reacciones de intercambio de grupos carboxilato periféricos manteniendo el núcleo central metálico y comportamiento de imán unimolecular.

El número de Mn_{12} descritos hasta la fecha siguiendo esta aproximación es considerable. Una pequeña representación de los diferentes ligandos utilizados se muestra en la Tabla 1.1. Además de ligandos tipo alcano o aromáticos, más recientemente se han descrito otros nuevos ligandos funcionalizados con grupos tioles para su deposición en superficies.

Tres son las principales rutas sintéticas utilizadas convencionalmente para la síntesis de complejos de la familia del Mn_{12}.

1)Preparación directa a partir de la reacción de comproporcionación entre una fuente de Mn^{II} y Mn^{VII} *(MnO_4^-)* en presencia del ácido carboxílico deseado *(RCO_2H)*. Esta aproximación corresponde al método original descrito por Lis[1] para sintetizar el primer complejo de Mn_{12}, $[Mn_{12}O_{12}(O_2CCH_3)_{16}(H_2O)_4]$ *(2)* ó Mn_{12} acetato.

$$44Mn^{2+} + 16Mn^{7+} \rightarrow 5[Mn_{12}]^{40+}$$

2)Una de las reacciones más utilizadas ha sido la reacción de substitución de ligandos a partir del precursor Mn_{12} acetato. Se basa en la destilación del azeótropo ácido acético/tolueno en presencia del ácido carboxílico substituyente. Dicho proceso se

debe realizar reiteradamente para asegurar una completa substitución de los 16 carboxilatos periféricos entorno al núcleo metálico *(ver Fig. 1.2)*. Más recientemente, una vía paralela a esta aproximación ha sido desarrollada en nuestro grupo de investigación. Es decir, la obtención de Mn_{12} pivalato como precursor, $[Mn_{12}O_{12}(O_2C^tBu)_{16}(H_2O)_4]$ *(3)*, mediante el intercambio de acetatos en presencia de ácido piválico, $^tBuCO_2H$ *(4)*. A diferencia del tradicionalmente utilizado Mn_{12} acetato, la inclusión de grupos *terc*-butilo favorece la reacción de substitución de ligando gracias a: I) aumentar de forma significativa su solubilidad en los disolventes orgánicos más comunes, limitada en el caso del Mn_{12} acetato; II) el mayor impedimento estérico creado entre los grupos carboxilatos adyacentes y su constante de disociación *(pK_a=4.96)*, favorecen el desplazamiento ácido de ligandos en una única etapa.[2]

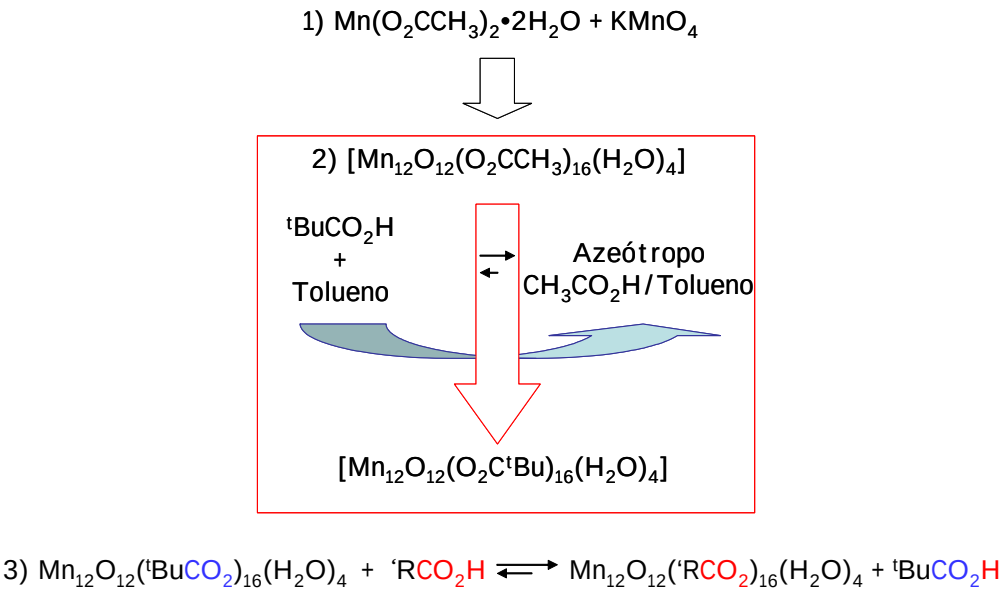

Fig. 1.2. Esquema sintético para la obtención de complejos de Mn_{12}. 1) Método descrito por Lis, 2-3) reacciones de substitución de ligando.

3)Adicionalmente, el desplazamiento ácido de ligandos por reacción entre dos clústeres de Mn_{12} a través de cantidades equimolares, da lugar al intercambio mutuo de los 8 carboxilatos periféricos en posición axial.[3] Esta posición se encuentra sometida a una mayor congestión estérica favoreciendo un equilibrio de intercambio de ligandos entre los dos centros metálicos con diferenciado carácter ácido.

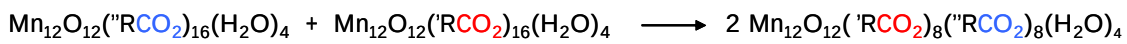

En el presente capítulo se estudiarán la síntesis y caracterización de complejos metálicos de la familia del Mn_{12} obtenidos mediante reacciones de substitución. Los grupos carboxilato *(RCO_2^-)* en estudio corresponderán a ligandos multifuncionales cuyas estructuras moleculares se pueden encuadrar dentro de dos familias diferentes: I) ligandos quirales en busca de nuevos materiales magneto-ópticos y II) ligandos de capa electrónica abierta que presenten interesantes propiedades magnéticas y

electroquímicas. Los materiales magneto-ópticos pueden ser utilizados como sistemas cuyo almacenamiento de información puede ser modulado a través de métodos ópticos. La detección espectroscópica permite obtener una mayor sensibilidad así como una mayor rapidez de lectura en comparación con los métodos magnéticos convencionales. Ello, junto con la posibilidad de observar nuevas fenomenologías relacionadas con el sinergismo entre propiedades magneto-ópticas[4] nos ha conducido a sintetizar por primera vez imanes unimoleculares quirales.

Tabla 1.1 complejos $[Mn_{12}O_{12}(O_2CR)_{16}(H_2O)_4]\cdot S$

R	Isómeros	Solvato	Síntesis
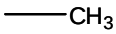	1,1,1,1	$2HOAc\cdot 4H_2O$	Método I
	1,1,1	$4H_2O$	Método II
	2,2	-	Método I
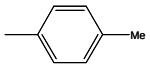	1,1,2	$3H_2O$	Método I
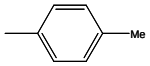	1,2,1	$4MePhCO_2H$	Método I
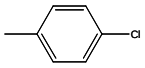	2,2	$8CH_2Cl_2$	Método I
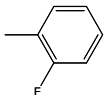	2,2	$4CH_2Cl_2\cdot HO_2\ CC_6H_4\text{-}2F$	Método II
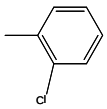	1,2,1	$8CH_2Cl_2\cdot 5H_2O$	Método II
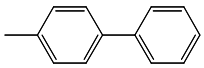	1,1,1,1	-	Método II
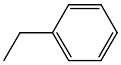	1,2,1	-	Método II
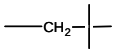	1,2,1	$CH_2Cl_2\cdot CH_3NO_2$	Método II

Método I: comproporcionación. Método II: substitución de ligando.

1.2. Ácidos carboxílicos ópticamente activos

1.2.1. Síntesis y caracterización

Los ácidos carboxílicos quirales escogidos *(RCO_2H)* se muestran en la Figura 1.3. Tal y como se puede comprobar, desde un punto de vista estructural, estos presentan una cadena orgánica de naturaleza variable y centro estereogénico lo más cercano posible al metal, siendo $R=CHEtC_6H_5$ *(5)*, $CHMeC_{10}H_{60}OMe$ *(6)*, CHMeCl *(7)*.

Estos trabajos se realizaron en colaboración con el grupo del Prof. J. Tejada de la Universidad de Barcelona, quienes realizaron gran parte de las medidas de

caracterización magnética en sólido y en solución, el grupo del Prof. B. Williamson de la Universidad de Canterbury en Nueva Zelanda, donde se realizaron las medidas de dicroismo magnético circular y con el Dr. D.B. Amabilino del *Institut de Ciència de Materials* de Barcelona en la realización de los espectros de dicroísmo circular.

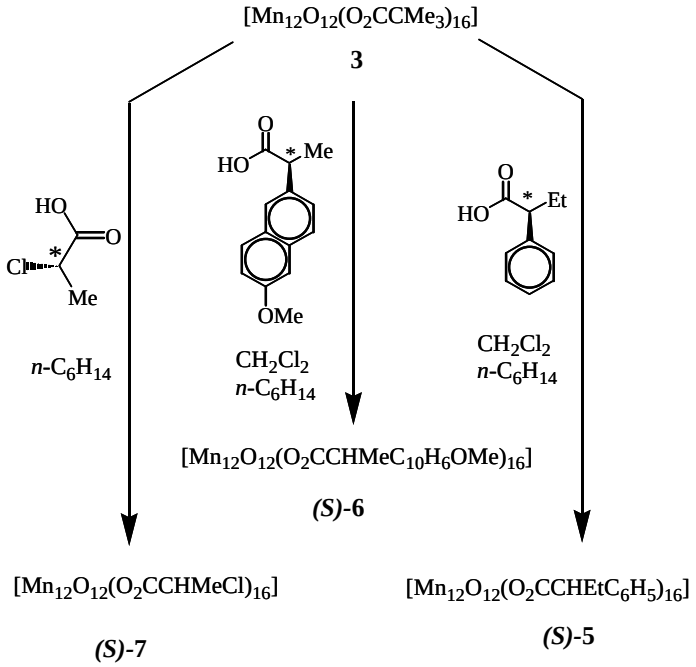

Fig. 1.3. Estructura molecular de ligandos ópticamente activos y sus correspondientes imanes unimoleculares de Mn_{12} enantioméricos a través de reacciones de substitución de ligando. Su purificación se llevó a cabo través de difusiones mediante la mezcla de los disolventes orgánicos expresados o bien por evaporación lenta.

Los complejos de Mn_{12} derivados de los ligandos quirales fueron obtenidos mediante una reacción de sustitución a partir del complejo **3**, Mn_{12} pivalato *(Fig. 1.3)*. Una vez los complejos fueron obtenidos y caracterizados químicamente, se procedió a su caracterización magneto-óptica. Las medidas de susceptibilidad magnética ac realizadas a campo cero *($H_{dc}=0$)* muestran, para los tres compuestos, señales fuera de fase dependientes de la frecuencia aplicada a través de un campo oscilante externo *($H_{ac}=3.5$ Oe)*. La presencia de dos máximos característicos en las regiones 2-4 K y 4-8 K, corresponden a la existencia de dos especies moleculares con diferente barrera energética efectiva y por consiguiente, diferente velocidad de relajación de la magnetización. También se realizaron los experimentos de magnetización en función del campo a varias temperaturas para los tres complejos. Además de la observación de fenómenos de histéresis, el incremento en la velocidad de relajación de la magnetización se produce a campos resonantes H_r o bien a campo nulo, como manifestación de la relajación del momento magnético por efecto túnel a través de la barrera energética. Tanto las medidas ac como las medidas de magnetización demostraron que los Mn_{12} quirales mantienen el comportamiento típico de imán unimolecular. A modo de ejemplo, las curvas ac y la magnetización en función del campo correspondientes al compuesto *(R)*-**7** se muestran en la Figura 1.4.

F

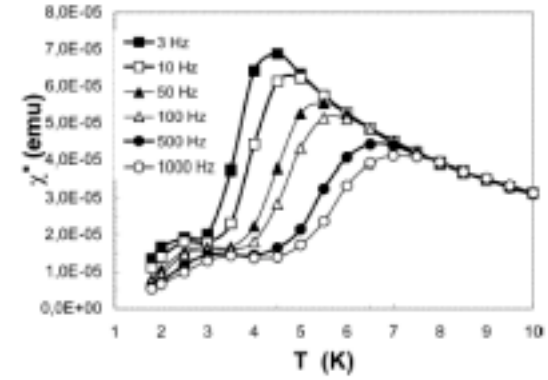

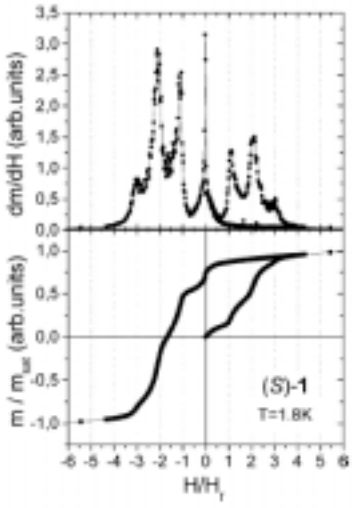

o
n
e
nte en fase de la susceptibilidad magnética para *(R)*-**7** en función de la temperatura a diferentes frecuencias y campos magnéticos H_{dc}= 0 y H_{ac}= 3.5 Oe *(iz.)*; magnetización a campo variable y su correspondiente derivada *(der.)*.

1.2.2. Propiedades magneto-ópticas: dicroísmo circular natural y dicroísmo circular magnético

Los espectros de UV-Vis visible de los complejos enantioméricos son similares a los descritos para los Mn_{12} no quirales, con una suave absorción entre 800 nm y su máximo alrededor de 260-240 nm. Por el contrario, el dicroísmo natural circular *(CD)* muestran efecto Cotton bien definidos, que no están presentes en los espectros de los ligandos quirales libres.[5] Estas absorciones se atribuyen a transiciones electrónicas ligando-metal y por consiguiente a la transferencia de quiralidad al núcleo metálico del Mn_{12}. La efectividad a inducir la actividad óptica al núcleo metálico depende del centro estereogénico y naturaleza del medio utilizado, dando lugar a variaciones de intensidad y desplazamiento en las bandas de absorción asociadas. De esta manera, los centros estereogénicos de *(S)*-**5** y *(S)*-**6** inducen a efectos Cotton de baja intensidad mientras que para un mismo complejo estudiado *(S)*-**7**, las medidas realizadas bien sea en disolución o estado sólido *(KBr)* implican evidentes cambios espectrales *(Fig. 1.5)*. A efectos comparativos, el correspondiente enantiómero *(R)*-**7** también fue sintetizado y caracterizado.

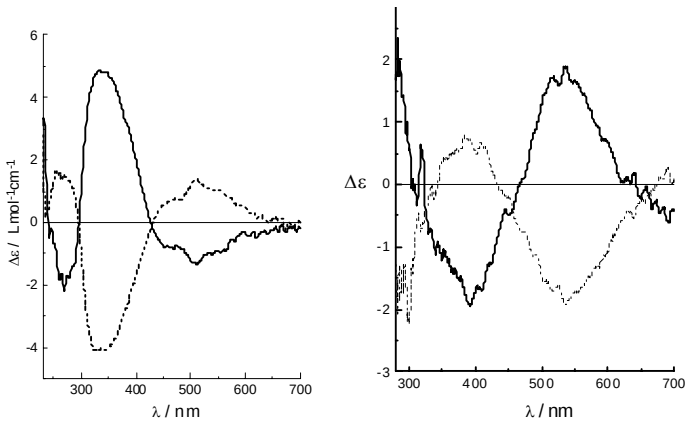

Fig. 1.5. Espectros de CD de los enantiómeros *(S)*-**7** *(línea continua)* y *(R)*-**7** *(línea discontinua)* en diclorometano *(iz.)* y KBr *(der.)* mostrando efectos Cotton opuestos.

De los tres complejos quirales obtenidos, el compuesto *(R)*-**7** presenta unas temperaturas de bloqueo superiores y una mayor intensidad en el CD, siendo un candidato idóneo en el estudio de las propiedades magneto-ópticas. En previsión a estos resultados se obtuvieron los espectros MCD a bajas temperaturas. En estos experimentos, la aplicación de un campo magnético uniforme paralelo a la dirección del haz de luz permite medir el grado de polarización de los espines en el estado fundamental. La absorción de luz polarizada circularmente en las transiciones ópticas MCD implican componentes del dipolo eléctrico no nulas perpendiculares entre sí y el campo magnético externo. En la Figura 1.6 se muestran los espectros de MCD de *(R)*- y *(S)*-**7**. La intensidad de la señal MCD está compuesta por una serie de componentes denominados términos C de Faraday con origen en las diferencias de población entre los niveles de Zeeman del estado electrónico fundamental, siendo dependientes de la temperatura y del campo magnético aplicado. A temperaturas superiores a los 3 K, las intensidades de los términos C son reversibles con los cambios del campo magnético externo. No obstante, por debajo de los 3 K se observan fenómenos de histéresis después de eliminar el campo magnético aplicado. La repetición de estos experimentos con otros complejos de Mn_{12} aquirales demostraron un comportamiento prácticamente muy parecido, lo que indica que cualquier efecto magneto-quiral es demasiado débil para ser observado con esta técnica y en las condiciones experimentales presentes.*

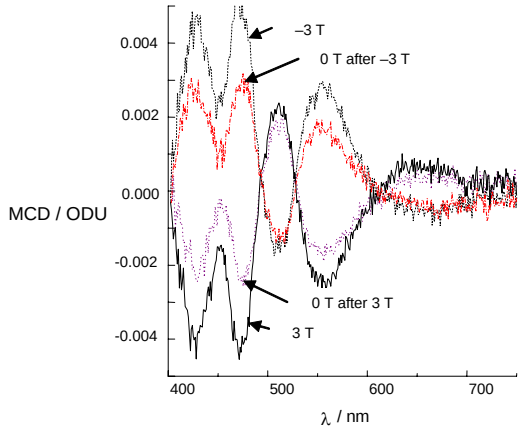

Fig. 1.6. Espectro de MCD correspondiente a la medida de una disolución congelada de *(S)*-**7** a 1.65 K en mezclas diclorometano-tolueno (1:1) a 3, -3 y 0 T tras eliminar el campo magnético aplicado.

1.3. Ácidos carboxílicos de capa electrónica abierta

1.3.1. Síntesis y caracterización

La segunda familia de ligandos funcionales que se estudió a lo largo de esta Tesis fue la familia de radicales policlorotrifenilmetílicos (PTM),[6] y más concretamente el ácido carboxílico PTMMC *(8)* mostrado en el Esquema 1.[7] Dicho ligando, además de poseer una estructura de capa electrónica abierta, posee unas interesantes propiedades redox siendo posible su oxidación o reducción de forma reversible. La elección de este ligando se realizó en base a su elevada estabilidad química y térmica, con origen en los tres anillos aromáticos totalmente o parcialmente clorados, lo cual origina una elevada protección entorno al carbono radicalario central.

* Para más información ver artículos A y B

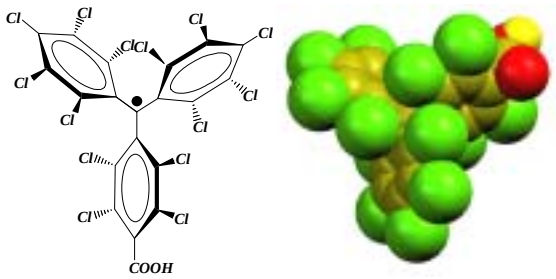

Esquema 1. Estructura molecular del PTMMC.

La reacción de substitución de ligando se llevó a cabo a partir de los precursores **2**, Mn_{12} acetato, y **3**, Mn_{12} pivalato, indistintamente. Sorprendentemente, y a diferencia de los ligandos carboxilato anteriormente estudiados, el radical **8** desencadenó la fragmentación del núcleo central del Mn_{12}. Como consecuencia, un nuevo clúster de baja nuclearidad se obtuvo correspondiente a una estructura trinuclear de Mn^{II} con topología lineal *(Fig. 1.7)*.[8] De esta manera, el Mn central se encuentra hexacoordinado a través de 6 radicales carboxilato **8** que actúan de puente con los dos iones Mn externos. Estos últimos, completan su esfera de coordinación octaédrica a través de tres moléculas de disolvente adicionales, H_2O ó EtOH.

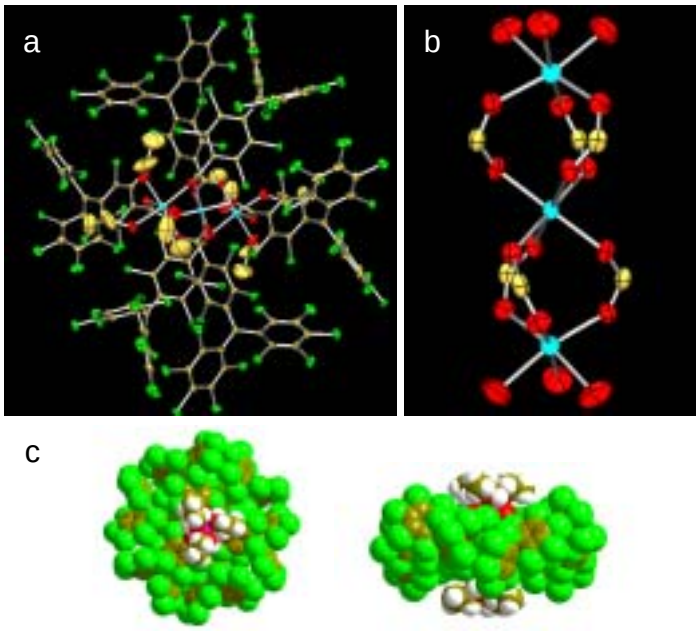

Fig. 1.7. Estructura molecular de $[Mn_3(PTMMC)_6(EtOH)_6]\cdot 6EtOH$ *(a)* mostrando la topología lineal del núcleo metálico corrspondiente a un trímero de Mn^{II} *(b)*. Geometría en forma discoidal en las perspectivas frontal y lateral, respectivamente *(c)*.

Las medidas magnéticas de $\chi\cdot T$ realizadas muestran la tendencia de interacciones de carácter antiferromagnético a bajas temperaturas. Sin embargo, las medidas de magnetización a campo variable no alcanzan valores de saturación incluso a campos magnéticos externos de 7 teslas. Para el intervalo de temperaturas estudiado *(2-10 K)* los valores iniciales de magnetización siguen la ley de Brillouin hasta alcanzar las 2T, campo a partir del cual la magnetización se incrementa linealmente con el campo. Este comportamiento, característico de especies ricas en especies Mn^{II} *(S=5/2)*, se explica a través del posible cruce entre niveles desdoblados por la aplicación del campo magnético externo. De esta manera, se genera una alta densidad de estados magnéticos

energéticamente solapados y por consiguiente accesibles térmicamente incluso a bajas temperaturas *(Fig. 1.8)*.

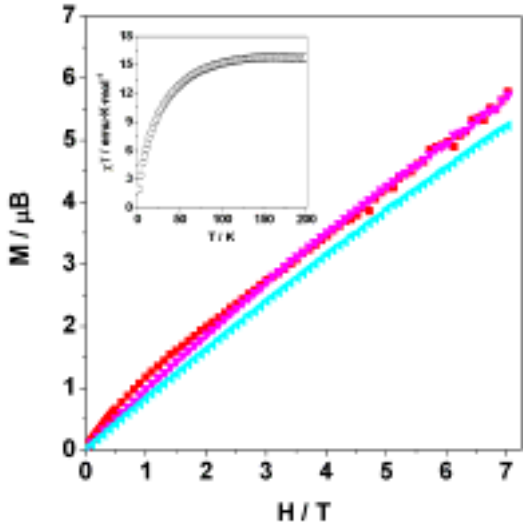

Fig. 1.8. Magnetización frente al campo magnético externo aplicado a 1.8 K *(rojo)*, 5K *(magenta)* y 10K *(celeste)*. Insertado en la figura se representa la dependencia χT con la temperatura en el intervalo 1.8-200 K.

Dada la imposibilidad de obtener el compuesto deseado de Mn_{12} por la vía de substitución de ligando convencional, se ensayaron paralelamente rutas sintéticas alternativas tales como la reacción directa a partir de Mn^{II} en presencia del radical **8**, así como reacciones de comproporcionación en medio orgánico entre fuentes de Mn^{II} y Mn^{VII} a partir de $[_nBu_4N]MnO_4$ *(10)*. Sin embargo, en ambos casos se obtuvieron las mismas formas estructurales, $[Mn_3(PTMMC)_6(EtOH)_6]\cdot 6ETOH$ *(9)*. La ausencia de complejos de valencia mixta y estabilización del Mn en su estado de oxidación *(II)* se atribuyen supuestamente a procesos de descarboxilación oxidativa.[9] La presencia de ácidos fuertes hábiles catalizan los procesos de ruptura hemolítica por descarboxilación oxidativa a través de intermedios catiónicos tipo carboxilato-Mn^{III}.[10-12]

1.3.2 Efecto de la acidez y volumen de los ácidos carboxílicos en la estabilidad relativa de los complejos de Mn_{12}

La ruptura del núcleo de $[Mn_{12}(\mu_3\text{-}O)_{12}]$ cuando se usa el ligando policlorotrifenilmetílico descrito en el apartado anterior, se puede atribuir de forma tentativa a dos causas principales: I) el elevado volumen de este ligando que conlleva a la generación de congestiones estéricas; y II) su marcada acidez. Así, para profundizar en el origen de dicho comportamiento, se ensayaron nuevas reacciones de substitución de ligando en presencia de ácidos carboxílicos *(RCO_2H)* cuya cadena orgánica R difiere gradualmente en el tamaño así como en el grado de acidez *(Tabla 1.2)*. Dicha serie permite estudiar el efecto de los ligandos, ya sea por impedimento estérico *($R=C(CH_3)_3$)* o bien por efectos inductivos *($R=CF_3$, CCl_3, CBr_3)*, favoreciéndose en este último caso los procesos de descarboxilación oxidativa catalizada en presencia de ácidos carboxílicos fuertes.

Tabla 1.2 Volumen de Van der Waals referente al grupo orgánico R, pKa de los ligandos protonados y temperatura de descomposición *(T_d)* del Mn_{12} cuando proceda.

R	R volumen ($Å^3$)[13]	pKa de RCO_2H[14]	Mn_{12}	T_d (ºC)
CBr_3	92.8	2.13	No	-
CCl_3	71.0	1.10	No	-
$C(CH_3)_3$	70.7	4.96	Sí	150
$CHCl_2$	56.2	1.37	Sí	110
CF_3	34.1	0.67	Sí	130
CH_3	26.9	4.79	Sí	180

Estos trabajos se realizaron conjuntamente en colaboración con el Dr. Philippe Gerbier de la Universidad de Montpellier en los estudios de caracterización térmica y el Dr. Javier Campo del Instituto de Ciencia de los Materiales de Aragón en las medidas magnéticas.

Las reacciones de substitución de ligando en presencia de ácidos carboxílicos de mayor volumen y acidez, como son el CCl_3CO_2H *(11)* y CBr_3CO_2H *(12)*, demostraron que en ningún caso se formaban los correspondientes complejos de Mn_{12}. Por el contrario, los estudios de caracterización estructural por espectroscopia de rayos-X demostraron la formación de complejos de baja nuclearidad con estructuras moleculares equivalentes a las ya descritas en complejos de Mn_3 y/o Mn_6 *(Fig. 1.9)*.[15] La estructura trinuclear de Mn_3 corresponde a un complejo de valencia mixta *($Mn^{II}{\cdot}2Mn^{III}$)* cuyos átomos de Mn se enlazan entre sí a través del ligando puente μ_3-O^{2-}.[16] La esfera de coordinación se completa a través de 6 carboxilatos periféricos y tres moléculas de disolvente, $[Mn_3O(O_2CR)_6(S)_3]$. Para el caso de los complejos de Mn_6 la estructura nuclear consiste en 6 átomos de Mn con valencia mixta *($4Mn^{II}{\cdot}2Mn^{III}$)* dispuestos en los vértices de dos tetraedros que comparten una misma arista y coordinados a través de dos ligandos puentes μ_4-O^{2-}. La esfera de coordinación se completa a través de 10 carboxilatos periféricos puente y 4 moléculas de disolvente coordinadas, $[Mn_6O_2(O_2CR)_{10}(S)_4]$.[17]

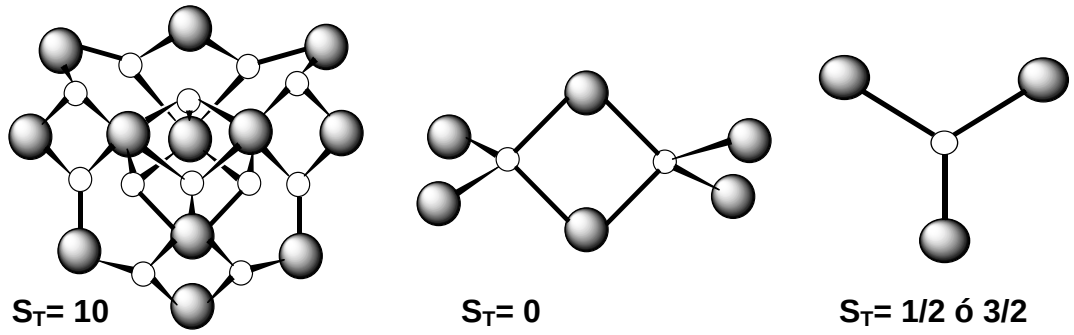

Fig. 1.9. Representación esquemática de los núcleos metálicos y sus estados de espín asociados a clústeres de Mn_{12}, Mn_6 y Mn_3, respectivamente.

Las medidas de susceptibilidad magnética $\chi{\cdot}T$ en función de la temperatura muestran un comportamiento antiferromagnético para los complejos de Mn_6 obtenidos *($R=CBr_3$)*. El estado fundamental de espín corresponde a S=0 tal y como confirman las medidas de

magnetización realizadas a campo variable. Por lo que respecta al complejo de Mn_3, la frustración de espín asociada a la interacción magnética de la estructura trinuclear Mn_3O, conlleva a dos estados fundamentales de espín posibles, S=1/2 ó S=3/2, en función del tipo de ligandos.[18] Particularmente, en presencia de carboxilatos periféricos donde R=CCl_3 el estado fundamental corresponde a S=3/2.

La imposibilidad de obtener complejos de Mn_{12} derivados de los ligandos carboxílicos **11** y **12** se atribuyó inicialmente a la presencia de elevadas congestiones estéricas. Sin embargo, el uso de carboxilatos voluminosos como el pivalato *(R=C(CH$_3$)$_3$)*, se ha mostrado eficiente en la obtención de complejos de Mn_{12},[19] lo que confirma que ambos factores, tanto el volumen como la acidez tienen un efecto considerable. El mismo comportamiento se observa si nos centramos en la estabilidad térmica de los complejos de Mn_{12} mostrados en la Tabla 1.2. Las temperaturas de descomposición *(T_d)* relativas *(R=CH$_3$) > (R= ^{t}Bu) > (R=CF$_3$)*, no se correlacionan con el volumen de los grupos R: *(^{t}Bu) > (CF$_3$) > (CH$_3$)*, que se muestran en la Figura 1.10. Adicionalmente, no existe tampoco correlación con el pKa : *(R=Me) ~ (R= ^{t}Bu) > (R=CF$_3$)*. Ello confirma que la estabilidad térmica relativa depende de ambos factores.†

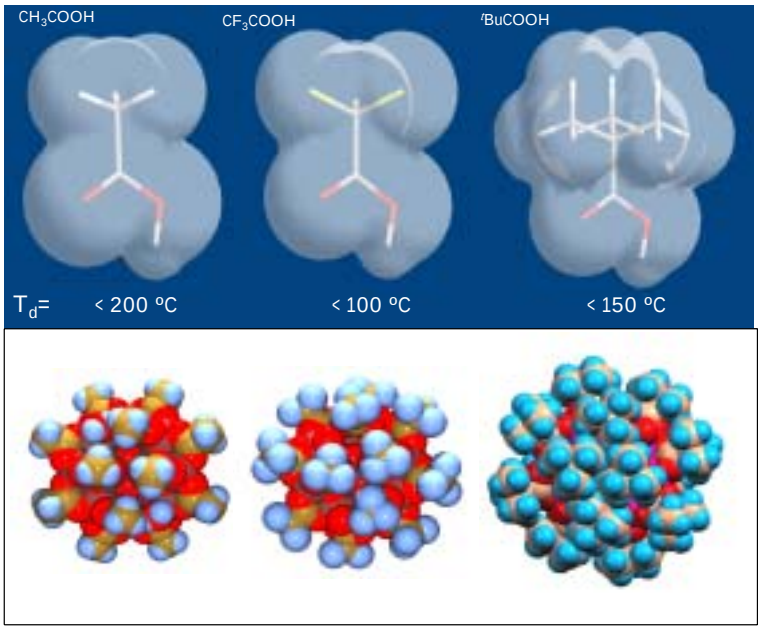

Fig. 1.10. Representación de estructuras moleculares de Mn_{12} en función de los volúmenes de Van der Waals mostrando la mayor congestión estérica entre los 4 substituyentes carboxilatos localizados a lo largo del eje axial: [$Mn_{12}O_{12}(O_2CCH_3)_{16}(H_2O)_4$] *(2)*, [$Mn_{12}O_{12}(O_2CCF_3)_{16}(H_2O)_4$] *(13)* y [$Mn_{12}O_{12}(O_2C^tBu)_{16}(H_2O)_4$] *(3)*, respectivamente.

Reacciones térmicas

Para completar los estudios anteriormente mencionados, se ensayaron reacciones de termólisis de los complejos de Mn_{12} con los nuevos carboxilatos mostrados en la tabla

† Para más información ver artículo C

1.2. En concreto, se calentaron bajo reflujo en disolución aquellos complejos de Mn_{12} que exhiben baja estabilidad térmica y se estudiaron los productos de reacción resultantes.

En el caso del complejo **3**, Mn_{12} pivalato, previo tratamiento térmico en una disolución de tolueno a reflujo, se aislaron nuevamente complejos pertenecientes a la familia del Mn_6, corroborándose la obtención de especies metálicas de baja las cuales parecen ser termodinámicamente más estables.[‡] Sin embargo, tras la reacción de substitución en presencia de grupos voluminosos *($R=C(CH_3)_3$)* a grupos con menor impedimento estérico *($R=CHCl_2$)*, pasamos de una estructura discreta a un sistema polimérico 1-D. Para este caso particular, la combinación de efectos estéricos e inductivos le confieren a la estructura del Mn_{12} una baja estabilidad térmica. Las reacciones de termólisis favorecen la fragmentación de su núcleo intrínseco dando lugar a mezclas de compuestos. Por un lado se obtienen complejos de Mn_6 supuestamente formados a través de la agregación térmica de complejos de Mn_3. Estos últimos, sin embargo, aparecen como residuo de reacción dando lugar a especies catenarias *(1D)*–$[[Mn_3O(O_2CCHCl_2)_6(H_2O)]$-$(O_2CCHCl_2)$-$[Mn(H_2O)_4]$-$(O_2CCHCl_2)]$- *(14) (Fig. 1.11)*.

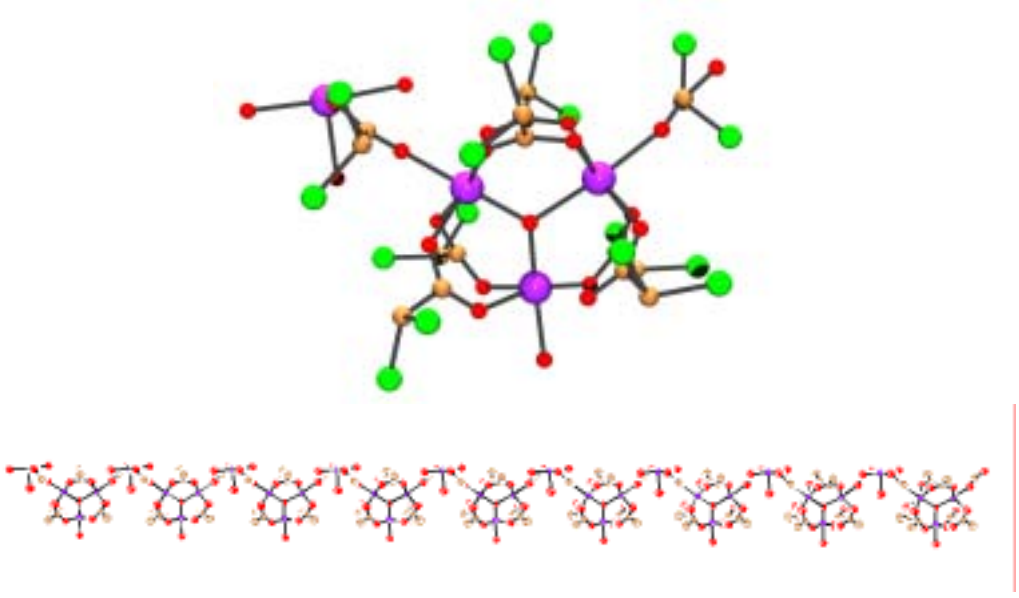

Fig. 1.11. Estructura molecular polimérica *(1D)*–$[[Mn_3O(O_2CCHCl_2)_6(H_2O)]$-$(O_2CCHCl_2)$-$[Mn(H_2O)_4]$-$(O_2CCHCl_2)]$- *(14)*

Para acabar de justificar la obtención de complejos metálicos de baja nuclearidad se estudió la fragmentación de la estructura metálica del Mn_{12} a partir de ácidos carboxílicos con marcada acidez y poco impedidos estéricamente. Dichas características se combinan perfectamente mediante el uso del ácido propiólico $HC{\equiv}CCO_2H$ *(15)*, cuya cadena orgánica lineal minimiza las congestiones estéricas entre carboxilatos adyacentes en la esfera de coordinación. La substitución ácida de ligando en presencia del precursor **3**, Mn_{12} pivalato, da lugar a su derivación manteniendo la estructura nuclear. Sin embargo, y a pesar de haberse minimizado los efectos estéricos, su marcada acidez le confiere una temperatura de descomposición *(158 ºC)* similar a la del

[‡] Para más información ver artículo D

complejo precursor **3** *(150 ºC)*, mostrando a su vez una repentina degradación exotérmica de la estructura nuclear. Como consecuencia, de su fragmentación se obtienen tríadas de Mn^{II} con estructura lineal muy parecida a la ya descrita en el caso del radical **8** *(Fig. 1.12)*. Los procesos de descarboxilación oxidativa de ligando vuelven a ser responsables de la reducción del Mn a su estado de oxidación más bajo, tal y como es de esperar, en presencia de ácidos fuertes. Sin embargo, la gran diferencia de tamaños se ve reflejada en los cambios de dimensionalidad correspondientes al empaquetamiento molecular. El gran volumen de los grupos carboxilato **8** entorno a la esfera de coordinación da lugar a sistemas 0-D, $[Mn_3(PTMMC)_6(H_2O)_6]$ *(9)*, con morfología discoidal *(ver Fig. 1.7)*. Sin embargo, para el caso del ácido carboxílico **15**, la minimización de las congestiones estéricas entre carboxilatos adyacentes dentro de la esfera de coordinación, conlleva a la formación de la estructura $[Mn_3(O_2CC{\equiv}CH)_6(H_2O)_4]{\cdot}2H_2O$ *(16)* extendida en el plano *(2-D) (Fig. 1.13)*. De esta manera, los grupos propiolato muestran distintos modos de coordinación en la estructura actuando como ligandos puente μ_3-(O_1, O_2, O'_2)-$O_2CC{\equiv}CH$, μ_2-(O_1, O_2)-$O_2CC{\equiv}CH$ y μ_2-(O_1)-$O_2CC{\equiv}CH$.

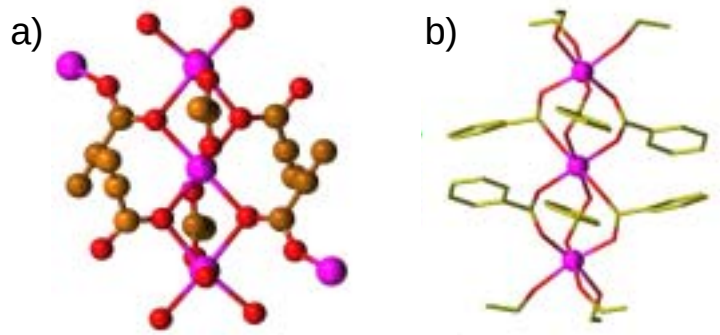

Fig. 1.12. Topología lineal correspondiente a la unidad estructural de los núcleos de Mn(II). a) Mn_3-$O_2CC{\equiv}CH$ *(16)* y b) Mn_3-PTMMC *(9)*.

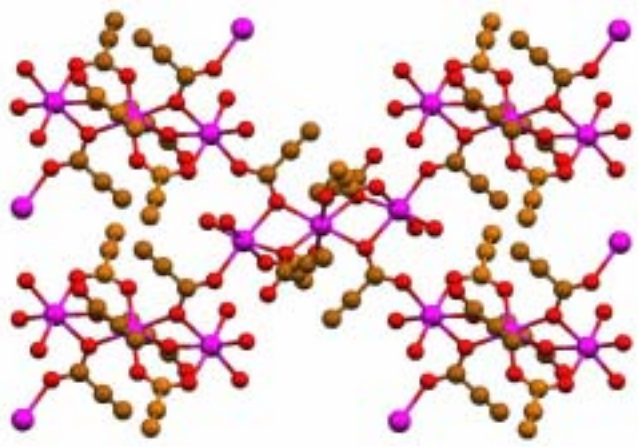

Fig. 1.13. Estructura molecular extendida en el plano correspondiente al trímero Mn_3-$O_2CC{\equiv}CH$ *(16)*.

En resumen, el volumen no sólo afecta a la estabilidad térmica de los Mn_{12} sino también a la naturaleza y topología nuclear de los productos resultantes. El aumento de tamaño en las cadenas orgánicas R influye significativamente en un mayor incremento de las repulsiones estéricas entre carboxilatos adyacentes. Por consiguiente, además de la obtención de sistemas metálicos de baja nuclearidad, se observan cambios en la dimensionalidad de los sistemas generados por fragmentación. Estas alteraciones estructurales varían desde O-D en el caso de ligandos altamente voluminosos, como es el PTMMC *(8)*,[§] hasta 2-D en el caso del ácido propiólico *(15)*.

[§] Para más información ver artículos E

1.4. Referencias

1. T. Lis, *Acta Crystallogr., Sect. B*, **1980**, *36*, 2042.
2. Ph. Gerbier, D. Ruiz-Molina, N. Domingo, D.B. Amabilino, J. Vidal-Gancedo, J. Tejada, J. Veciana, *Monatsch. Chem.*, **2003**, *134*, 265.
3. M. Soler, P. Artus, K. Folting, J.C. Huffman, D.N. Hendrickson, G. Christou, *Inorg. Chem.*, **2001**, *40*, 4902.
4. G.L.J.A. Rikken, E. Raupach, *Nature*, **1997**, *390*, 493.
5. M. Vargek, T.B. Freedman, E. Lee, L.A. Nafie, *Chem. Phys. Lett.*, **1998**, *287*, 359.
6. M. Ballester, *Acc. Chem. Rev.*, **1985**, *18*, 380.
7. D. Maspoch, L. Catala, Ph. Gerbier, D. Ruiz-Molina, J. Vidal-Gancedo, K. Wurst, C. Rovira, J. Veciana, *Chem. Eur. J.*, **2004,** *8*, 3635.
8. R.T.W. Scott, S. Parson, M. Murugesu, W. Wernsdorfer, G. Christou, E.K. Brechin, *Chem. Commun.*, **2005**, 2083.
9. J. M. Anderson, J.K. Kochi, *J. Am. Chem. Soc.*, **1970**, *92*, 2450.
10. S.S. Lande, J.K. Kochi, *J. Am. Chem. Soc.*, **1968**, *90*, 5196.
11. R.A. Sheldon, J.K. Kochi, *J. Am. Chem. Soc.*, **1968**, *90*, 6688.
12. J.M. Anderson, J.K. Kochi, *J. Org. Chem.*, **1970**, *35*, 986.
13. Hyperchem QSAR Properties Software, v. 7.5, Hypercube, Inc.
14. Advanced Chemistry Development (ACD) Software, Solaris, v. 4.67.
15. G. Christou, *Acc. Chem. Res.*, **1989**, *22*, 328.
16. J.B. Vincent, H.R. Chang, K. Folting, J.C. Huffman, G. Christou, D.N. Hendrickson, *J. Am. Chem. Soc.*, **1987**, *109*, 5703.
17. A.R. Schake, J.B. Vincent, Q. Li, P.D.W. Boyd, K. Folting, J.C. Huffman, D.N. Hendrickson, G. Christou, *Inorg. Chem.*, **1989**, *28*, 1915.
18. J.K. McCusker, H.G. Jang, S. Wang, G. Christou, D.N. Hendrickson, *Inorg. Chem.*, **1992**, *31*, 1874.
19. A. Graham, S. Meier, S. Parsons, R.E.P. Winpenny, *Chem. Commun.*, **2000**, 811.

Artículos relacionados: Capítulo 1

Síntesis y caracterización de nuevos Mn_{12} multifuncionales

Artículo A

Título:
Synthesis and characterization of a new chiral nanomagnet

Autores:
N. Domingo, Ph. Gerbier, J. Gómez, D. Ruiz-Molina, D.B. Amabilino, J. Tejada, J. Veciana

Revista:
Polyhedron

Available online at www.sciencedirect.com
SCIENCE DIRECT®
PERGAMON
Polyhedron 22 (2003) 2355–2358
POLYHEDRON
www.elsevier.com/locate/poly

Synthesis and characterization of a new chiral nanomagnet

Neus Domingo [a,*], Philippe Gerbier [b], Jordi Gómez [b], Daniel Ruiz-Molina [b], David B. Amabilino [b], Javier Tejada [a], Jaume Veciana [b]

[a] Facultat de Física, Universitat de Barcelona, Avinguda Diagonal 647, 08028 Barcelona, Catalonia, Spain
[b] Institut de Ciència de Materials de Barcelona (CSIC), Campus Universitari, 08193 Bellaterra, Catalonia, Spain

Received 8 October 2002; accepted 7 March 2003

Abstract

The dodecanuclear complexes formed between manganese ions and carboxylate anionic ligands are the single molecule magnets (SMMs) with greatest synthetic accessibility and richness of magnetic properties. In this work, we describe a recently synthesized chiral SMM which presents both spontaneous magnetization and optical activity. This objective has been targeted because of the possibility of observing new phenomena related with the synergy between structural chirality, optical activity, and magnetic ordering.

Keywords: Single molecule magnet; Susceptibility; Chirality; Manganese; Magnetic clusters

1. Introduction

In 1993 it was discovered for the first time that the acetate-coated dodecamanganese cluster $[Mn_{12}O_{12}(O_2CCH_3)_{16}(H_2O)_4]\cdot 4H_2O\cdot 2CH_3CO_2H$ ($[Mn_{12}Ac]$) functions as a nanoscale molecular magnet and for this reason the term of single molecule magnet (SMM) was coined. Since then, a few more families of complexes that function as SMMs have been obtained. There are basically two different synthetic procedures available for making new $[Mn_{12}O_{12}(O_2CR)_{16}(H_2O)_4]$ complexes: the original method used by Lis [1] to synthesize the acetate Mn_{12} complex and a second synthetic approach, based on ligand-substitution reactions, which are driven by the greater acidity of the added carboxylic acids RCO_2H and/or the removal by distillation of an azeotrope of acetic acid and toluene (see Eq. (1)).

$$[Mn_{12}Ac] + 16RCO_2H \rightarrow [Mn_{12}O_{12}(O_2CR)_{16}(H_2O)_4] + 16MeCO_2H \quad (1)$$

The advantage of this second method is that reaction yields are generally larger than those obtained in the first approach. More recently, a new functionalization of Mn_{12} SMM with ligands other than carboxylate or site-specific modifications to yield mixed carboxylate $[Mn_{12}O_{12}(O_2CR)_8\cdot(O_2CR')_8(H_2O)_4]$ complexes have been achieved [2,3]. The interest for the development of these new synthetic methodologies lies in the variety of reactivity studies and applications that can be achieved with an intrinsic SMM behavior.

Optically active molecular magnetic materials are interesting from various perspectives, but not least from the viewpoint of combining optical and magnetic effects [4,5]. During the last few years, increasing interest about new phenomena of magnetochirality has appeared, particularly after its first experimental observation by Rikken and Raupach [6] in 1997, and due to its possible contributions to the answer of the origin of homochirality of life [7–10]. In this context, we report here the magnetic characterization and natural circular dichroism (CD) properties of enantiomeric SMMs of the $[Mn_{12}O_{12}(OOCR)_{16}]S_x$ (S = solvent) family [11]. The synthesis of the (*R*)-, (*S*)-, and (*RS*)-chloropropionate

* Corresponding author.
E-mail address: neus@ubxlab.com (N. Domingo).

0277-5387/03/$ - see front matter
doi:10.1016/S0277-5387(03)00308-5

Mn_{12} clusters was achieved, and the optical activity of the chiral compounds was confirmed by CD spectroscopy.

2. Experimental

2.1. Synthesis of chiral SMM

The synthesis of the clusters (*R*)- and (*S*)-$[Mn_{12}O_{12}(O_2CCHClMe)_{16}(H_2O)_4]\cdot CHClMeCO_2H$ ((*R*)- and (*S*)-**1**) described here was achieved using a modification of the synthetic route shown in Eq. (1) using the pivaloate leaving anion strategy reported recently [12]. The synthesis will be detailed elsewhere [13].

2.2. Physical measurements

Magnetic characterization was performed in a commercial Quantum Design MPMS2 SQUID (rf) magnetometer equipped with a 5 T magnet and placed in a cryostat with a working temperature ranging from 1.8 to 300 K. Microcrystals were first oriented and restrained in Eicosan to prevent torquing. Alignment in Eicosan was performed while keeping the samples in a 5 T field at a temperature above the melting point (312 K) of Eicosane for 15 min and then decreasing the temperature gradually to constrain the sample.

3. Results and discussion

The optical activity of the chiral compounds (*R*)- and (*S*)-$[Mn_{12}O_{12}(O_2CCHClMe)_{16}(H_2O)_4]\cdot CHClMeCO_2H$ ((*R*)- and (*S*)-**1**) in solution was confirmed by natural circular dichroism (NCD) spectra shown in Fig. 1. Three different contributions can be distinguished: a weak Cotton effect in the region of 520 nm and a more intense one at 345 nm of opposite sign, and a further weak signal at 260 nm. On the other hand, UV–Vis absorption spectrum is characterized by a featureless rise in the extinction coefficient from approximately 800–200 nm, with a plateau between 260 and 240 nm, as in the acetate cluster [14]. Thus, the optical activity arising from the manganese ions in the visible region has a high *g*-value, a prerequisite for the observation of magnetochiral effects.

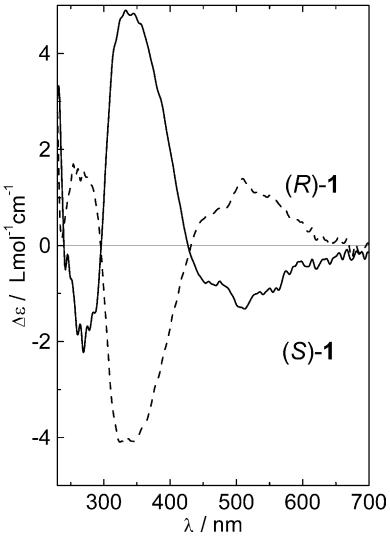

Fig. 1. The CD spectrum of the chiral manganese clusters in dichloromethane at room temperature.

For magnetic characterization in the solid state, polycrystalline samples were oriented in an Eicosan matrix. a.c. magnetic susceptibility was measured in the temperature range from 1.8 to 10 K and at six different frequencies between 3 and 1000 Hz. The in-phase component of the a.c. susceptibility shows two different frequency-dependent peaks, one in the low-temperature region of 2.5–4 K and another in the high-temperature region of 4–7 K, followed by a Curie decrease as temperature is raised (Fig. 2). The out-of-phase component is shown in Fig. 3. It also exhibits two frequency-dependent peaks, the one in the low-temperature region being almost one order of magnitude lower than the one in the high-temperature region. This result has already been observed for other Mn_{12} complexes [15–17] and indicates the presence of two different relaxation mechanisms in the compounds governed by two different effective energy barriers and characteristic relaxation times.

Magnetization relaxation times (τ) are obtained from the relationship $\varpi\tau = 1$ at the maxima of the χ''_M vs. temperature curves, the position of which is defined to be the blocking temperature. Least-square fit of data pairs (w, T_B) for the two peaks obtained for the χ''_M data to the Arrhenius law (Eq. (1))

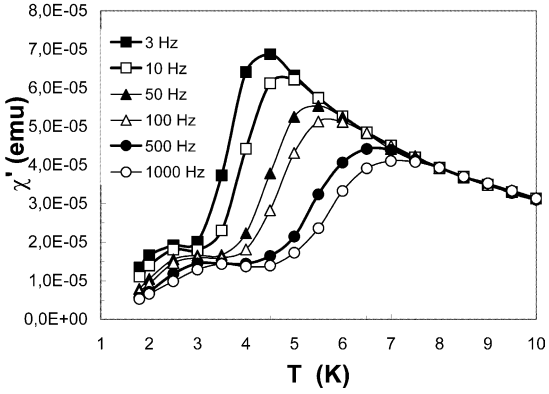

Fig. 2. In-phase component of the a.c. magnetic susceptibility for (*R*)-**1** isomer as a function of the temperature at six different frequencies, measured with applied magnetic fields of $H_{a.c.} = 3.5$ Oe and $H_{d.c.} = 0$ Oe.

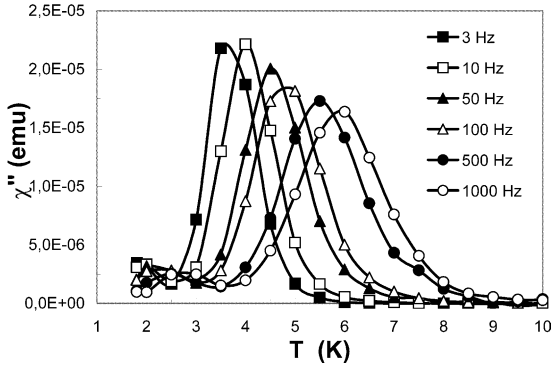

Fig. 3. Out-of-phase component of the a.c. magnetic susceptibility for (*R*)-**1** isomer as a function of the temperature at six different frequencies, measured with applied magnetic fields of $H_{a.c.} = 3.5$ Oe and $H_{d.c.} = 0$ Oe.

$$\frac{1}{\tau} = \frac{1}{\tau_0}\exp\left(\frac{-U_{eff}}{kT_B}\right)$$

where U_{eff} is the effective anisotropy energy barrier, k the Boltzmann constant, and T the temperature, leads to values for the energy barrier of 21.7 and 50.7 K, for the low-temperature peak and the high-temperature peak, respectively, with an attempt frequency of τ_0 of 10^{-6} s for the former and 3×10^{-7} s for the latter. The contribution of each mechanism to the overall signal can be obtained from the adjustment of Curie tail of the in-phase component for high temperatures. It is found that almost a 15% of the molecules follow the fast relaxation mechanism governed by the low energy barrier, while the other 85% behave under the highest energy barrier, more typical for these Mn_{12} clusters.

Field dependence of magnetization at 1.8 K is shown in Fig. 4(b). Typical step hysteresis behavior is observed at regular applied fields of $H = nH_r$, where H_r is the resonant field for Mn_{12} clusters taken as 0.46 T. These steps, clearly seen as peaks in the field derivative of the signal shown in Fig. 4(a), correspond to an increase of relaxation of magnetization due to resonant field tunneling of magnetic moment through the anisotropy energy barrier, between two levels with the same energy, one on each side of the barrier. The steps in this case are not very sharp and well defined as it is the case for monocrystalline samples because of a certain lack of orientation of some microcrystals. The big decay of the signal for zero applied field corresponds to the influence of the fast relaxation particles that still behave superparamagnetic at the lowest working temperature of 1.8 K. No difference is observed between the two enantiomers.

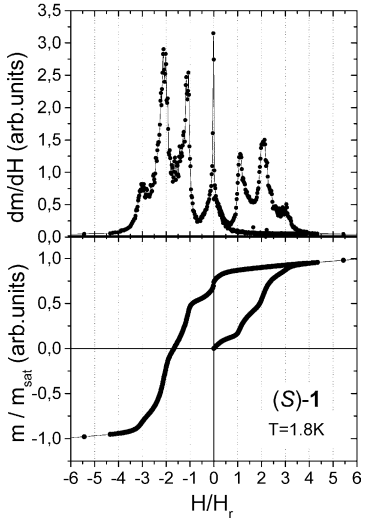

Fig. 4. Field dependence of magnetization (b) and its derivative (a) for oriented microcrystalline sample of the (*S*)-**1** enantiomer in Eicosan matrix, measured at 1.8 K.

4. Conclusions

We have prepared and characterized enantiomeric SMMs which present magnetic ordering and tunneling behavior typical of these dodecamanganese clusters. From the a.c. magnetic susceptibility measurements we have determined the presence of two relaxation barriers in a proportion of 15:85 for the fast and slow, respectively, indicative of the presence of two different clusters in the microcrystalline solid. The presence of significant optical activity in the visible part of the electromagnetic spectrum with a relatively high g-value bodes well for the observation of magnetochiral dichroism in these SMMs.

Acknowledgements

This work was supported by grants from the Programa Nacional de Materiales of the DGI (Spain), under project MAGMOL (MAT2000-1388-C03-01), and the 3MD Network of the TMR program of E.U. (contract ERBFMRX CT980181). N.D. also acknowledges a grant from the Ministry of Education and Science, Spain.

References

[1] T. Lis, Acta Cryst. B 36 (1980) 2042.
[2] C. Boskovic, M. Pink, J.C. Huffman, D.N. Hendrickson, G. Christou, J. Am. Chem. Soc. 123 (2001) 9914.
[3] P. Artus, C. Boskovic, J. Yoo, W.E. Streib, L.-C. Brunel, D.N. Hendrickson, G. Christou, Inorg. Chem. 40 (2001) 4199.
[4] (a) S. Decurtins, Philos. Trans. R. Soc. London, Ser. A 357 (1999) 3025;
(b) K. Nakayama, T. Ishida, R. Takayama, D. Hashizume, M. Yasui, F. Iwasaki, T. Nogami, Chem. Lett. (1998) 497;
(c) H. Kumagai, K. Inoue, Angew. Chem., Int. Ed. Engl. 38 (1999) 1601;
(d) R. Andrés, M. Brissard, M. Gruselle, C. Train, J. Vaisser-

mann, B. Malézieux, J.-P. Jamet, M. Verdaguer, Inorg. Chem. 40 (2000) 4633;
(e) E. Coronado, J.R. Galán-Mascarós, C.J. Gómez-García, J.M. Martínez-Agudo, Inorg. Chem. 40 (2001) 113;
(f) A. Caneschi, D. Gatteschi, N. Lalioti, C. Sangregorio, R. Sessoli, J. Chem. Soc., Dalton Trans. (2000) 3907;
(g) M. Minguet, D. Luneau, E. Lhotel, V. Villar, C. Paulsen, D.B. Amabilino, J. Veciana, Angew. Chem., Int. Ed. Engl. 41 (2002) 586;
(h) M. Minguet, D.B. Amabilino, K. Wurst, J. Veciana, J. Chem. Soc., Perkin Trans. 2 (2001) 670.
[5] L.D. Barron, A.D. Buckingham, Acc. Chem. Res. 34 (2001) 781.
[6] G.L.J.A. Rikken, E. Raupach, Nature 390 (1997) 493.
[7] L.D. Barron, J. Am. Chem. Soc. 108 (1986) 5539.
[8] L.D. Barron, Science 266 (1994) 1491.
[9] B.L. Feringa, R.A. Delden, Angew. Chem., Int. Ed. Engl. 38 (1999) 3418.
[10] G.L.J.A. Rikken, E. Raupach, Nature 405 (2000) 932.
[11] G. Christou, D. Gatteschi, D.N. Hendrickson, R. Sessoli, MRS Bull. 25 (2000) 26.
[12] P. Gerbier, D. Ruiz-Molina, N. Domingo, D.B. Amabilino, J. Vidal-Gancedo, J. Tejada, D.N. Hendrickson, J. Veciana, Monatsch. Fur Chimie, 134 (2003) 265.
[13] P. Gerbier, N. Domingo, J. Gómez, D.B. Amabilino, D. Ruiz-Molina, J. Tejada, B.E. Williamson, J. Veciana, Chem. Commun., in preparation.
[14] M.R. Cheeseman, V.S. Oganesyan, R. Sessoli, D. Gatteschi, A.J. Thomson, Chem. Commun. (1997) 1677.
[15] S.M.J. Aubin, Z. Sun, H.J. Eppley, E.M. Rumberger, I.A. Guzei, K. Folting, P.K. Grantzel, A.L. Rheingold, G. Christou, D.N. Hendrickson, Inorg. Chem. 40 (2001) 2127.
[16] C. Boskovic, M. Pink, J.C. Huffman, D. Hendrickson, G. Christou, J. Am. Chem. Soc. 123 (2001) 9914.
[17] K. Takeda et al., Phys. Rev. B 65 (2002) 094424.

Artículo B

Título:
Chiral, single-molecule nanomagnets: synthesis, magnetic characterization and natural and magnetic circular dichroism

Autores:
Ph. Gerbier, N. Domingo, J. Gómez-Segura, D. Ruiz-Molina, D.B. Amabilino, J. Tejada, B.E. Williamson, J. Veciana

Revista:
Journal of Materials Chemistry

ARTICLE

Journal of Materials Chemistry
www.rsc.org/materials

Chiral, single-molecule nanomagnets: synthesis, magnetic characterization and natural and magnetic circular dichroism

Philippe Gerbier,[a] Neus Domingo,[b] Jordi Gómez-Segura,[a] Daniel Ruiz-Molina,[a] David B. Amabilino,[b] Javier Tejada,*[b] Bryce E. Williamson*[c] and Jaume Veciana*[a]

[a]*Institut de Ciència de Materials de Barcelona (CSIC), Campus Universitari, 08193 Bellaterra, Catalonia, Spain. E-mail: vecianaj@icmab.es; Fax: 34 93 5805729; Tel: 34 93 580 1853*

[b]*Facultat de Física, Universitat de Barcelona, Avinguda Diagonal 647, 08028 Barcelona, Catalonia, Spain. E-mail: jtejada@ubxlab.com; Fax: 34 93 490 6682; Tel: 34 93 402 1158*

[c]*Department of Chemistry, University of Canterbury, Christchurch, New Zealand. E-mail: bryce.williamson@canterbury.ac.nz; Fax: 64 3 364 2110; Tel: 64 3 364 2439*

Received 1st March 2004, Accepted 4th June 2004
First published as an Advance Article on the web 5th July 2004

The first three chiral dodecamanganese clusters that behave as single-molecule magnets are reported. All reveal natural optical activity, which is stronger for the 2-chloropropionate derivative than for either the (*S*)-6-methoxy-α-methyl-2-naphthaleneacetate or the (*S*)-2-phenylbutyric acetate compounds. For the cluster with 2-chloropropionate moieties at its periphery, the magnetic circular dichroism was investigated and found to display large optical hysteresis, which depends on the direction in which the magnetic field direction is swept.

Introduction

The use of synthetic methodologies and self-assembly – the so-called bottom-up approach[1] – offers a potential alternative or complementary approach to lithographic techniques for the creation of monodisperse, nanoscale magnetic materials of a precise size,[2] as well as facilitating the incorporation of other functional characteristics, such as chirality.[3] Several macroscopic chiral magnets have been prepared,[4] but the introduction of magnetic order and natural optical activity at a *molecular* level is a novel and highly relevant objective in the context of recent revelations concerning the observation of magneto-chiral effects.[5]

All families of single-molecule magnets (SMMs) synthesised to date show low blocking temperatures (T_B) above which they behave as superparamagnets.[6] Among the highest T_B values (*ca.* 4 K) so far reported are those of the Mn_{12} family.[7] These possess a $[Mn_{12}(\mu_3\text{-}O)_{12}]$ core comprising a central $[Mn^{IV}_4O_4]^{8+}$ cubane held within a non-planar ring of eight Mn^{III} ions by eight μ_3-O ions. Peripheral ligation is provided by 16 carboxylate groups and three or four H_2O ligands.[8] Since their discovery, interest in preparing new SMMs with larger dimensionalities, higher-spin ground states and multifunctional properties has grown considerably. In this context, optically active molecular magnetic materials are interesting from various perspectives, not least from the viewpoint of combining optical and magnetic effects.[5]

In this paper we report the synthesis of the (*R*)-, (*S*)- and (*RS*)-isomers of Mn_{12} SMM **1**, and the (*S*)-enantiomers of **2** and **3** (Scheme 1), along with their magnetic characterization and the natural and magnetic circular dichroic properties of **1**. We show that the molecules exhibit natural optical activity. The magnetic circular dichroism (MCD) of **1** reveals significant optical hysteresis whose cause is the remnant magnetization of molecules isolated from each other in a glassy matrix.

Results

Synthesis

There are two synthetic approaches to making $[Mn_{12}O_{12}(O_2CR)_{16}(H_2O)_4]$ complexes. The first, involving the comproportionation between a Mn^{II} source and Mn^{VII} from MnO_4^- in the presence of the desired carboxylic acid (RCOOH), was the original method used by Lis[9] to synthesise the well-known Mn_{12}–acetate complex. The other, which has been used to prepare a wide variety of derivatives, is based on a ligand substitution reaction from the Mn_{12}–carboxylate complex.[10] Recently, we described a modification of the latter method, using $[Mn_{12}O_{12}(O_2C^tBu)_{16}(H_2O)_4]$ (**4**) as a starting material, that favours acidic ligand replacement.[11] This method allowed us to obtain some very chemically and thermally sensitive Mn_{12} complexes, whose preparation had remained elusive by direct replacement of the acetate groups of Mn_{12}–acetate.

As shown in Scheme 1, the complexes were prepared by treating **4** with an excess of the chiral acids. Complex **1** was prepared in (*R*)-, (*S*)- and (*RS*)-forms (the latter of which exists as several diastereomers). These three complexes were purified individually by solvent evaporation as small black crystals, whereas complexes (*S*)-**2** and (*S*)-**3** were collected as black microcrystals from a non-solvent, slow-diffusion process. Unfortunately, despite numerous attempts, single crystals suitable for X-ray studies could not be obtained. The complexes were identified unambiguously by MALDI-TOF mass spectrometry,[12] IR spectroscopy, elemental analysis and magnetometry.

Magnetochemical characterization

Ac magnetic susceptibility measurements performed on solid-state samples of (*S*)-**2**, (*S*)-**3** and the (*R*)- and (*S*)-enantiomers of **1** in the temperature range 1.8–10 K and at frequencies between 1 and 1×10^3 Hz reveal characteristic SMM

DOI: 10.1039/b403062a

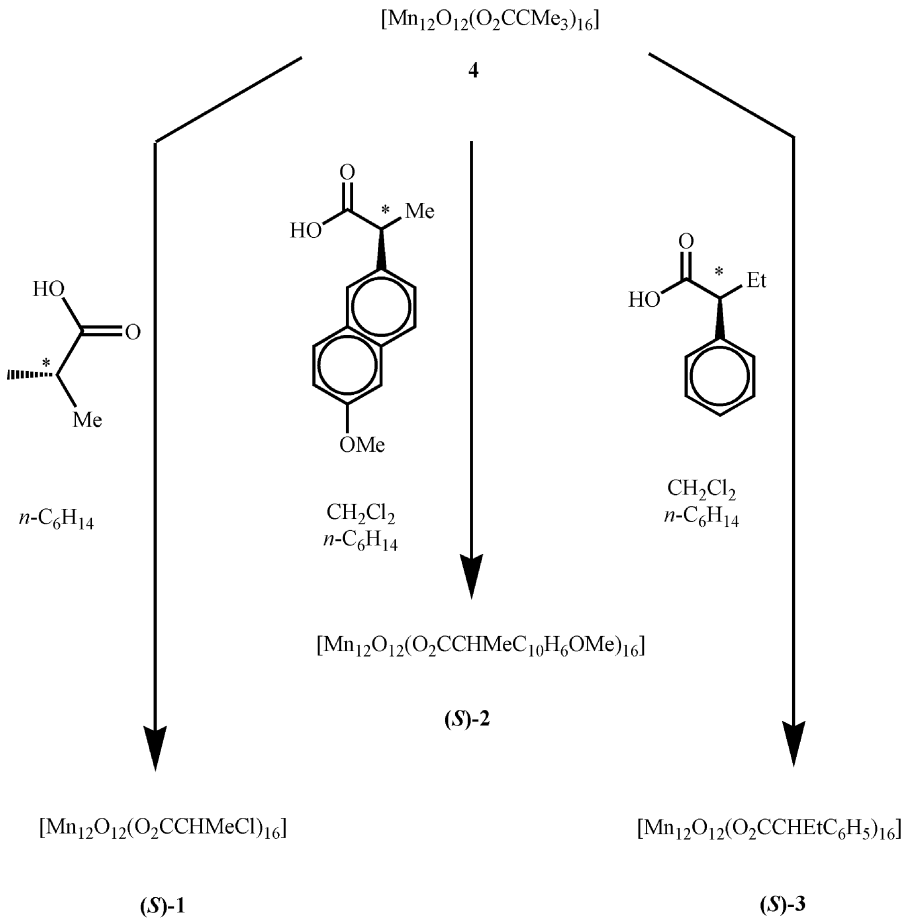

Scheme 1

behaviour.[7a,13,14] Both the in-phase and out-of-phase components of the ac magnetic susceptibilities (Figs. 1 and 2) show two frequency-dependent maxima, one in the 2–4 K region (low-temperature blocking) and the other in the 4–8 K region (high-temperature blocking).

The appearance of these two maxima is consistent with the existence of two inequivalent molecular species with different effective energy barriers and hence different magnetization relaxation rates.[15] The proportion of each species can be obtained by fitting high-temperature tails of the in-phase data to the Curie–Weiss law. For complex (*S*)-**1** the species with the higher barrier (higher blocking temperature) is prevalent (Fig. 1, the *R*-enantiomer gives the same behaviour), constituting about 85% of the total. For complex (*S*)-**2** the situation is reversed (Fig. 2) – the lower-barrier species now predominates with a proportion of around 65%. The ac susceptibility of (*S*)-**3** (not shown) shows a very weak peak for the higher-barrier species followed by a rise at lower temperatures indicative of a strong predominance of the form with the low blocking temperature.

Analysis of the temperature and frequency dependence of the out-of-phase component of the ac susceptibility by a least-squares fit to the Arrhenius law [eqn. (1)] allows the characterization of the two species in terms of the corresponding

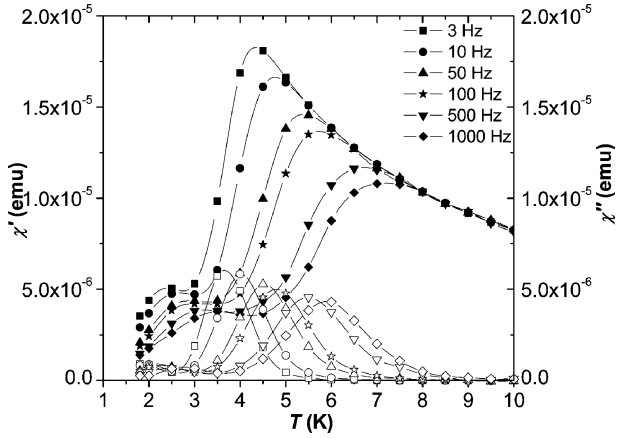

Fig. 1 Ac magnetic susceptibility of complex (*S*)-**1** as a function of temperature at six frequencies between 3 and 1000 Hz, with applied external fields of H_{ac} = 3.8 Oe and H_{dc} = 0 Oe. Solid and open symbols indicate the in-phase (χ') and out-of-phase (χ'') components, respectively.

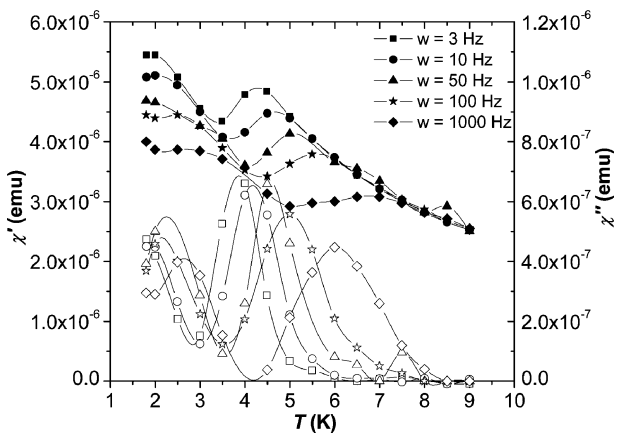

Fig. 2 Ac magnetic susceptibility of complex (*S*)-**2** as a function of temperature at five frequencies between 3 and 1000 Hz, with applied external fields of H_{ac} = 3.8 Oe and H_{dc} = 0 Oe. Solid and open symbols indicate the in-phase (χ') and out-of-phase (χ'') components, respectively.

Table 1 Effective anisotropy energy barriers and attempt times for Mn_{12} complexes (*S*)-**1** (the *R*-enantiomer gives essentially identical behaviour) and (*S*)-**2**

Complex	T_B/K	U_{eff}/K	τ_0/s
(*S*)-**1**	2–4	33 ± 2	$(4 \pm 1) \times 10^{-9}$
	4–8	56 ± 3	$(7 \pm 2) \times 10^{-8}$
(*S*)-**2**	2–4	30 ± 3	$(1.1 \pm 0.6) \times 10^{-8}$
	4–8	61 ± 3	$(4 \pm 2) \times 10^{-8}$

attempt time, τ_0, and the effective anisotropy potential energy barrier, U_{eff}:

$$\omega = \frac{1}{\tau_0}\exp(-U_{eff}/kT) \quad (1)$$

Here $\omega = \tau^{-1}$ is the frequency of the ac magnetic field, k is the Boltzmann constant and T is the temperature corresponding to the out-of-phase maximum. The results for complexes **1** and (*S*)-**2** are summarised in Table 1. Those for (*S*)-**3** could not be determined reliably on account of the weakness of the signals.

Magnetization hysteresis data for polycrystalline samples of complexes **1** and (*S*)-**2** were obtained at three temperatures between 1.8 and 2.5 K using a SQUID magnetometer. The samples were first magnetically saturated in a 4.0 T field, then the field was cycled down to −4.0 T and back up to +4.0 T. The field of reversibility (the point at which the curves obtained by scanning in each direction coincide) at 1.8 K is about 3 T for **1** and around 2 T for (*S*)-**2**, and saturation is not reached for the highest field of measurement. For complexes **1**, pronounced steps appeared at zero field, consistent with the presence of the two frequency-dependent peaks in the ac magnetic susceptibility data – while magnetic relaxation of the species with the higher barrier is blocked in this temperature range, the low-temperature species remains superparamagnetic and thus undergoes rapid relaxation near zero field. Moreover, the height of the step depends on the fraction of molecules that undergoes the fast relaxation mechanism, which is a minority (*ca.* 15%) for complex **1** but a majority (*ca.* 65%) for complex **2**. Thus, for (*S*)-**2**, the remnant magnetization at zero field is only of the order of 15% of the saturation value, while the coercive field at 1.8 K is only a few hundred Oe.

In addition to the zero-field steps, smaller steps are observed at field intervals of approximately 4.6 kOe in both complexes, although for (*S*)-**2** they are very difficult to observe due to the predominance of the low-barrier species. These can be ascribed to spin-tunnelling relaxation that becomes appreciable for the high-barrier species when spin states on either side of the anisotropy barrier are brought into resonance.[6h,16] Tunnelling will also contribute to the zero-field steps since the spin states are at resonance under those conditions. However, even for complexes **1**, this contribution will be very small in comparison with that from superparamagnetic relaxation of the species with the low blocking temperature.

Optical and magneto-optical activity

The UV-vis absorption spectra of the dodecanuclear manganese compounds described here are similar to those of achiral complexes of this type,[17] showing a featureless rise from 800 to a plateau between *ca.* 260 and 240 nm, before rising again at shorter wavelengths. In contrast, the natural circular dichroism (CD) spectra of the Mn_{12} clusters at room-temperature show well-defined Cotton effects, which are not present in the CD of the parent ligands[18] and must be associated with electronic transitions of the Mn_{12} core, thus establishing the transfer of chirality from the ligand to the metal environment (Figs. 3–5).

The CD spectra of the enantiomers of **1** in dichloromethane solution (Fig. 3) show mirror-image Cotton effects. The

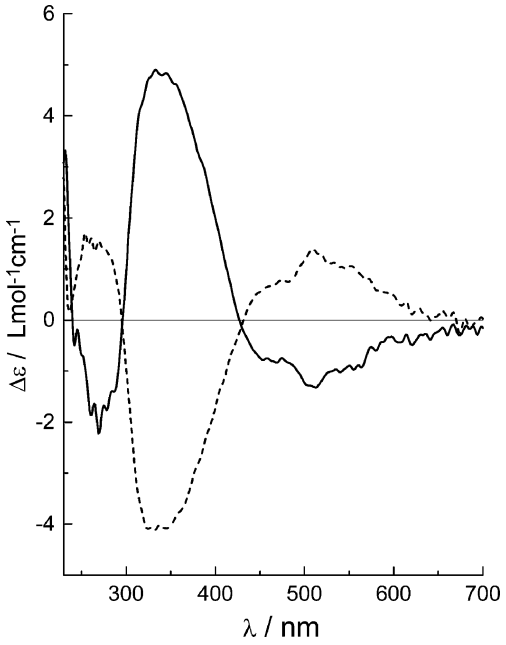

Fig. 3 Room-temperature natural CD spectrum of the enantiomers of **1** [(*S*) solid line and (*R*) dashed line] dissolved in dichloromethane.

(*S*)-enantiomer exhibits a broad, structured, negative band centred at *ca.* 510 nm, a stronger positive band at *ca.* 340 nm and another weaker, negative one at *ca.* 260 nm. Solid-state CD spectra of ground microcrystals[19] pressed in KBr matrices (Fig. 4) reveal pronounced Cotton effects at *ca.* 550 and 400 nm, similar to those in liquid solution, but with slight wavelength shifts and with the intensity of 400 nm band being much reduced.

The CD for (*S*)-**2** in dichloromethane (Fig. 5) shows Cotton effects near 500 and 400 nm, that are similar to, but substantially weaker than, the longer-wavelength CD features of (*S*)-**2**. The spectrum of (*S*)-**3** is practically the mirror image of (*S*)-**2**, but with a consistent shift of *ca.* 30 nm to the blue.

The ligand dependence of intensity indicates that stereogenic centres in the 2-chloropropionate groups are more effective at inducing optical activity in the core cluster than are those of the other ligands. The alteration of the spectra of **1** with the nature

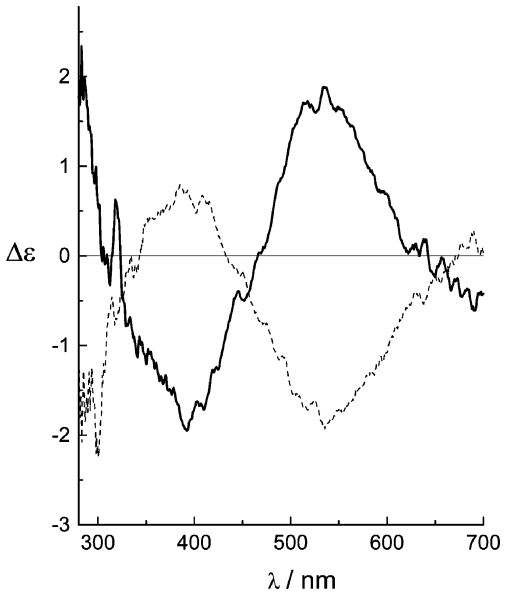

Fig. 4 Room-temperature natural CD spectrum of ground microcrystals of the enantiomers of **1** [(*S*) dashed line and (*R*) solid line] suspended in a KBr matrix.

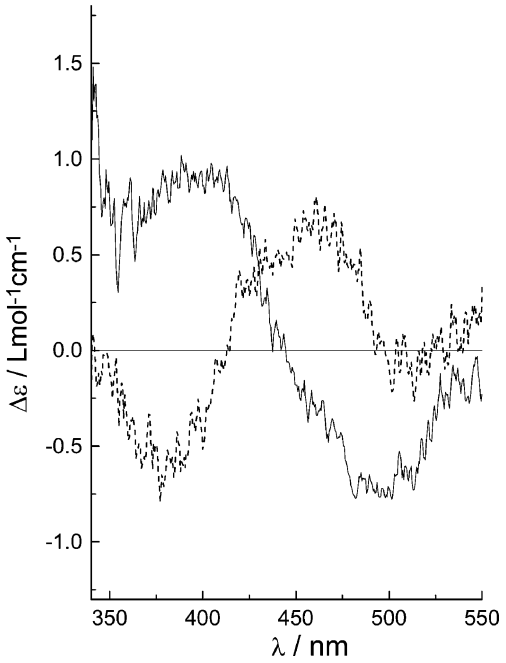

Fig. 5 Room-temperature natural CD spectrum of (*S*)-**2** (solid line) and (*S*)-**3** (dashed line) dissolved in dichloromethane.

of the host medium – in liquid $CHCl_2$ the Cotton effect at 340 nm is much more intense than in solid KBr – suggests an additional degree of complexity, the explanation of which is not apparent to us at present.

From the predominance of the higher-blocking-temperature species and the stronger natural CD, we anticipated that the most interesting MCD results would be observed for the enantiomers of **1**. Accordingly, measurements were made on samples of (*R*)- and (*S*)-**1** in a 1:1 toluene–dichloromethane glass. The resulting spectra (Fig. 6) are very similar to (though not identical to) those of the achiral cluster $[Mn_{12}O_{12}(O_2CMe)_{16}(H_2O)_4]$ recorded in a DMF–MeCN glass. They are composed of a series of Faraday *C* terms, which arise from population differences between the Zeeman levels of the ground electronic state and therefore have magnitudes that depend on both temperature and magnetic-field strength.[20]

At temperatures above *ca.* 3 K, the *C*-term intensities are reversible with changes of the magnetic field and are consistent with the samples comprising randomly oriented molecular clusters with effective uniaxial *g* values of $g_{\|} = 40$. However, at lower temperatures hysteresis is observed, manifest as a large remnant MCD that persists after the removal of the applied magnetic field.

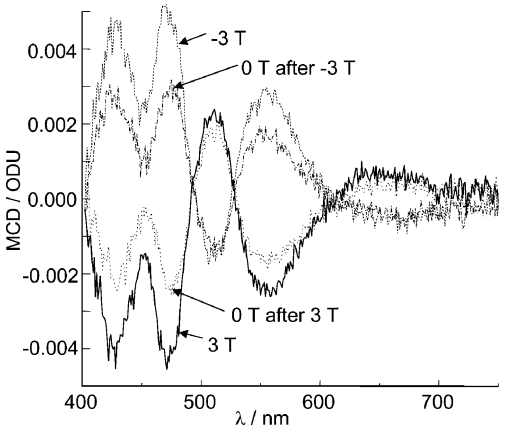

Fig. 6 1.65 K MCD spectra of (*S*)-**1** in 1:1 dichloromethane–toluene glass at 3, −3, and at 0 T after removing the applied fields.

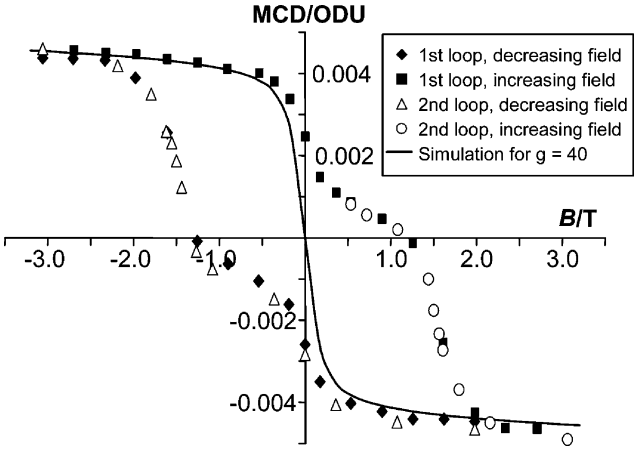

Fig. 7 MCD hysteresis loop at 1.65 K for the 472 nm band of (*S*)-**1** in a 1:1 dichloromethane–toluene glass.

When the field direction is reversed, the signs of the *C* terms and the subsequent zero-field remnant bands are also reversed. More generally, cycling of the applied magnetic field generates a symmetric hysteresis loop [shown for the *ca.* 470 nm band of (*S*)-**1** at 1.65 K in Fig. 7] with a coercive field of approximately 1.25 T.

MCD experiments conducted on the achiral propionate cluster $[Mn_{12}O_{12}(O_2CEt)_{16}(H_2O)_4]$ in the same glass show the same spectrum within experimental error and essentially the same symmetric hysteretic behaviour as the chiral compounds. Any magneto-chiral effect is clearly too weak to be observed under these conditions. However, the magnitude of the MCD hysteresis is quite remarkable and is comparable with traditional SQUID magnetization curves.[21]

Conclusions

The use of enantiopure 2-chloropropionate groups as the peripheral ligands endow appreciable natural optical activity upon the dodecamanganese core that they surround. This feature is very dependent on the particular chiral ligand, since neither (*S*)-6-methoxy-α-methyl-2-naphthaleneacetate nor the (*S*)-2-phenylbutyric acetate compounds reveal such significant Cotton effects in their CD spectra. These new chiral single-molecule magnets, the first of their kind, also reveal optical bistability when monitored using MCD. While no difference was observed in the MCD spectra of the enantiomers of **1**, the natural and magnetic circular dichroic properties of the isolated molecules in dichloromethane–toluene glass bode well for the observation of magneto-chiral dichroism in these SMMs under more sensitive experimental conditions.

Experimental

General methods

All chemicals and solvents were used as received. Preparations and manipulations were done under aerobic conditions. $[Mn_{12}O_{12}(O_2C^tBu)_{16}(H_2O)_4]$ (**4**) was prepared according to the literature procedure.[11] LDI and MALDI-TOF MS spectra were recorded using a Kratos Analytical KOMPACT MALDI-2 K-PROBE instrument, which uses a 3 ns pulse from a nitrogen laser (λ = 337 nm).[12] Natural CD spectra were recorded using spectroscopic-grade solvent (Romel) in a 1 cm cell at sample concentrations of 10^{-3} to 10^{-5} M using a Jasco J-720 Spectropolarimeter, and were analyzed using the associated J700 software.

Magnetic measurements

Ac and dc magnetic measurements were carried out on a Quantum Design MPMS SQUID magnetometer equipped with a 5 T magnet. The instrument has a 1.8–300 K operational range, an ac field range of 0–3.8 Oe and an oscillating frequency range of 0–1500 Hz. Samples prepared for variable field magnetization measurements were restrained in an epoxy matrix under an applied magnetic field of 5 T, to orient the molecules and to prevent torque.

Magnetic circular dichroism

MCD and simultaneous absorption spectra were measured using a spectrometer that has been described elsewhere[22] and an Oxford Instruments SM4 6-T superconducting cryomagnet. Temperatures between 1.6 and 4.2 K were achieved by pumping the vapour above the liquid-He cryogen while controlling the pressure with a manostat and monitoring it with a capacitance manometer. Spectra were measured using 1- or 2-mm path-length strain-free cells and spectroscopic-grade solvents that were degassed by the freeze–pump–thaw method. Hysteresis curves were measured point-by-point at a fixed wavelength, allowing *ca.* 5–10 min relaxation between field steps.

$[Mn_{12}O_{12}(O_2CCHClCH_3)_{16}(H_2O)_4]\cdot CH_3CCHClO_2H$ (1)

To a solution of complex **4** (0.24 g, 0.096 mmol) in hexane (5 mL) was added either (*R*)-2-chloropropionic acid or (*S*)-2-chloropropionic acid (0.25 g, 2.3 mmol). Evaporation of the solvent *in vacuo* gave small dark crystals of the corresponding chiral cluster **1** in a nearly quantitative yield (250 mg, 98%). Anal. calc. for $C_{51}H_{77}Cl_{17}O_{50}Mn_{12}$: C, 22.23; H, 2.80. Found: C, 22.11, H, 2.79%. IR (KBr, cm^{-1}): 3430 (s, b); 2987 (m); 1727 (w); 1607 (s); 1574 (s); 1455 (s); 1421 (s); 690 (m). MALDI-TOF MS (9-nitroanthracene matrix, negative-ion mode): $[Mn_{12}O_{12}(O_2CR)_n]^-$: $n = 15$ (10%) $m/z = 2457$; $n = 14$ (20%) $m/z = 2350$; $n = 13$ (20%) $m/z = 2243$; $[Mn_2(O_2CR)_5]^-$ (50%) $m/z = 645$; $[Mn(O_2CR)_3]^-$ (100%) $m/z = 376$.

$[Mn_{12}O_{12}(O_2CCH(CH_3)C_{10}H_{60}OCH_3)_{16}(H_2O)_4]$ [(*S*)-2]

Pivaloate anions were replaced by addition of (*S*)-6-methoxy-α-methyl-2-naphthaleneacetic acid (Lancaster, 99%) with 1:24 ratio in CH_2Cl_2. The reaction mixture was layered with hexanes and complex **2** was isolated from the excess ligand. Anal. calc. for $C_{224}H_{216}Mn_{12}O_{64}$: C, 58.59; H, 4.74. Found: C, 58.36; H, 4.75%. IR (KBr, cm^{-1}): 3434 (s, b); 2934 (m); 1634 (m); 1606 (s); 1570 (s); 1411 (s); 675 (m); 475 (m). MALDI-TOF MS (negative-ion mode, α-anthracene): $[Mn_{12}O_{12}(O_2CR)_n]^-$: ($n$ = 14–5); $n = 14$ (20%) $m/z = 4061$; $[Mn_2(O_2CR)_5]^-$ (45%) $m/z = 1256$; $[Mn(O_2CR)_3]^-$ (100%) $m/z = 743$.

$[Mn_{12}O_{12}(O_2CCH(Ph)CH_2CH_3)_{16}(H_2O)_4]\cdot 2CH_2Cl_2$ [(*S*)-3]

A ligand-substitution reaction was performed as described for complex **2** but an excess of (*S*)-2-phenylbutyric acid (Lancaster, 99%) was added. The reaction mixture was left undisturbed to full evaporation at room temperature to be subsequently rinsed and decanted in pentane several times. Anal. calc. for $C_{162}H_{188}Cl_4O_{48}Mn_{12}$: C, 52.52; H, 5.11. Found C: 52.50; H, 5.00%. IR (KBr, cm^{-1}): 3445 (m, b); 3061 (w); 3028 (w); 2963 (m); 2929 (m); 2873 (m); 1592 (s); 1572 (s); 1540 (s, b); 1411 (s, b); 698 (s); 617 (m, b). MALDI-TOF MS (negative-ion mode): $[Mn_{12}O_{12}(O_2CR)_n]^-$: ($n$ = 14–8); $n = 14$ (20%) $m/z = 3136$; $[Mn_2(O_2CR)_5]^-$ (60%) $m/z = 923$; $[Mn(O_2CR)_3]^-$ (100%) $m/z = 542$.

Acknowledgements

This work was supported by grants from the Programa Nacional de Materiales of the DGI (Spain, MAT2003-04699), the European Community with Nanomagicq (IST-2001-33186) and the University of Canterbury (internal research grant U6501). Ph. G. is grateful to the Région Languedoc-Roussillon for its financial support. N. D. acknowledges the grant AP2000-1842 of the FPU program of the Ministerio de Educación Cultura y Deportes (Spain).

References

1 G. M. Whitesides, J. P. Mathias and C. T. Seto, *Science*, 1991, **254**, 1312; J. S. Lindsey, *New J. Chem.*, 1991, **15**, 153; D. Philp and J. F. Stoddart, *Angew. Chem., Int. Ed. Engl.*, 1996, **35**, 1155; D. S. Lawrence, T. Jiang and M. Levett, *Chem. Rev.*, 1995, **95**, 2229; I. W. Hamley, *Angew. Chem., Int. Ed.*, 2003, **42**, 1692.

2 J. I. Martín, J. Nogués, K. Liu, J. L. Vicent and I. K. Schuller, *J. Magn. Magn. Mater.*, 2003, **256**, 449.

3 For examples of self-assembled chiral nanostructures, see: M. S. Spector, J. V. Selinger, A. Singh, J. M. Rodriguez, R. R. Price and J. M. Schur, *Langmuir*, 1998, **14**, 3493; T. Ishi-I, M. Crego-Calama, P. Timmerman, D. N. Reinhoudt and S. Shinkai, *J. Am. Chem. Soc.*, 2002, **124**, 14 631; L. J. Childs, N. W. Alcock and M. J. Hannon, *Angew. Chem., Int. Ed.*, 2002, **41**, 4244; G. Li, W. Fudickar, M. Skupin, A. Klyszcz, C. Draeger, M. Lauer and J.-H. Fuhrhop, *Angew. Chem., Int. Ed.*, 2002, **41**, 1828; R. Raval, *J. Phys.: Condens. Matter*, 2002, **14**, 4119.

4 A. Caneschi, D. Gatteschi, P. Rey and R. Sessoli, *Inorg. Chem.*, 1991, **30**, 3936; R. Andrés, M. Brissard, M. Gruselle, C. Train, J. Vaissermann, B. Malézieux, J.-P. Jamet and M. Verdaguer, *Inorg. Chem.*, 2000, **40**, 4633; E. Coronado, J. R. Galán-Mascarós, C. J. Gómez-García and J. M. Martínez-Agudo, *Inorg. Chem.*, 2001, **40**, 113; M. Minguet, D. Luneau, E. Lhotel, V. Villar, C. Paulsen, D. B. Amabilino and J. Veciana, *Angew. Chem., Int. Ed.*, 2002, **41**, 586; E. Coronado, C. J. Gómez-García, A. Nuez, F. M. Romero, E. Rusanov and H. Stoeckli-Evans, *Inorg. Chem.*, 2002, **41**, 4615; E.-Q. Gao, S.-Q. Bai, Z.-M. Wang and C.-H. Yan, *J. Am. Chem. Soc.*, 2003, **125**, 4984.

5 G. L. J. A. Rikken and E. Raupach, *Nature*, 1997, **390**, 493; G. L. J. A. Rikken and E. Raupach, *Nature*, 2000, **405**, 932; L. D. Barron and A. D. Buckingham, *Acc. Chem. Res.*, 2001, **34**, 781.

6 (*a*) R. Sessoli, H.-L. Tsai, A. R. Schake, S. Wang, J. B. Vincent, K. Folting, D. Gatteschi and D. N. Hendrickson, *J. Am. Chem. Soc.*, 1993, **115**, 1804; (*b*) C. Sangregorio, T. Ohm, C. Paulsen, R. Sessoli and D. Gatteschi, *Phys. Rev. Lett.*, 1997, **78**, 4645; (*c*) A. L. Barra, A. Caneschi, A. Cornia, F. F. De Biani, D. Gatteschi, C. Sangregorio, R. Sessoli and L. Sorace, *J. Am. Chem. Soc.*, 1999, **121**, 5302; (*d*) C. Cadiou, M. Murrie, C. Paulsen, V. Villar, W. Wernsdorfer and R. E. P. Winpenny, *Chem. Commun.*, 2001, 2666; (*e*) C. Boskovic, W. Wernsdorfer, K. Folting, J. C. Huffman, D. N. Hendrickson and G. Christou, *Inorg. Chem.*, 2002, **41**, 5107; (*f*) E. C. Yang, D. N. Hendrickson, W. Wernsdorfer, M. Nakano and G. Christou, *J. Appl. Phys.*, 2002, **91**, 7382; (*g*) J. J. Sokol, A. G. Hee and J. R. Long, *J. Am. Chem. Soc.*, 2002, **124**, 7656; (*h*) D. Gatteschi and R. Sessoli, *Angew. Chem., Int. Ed.*, 2003, **42**, 268; (*i*) E.-C. Yang, N. Harden, W. Wernsdorfer, L. Zakharov, E. K. Brechin, A. L. Rheingold, G. Christou and D. N. Hendrickson, *Polyhedron*, 2003, **22**, 1857; (*j*) E.-C. Yang, W. Wernsdorfer, S. Hill, R. S. Edwards, M. Nakano, S. Maccagnano, L. N. Zakharov, A. L. Rheingold, G. Christou and D. N. Hendrickson, *Polyhedron*, 2003, **22**, 1727.

7 For reviews and recent examples, see: (*a*) G. Christou, D. Gatteschi, D. N. Hendrickson and R. Sessoli, *MRS Bull.*, 2000, **25**, 26; (*b*) N. E. Chakov, K. A. Abboud, L. N. Zakharov, A. L. Rheingold, D. N. Hendrickson and G. Christou, *Polyhedron*, 2003, **22**, 1759.

8 D. Ruiz-Molina, G. Christou and D. N. Hendrickson, *Mol. Cryst. Liq. Cryst.*, 2000, **343**, 17.

9 T. Lis, *Acta Crystallogr., Sect. B*, 1980, **36**, 2042.

10 See, for example: S. M. J. Aubin, Z. Sun, H. J. Eppley, E. M. Rumberger, I. A. Guzei, K. Folting, P. K. Gantzel, A. L. Rheingold, G. Christou and D. N. Hendrickson, *Polyhedron*, 2001, **20**, 1139; M. Soler, P. Artus, K. Folting, J. C. Huffman, D. N. Hendrickson and G. Christou, *Inorg. Chem.*, 2001, **40**, 4902; J. T. Brockman, K. A. Abboud, D. N. Hendrickson and G. Christou, *Polyhedron*, 2003, **22**, 1765.

11 P. Gerbier, D. Ruiz-Molina, N. Domingo, D. B. Amabilino, J. Vidal-Gancedo, J. Tejada, D. N. Hendrickson and J. Veciana, *Monatsch. Chem.*, 2003, **134**, 265.
12 D. Ruiz-Molina, P. Gerbier, E. Rumberger, D. B. Amabilino, I. A. Guzei, K. Folting, J. C. Huffman, A. Rheingold, G. Christou, J. Veciana and D. N. Hendrickson, *J. Mater. Chem.*, 2002, **12**, 1152.
13 F. Luis, E. del Barco, J. M. Hernández, E. Remiro, J. Bartolomé and J. Tejada, *Phys. Rev. B*, 1999, **59**, 11 837; A. Caneschi, D. Gatteschi, C. Sangregorio, R. Sessoli, L. Sorace, A. Cornia, M. A. Novak, C. Paulsen and W. Wernsdorfer, *J. Magn. Magn. Mater.*, 1999, **200**, 182.
14 N. Domingo, Ph. Gerbier, J. Gómez, D. Ruiz-Molina, D. B. Amabilino, J. Tejada and J. Veciana, *Polyhedron*, 2003, **22**, 2355.
15 D. Ruiz, Z. Sun, B. Albela, K. Folting, J. Ribas, G. Christou and D. N. Hendrickson, *Angew. Chem., Int. Ed.*, 1998, **37**, 300; Z. Sun, D. Ruiz, N. R. Dilley, M. Soler, J. Ribas, K. Folting, M. B. Maple, G. Christou and D. N. Hendrickson, *Chem. Commun.*, 1999, 1973.
16 J. M. Hernández, X. X. Zhang, F. Luis, J. Bartolomé, J. Tejada and R. Ziolo, *Europhys. Lett.*, 1996, **4**, 301; J. R. Friedman, M. P. Sarachik, J. Tejada and R. Ziolo, *Phys. Rev. Lett.*, 1996, **76**, 3830; J. M. Hernández, X. X. Zhang, F. Luis, J. Tejada, J. R. Friedman, M. P. Sarachik and R. Ziolo, *Phys. Rev. B*, 1997, **55**, 5858; F. Luis, J. Bartolomé, J. F. Fernández, J. Tejada, J. M. Hernández, X. X. Zhang and R. Ziolo, *Phys. Rev. B*, 1997, **55**, 11 448; J. R. Friedman, M. P. Sarachik, J. M. Hernández, X. X. Zhang, J. Tejada, E. Molins and R. Ziolo, *J. Appl. Phys.*, 1997, **81**, 3978; E. M. Chudnovsky and J. Tejada, *Macroscopic Quantum Tunneling of the Magnetic Moment*, Cambridge University Press, Cambridge, 1998; J. Tejada, J. M. Hernández and E. del Barco, *J. Magn. Magn. Mater.*, 1999, **196–197**, 552; F. Luis, J. M. Hernández, J. Bartolomé and J. Tejada, *Nanotechnology*, 1999, **10**, 86.
17 M. R. Cheeseman, V. S. Oganesyan, R. Sessoli and D. Gatteschi, *Chem. Commun.*, 1997, 1677; E. L. McInnes, E. Pidcock, V. S. Oganesyan, M. R. Cheeseman, A. K. Powell and A. J. Thomson, *J. Am. Chem. Soc.*, 2002, **124**, 9219–9228.
18 M. Vargek, T. B. Freedman, E. Lee and L. A. Nafie, *Chem. Phys. Lett.*, 1998, **287**, 359.
19 M. Minguet, D. B. Amabilino, K. Wurst and J. Veciana, *J. Chem. Soc., Perkin Trans. 2*, 2001, 670.
20 S. B. Piepho and P. N. Schatz, *Group Theory in Spectroscopy with Applications to Magnetic Circular Dichroism*, Wiley-Interscience, New York, 1983.
21 N. Domingo, B. E. Williamson, J. Gómez-Segura, Ph. Gerbier, D. Ruiz-Molina, D. B. Amabilino, J. Veciana and J. Tejada, *Phys. Rev. B*, 2004, **69**, 52 405.
22 V. S. Langford and B. E. Williamson, *J. Phys. Chem. A*, 1997, **101**, 3119.

Artículo C

Título:
Trihaloacetic acids: an investigation of steric and inductive ligand effects on the synthesis of $[Mn_{12}O_{12}(O_2CCX_3)_{16}(H_2O)_4]$ single-molecule magnets

Autores:
J. Gómez-Segura, E. Lhotel, C. Paulsen, D. Luneau, K. Wurst, J. Veciana, D. Ruiz-Molina, Ph. Gerbier

Revista:
New Journal of Chemistry

Artículo D

Título:
Examining the thermolysis reactions of nanoscopic Mn_{12} single molecule magnets

Autores:
Ph. Gerbier, D. Ruiz-Molina, J. Gómez, K. Wurst, J. Veciana

Revista:
Polyhedron

Available online at www.sciencedirect.com
SCIENCE DIRECT®
PERGAMON
Polyhedron 22 (2003) 1951–1955
POLYHEDRON
www.elsevier.com/locate/poly

Examining the thermolysis reactions of nanoscopic Mn_{12} single molecule magnets

Philippe Gerbier [a,*], Daniel Ruiz-Molina [b,*], Jordi Gómez [b], Klaus Wurst [c], Jaume Veciana [b]

[a] UMR 5637, Université Montpellier 2, C.C.007, Place E. Bataillon, 34095 Montpellier, France
[b] Institut de Ciència de Materials de Barcelona (CSIC), Campus UAB, 08193 Cerdanyola, Spain
[c] Anorganische und Theorische Chemie, Universität Innsbruck, Innrain 52a, A-6020, Innsbruck, Austria

Received 6 October 2002; accepted 28 October 2002

Abstract

The thermal behavior of three Mn_{12} single molecule magnets $[Mn_{12}O_{12}(O_2CC_6H_5)_{16}(H_2O)_4]\cdot CH_2Cl_2\cdot C_6H_5CO_2H$ (**1**), $[Mn_{12}O_{12}(O_2C^tBu)_{16}(H_2O)_4]$ (**2**) and $[Mn_{12}O_{12}(O_2CCHCl_2)_{16}(H_2O)_4]$ (**3**) is reported. Aromatic ligands allow the complex **1** to be stable up to 300 °C whereas alkyl groups decrease drastically the domain of thermal stability for the complexes **2** and **3**. Moreover, the thermal decarboxylation of complexes **2** and **3** generates $[Mn_6O_2(O_2CR)_{10}L_4]$ (L = H_2O, HO_2CR) complexes as characterized by single crystal X-ray diffraction when R = ^{t}Bu.

Keywords: Mn_{12}; Single molecule magnets; Thermal stability; Thermolytic synthetic methods

1. Introduction

The use of synthetic methodologies, the so-called *bottom-up approach*, offers a potential alternative to obtain monodispersed nanoscale magnetic materials of a sharply defined size. In this order, the discovery of large metal cluster complexes with interesting magnetic properties characteristic of nanoscale magnetic particles, such as out-of-phase ac magnetic susceptibility signals and stepwise magnetization hysteresis loops, represented an important discovery to access ultimate high-density information storage devices and quantum computing applications [1]. Moreover, such clusters are composed of a single and sharply defined size and are agreeable to variations in peripheral carboxylate ligation making them soluble in different solvents. Different families of complexes that function as single molecule magnets (SMMs) based on manganese [2], nickel [3], cobalt [4] iron [5] and mixtures of metals [6] have been obtained. However, even though different families of SMMs have been synthesized (vide supra), all of them show low blocking temperatures (T_B) above which they behave as superparamagnets. One of the highest T_B ($\approx$6 K) so far reported corresponds to the Mn_{12} family. These complexes possess a $[Mn_{12}(\mu_3\text{-}O)_{12}]$ core comprising a central $[Mn_4^{IV}O_4]^{8+}$ cubane held within a non-planar ring of eight Mn^{III} ions by eight μ_3-O^{2-} ions. Peripheral ligation is provided by sixteen carboxylate groups and three or four H_2O ligands [7]. Since the above discoveries, the interest to obtain new SMMs with larger dimensionalities, anisotropies and high-spin ground states has grown considerably and for this reason different chemical synthetic methods to obtain new SMM with higher T_B are being widely explored worldwide.

In our group, the motivating physical work has been the exploration of new synthetic methods to obtain nanoscale clusters via thermolysis reaction. More precisely, in this work we have explored the thermal

* Corresponding authors. Fax: +34-935-805-729 (D.R.); +33-4-67-14-38-52 (Ph.G.).
E-mail addresses: gerbier@univ-montp2.fr (P. Gerbier), dani@icmab.es (D. Ruiz-Molina).

0277-5387/03/$ - see front matter
doi:10.1016/S0277-5387(03)00158-X

behavior of three different Mn_{12} SMM: $[Mn_{12}O_{12}(O_2CC_6H_5)_{16}(H_2O)_4]\cdot CH_2Cl_2\cdot C_6H_5CO_2H$ (**1**), $[Mn_{12}O_{12}(O_2C^tBu)_{16}(H_2O)_4]$ (**2**) and $[Mn_{12}O_{12}(O_2CCHCl_2)_{16}(H_2O)_4]$ (**3**). We will show how the different carboxylate ligands of complexes **1–3** influence their thermal stability. In this order, the thermal treatment of complexes **2** and **3** toluene yields the lower nuclearity Mn_6 clusters, whereas complex **1** remains thermally stable without any side-decomposition reaction.

2. Experimental

All the reagents were used as received. Microanalyses were performed by the Servei d'Analisi of the Universitat de Barcelona. $[Mn_{12}O_{12}(O_2CC_6H_5)_{16}(H_2O)_4]\cdot CH_2Cl_2\cdot C_6H_5CO_2H$ (**1**) [8], $[Mn_{12}O_{12}(O_2C^tBu)_{16}(H_2O)_4]$ (**2**) [9] and $[Mn_{12}O_{12}(O_2CCHCl_2)_{16}(H_2O)_4]$ (**3**) [10] were prepared following the methodology previously described. Dc magnetic measurements were carried out on a Quantum Design MPMS SQUID magnetometer equipped with a 5.5 T magnet in the temperature range of 1.8–300 K. Pascal's constants were used to subtract the diamagnetic contribution of the substances analyzed. Simultaneous TG/DTA measurements were performed under an N_2+O_2 flow (60 ml min^{-1}) at a heating rate of 5 °C min^{-1} on a Setaram Labsys TG-TDA12 thermogravimetric analyzer.

2.1. X-ray crystallography

X-ray data were collected at 223 K, on a Kappa CCD diffractometer with monochromatic Mo Kα ($\lambda = 0.71073$ Å) radiation. Data were collected via ϕ- and ω-multiscans and reduced with the program DENZO-SMN without absorption correction. The structure was refined by a full-matrix least-squares method (Table 1).

2.2. $[Mn_6O_2(O_2C^tBu)_{10}(C_3H_4N_2)_4]\cdot C_6H_5CH_3$ (**4**)

A solution of complex **2** (1.00 g, 0.4 mmol) in toluene (20 ml) was refluxed for 24 h. To the cooled solution was added pyrazole (0.60 g, 8.8 mmol) and the mixture was heated in order the help the dissolution of the solids. The filtered solution was left undisturbed overnight at room temperature in an open Erlenmeyer flask to afford X-ray quality diamond-shaped crystals (0.94 g, 65%). FTIR (KBr, cm^{-1}): 3333 (medium, NH str); 2958 (medium, C–H str); 1587, 1570, 1482, 1416 (strong, CO_2^- str); 1430 (weak, ^{t}Bu bend). Elemental analysis Calcd for $C_{69}H_{114}N_8O_{22}Mn_6$: C 47.70, H 6.57, N 6.45. Found: C 47.59, H 6.52, N 5.96%.

Table 1
Crystallographic data for $[Mn_6O_2(O_2C^tBu)_{10}(C_3H_4N_2)_4]\cdot C_6H_5CH_3$ (**4**)

Parameter	Complex **4**
Formula	$C_{69}\ H_{110}\ Mn_6\ N_8\ O_{22}$
Formula wt. (g mol^{-1} [a])	1733.29
Crystal system	Orthorhombic
Space group	*Pbcn*
a (Å)	14.1338(3)
b (Å)	22.9458(4)
c (Å)	27.0464(3)
α (°)	90
β (°)	90
γ (°)	90
V (Å^3)	8771.5 (3)
Z	4
T (K)	223(2)
Crystal size (mm)	$0.35\times0.30\times0.15$
Radiation l (Å [b])	0.71073
ρ_{calc} (g cm^{-3})	1.313
Data collected	$1\le 2\theta\le 24$
$R(R_w)$ [c]	0.0389(0.0557)

$f_{gof}=[\Sigma w(|F_o|-|F_c|)^2]/(n-p)]^{1/2}$; n = observed reflections, p = refined parameters. [c] $F>3\sigma(F)$.

[a] Including solvent molecules.

[b] Graphite monochromator.

[c] $R=\Sigma F_o|-|F_c||/\Sigma|F_o|$. $R_w=[\Sigma w(|F_o|-|F_c|)^2]^{1/2}$, where $w=1/s^2|F_o|$.

3. Results and discussion

3.1. Thermal stability: TGA/DTA experiments

Thermogravimetric analyses (TGA) combined with differential thermal analyses (DTA) were carried out on complex **1** and **2**. At the first glance, the TG curves (Fig. 1) seem to indicate a marked difference between their thermal stabilities, complex **1** being more stable at higher temperatures.

Both complexes exhibit a weight loss in the temperature range of 70–140 °C that has been attributed to the elimination of 4 H_2O+1 CH_2Cl_2 (obs.: 5.9%, th.: 4.7%) for complex **1** and 4 H_2O+1 ^{t}BuCO$_2$H (obs.: 7.0%, th.: 6.8%) for complex **2**. An increase of the temperature evidenced that complex **1** remained stable at least up to 210 °C where an additional weight loss of approximately 5% was observed ($-C_6H_5CO_2H=4\%$). A further increase of the temperature yields the final exothermal degradation with an overall weight loss of 67.4%. On the contrary, complex **2** is stable up to 150 °C, whereupon it underwent an impressive thermal degradation as ascertained by an abrupt two-step weight loss (48.2%) associated to a broad intense exothermal peak in the DTA curve.

Where does the different thermal stability of complexes **1** and **2** arise from? One of the most reasonable answer is that this difference may arise from electronic effects afforded by the organic group attached to the carboxylate moieties, and therefore to the acidity of

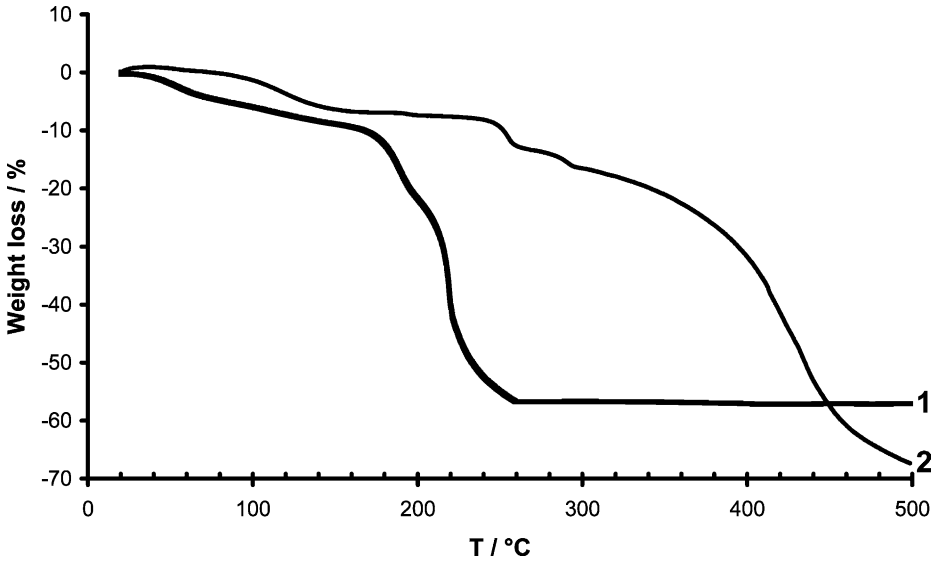

Fig. 1. TGA of complexes **1** and **2** under an air flow.

their associated protonated form. On the other hand steric considerations of the peripheral ligands may be also of interest to explain this observation. To give more insight into the origin of the different thermal stabilities, DTA experiments were carried out over a polycrystalline sample of complex **3**. The $-CHCl_2$ group has similar dimensions than the ^{t}Bu group although its acidity is higher due to the presence of the chlorine atoms. The DTA curves of complex **3** indicated that it becomes thermally unstable over 110 °C as ascertained by a broad intense exothermal peak and by IR spectroscopy. The IR spectra of a polycrystalline sample of complex **3** treated at four different temperatures are shown in Fig. 2. As can be seen there, at temperatures above 110 °C the different patterns of absorption experience considerable variations, indicating that decomposition side reactions take place. This fact seems to indicate that both, the steric compression afforded by bulky carboxylic groups and their different acidic character influence the relative thermal stability of Mn_{12} complexes.

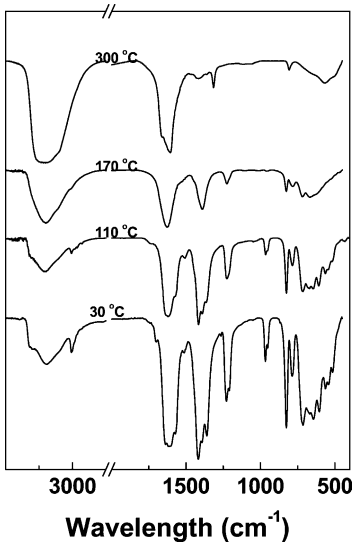

Fig. 2. Infrared spectra of complex **3** recorded in KBr after thermal treatments at 30, 110, 170 and 300 °C.

3.2. Mass spectrometry

The mass spectra of complexes **1–3** have been recorded. Since the Mn_{12} clusters absorb at the wavelength of the laser light used in the TOF MS instrument, mass spectra were recorded both with and without a matrix under different experimental conditions [11]. In the case of complex **1**, the high mass region (>700 Da) LDI-TOF mass spectrum recorded in positive mode, reveals no peak corresponding to the molecular ion but does show a series of peaks corresponding to the $[Mn_{12}O_{12}(O_2CC_6H_5)_{14}]^+$ ion at $m/z \sim 2547$ and fragments of it resulting from the stepwise loss of several $C_6H_5CO_2$ units ($\Delta m/z \sim 121$). In the low-mass region of the spectrum (<700 Da) a series of peaks, which could not be directly assigned to fragmentations involving the presence of the benzoate anion, are observed. These fragments may arise from rearrangement of the original cluster, and their explanation must involve the presence of manganese, oxygen and carbon atoms. Finally, it has to be emphasized that the benzoate complex **1** yielded good quality mass spectra independently of the matrix and polarity used.

The MALDI-TOF MS mass spectrum of complex **2** in the positive mode using 2-amino-4-methyl-5-nitropyridine (AMNP) as a matrix exhibits the most abundant pseudo-molecular peak was observed at $m/z = 2065$ [M-$4H_2O$-4^tBuCO_2]$^+$. In addition to such peak, an intense pattern centered at about $m/z = 1475$, which was not

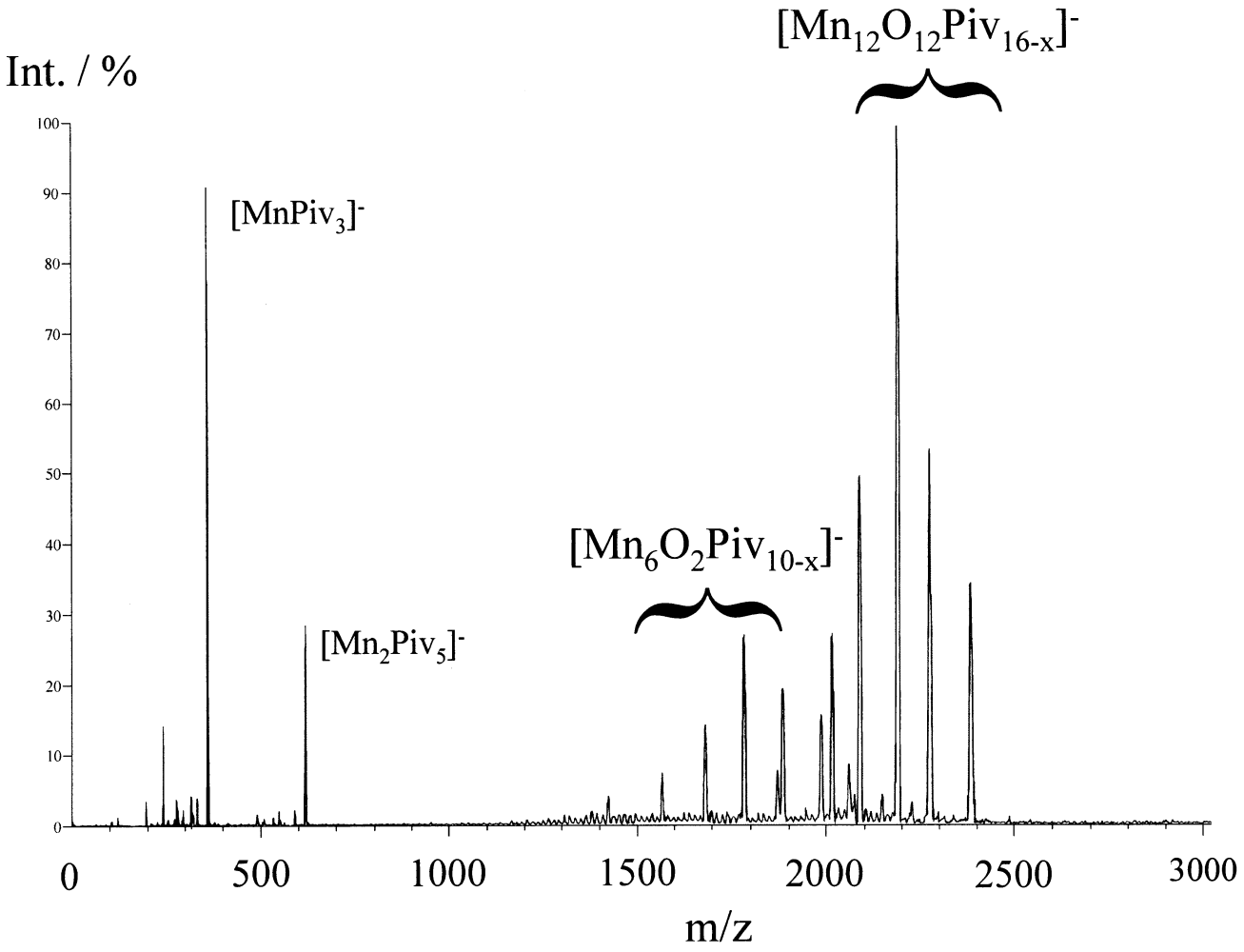

Fig. 3. Negative-ion mode MALDI-TOF spectrum of complex **2** using AMNP as a matrix.

observed for complex **1**, appears (Fig. 3). Since most of the peaks are related each other by the gain or the loss of a pivalate ($m/z = 101$) ligand, this spectral zone should be attributed to a family of mixed ligand complexes derived from the already known mixed valence Mn(II, III) complexes $[Mn_6O_2(O_2C^tBu)_{10}L_4]$ [12].

3.3. Thermolysis reaction

A toluene solution of **2** was refluxed for 24 h. On cooling, a red–brown microcrystalline precipitate was obtained. Such precipitate was characterized as an incompletely coordinated $[Mn_6O_2(O_2C^tBu)_{10}L_4]$ (L = H_2O, $^tBuCO_2H$) complex by comparison with the IR spectra of related Mn_6 complexes prepared as previously described in the literature. [13] This fact, together with previous mass spectrometry experiments, seems to indicate that in a first step, some of the Mn^{III} and Mn^{IV} ions constitutive of the starting complex are reduced to Mn^{II} ions by an oxidative decarboxylation mechanism of the ligands (Eq. (2)) [14].

$$[Mn_{12}^{(III,IV)}O_{12}(O_2C^tBu)_{16}(H_2O)_4] \rightarrow [Mn^{II}(O_2C^tBu)_2(H_2O)_x] + {}^t Bu^{\bullet} + CO_2 + H_2O + \ldots \quad (2)$$

Most likely, in a second step, the aggregation–dehydration reaction of the so-formed Mn^{II} pivalates lead to the hexamanganese mixed valence complexes according to Eq. (3) where L = H_2O, $^tBuCO_2H$.

$$6[Mn^{II}(O_2C^tBu)_2(H_2O)_x] \rightarrow [Mn_6^{(II,III)}O_2(O_2C^tBu)_{10}L_4] \quad (3)$$

Such ligands were subsequently replaced by reaction with pyrazole ligands. Indeed, addition of pyrazole to a warm mixture of $[Mn_6O_2(O_2C^tBu)_{10}L_4]$ and posterior cooling of the solution yielded nice brown diamond-shaped crystals of $[Mn_6O_2(O_2C^tBu)_{10}(C_3H_4N_2)_4]\cdot C_6H_5CH_3$ (**4**) suitable for X-ray structure determination. The ORTEP plot of complex **4** is shown in Fig. 4. The structure is similar to those previously found for related Mn_6 consisting of an edge-sharing bitetrahedral cage bridged by two μ_4-oxides and a mixture of six 1,3- and

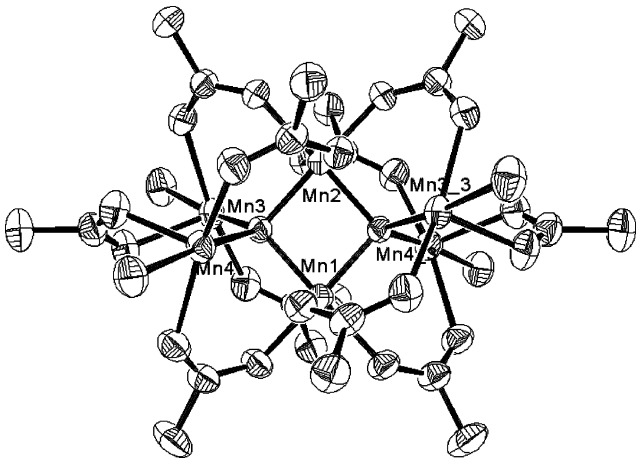

Fig. 4. ORTEP drawing of the Mn_6 core of complex **4** with thermal ellipsoids at 50% of probability. The hydrogen atoms and the organic peripheral groups were omitted for clarity.

four 1,1,3- pivalate ligands. The four pyrazole ligands are bound to the wing-tip sites of the manganese octahedrons. Magnetic measurements carried out on complex **4**, showed an antiferromagnetic coupling of the manganese ions leading to a $S = 0$ ground state as exactly observed with other related complexes.

Finally it has to be emphasized that thermal treatment of a toluene solution of **3** yielded a related $[Mn_6O_2(O_2CCHCl_2)_{10}L_4]$ ($L = H_2O$, HO_2CCHCl_2) complex as ascertained by different spectroscopic techniques and magnetic measurements. However, despite recurrent diffusion and crystallization experiments, the obtaining of single crystals of enough quality to solve its X-ray structure remained elusive. On the other side, similar thermal studies over a toluene solution of complex **1** revealed that it remains stable over several hours, even days. Such results are in agreement with the larger stability of complex **1** when compared to complexes **2** and **3** as ascertained by TG/DTA experiments and the lack of peaks associated to clusters with reduced dimensionalities in its MALDI-TOF spectra.

4. Conclusion

The thermolytic studies of Mn_{12}-based SMMs have shown that their thermal stability was highly dependent of parameters such as the electron-withdrawing ability and the bulkiness of the peripheral organic groups. The thermal degradation of SMM with non-aromatic groups follows an oxidative decarboxylation of the ligands by the Mn^{III} and Mn^{IV} ions which generates Mn^{II} ions, carbon dioxide and an organic radical. Interestingly, the thermal decarboxylation of SMM is found to open new synthetic methods to prepare others manganese clusters upon a thermal treatment.

4.1. Supplementary material

Complete lists with atomic coordinates, anisotropic displacement parameters, bond lengths and angles have been deposited at the Cambridge Crystallographic Data Centre (CCDC No. 195546), 12 Union Road, Cambridge, CB2 1EZ, UK (fax: +44-1223-336033; e-mail: deposit@ccdc.cam.ac.uk or www: http://www.ccdc.cam.ac.uk).

Acknowledgements

This work was supported from DGI (MAT 2002-00433), DGI (MAT 2000-1388-C03-01) and the 3MD Network of the TMR program of the E.U. (contract ERBFMRXCT 980181). Ph.G. is grateful to the CSIC and to the Région Languedoc-Roussillon for their financial support.

References

[1] G. Christou, D. Gatteschi, D.N. Hendrickson, R. Sessoli, MRS Bull. 25 (2000) 56.
[2] C. Boskovic, W. Wernsdorfer, K. Folting, J.C. Huffman, D.N. Hendrickson, G. Christou, Inorg. Chem. 41 (2002) 5107 (and referenced cited therein).
[3] C. Cadiou, M. Murrie, C. Paulsen, V. Villar, W. Wernsdorfer, R.E.P. Winpenny, Chem. Commun. 24 (2001) 2666.
[4] E.C. Yang, D.N. Hendrickson, W. Wernsdorfer, M. Nakano, G. Christou, J. Appl. Phys. 91 (2002) 7382.
[5] (a) C. Sangregorio, T. Ohm, C. Paulsen, R. Sessoli, D. Gatteschi, Phys. Rev. Lett. 78 (1997) 4645.;
(b) A.L. Barra, A. Caneschi, A. Cornia, F.F. De Biani, D. Gatteschi, C. Sangregorio, R. Sessoli, L. Sorace, J. Am. Chem. Soc. 121 (1999) 5302.
[6] J.J. Sokol, A.G. Hee, J.R. Long, J. Am. Chem. Soc. 124 (2002) 7656.
[7] D. Ruiz-Molina, G. Christou, D.N. Hendrickson, Mol. Cryst. Liq. Cryst. 343 (2000) 17.
[8] R. Sessoli, H.-L. Tsai, A.R. Schake, S. Wang, J.B. Vincent, K. Folting, D. Gatteschi, G. Christou, D.N. Hendrickson, J. Am. Chem. Soc. 115 (1993) 1804.
[9] Ph. Gerbier, D. Ruiz-Molina, N. Domingo, D.B. Amabilino, J. Vidal-Gancedo, J. Tejada, D.N. Hendrickson, J. Veciana, Monatsch, Chem.134 (2003) 265.
[10] M. Soler, P. Artus, K. Folting, J.C. Huffman, D.N. Hendrickson, G. Christou, Inorg. Chem. 40 (2001) 4902.
[11] D. Ruiz-Molina, Ph. Gerbier, E. Rumberger, D.B. Amabilino, I.A. Guzei, K. Folting, J.C. Huffman, A. Rheingold, G. Christou, J. Veciana, D.N. Hendrickson, J. Mater. Chem. 12 (2002) 1152.
[12] A.R. Schake, J.B. Vincent, Q. Li, P.D.W. Boyd, K. Folting, J.C. Huffman, D.N. Hendrickson, G. Christou, Inorg. Chem. 28 (1989) 1915.
[13] (a) M. Murrie, S. Parsons, R.E.P. Winpenny, J. Chem. Soc., Dalton Trans. 1 (1998) 1423;
(b) A.R.E. Baikie, A.J. Howes, M.B. Hursthouse, A.B. Quick, P. Thornton, J. Chem. Soc., Chem. Commun. (1986) 1587;
(c) A.S. Batsanov, Yu.T. Struchkov, G.A. Timko, N.V. Gerbeleu, O.S. Manole, S.V. Grebenko, Koord. Khim. 20 (1994) 604.
[14] J.M. Anderson, J.K. Kochi, J. Am. Chem. Soc. 92 (1970) 2450.

Artículo E

Título:
An unusually stable trinuclear manganese (II) complex bearing bulk carboxylic radical ligands

Autores:
D. Maspoch, J. Gómez-Segura, N. Domingo, D. Ruiz-Molina, K. Wurst, C. Rovira, J. Tejada, J. Veciana

Revista:
Inorganic Chemistry

An unusually stable trinuclear manganese (II) complex bearing bulk carboxylic radical ligands

Daniel Maspoch,[a,d] Jordi Gómez-Segura,[a] Neus Domingo,[b] Daniel Ruiz-Molina,*[a] Klaus Wurst,[c] Concepció Rovira,[a] Javier Tejada[b] and Jaume Veciana*[a]

Institut de Ciència de Materials de Barcelona (CSIC), Campus Universitari, 08193 Bellaterra, Catalonia, Spain, Facultad de Física, Universitat de Barcelona, Diagonal 647, 08028-Barcelona, Spain, Institut für Allgemeine Anorganische und Theoretische Chemie, Universität Innsbruck, A-6020, Innrain 52a, Austria, Institute for Nanotechnology, Northwestern University, 2145 Sheridan Road, Evanston, Illinois 60208, United States of America

RECEIVED DATE (will be automatically inserted after manuscript is accepted)

A trinuclear Mn(II) cluster based on the versatile PTM carboxylic radical ligand has been characterized by X-ray crystallography and magnetic measurements, representing a rare example of a Mn(II) trinuclear linear structure with six open-shell ligands.

Design of new molecular clusters containing numerous open-shell centers is a topic of great current interest because of their nanosized structures and resultant magnetic properties.[1] In their development, carboxylate-based ligands have become basic thanks to their capacity to act as bridge-like linkers. So far, a large diversity of molecular polynuclear systems involving carboxylate ligands, such as manganese or ferric clusters with "single-molecular magnet" behavior,[2] metallic [Cr(III), Co(II), etc.] wheels[3] or large first-transition metal-based cluster aggregates,[4] have been described. Moreover, the formation of such polynuclear clusters has been shown to be favored by the use of highly sterically demanding carboxylates.[5] For instance, bulky carboxylate-based ligands such as triphenylacetate, pivalate or halogen-substituted carboxylates have induced a series of unusual polynuclear cages.[6]

To complement such studies, our group has recently initiated a scientific project focused to the use of new bulky carboxylic ligands with an additional open-shell character, the so-called polychlorinated triphenylmethyl (PTM) radicals.[7] The open-shell character of these ligands is expected to enhance the magnetic dimensionality in comparison with systems made up from paramagnetic metal ions and diamagnetic coordinating ligands, according to the well-known "metal-radical" approach[8]. In a previous work, we showed for the first time how the monocarboxylic polychlorinated triphenylmethyl radical (**1**, PTMMC) (Figure 1), in addition to be highly sterically demanding, is capable to interact magnetically with a coordinated Cu(II) metal ion.[9] This was a seminal work on the quest for new 0-D clusters combining open-shell ligands.[10]

Following this approach, herein we report the synthesis, structural and magnetic characterization of a new trinuclear Mn(II) complex $[Mn_3(PTMMC)_6(EtOH)_6]\cdot 6EtOH$ (**2**) bearing six carboxylic ligands **1**, representing a rare example of a manganese cluster with several carboxylic radical ligands.

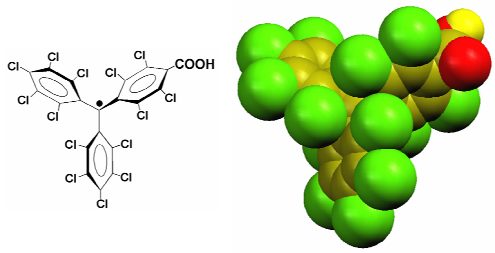

Figure 1. Space-filling diagram representing the molecular structure of **1**.

Reaction of $Mn(MeCO_2)_2\cdot 4H_2O$ and radical **1** (1:2) in EtOH at room temperature for 3 hours, followed by slow evaporation produced red blocks of **2** after two months. Single-crystal X-ray analysis revealed a nanosized trinuclear manganese complex connected by six bridge-like bidentate PTMMC radicals (Figure 2).[11] Complex **2** has a crystallographic S6 symmetry, involving a threefold axes crossing the two outermost Mn^{II} ions and the central Mn^{II} ion, which is located on an inversion center. This leads to a linear manganese complex, with a central Mn(II) site connected to both lateral Mn^{II} ions through six carboxylate-substituted radicals **1**. All carboxylates are coordinated in a syn-syn geometry with bond distances of 2.154(2) and 2.146(2) Å, which separates Mn ions with a distance of 4.27 Å. Remaining coordinative positions of each external Mn ions are occupied by three ethanol molecules. In this configuration, complex **2** adopts a quasi planar disk-like geometry formed by all six voluminous radicals **1** surrounding the trimeric Mn^{II} core and the ethanol molecules that are pointing out of the disk plane (Figure 3).

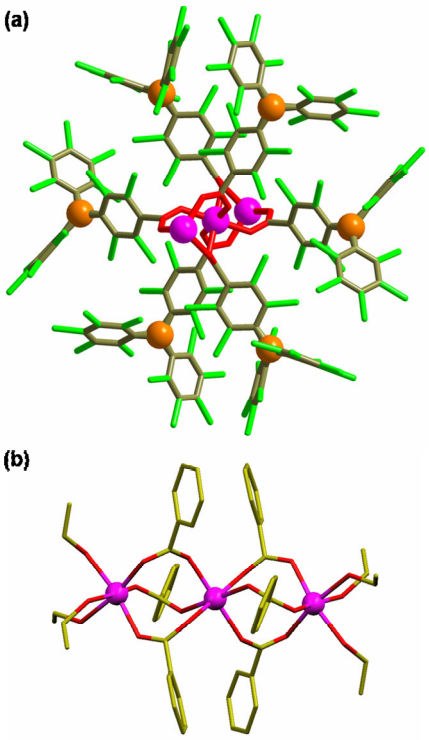

Figure 2. (a) Structure and (b) core-shell of **2** (Mn, violet balls; C, brown; O, red; Cl, green). In (a), radical methyl C atoms are represented as orange balls. Ethanol and solvent molecules are omitted for clarity.

This causes an intramolecular distance of 2.4-2.5 nm between external chlorine atoms of opposite PTMMC radicals. External positions of chlorine atoms also induce a stacking of **2** through Cl····Cl contacts. Sheets of **2** connected through 24 Cl····Cl contacts per molecule are laterally shifted and also held together through 24 Cl····Cl contacts per molecule, yielding an ABCABC arrangement.

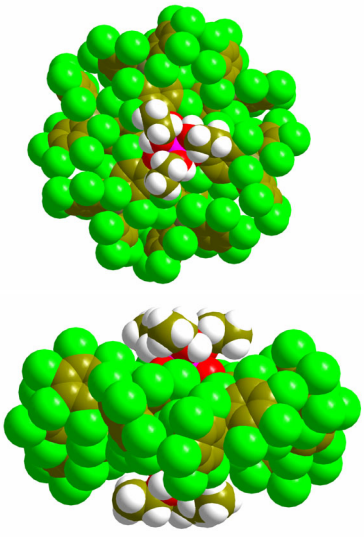

Figure 3. Disk-like geometry (front and lateral view) of complex **2**. Note that ethanol ligands point out the plane formed by the trinuclear Mn^{II} connected by the six radicals **1**.

Magnetic-susceptibility measurements were done on single-crystals of **2** embedded on eicosane (Figure 4) to fix at low temperature their relative positions with respect the external magnetic field. The $\chi \cdot T$ versus T plot (insert of Figure 4) shows a $\chi \cdot T$ value of 16.1 emu·K·mol^{-1} at 300 K, which is in good agreement with the value of 15.4 emu·K·mol^{-1} expected for three Mn(II) ions (S=5/2) and six radical ligands (S=1/2). This value remains constant on decreasing the temperature down to 150 K, whereupon a continuous decrease is observed until a value of 1.46 emu·K·mol^{-1} at 1.8 K is reached. Such decrease of the $\chi \cdot T$ value is consistent with the presence of dominant intramolecular antiferromagnetic interactions through the Mn···O···C···O···Mn pathway, and in less degree, intermolecular antiferromagnetic interactions through Cl····Cl contacts. In support of this is the fact that intermolecular magnetic interactions between metal complexes derived from PTMMC radical are generally very weak.[7,8] Variable-field magnetization was also measured at different temperatures (1.8, 2.0, 2.5, 3.0, 3.5, 5.0, 7.5 and 10.0 K) over an applied field range of 0-7 T. At a given temperature, the magnetization value increases following the Brillouin law up to 2 T, whereupon a linear increase with the applied field is observed (Figure 4). Variations on the temperature slightly modify the M vs. H plots. In all the temperature range studied the magnetization values never saturates even at the highest field due to field induced level crossings and the high density of spin states being populated. Accordingly, the magnetization value at 7 T in all the temperature range studied oscillate between 5.1 and 5.8 μB, which are far from the 10.5 μB expected for the saturation value.

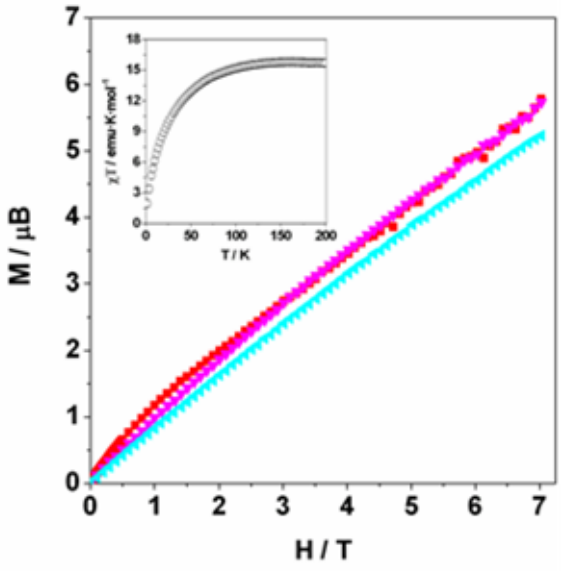

Figure 4. Magnetic field dependence of the magnetization for **2** at 1.8K (■, red), 5K (▼, magenta) and 10K (◀, cyan). Inset shows the temperature dependence of χ•T product from 1.8 to 200 K.

The results previously described for **2** differ from those recently described for a related linear trinuclear $[Mn^{III}Mn^{II}_2]$ complex, which exhibits ferromagnetic

exchange between the three Mn ions and a single-molecule magnet behavior.[12] Therefore, on the quest for new polynuclear complexes with topologies that endorse high-spin ground states and the presence of Jahn–Teller distorted Mn^{III} ions, new reactions with the carboxylic ligand **1** were assayed. Among them, ligand substitution reactions with radical **1** on $[Mn_{12}O_{12}(piv)_{16}(H_2O)_4]$ (**3**) and on $Mn(MeCO_2)_3{\cdot}2H_2O$ were performed. Ligand replacement of the pivaloic carboxylates (piv= $^tBuCO_2^-$) of complex **3** by radical **1** in an ethanol/CH_2Cl_2 mixture did not yield the expected Mn_{12} derivative but a mixture of products from where complex $[Mn_3(PTMMC)_6(EtOH)_6]{\cdot}6EtOH$ (**2**) was characterized by X-ray crystallography and magnetic susceptibility measurements. Surprisingly radical **1** is able to disrupt the Mn_{12} core to yield the linear trinuclear Mn(II) complex **2**, most likely due to its strong acid character and large dimensions.[13] Similar results were obtained on a further attempt to obtain the corresponding Mn_{12} derivative by a direct comproportionation reaction between a Mn^{II} source and Mn^{VII} (MnO_4^-) in the presence of the carboxylic acid **1**. Final efforts to obtain a $Mn^{II}{\cdot}Mn^{III}$ mixed valence complex were attempted by direct reaction of radical **1** with a source of Mn^{3+}, like $Mn(MeCO_2)_3{\cdot}2H_2O$. Intriguingly, this reaction yielded once more complex **2**, fact that has been attributed to a competitive oxidative decarboxylation of Mn^{III} catalyzed in the presence of **1**.[14]

In summary, we have described a new example of a linear trinuclear Mn(II) complex bearing six PTM carboxylic radicals that exhibit intramolecular antiferromagnetic interactions. Surprisingly, the different synthetic strategies used with radical **1**, yielded unambiguously complex **2** as the main reaction product. Further work is currently underway to better understand the different synthetic mechanisms and to explore new Jahn-Teller distorted metal ions such as Co(II).

Acknowledgement. This work was supported by Programa Nacional de Materiales of the Dirección General de Investigación (Spain), under project NanoMultiFun (MAT2003-04699) and by the EU under the QuEMolNa Marie-Curie Network (MRTN-CT-2003-504880). D. M. is grateful to the Generalitat de Catalunya for a predoctoral grant.

Supporting Information Available: Experimental details, crystallographic data and detailed magnetic field dependence of the magnetization plot for **2**. This material is available free of charge via the Internet at http://pubs.acs.org.

*To whom correspondence should be addressed. E-mail: vecianaj@icmab.es and dani@icmab.es
[a] Institut de Ciència de Materials de Barcelona (CSIC).
[b] Facultad de Física, Universitat de Barcelona.
[c] Institut für Allgemeine Anorganische und Theoretische Chemie, Universität Innsbruck.
[d] Present address: Institute for Nanotechnology, Northwestern University.

(1) (a) Leuenberger, M. N.; Loss, D. *Nature* **2001**, *410*, 789. (b) Sessoli, R.; Gatteschi, D.; Caneschi, A.; Novak, M. A. *Nature* **1993**, *365*, 141.
(2) (a) Tasiopoulos, A. J.; Vinslava, A.; Wernsdorfer, W.; Abboud, K. A.; Christou, G. *Angew. Chem. Int. Ed.* **2004**, *43*, 2117. (b) Brechin, E. K.; Boskovic, C.; Wernsdorfer, W.; Yoo, J.; Yamaguchi, A.; Sañudo, E. C.; Concolino, T. R.; Rheingold, A. L.; Ishimoto, H.; Hendrickson, D. N.; Christou, G. *J. Am. Chem. Soc.* **2002**, *124*, 9710. (c) Gatteschi, D.; Sessoli, R.; Cornia, A. *Chem. Commun.* **2002**, 725. (d) Price, D. J.; Batten, S. R.; Moubaraki, B.; Murray, K. S. *Chem. Commun.* **2002**, 762. (e) Scott, R. T. W.; Parsons, S.; Murugesu, M.; Wernsdofer, W.; Christou, G.; Brechin, E. K. *Chem. Commum.* **2005**, 2083.
(3) (a) McInnes, E. J. L.; Anson, C.; Powell, A, K.; Thompson, A. J.; Poussereau, S.; R. Sessoli. *Chem. Commun.* **2001**, 89. (b) Taft, K. L.; Delfs, C. D.; Delfs, G. C.; Papaefthymiou, G. C.; Foner, S.; Gatteschi, D.; Lippard, S. J. *J. Am. Chem. Soc.* **1994**, *116*, 823.
(4) (a) Murugesu, M.; King, P.; Clérac, R.; Anson, C. E.; Powell, A. K. *Chem. Commun.* **2004**, 740. (b) Murrie, M.; Biner, D.; Stoeckli-Evans, H.; Güdel, H. U. *Chem. Commun.* **2003**, 230.
(5) Graham, A.; Meier, S.; Parsons, S.; Winpenny, R. E. P. *Chem Commun.* **2000**, 811.
(6) (a) Mabbs, F. E.; McInnes, E. J. L.; Murrie, M.; Parsons, S.; Smith, G. M.; Wilson, C. C.; Winpenny, R. E. P. *Chem. Commun.* **1999**, 643. (b) Cadiou, C.; Coxal, R. A.; Graham, A.; Harrison, A.; Helliwell, M.; Parsons S.; Winpenny, R. E. P. *Chem. Commun.* **2002**, 1106. (c) Fernández, G.; Corbella, M.; Mahía, J.; Maestro, M. A. *Eur. J. Inorg. Chem.* **2002**, 2502.
(7) Maspoch, D.; Gerbier, P.; Catala, L.; Vidal-Gancedo, J.; Wurst, K.; Rovira, C.; Veciana, J. *Chem. Eur. J.* **2002**, *8*, 3635.
(8) (a) Maspoch, D.; Ruiz-Molina, D.; Wurst, K.; Domingo, N.; Cavallini, M.; Biscarini, F.; Tejada, J.; Rovira, C.; Veciana, J. *Nature Mater.* **2003**, *2*, 190. (b) Maspoch, D.; Ruiz-Molina, D.; Veciana, J. *J. Mater. Chem.* **2004**, *14*, 2713.
(9) Maspoch, D.; Ruiz-Molina, D.; Wurst, K.; Rovira, C.; Veciana, J. Chem. Commun. **2002**, 2958.
(10) (a) Canechi, A.; Gatteschi, D.; Laugier, J.; Rey, P.; Sessoli, R.; Zanchini, C. *J. Am. Chem. Soc.* **1988**, *110*, 2795. (b) Omata, J.; Ishida, T.; Hashizume, D.; Iwasaki, F.; Nogami, T. *Inorg. Chem.* **2001**, *40*, 3954.
(11) For a complex with a similar manganese core-shell see: Menage, S.; Vitols, S. E.; Bergerat, P.; Codjovi, E.; Kahn, O.; Girerd, J.-J.; Guillot, M.; Solans, X.; Calvet, T. *Inorg. Chem.* **1991**, *30*, 2666.
(12) Scott, R. T. W., Parsons, S., Murugesu, M., Wernsdorfer, W., Christou, G., Brechin, E. K. *Chem. Commun.* **2005**, 2083.
(13) Gómez-Segura, J.; Lhotel, E.; Paulsen, C.; Luneau, D.; Wurst, K.; Veciana, J.; Ruiz-Molina, D.; Gerbier, P. *New J. Chem.* **2005**, *29*, 1.
(14) Anderson, J. M.; Kochi, J. K. *J. Am. Chem. Soc.* **1970**, *92*, 2450.

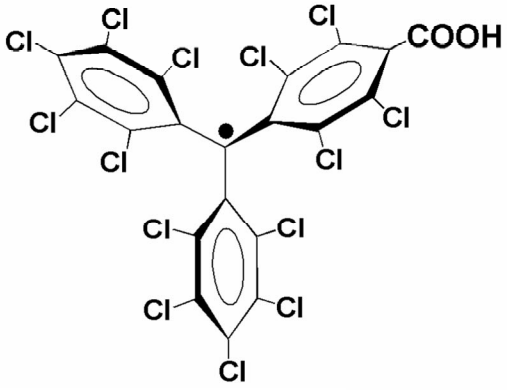

Open-Shell Organic Ligand

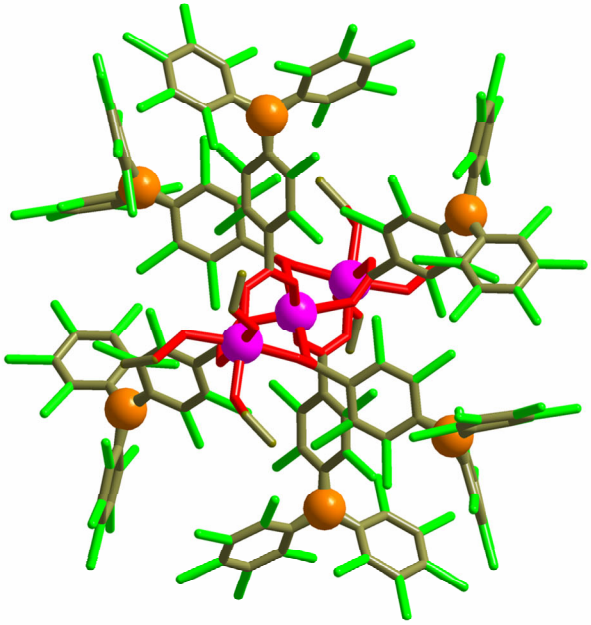

Capítulo 2

Propiedades magnéticas: sinergismo magneto-óptico y fenómenos de relajación

Los trabajos presentados en este capítulo de la Tesis tienen como objetivo una mejor comprensión de la influencia del entorno y red cristalina en los fenómenos de relajación magnética de los imanes unimoleculares de Mn_{12}. Esta información es de gran utilidad para entender la presencia de nuevas fenomenologías, la existencia de al menos dos modos de relajación magnética, así como las posibles variaciones en las propiedades de los Mn_{12} en la traslación de sus propiedades macroscópicas una vez depositados en superficie. La dificultad en obtener imanes 3-D con materiales moleculares se ha convertido en ventajas en el caso de estudiar los denominados imanes unimoleculares, ya que permiten observar fenómenos cuánticos atribuibles a su tamaño nanoscópico, al mismo tiempo que pueden considerarse como objetos macroscópicos en el conjunto de la red cristalina. La coexistencia de propiedades magnéticas intermedias entre la naturaleza cuántica y clásica de la física favorece en estos materiales el estudio de la influencia que el tamaño pueda suponer en las propiedades magnéticas. Por consiguiente, variaciones del entorno cristalino alrededor de un imán unimolecular pueden alterar la relajación espín-fonón, fenómenos cuánticos de efecto túnel, o bien interacciones intermoleculares, normalmente de origen dipolar. Para intentar entender mejor esta influencia, en el presente trabajo se han estudiado los imanes unimoleculares en dos entornos diferentes, I) sistemas amorfos y II) sistemas cristalinos. Dentro de los materiales amorfos se investigaron las propiedades magnéticas y estructurales de compuestos de Mn_{12} tras la pérdida completa de cristalinidad o bien moléculas aisladas en disoluciones diluidas congeladas en estado vítreo. Estos medios son apropiados para la realización de estudios magneto-ópticos tales como el dicroísmo circular magnético *(MCD)*. Sin embargo, la preparación de materiales cristalinos supuso en algunos casos la obtención de monocristales de grandes dimensiones y en otros casos la reducción controlada del tamaño de partícula mediante las técnicas de fluidos comprimidos caracterizables mediante magnetometría SQUID. Todos estos estudios además se complementaron con el uso de técnicas neutrónicas. La combinación de técnicas experimentales de preparación y caracterización utilizadas, juntamente con el interés de cada una de ellas, se muestra esquemáticamente a continuación *(Esquema 1)* previa revisión de los diversos resultados obtenidos.

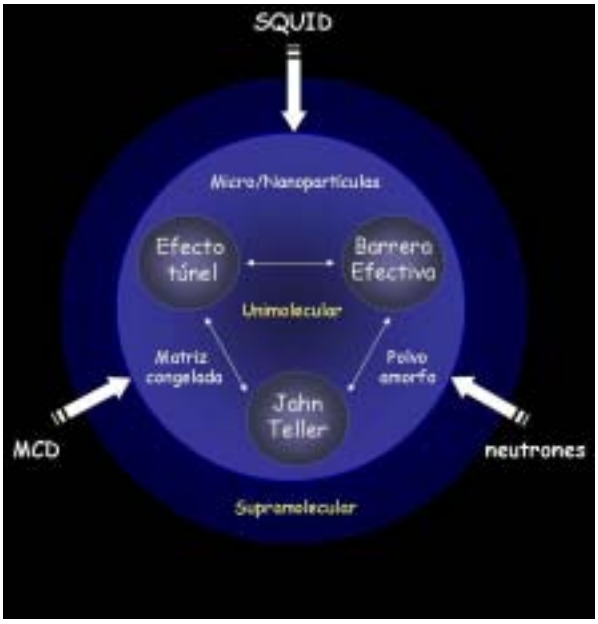

Esquema 1

2.1. Mn_{12} en un entorno amorfo

2.1.1. Medidas en disolución/matrices congeladas

El estudio de complejos de Mn_{12} aislados que no presenten interacción intermolecular es un reto en el camino hacia una mejor comprensión de sus mecanismos de relajación. No obstante, dada la imposibilidad de obtener una sola molécula aislada se decidió estudiar estos sistemas moleculares en matrices inertes, como puede ser una disolución diluida congelada. Así, se obtuvieron disoluciones diluidas de los compuestos $[Mn_{12}O_{12}(O_2CCH_3)_{16}(H_2O)_4]$ *(2)* y $[Mn_{12}O_{12}(O_2CC_6H_5)_{16}(H_2O)_4]$ *(17)* en dos mezclas diferentes compuestas de disolventes orgánicos CH_2Cl_2/tolueno y CH_3CN/dmf *(dfm=N,N'-dimetilformamida)*, y se estudiaron sus propiedades magnéticas. Estos trabajos se realizaron en colaboración con el grupo del Prof. Javier Tejada en la Universidad de Barcelona, el Dr. David B. Amabilino del *Institut de Ciència de Materials* de Barcelona *(CSIC)* y el grupo del Prof. Bryce E. Williamson en la Universidad de Canterbury *(Nueva Zelanda)*.

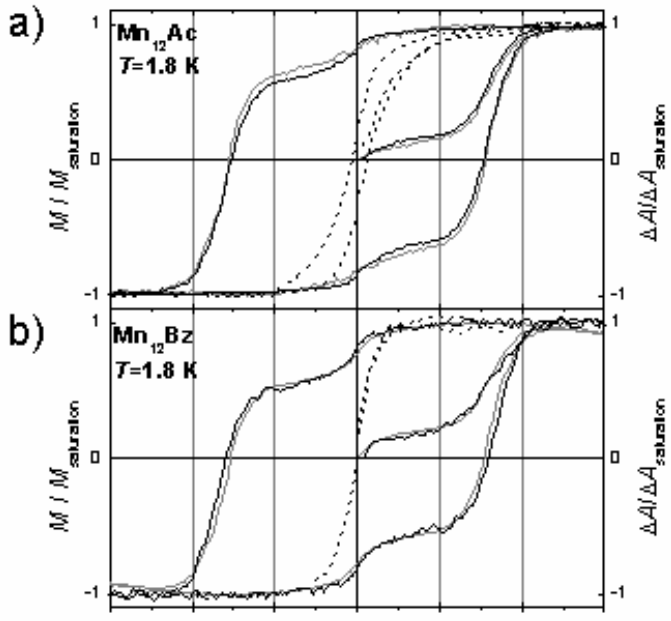

Fig. 2.1. Curvas de magnetización obtenidas por magnetometría SQUID *(en gris)* y MCD a 21200 cm^{-1} *(en negro)* de los sistemas Mn_{12} acetato (Mn_{12} Ac) *(2) (a)* y benzoato (Mn_{12} Bz) *(17) (b)*. Las curvas representadas en línea negra continua indican la magnitud del MCD en una disolución congelada de diclorometano:tolueno *(1:1)* mientras que las líneas trazadas discontinuas corresponden a un vidrio orgánico de dmf:acetonitrilo *(2:1)*.

Tal y como se puede ver en la Figura 2.1, las curvas de magnetización presentan fenómenos de histéresis similares a los observados para las medidas en materiales cristalinos, lo que confirma estudios previos realizados por Sessoli y col. Dichos estudios magnéticos ya indicaron que el interesante comportamiento magnético de los imanes unimoleculares tenía un origen puramente intrínseco a la molécula y no debido a interacciones de largo alcance. Sin embargo, la mayor diferencia destacable es la falta de saltos en las medidas de magnetización correspondientes a la relajación por efecto túnel, los cuales aparecen normalmente a intervalos periódicos de campo magnético aplicado. Este hecho se ha atribuido a la falta de orientación de las moléculas aisladas dado que sus momentos magnéticos son tan pequeños que el campo magnético externo aplicado no es suficiente para orientarlas. No obstante, a campo cero se observa un único salto que depende de la proporción de especies de relajación rápida. A pesar de que a campo cero, e independientemente a su orientación, todas las moléculas pueden

presentar efecto túnel resonante, este fenómeno es despreciable frente a la contribución superparamagnética de dichas especies. Finalmente, destacar que la proporción relativa entre ambas especies de relajación, lenta y rápida, se puede detectar no por sólo por las curvas de magnetización sino especialmente por las medidas ac fuera de fase, siendo éstas muy sensibles no tan sólo al disolvente utilizado sino incluso a la velocidad de formación del estado vítreo.

Para completar los resultados anteriormente mencionados, se obtuvieron los espectros de MCD de las mismas disoluciones. El objetivo era validar el uso de técnicas ópticas para la detección de estos sistemas moleculares, debido a una mayor sensibilidad en comparación a los métodos magnéticos convencionales, así como la lectura de dicha información con una mayor rapidez. La técnica del MCD se basa en la diferente absorción de la luz polarizada circularmente en sentido levógiro y dextrógiro por un material bajo un campo magnético. A diferencia del dicroísmo circular *(CD)*, los materiales aquirales pueden exhibir MCD *(efecto Faraday)* debido a que el campo magnético conlleva a la ruptura de la degeneración y mezcla de los estados electrónicos de espín y orbital. En especies paramagnéticas, la intensidad del MCD asociado a una transición depende del acoplamiento espín-órbita y varía con el campo magnético aplicado y la temperatura de una forma determinada según los parámetros g y de desdoblamiento a campo cero *(ZFS)*.

Los espectros de MCD representados en la Figura 2.2 se adquirieron a la temperatura de 4.2 K. La intensidad de la señal óptica medida mantiene la reversibilidad al invertir el signo de la magnitud del campo magnético aplicado. Adicionalmente, tal y como se observó en la Figura 2.1, a temperaturas suficientemente bajas *(1.8 K)* se siguió la evolución de la señal de MCD a 21200 cm^{-1} en función del campo magnético, dando lugar a la observación de curvas de histéresis asociadas.[1] La polarización de la magnetización a campo cero es observada ópticamente en dichas curvas, siendo igualmente detectable su presencia en los espectros de MCD mediante la presencia de una señal de intensidad remanente tras eliminar el campo magnético aplicado.

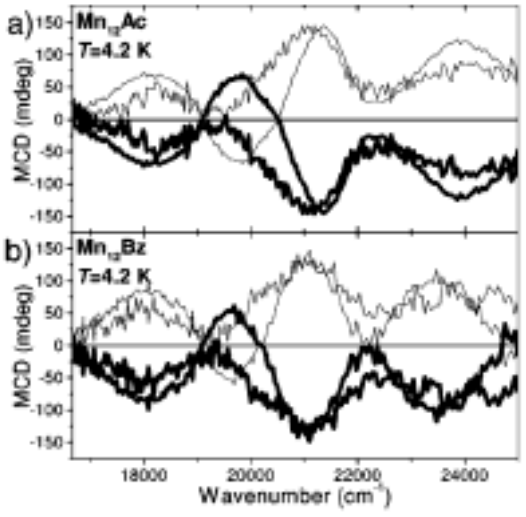

Fig. 2.2. Espectros MCD de los sistemas Mn_{12} acetato ($Mn_{12}Ac$) *(2) (a)* y benzoato ($Mn_{12}Bz$) *(17) (b)* a 4.2 K obtenidos en diclorometano:tolueno *(1:1) (en negro)* y dmf:acetonitrilo *(2:1) (en gris)* a campo magnético $H = 10^4$ Oe *(curvas de mayor grosor)* y $H = -10^4$ Oe *(curvas de menor grosor)*.

Finalmente, la observación directa de los fenómenos de relajación por efecto túnel, pese a no ser evidentes en las curvas de histéresis, fue detectada por primera vez a través de métodos magneto-ópticos. Para ello se saturó la muestra aplicando un campo magnético

de -2.5x10^4 Oe y se estudió el desvanecimiento de la intensidad de señal tras el cambio rápido a campo cero o bien a campos positivos de poca intensidad *(Fig. 2.3)*. La presencia de un máximo a campo cero indica claramente la existencia de fenómenos de relajación por efecto túnel en sistemas cuyas moléculas disponen de una orientación al azar.*

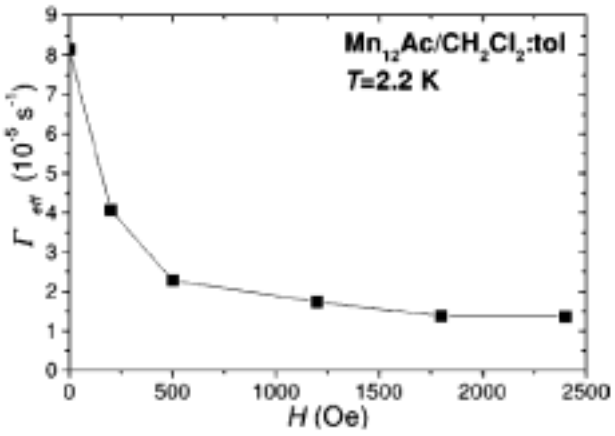

Fig. 2.3. Observación óptica del efecto túnel magnético a partir de la caída de señal MCD en función del campo magnético aplicado.

Durante la realización de nuestras investigaciones, Thomson y col.,[2] aportaron estudios detallados sobre la caracterización de Mn_{12} mediante MCD, siendo dicha contribución de gran importancia en la interpretación y comprensión de nuestros resultados.

Finalmente, destacar que a modo de comprobación también se registraron los espectros de MCD correspondientes a los dos enantiómeros del compuesto quiral *(R)* y *(S)*-$[Mn_{12}O_{12}(O_2CCHMeCl)_{16}]$ *(7)*, descritos en el Capítulo 1. Los estudios se realizaron en las mismas condiciones que en el caso de los Mn_{12} aquirales anteriormente descritos, demostrando que la respuesta de los espectros de MCD es muy similar. Estos resultados indican que cualquier efecto magneto-quiral, así como su enantioselectividad, son claramente demasiado pequeños para detectarse, dentro del margen de error, en las condiciones experimentales utilizadas. Para ello, se tiene previsto el uso del dicroísmo magneto-quiral,[3] que permitiría la posible diferenciación entre los dos enantiómeros.

2.1.2. Medidas en polvo amorfo

Existe cierta controversia sobre el origen de los fenómenos de relajación túnel en los complejos de Mn_{12}. Estudios teóricos han apuntado claramente a la influencia de los cambios de simetría local en el entorno de la molécula, tales como la presencia de dislocaciones en el sistema, en el origen del efecto túnel cuántico del Mn_{12}. Así, con el fin de verificar la validez de tales modelos teóricos se inició un estudio de dispersión inelástica de neutrones con técnicas de tiempo de vuelo *(TOF)* en el *Institut Max von Laue-Paul Langevin* de Grenoble *(ILL)* para medir los niveles de energía de la molécula de Mn_{12} en diferentes entornos e incluso en entornos amorfos, es decir, con el máximo de dislocaciones. Estos estudios se realizaron en colaboración con el Dr. Javier Campo y el Dr. Fernando Luis del Instituto de Ciencia de Materiales de Aragón *(CSIC)*.

* Para más información ver artículo F

Para realizar estos estudios fue necesaria la preparación de una muestra en fase amorfa, particularmente a partir de Mn_{12} acetato deuterado, $[Mn_{12}O_{12}(O_2CCD_3)_{16}(D_2O)_4]$ *(18)*. Su obtención en fase cristalina se realizó a través de la síntesis descrita originalmente por Lis *(ver Capítulo 1)* mediante el uso de los reactivos de partida completamente deuterados. A partir del producto cristalino se preparó la fase amorfa por dilución en acetonitrilo. Tras sucesivos procesos cíclicos de disolución y evaporación lenta del disolvente bajo presión reducida y suave calentamiento, se eliminan las moléculas de cristalización correspondientes al ácido acético. El grado de amorfismo se controló después de cada etapa de evaporación a través de técnicas de difracción de rayos-X en polvo hasta obtener la fase amorfa, tal y como se compara en los difractogramas de la Figura 2.4 b.

Los estudios magnéticos medidos con un magnetómetro SQUID demuestran que las propiedades magnéticas apenas varían cuando el material pierde su cristalinidad. Adicionalmente, los estudios con técnicas neutrónicas confirmaron dichos resultados. En la Figura 2.4 se muestran varios espectros medidos a bajas temperaturas en muestras amorfas del complejo **18**, Mn_{12} acetato deuterado. Estos espectros son básicamente idénticos a los ya estudiados para dicho compuesto en forma cristalina, tanto en lo que se refiere a la forma, como a la periodicidad y localización de las transiciones.

En resumen, los resultados obtenidos indican que la posición de los niveles de energía de la molécula de Mn_{12} no depende del entorno ni del grado de amorfismo. Es decir, son una propiedad intrínseca al Mn_{12} y no a su entorno. Dicho de otra manera, la molécula de Mn_{12} se comporta de manera *rígida*, es decir, difícilmente influenciable por el entorno. Estos resultados, no obstante, sólo son validos para el caso del Mn_{12}-acetato que presenta de forma muy reproducible un único mecanismo de relajación independiente del entorno. Sin embargo, no serían aplicables a otros sistemas de Mn_{12} para los cuales se observan como mínimo dos mecanismos de relajación, uno lento y otro rápido, según el entorno y la red de cristalización. Así, de forma indirecta, estos experimentos también confirman que la observación de los dos mecanismos de relajación no se debe a dislocaciones o imperfecciones de la red cristalina, sino probablemente a alteraciones de las elongaciones de Jahn-Teller, tal y como sostienen otros grupos de investigación en el campo del Magnetismo Molecular.

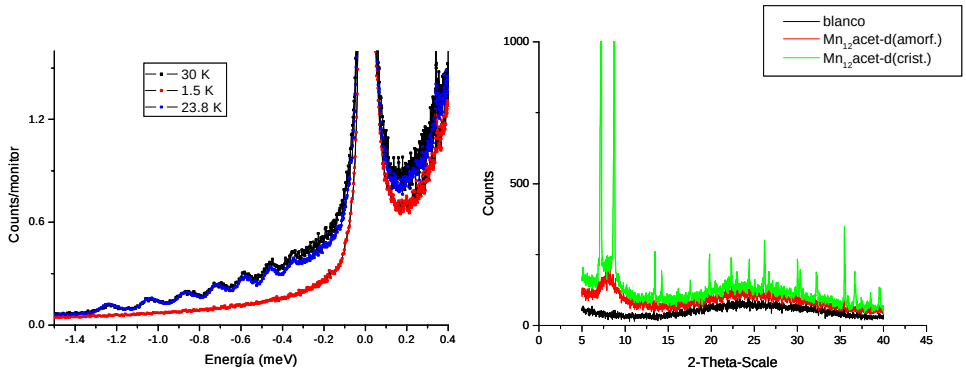

Fig. 2.4. Niveles de energía a campo magnético nulo correspondientes al sistema $[Mn_{12}O_{12}(O_2CCD_3)_{16}(D_2O)_4]$ *(18)* amorfo medidos en el instrumento de dispersión inelástica a distintas temperaturas *(iz.)*. Difractogramas correspondientes a las fases cristalina *(en verde)* y amorfa *(en rojo) (der.)*.

2.2. Mn_{12} en un entorno cristalino

2.2.1. Micro/nanopartículas cristalinas: Influencia del tamaño y morfología cristalina en las propiedades magnéticas

Uno de los objetivos de la Tesis fue la obtención de micro/nanopartículas cristalinas de complejos de Mn_{12} con un elevado control de las características finales, como son la distribución de tamaños, morfología y naturaleza polimórfica. Con ello se pretenden evitar las considerables variaciones tanto de forma como de tamaño que se obtienen en los productos de Mn_{12} obtenidos mediante las técnicas clásicas de cristalización, hecho que facilitaría una mejor interpretación de los resultados. Un ejemplo de dicha dispersión se muestra en la Figura 2.5 correspondiente a métodos cristalización por difusión en mezclas de disolventes *($CHCl_3$/hexano)*. La presencia de moléculas orgánicas de cristalización o bien ocluidas, además del mayor número de defectos, favorecen la ruptura mecánica de los cristales y la progresiva pérdida de cristalinidad.

Otro de los objetivos para obtener una serie de partículas cristalinas de complejos de Mn_{12} con tamaños y formas controlados es el estudio de los fenómenos de confinamiento[4] *(disminución de tamaño, relación volumen/superfice, etc.)* y la identificación del origen de los diversos mecanismos de relajación en los Mn_{12}. Estos estudios se realizaron en colaboración con la Dra. Nora Ventosa del *Institut de Ciència de Materials* de Barcelona, en el procesado de las muestras y reducción del tamaño por fluidos comprimidos *(FC)*, y el Dr. Javier Campo del Instituto de Ciencia de Materiales de Aragón, en las medidas de caracterización magnética.

Por ejemplo, a nivel molecular, la derivación de nanopartículas basadas en *prussian blue*, $M_i^{m+}[M'(CN)_6]^{n-}$, se ha estudiado dispersas en el interior de polímeros de coordinación orgánicos.[5,6] La influencia del tamaño en las propiedades magnéticas puede verificarse a través de posibles desplazamientos en la temperatura de bloqueo, observación de curvas de susceptibilidad ac o bien curvas de histéresis magnética.[7,8] Sin embargo, en el caso de los Mn_{12} su interés es diferente, dado que la propiedad magnética es intrínseca a cada molécula y no debido a interacciones de largo alcance como en el caso anterior. Así, la variación de tamaño se espera que pueda afectar, si varía, de forma diferente, principalmente debido al entorno cristalino.

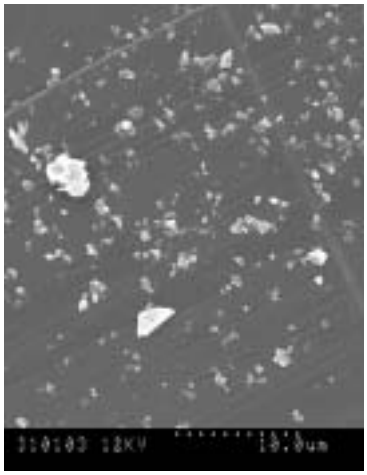

Fig. 2.5. Imagen SEM de una muestra de Mn_{12} benzoato, $[Mn_{12}O_{12}(O_2CC_6H_5)_{16}(H_2O)_4]$ *(17)*, obtenida por difusión de hexanos en una disolución de $CHCl_3$. Se observa una considerable dispersión de tamaños y formas además de una pérdida de la cristalinidad. De manera inevitable, esto repercute en los fenómenos de relajación magnética.

El método utilizado para obtener las partículas de Mn_{12} con una distribución de tamaños y formas lo más monodispersa posible es el método de cristalización con fluidos comprimidos *(p.ej. el CO_2)* y/o mezclas a alta presión de disolventes convencionales y FC.[9-11] Las técnicas de cristalización a alta presión, con FC, además de ser muy interesante desde el punto de vista ecológico, permiten un mayor control de las características físicas de las partículas cristalinas finales *(tamaño, distribución de tamaños, morfología y naturaleza polimórfica)* mediante el control de los parámetros de operación. Concretamente, la obtención de las partículas se llevó a cabo mediante técnicas de procesado en muestras cristalizables por el método de cristalización GAS.[12] A pesar de que estas técnicas de cristalización por FC han sido ampliamente desarrolladas, nunca antes se habían utilizado en el control del tamaño cristalino en materiales moleculares magnéticos. Para ello, se preparó una disolución inicial de Mn_{12} de concentración conocida en un disolvente orgánico *($CHCl_3$)* miscible en CO_2. La cristalización por precipitación se produce en el interior de un autoclave bajo control de las condiciones de trabajo temperatura, presión y fracción molar de CO_2. La disolución de Mn_{12} de partida se expande de forma repetida con el CO_2 comprimido hasta alcanzar las condiciones de trabajo deseadas en el interior del autoclave. De esta manera, el poder de solvatación del disolvente orgánico decrece causando una sobresaturación en la mezcla y posterior precipitación del soluto en forma particulada con distribución de tamaños uniforme. Por lo que respecta al tamaño de partícula, éste puede controlarse a partir del contenido en CO_2 del sistema presurizado,[13] bien sea por debajo de la micra hasta alcanzar las medidas de unos cientos de micras.

Siguiendo el procedimiento anteriormente descrito, se obtuvieron partículas del compuesto **17,** Mn_{12} benzoato, de tamaño y forma cristalina lo más monodispersas posibles dentro del intervalo de las micras, presentando todas ellas la misma fase cristalina tal y como mostraron los estudios de caracterización por rayos-X. A modo de ejemplo, en la Figura 2.6 se muestra una fotografía SEM de una serie de cristales de tamaño reducido procesados por cristalización con FC.

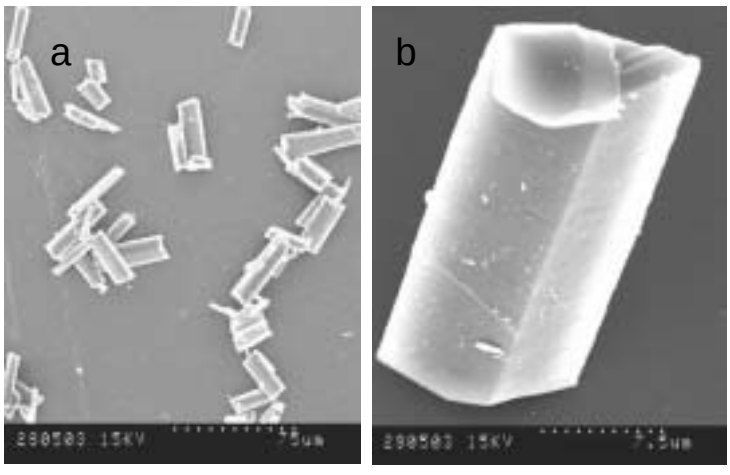

Fig. 2.6. Imágenes SEM sobre muestras cristalinas de Mn_{12} benzoato *(17)* procesado por el método GAS. *(b)* corresponde a una magnificación de *(a)*.

Tal y como se puede observar, los cristales obtenidos presentan además una morfología perfectamente definida, en este caso de paralelepípedos, una distribución de tamaños muy monodispersa. Finalmente, se desarrollaron estudios magnéticos adicionales *(M vs H, ac a diversos campos, relajación, etc)* observándose variaciones en el

comportamiento de relajación magnética según el tamaño de la partícula. Estos resultados, aunque preliminares, son de gran importancia ya que supondrían que muchos de los resultados anteriormente descritos en la literatura corresponderían a un promedio de las medidas. De esta manera se observa una disminución en los valores calculados de la barrera energética *(U)* a medida que se reduce el tamaño cristalino.[†]

2.2.2 Estudios en monocristal mediante técnicas neutrónicas

Para estos estudios se prepararon imanes unimoleculares de la familia del Mn_{12} que dispongan de una presencia mínima de átomos de hidrógenos o bien estén deuterados. Teniendo en cuenta los estudios previos realizados *ver (Capítulo 1)*, se descartó el uso de ácidos trihaloacéticos debido a favorecer la fragmentación del núcleo central metálico del Mn_{12}. Así, para minimizar o bien evitar la presencia de átomos de hidrógeno, los compuestos derivados $[Mn_{12}O_{12}(O_2CCHCl_2)_{16}(H_2O)_4]$ *(19)* o bien deuterado $[Mn_{12}O_{12}(O_2CCD_3)_{16}(D_2O)_4]$ *(18)* resultan excelentes candidatos para experimentos de neutrones, ya sea en forma de polvo microcristalino o como monocristales.

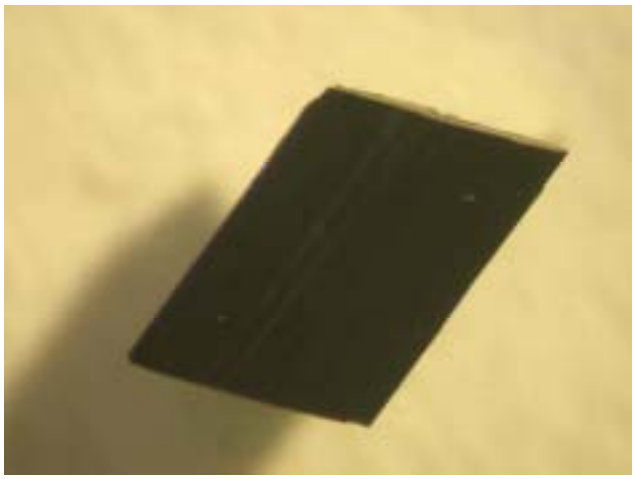

Fig. 2.7. Monoscristal estable del complejo $[Mn_{12}O_{12}(O_2CCHCl_2)_{16}(H_2O)_4]$ *(19)*.

La utilización de las técnicas neutrónicas favorece la determinación estructural nuclear y magnética de los compuestos debido a la naturaleza magnética de los neutrones, sin embargo, requieren de grandes cantidades de muestra, del orden de los gramos en muestras de polvo microcristalino y mucho más difícil resulta la obtención de monocristales que reúnan las dimensiones y características adecuadas. Después de diversos intentos, finalmente se encontraron las condiciones óptimas para la obtención de cristales de grandes dimensiones *(siempre considerando que se trata de un material molecular)* superando el orden de los 2-3 mm, tal y como se muestra en la Figura 2.7. El método más utilizado consiste en la difusión de n-hexanos sobre una solución saturada del complejo en CH_2Cl_2. Este método permite modular la velocidad de mezcla de ambos disolventes durante la cristalización, siendo particularmente efectiva en el caso del complejo **19**, Mn_{12} dicloroacetato, debido a una mayor afinidad de los grupos halogenados con el CH_2Cl_2.

[†] Para más información ver artículo G

Ordenamiento dipolar y transiciones de fase cuánticas en Mn_{12}

La difracción de neutrones se utilizó para determinar la imanación de un cristal molecular del complejo **18**, Mn_{12} acetato deuterado, de dimensiones (0.5 × 0.5 × 1.5 mm^3). La fase de cristalización de tipo tetragonal y la disposición de cada una de las moléculas con su eje fácil de imanación a lo largo del eje cristalográfico c *(modelo Ising)*, permiten estudiar posibles fenómenos de transición de fase cuántica ya observados en ferromagnetos 3-D que cumplen dicho modelo.[14] Sin embargo, en cristales de Mn_{12} cada molécula se comporta a bajas temperaturas como un imán unimolecular 0-D con estado fundamental de espín S=10 y una elevada anisotropía magnética en el eje c. La aplicación de un campo magnético perpendicular a dicho eje cristalográfico induce un túnel cuántico entre espines con orientaciones antiparalelas, permitiendo que el sistema alcance el equilibrio térmico en tiempos razonables. Por debajo de 0.9 K, las interacciones dipolares magnéticas intermoleculares convierten dicho equilibrio en una fase donde los imanes se ordenan ferromagnéticamente en el eje c. No obstante, si el campo perpendicular aplicado es superior o igual a 5.5 T, el estado magnético fundamental de cada molécula es una superposición con los espines orientados en sentido opuesto, suprimiendo las correlaciones ferromagnéticas de largo alcance.‡

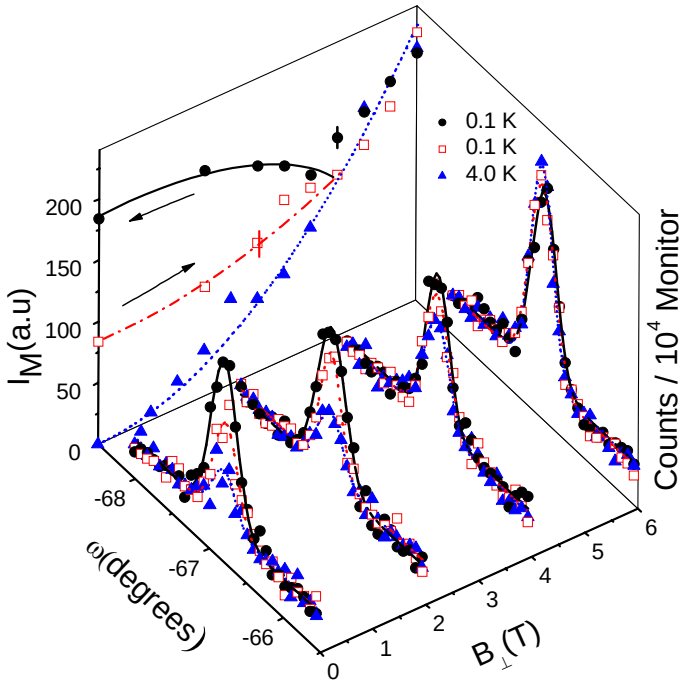

Fig. 2.8. w-scans e intensidad magnética a varias temperaturas en función del campo perpendicular aplicado.

Estos resultados suponen un gran interés no sólo para la comunidad del magnetismo molecular sino también para una amplia comunidad de científicos cuya motivación se basa en el estudio de las transiciones cuánticas y los sistemas nanomagnéticos.

Actualmente se están iniciando estudios de difracción de neutrones que permitan determinar la estructura nuclear en sistemas de Mn_{12} a bajas temperaturas. El objetivo principal es el de establecer correlaciones magneto-estructurales midiendo la estructura

‡ Para más información ver artículo H

nuclear del sistema y poder determinar el grado de distorsión de los octaedros de coordinación del Mn^{3+} a través del correcto posicionamiento de los átomos de oxígeno que conforman su entorno. Sin embargo, a pesar de que la adquisición de datos en este tipo de técnicas es relativamente rápida no podemos decir lo mismo acerca de la reducción de datos *(correcciones, escalado, integración, etc...).* Ello requiere un proceso largo y laborioso que no está actualmente optimizado. No obstante, la estructura del complejo **19**, Mn_{12} dicloroacetato, ha sido resuelta y actualmente el estudio se encuentra en fase de análisis y discusión de resultados.

2.3. Referencias[§]

1. M. R. Cheesman, V.S. Oanesyan, R. Sessoli, D. Gatteschi, A.J. Thomson, *Chem. Commun.*, **1997**, 1677.
2. E.J.L. McInnes, E. Pidcock, V.S. Oganesyan, M.R. Cheesman, A.K. Powell, A.J. Thomson, *J. Am. Chem. Soc.*, **2002**, *124*, 9219.
3. G.L.J.A. Rikken, E. Raupach, *Nature*, **1997**, *390*, 493.
4. G.T. Rado, H. Suhl, *Magnetism III*, Eds.; Academic Press: New York, **1963**, 271.
5. C.B. Murray, S. Sun, H. Doyle, T. Betly, *MRS Bull.*, **2001**, 985.
6. C. Liu, B. Zhou, A.J. Rondinone, Z.J. Zhang, *J. Am. Chem. Soc.*, **2000**, *122*, 6263.
7. H. Bönnemann, W. Brijoux, R. Brinkmann, T. Joussen, *Angew.Chem., Int. Ed. Engl.*, **1990**, *29*, 273.
8. K.-L. Tsai, J.L. Dye, *J. Am. Chem. Soc.*, **1991**, *113*, 1650.
9. P. York, *PSTT*, **1999**, *2*, 430.
10. J. Jung, M. Perrut, *J. Supercrit. Fluid*, **2001**, *20*, 179.
11. A. Shariati, C.J. Peters, *Curr. Opin. Solid ST M.*, **2003**, *7*, 371.
12. P.M. Gallagher, M.P. Coffey, V.J. Krukonis, N. Klasutis, *N. ACS. Symp. Ser.*, **1989**, *406*, 334.
13. P.M. Gallagher, M.P. Coffey, V.J. Krukonis, *J. Supercrit. Fluid*, **1992**, *5*, 130.
14. D. Bitko, T.F. Rosenbaum, G. Aeppli, *Phys. Rev. Lett.*, **1996**, *77*, 940.

[§] Referencias seleccionadas. Para más información ver anexos de los artículos.

Artículos relacionados: Capítulo 2

Propiedades magnéticas: sinergismo magneto-óptico y fenómenos de relajación

Artículo F

Título:
Magnetism of isolated Mn_{12} single-molecule magnets detected by magnetic circular dichroism: Observation of spin tunneling with a magneto-optical technique.

Autores:
N. Domingo, B.E. Williamson, J. Gómez-Segura, Ph. Gergier, D. Ruiz-Molina, D.B. Amabilino, J. Veciana, J. Tejada.

Revista:
Physical Review B

Magnetism of isolated Mn_{12} single-molecule magnets detected by magnetic circular dichroism: Observation of spin tunneling with a magneto-optical technique

N. Domingo,[1,*] B. E. Williamson,[2] J. Gómez-Segura,[3] Ph. Gerbier,[3] D. Ruiz-Molina,[3] D. B. Amabilino,[3] J. Veciana,[3] and J. Tejada[1]

[1]*Facultat de Física, Universitat de Barcelona, Avinguda Diagonal 647, 08028 Barcelona, Catalonia, Spain*

[2]*Department of Chemistry, University of Canterbury, Christchurch, New Zealand*

[3]*Institut de Ciència de Materials de Barcelona (CSIC), Campus Universitari, 08193 Bellaterra, Catalonia, Spain*

(Received 25 April 2003; published 20 February 2004)

We report magnetic and magneto-optical measurements of two Mn_{12} single-molecule magnet derivatives isolated in organic glasses. Field-dependent magnetic circular dichroism (MCD) intensity curves (hysteresis cycles) are found to be essentially identical to superconducting quantum interference device magnetization results and provide experimental evidence for the potential of the optical technique for magnetic characterization. Optical observation of magnetic tunneling has been achieved by studying the decay of the MCD signal at weak applied magnetic field.

DOI: 10.1103/PhysRevB.69.052405 PACS number(s): 75.50.Xx, 33.55.Fi, 75.45.+j, 78.67.Bf

Individual molecules that act as magnets are appealing from both fundamental scientific and technological points of view, especially given their potential as quantum computing components.[1] Much attention has focused on the family of molecules based on a dodecamanganese core, denoted generally as $[Mn_{12}O_{12}(O_2CR)_{16}(H_2O)_x]S_x$ (R=substituent, $x=3-4$, S=solvent). These systems behave as single-molecule magnets (SMM's),[2] but the vast majority of the previous studies on them have centered on crystalline materials. It is an intriguing and important challenge to investigate these molecules when they are isolated from each other, but since this is not currently feasible, we have chosen, in the interim, to study ensembles of molecules isolated from each other in inert matrices. On the other hand, the development of methods for measurement of magnetic and spin properties of isolated molecules is important when the detection limits of traditional superconducting quantum interference device (SQUID) instruments are reached. Key questions include what techniques can be used to study these phenomena and whether tunneling can be observed in isolated molecules using these other techniques. In order to answer these questions we have used two techniques, magnetic susceptibility and magnetic circular dichroism (MCD), and we will show that the magnetic and optical responses are essentially identical.

To a first approximation, the effective spin Hamiltonian for a Mn_{12} SMM is

$$H=-DS_z^2-g\mu_B\mathbf{S}\cdot\mathbf{H}+H', \tag{1}$$

where $D=0.55$ K is the zero-field splitting parameter for the ground-state manifold and $S=10$. H' contains terms that do not commute with S_z and are responsible for tunneling between different M_S states.

Isolated molecules of $Mn_{12}Ac$ ($R=CH_3$) and $Mn_{12}Bz$ ($R=C_6H_5$) can be obtained by dissolving them in noncoordinating organic solvents.[3] MCD requires optical isotropy and transparency, so the solvents were selected according to their facility for forming strain-free, transparent glasses at cryogenic temperatures.[4] Two mixtures were employed: (1) CH_2Cl_2:toluene (1:1 by volume) and (2) CH_3CN:dmf (where dmf=N,N'-dimethylformamide, 1:2 in volume). The molecular magnetic moments are so small that the torque imparted by applied magnetic fields up to 5×10^4 Oe is not enough to orient the molecules, which therefore remain randomly oriented in the frozen glass.

Magnetic measurements were performed using a commercial rf-SQUID magnetometer (MPMS2), with applied magnetic fields up to 5×10^4 Oe. Samples of 0.06 ml of 6-g/l solution were placed in a cylindrical Teflon container, which was sealed with a screw-on lid. The field dependencies of the magnetization for $Mn_{12}Ac$ and $Mn_{12}Bz$ in a glass of CH_2Cl_2:toluene ($Mn_{12}Ac/CH_2Cl_2$:tol and $Mn_{12}Bz/CH_2Cl_2$:tol) at $T=1.8$ K are shown in Figs. 1(a) and 1(b), respectively (gray curves). The lack of orientation prevents in this case observation of the steplike behavior in the magnetization hysteresis cycles seen at certain resonant fields and characteristic of tunneling.[5]

A quantitative description of the dynamics of the magnetization for a single molecule depends on the angle θ between the applied magnetic field and the molecule's easy axis of magnetization and can be expressed in terms of the differential equation

$$\frac{dM}{dH}=\frac{(H,T,\theta)}{\alpha}[M-M_{\mathrm{eq}}(H,T,\theta)]\sin\theta, \tag{2}$$

where $\alpha=dH/dt$ is the magnetic field sweeping rate, $M_{\mathrm{eq}}(H,T,\theta)$ is the equilibrium magnetization, and $\Gamma(H,T,\theta)$ is the relaxation rate that can be written as $\Gamma=\nu_0\exp(-U_{\mathrm{eff}}/k_BT)$. Here, ν_0 is the attempt frequency and U_{eff} is the effective potential-energy barrier, which includes the conditions of resonance that also depend on θ. At very low temperatures, when only the $M_S=\pm10$ levels are significantly populated, the equilibrium magnetization is closely approximated by

$$M_{\mathrm{eq}}=M_{\mathrm{sat}}\left[\tanh\left\{\frac{g\mu_B|S|H\cos\theta}{k_BT}\right\}+\frac{H\sin\theta}{H_a}\right]. \tag{3}$$

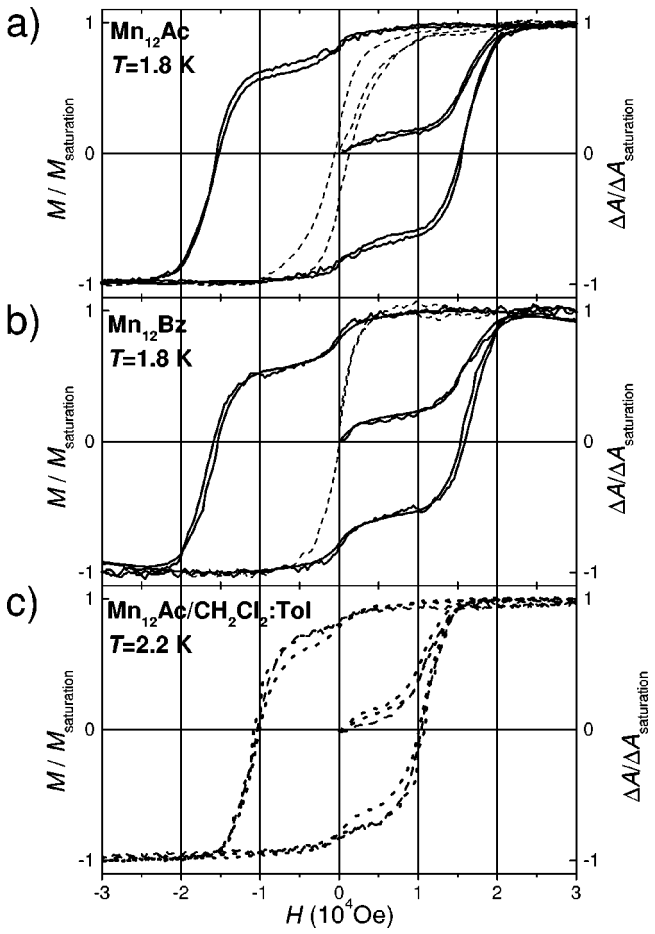

FIG. 1. Field dependence of SQUID magnetization (gray curves) and MCD at 21 200 cm^{-1} (black curves) for $Mn_{12}Ac$ (a) and $Mn_{12}Bz$ (b). In (a) and (b), the black solid curves indicate the magnitude of the MCD in 1:1 CH_2Cl_2:tol glasses, while the dashed lines correspond to the relevant SMM in a 1:2 CH_3CN:dmf glass. For (c), the gray dotted curve indicates the magnetization of $Mn_{12}Ac/CH_2Cl_2$:tol, while the black curves represent MCD measurements at 21 200 cm^{-1} (dotted line) and 19 700 cm^{-1} (dashed line).

The first term inside the brackets of Eq. (3) confers the tanh dependence that is typical paramagnetic behavior of an isolated pair of Zeeman levels, which is a good approximation for the low-temperature limit. The second (linear) term arises from misalignment of the easy axis of magnetization of the particles with the field, which causes mixing of states that differ by ± 1 in their M_S values. In order to simplify the analysis of the data, the linear contribution to the magnetization has been subtracted from the results shown in Fig. 1. The remaining part is sensitive to relaxation mechanisms and, at temperatures below the blocking temperature, gives rise to hysteresis.

The steps seen near zero field in Fig. 1 were observed at all temperatures between 1.8 and 3 K. They are consistent with the existence of two molecular species with different effective energy barriers and therefore different relaxation rates and blocking temperatures. While the species with the higher temperature barrier is blocked in this temperature range, the other remains superparamagnetic and thus undergoes a rapid change of magnetization near zero field. This hypothesis is confirmed by the presence of two frequency dependent peaks in both components of the ac-magnetic susceptibility of $Mn_{12}Ac/CH_2Cl_2$:tol and $Mn_{12}Bz/CH_2Cl_2$:tol.[6] The high-temperature blocking peak is usually placed between 3.5 and 6 K, while the low-temperature peak appears around 2 K. The low-temperature peak has also been observed in certain Mn_{12} derivatives, where it is ascribed to Jahn-Teller distortions of the core.[7] The height of the zero-field step depends on the fraction of molecules that undergo the fast relaxation mechanism, which is calculated from the ac-susceptibility peaks to be about 15% for $Mn_{12}Ac/CH_2Cl_2$:tol and 20% for $Mn_{12}Bz/CH_2Cl_2$:tol. Another contribution to the zero-field step arises from the fact that all molecules undergo resonant tunneling between spin states at zero field, irrespective of their orientation (see below), but this is very small in comparison with the superparamagnetic contribution seen here, and thus it can be considered as irrelevant.

MCD is the differential absorption of left and right circularly polarized light by a sample in longitudinal magnetic field,[8] and can be written as $\Delta A = A_L - A_R$. It provides a powerful tool for studying molecular systems with degenerate electronic states. For orbitally nondegenerate paramagnetic species, the intensity of the MCD associated with a given transition depends on the degree of spin-orbit coupling and varies with magnetic field and temperature in a manner that is determined by the ground- and excited-state parameters, including g factors and zero-field splittings (ZFS).[9] An analysis of MCD of $Mn_{12}Ac$ has been published recently,[10] wherein a quantitative description of the polarization of each optical transition is given. We have investigated the MCD of Mn_{12} SMM's using a spectrometer that is described elsewhere.[11] We show here that this spectroscopic technique is not only related with magnetization but permits effectively the same measurements as SQUID magnetometry, as it can be inferred by comparision of quantitative description of MCD shown by McInnes *et al.* with Eqs. (2),(3).

MCD spectra at $T = 4.2$ K are shown in Fig. 2. Four bands are observed for both $Mn_{12}Ac/CH_2Cl_2$:tol and $Mn_{12}Bz/CH_2Cl_2$:tol, but the change of solvents leads to significant differences. In CH_3CN:dmf the $\sim$19 700-cm^{-1} band almost disappears and there is a relative enhancement of the band at $\sim$21 100 cm^{-1}. McInnes *et al.*[10] have described the MCD spectra for Mn_{12} SMMs in the low-temperature limit with a simple model comprising B and C terms.[8] B terms are linearly proportional to the field and are associated with diamagnetism in either the ground or excited state of the electronic transition. C terms are associated with ground-state paramagnetism and, in the limit of a two-level Zeeman system assuming that equilibrium thermal populations are maintained, have the same tanh dependence on the applied magnetic field as the magnetization shown in Eq. (3).

The magnetic-field dependencies of the MCD signals at 21 200 cm^{-1} are shown in Figs. 1(a) and 1(b) for $Mn_{12}Ac$ and $Mn_{12}Bz$ in both CH_2Cl_2:tol and CH_3CN:dmf glasses. Measurements were made using the same experimental conditions as for the SQUID magnetization loops. The MCD signal was measured continuously while changing the field at

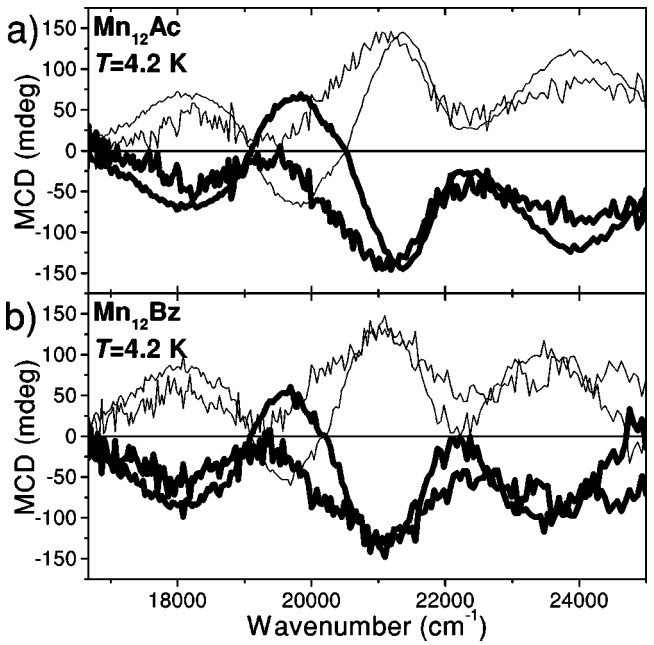

FIG. 2. MCD spectra for the relevant SMM in CH_2Cl_2:tol 1:1 (black lines) and CH_3CN:dmf 1:2 (gray lines) at $H=10^4$ Oe (thick lines) and $H=-10^4$ Oe (thin lines).

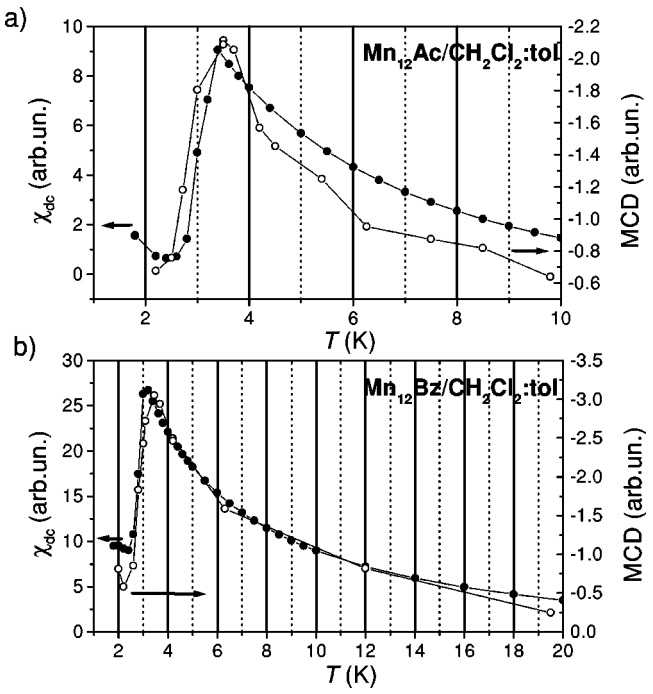

FIG. 3. ZFC measurements of (a) $Mn_{12}Ac$ and (b) $Mn_{12}Bz$ in 1:1 glasses of CH_2Cl_2:tol, with an applied magnetic field of $H=10^3$ Oe. Solid circles indicate SQUID measurements (referred to the left axis) and open circles stand for MCD measurements (referred to the right axis).

a rate of $\alpha=19.6$ Oe/s. By subtracting the linear B-term contributions, the MCD results can be directly compared with the SQUID magnetization data. As seen in Fig. 1, the hysteresis loops measured by the two methods are essentially identical. Moreover, as shown in Fig. 1(c), the MCD cycle measured for the 19 700-cm^{-1} band of $Mn_{12}Ac/CH_2Cl_2$:tol (which has been assigned polarization properties significantly different from those of the 21 200-cm^{-1} band[8]) is superimposable on the 21 200-cm^{-1} curve of the same sample after the linear contributions have been subtracted.

Comparing the MCD hysteresis cycles measured at the same wavelength for $Mn_{12}Ac/CH_2Cl_2$:tol and $Mn_{12}Ac/CH_3CN$:dmf [Fig. 1(a)], we see that, for the latter, there is a huge increase of the zero-field step. In addition, the remnant magnetization at zero field is reduced to about 30% of the saturation value, reproducing the previously reported results for the same system.[4] As noted above, the magnitude of the zero-field step should be correlated with the relative intensity of the low-temperature blocking peak of the in-phase component of the ac-magnetic susceptibility, both being determined by the proportion of molecules that undergo the fast relaxation mechanisms. Thus, it appears that there is a clear influence of the environment on the blocking barriers of these SMM's; the CH_3CN:dmf glass induces a much greater proportion of fast-relaxing molecules than is the case for CH_2Cl_2:tol mixture. These results are confirmed by ac-magnetic susceptibility measurements, where an increase of the high- or low-temperature blocking peak is observed for the glasses. For $Mn_{12}Bz$ the increase of fast-relaxing molecules due to the change of solvent is even greater [Fig. 1(b)], and for $Mn_{12}Bz/CH_3CN$:dmf there is no hysteretic behavior, even down to 1.7 K.

MCD spectroscopy can also be used for zero-field-cooled (ZFC) experiments and the measurements of tunneling phenomena. ZFC dc susceptibility data obtained for $Mn_{12}Ac/CH_2Cl_2$:tol and $Mn_{12}Bz/CH_2Cl_2$:tol using the SQUID and by MCD spectroscopy at 21 200 cm^{-1} are shown in Figs. 3(a) and 3(b). Results obtained for both techniques are in close accord. They show the blocking temperature peak at 3.5 K and the same Curie-Weiss $[\sim(T-T_c)^{-1}]$ behavior at higher temperatures. The low-temperature blocking peak is not clearly seen for these dc measurements because is out of the working temperature range.

The determination of information about tunneling in glasses is limited by the random orientation of the molecules. However, evidence of tunneling can be obtained by comparing the relaxation rates at zero field with those at small, nonzero fields. If relaxation resulted only from classical thermal effects, the highest energy barrier, and thus the slowest relaxation rate, should occur at zero field. When tunneling effects are significant, their contributions to relaxation will be greatest when conditions of resonance are attained between states of different M_S. For a sample of randomly oriented SMM's, the only resonance that occurs simultaneously for all molecules is at zero field, which should therefore correspond to a local maximum of the relaxation rate.

Decay measurements of the MCD signal where performed at 21 200 cm^{-1} for $Mn_{12}Ac/CH_2Cl_2$:tol at 2.2 K. A field of -2.5×10^4 Oe was applied to saturate the sample, then rapidly changed to zero or other weak positive fields. After an initial rapid decrease of signal due to the superparamagnetic

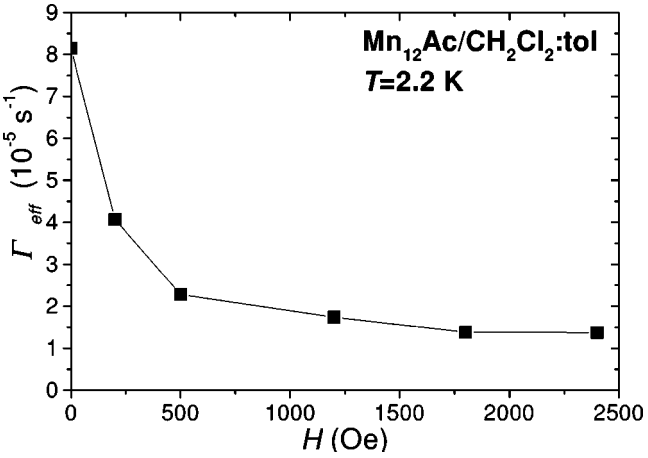

FIG. 4. Magnetic field dependence of the MCD decay rate.

particles, the decay curves could be accurately fitted with the equation $\Delta A(t)=\Delta A_{eq}+(\Delta A_{sat}-\Delta A_{eq})\exp(-\Gamma_{eff}t)$ where Γ_{eff} represents an effective decay rate for the entire randomly oriented ensemble. The field dependence of Γ_{eff} for $Mn_{12}Ac/CH_2Cl_2$:tol is shown in Fig. 4. The maximum at zero field clearly confirms the presence of tunneling. To our knowledge, this is the first observation of spin tunneling with a magneto-optical method.

To summarize, we have shown that MCD is a powerful technique for magnetic characterization of SMM's. The MCD signal is directly proportional to magnetization, reproducing the magnetometry experiments and can be accurately described through Eqs. (2), (3). Measurements performed on Mn_{12} SMM's at visible wavelengths have permitted determination of properties from blocking temperatures to quantum tunneling. Further development of optical methods for magnetization measurements has a special appeal with regard to quantum computing applications.

This work was supported by grants from the *Programa Nacional de Materiales* of the DGI (Spain), under project MAGMOL, the Information Society Technologies Program of the European Commission, under project NANOMAGIQC, and the 3MD Network of the TMR program of the E.U. (Contract No. ERBFMRX CT980181). B.E.W. acknowledges support through internal research Grant No. U6501 from the University of Canterbury, and N.D. acknowledges the Grant No. AP2000-1842 for FPU of the MECD (Spain).

*Corresponding author: Email: neus@ubxlab.com

[1] M. N. Leuenberger and D. Loss, Nature (London) **410**, 789 (2001); J. Tejada, E. M. Chudnovsky, E. Del Barco, J. M. Hernández, and T. P. Spiller, Nanotechnology **12**, 181 (2001).

[2] G. Christou, D. Gatteschi, D. N. Hendrickson, and R. Sessoli, MRS Bull. **25**, 26 (2000); A. Caneschi, D. Gatteschi, C. Sangregorio, R. Sessoli, L. Sorace, A. Cornia, M. A. Novak, C. Paulsen, and W. Wernsdorfer, J. Magn. Magn. Mater. **200**, 182 (1999).

[3] R. Sessoli, D. Rovai, C. Sangregorio, T. Ohm, C. Paulsen, and A. Caneschi, J. Magn. Magn. Mater. **177–181**, 1330 (1998).

[4] M. R. Cheesman, V. S. Oganesyan, R. Sessoli, D. Gatteschi, and A. J. Thomson, Chem. Commun. (Cambridge) **17**, 1677 (1997).

[5] J. R. Friedman, M. P. Sarachik, J. Tejada, and R. Ziolo, Phys. Rev. Lett. **76**, 3830 (1996); J. M. Hernández, X. X. Zhang, F. Luis, J. Tejada, J. R. Friedman, M. P. Sarachik, and R. Ziolo, Phys. Rev. B **55**, 5858 (1997); E. M. Chudnovsky and J. Tejada *Macroscopic Quantum Tunneling of the Magnetic Moment* (Cambridge University Press, Cambridge, England, 1998); D. Gatteschi and R. Sessoli, Angew. Chem., Int. Ed. **42**, 268 (2003).

[6] See EPAPS Document No. E-PRBMDO-69-023401 for ac magnetic susceptibility for microcrystalline powder of $Mn_{12}Bz$ in Araldit and in a 1:1 glass of CH_2Cl_2:toluene. A direct link to this document may be found in the online article's HTML reference section. The document may also be reached via the EPAPS homepage (http://www.aip.org/pubservs/epaps.html) or from ftp.aip.org in the directory /epaps/. See the EPAPS homepage for more information.

[7] D. Ruiz, Z. Sun, B. Albela, K. Folting, J. Ribas, G. Christou, and D. N. Hendrickson, Angew. Chem., Int. Ed. **37**, 300 (1998); Z. Sun, D. Ruiz, N. R. Dilley, M. Soler, J. Ribas, K. Folting, M. B. Maple, G. Christou, and D. N. Hendrickson, Chem. Commun. (Cambridge) **19**, 1973 (1999).

[8] S. B. Piepho and P. N. Schatz, *Group Theory in Spectroscopy with Applications to Magnetic Circular Dichroism* (Wiley Interscience, New York, 1983).

[9] V. S. Oganesyan and J. Thomson, J. Chem. Phys. **113**, 5003 (2000).

[10] E. J. L. McInnes, E. Pidcock, V. S. Oganesyan, M. R. Cheesman, A. K. Powell, and A. J. Thomson, J. Am. Chem. Soc. **124**, 9219 (2002).

[11] V. S. Langford and B. E. Williamson, J. Phys. Chem. A **101**, 3119 (1997).

Artículo G

Título:
Controlled crystallization of Mn_{12} single-molecule magnets by supercritical fluids and its influence on the magnetization relaxation

Autores:
M. Muntó, J. Gómez, J. Campo, N. Ventosa, J. Veciana, D. Ruiz-Molina

Revista:
Chemical Communications (en evaluación)

Controlled crystallization of Mn_{12} single-molecule magnets by compressed CO_2 and its influence on the magnetization relaxation

María Muntó,[a] Jordi Gómez-Segura,[a] Javier Campo,[b] Nora Ventosa,[a] Jaume Veciana*[a] and Daniel Ruiz-Molina*[a]

Receipt/Acceptance Data **[DO NOT ALTER/DELETE THIS TEXT]**
Publication data **[DO NOT ALTER/DELETE THIS TEXT]**
DOI: 10.1039/b000000x [DO NOT ALTER/DELETE THIS TEXT]

Microparticles of complex $[Mn_{12}O_{12}(O_2C_6H_5)_{16}(H_2O)_4]$ (1) with controlled size and polymorphism have been prepared by dense-gas crystallization techniques, showing a remarkable particle size influence on the magnetization relaxation rates.

Single-molecule magnets (SMM) have a large-spin ground state with appreciable magnetic anisotropy, resulting in a barrier for the spin reversal.[1] As a consequence, interesting magnetic properties such as out-of-phase ac magnetic susceptibility signals, magnetization hysteresis loops[2] and resonant magnetization tunneling, have been reported.[3] Although the origin of such properties has been unequivocally attributed to individual molecules rather than to the existence of long range magnetic intermolecular interactions, they have been shown to be very dependent on structural and crystalline restrictions. For instance, previous works have shown the influence of dislocations on the resonant spin tunneling of a crystal of Mn_{12} clusters[4] or the existence of at least two different magnetization relaxation processes,[5] being them highly influenced by the network characteristics.[6] For these reasons, the preparation of crystalline samples of SMMs with controlled structural parameters, such as morphology, size and polymorphism, has become a challenge. If succesful, this will give us a unique opportunity to study the influence of such structural parameters on the magnetization relaxation mechanisms.

One of the most effective crystallization methodologies used over the last decade for attaining such an objective, is based on the use of supercritical fluids.[7] Compressed fluids, have allowed for the straightforward preparation of crystalline solids with micro-/nanoscopic particle size, high polymorphic purity and smaller size dispersion. However, as far as we know, it has never been used before for the controlled crystallization of SMM's. In this work we report the controlled crystallization of $[Mn_{12}O_{12}(O_2C_6H_5)_{16}(H_2O)_4]$ (**1**) by the Gas Anti-Solvent crystallization technique (GAS), that utilizes compressed CO_2 as an anti-solvent.[8] These studies allowed us for: i) the preparation of crystalline samples of complex **1** with polymorphic purity, controlled particle size and narrower size distribution and ii) to establish the influence of the particle size on the magnetization relaxation rates.

As can be seen in Figure 1, the scanning electron microscopy (SEM) image of a sample of complex **1** obtained by a standard diffusion of *n*-hexane into CH_2Cl_2 (sample **1a**), reveals a broad distribution of sizes and morphologies, showing the crystals several defects and imperfections. Such distribution is even favoured in some cases by the loss of interstitial crystallization solvent molecules, and the subsequent fragmentation of the original crystalline material. On the contrary, the SEM image of a new sample obtained by the GAS crystallization method (sample **1b**), reveals the obtaining of crystals with a considerable improved size uniformity. Such differences were quantitatively confirmed by the light scattering particle size measurements gathered in Table 1. As can be seen there, sample **1b** exhibits a smaller particle size distribution with an uniformity index (U.I.) almost one order of magnitud larger. Moreover, in contraposition to most samples obtained by conventional crystallization techniques, the GAS processed sample is stable for long periods of time at room temperature since it crystallizes without guest solvent molecules, as confirmed by thermal studies and elemental analysis.

The magnetic characterization of samples **1a** and **1b** reveals two peaks in the out-of-phase ac signal (χ_M''), associated with the presence of at least two different magnetization relaxation mechanisms.[9] The existence of both out-of-phase peaks is not new and has already been described for several other Mn_{12} single-molecule magnets. However, a detailed study reveals unexpected differences on the resulting effective interconversion energy barriers. In the case of the slowest relaxation process, the effective energy barrier (U_{eff}) was 65.4 K and 63.7 K for **1a** and **1b**, respectively, whereas for the fastest relaxation mechanism was 38.4 K and 36.9 K for **1a** and **1b**, respectively.

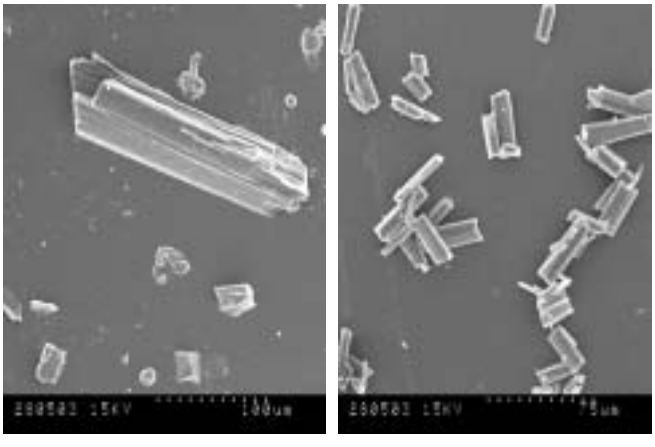

Fig. 1 Scanning Electron Microscopy images taken on sample **1a** (left) obtained by a conventional crystallization and **1b** (right), prepared by a GAS crystallization technique.

† Electronic Supplementary Information (ESI) available: [details of any supplementary information available should be included here]. See http://dx.doi.org/10.1039/b000000x/

* dani@icmab.es

Table 1. Operational parameters and results characteristic of microcrystals of complex **1**, obtained by the GAS method from CO_2-expanded $CHCl_3$ and by conventional antisolvent diffusion method with CH_2Cl_2/hexane solvent mixtures.

Exp	X_W	*Yield (%)*	*Diameter of particles (μm)*[a]			*U.I* [c]
			D(0.1)	D(0.5)	D(0.9)	
1d	0,85	75	5	15	35	15
1c	0,70	55	5	20	40	13
1b	0,50	35	5	30	65	8
1a[b]			2	50	150	1

[a] Volumetric particle size distributions, measured by light scattering technique, are given as 10, 50 and 90% quantizes. [b] Values correspond to the means of the particle size distributions. The average diameters of the particles were confirmed by SEM images. [c] Uniformity Index, is defined as U.I.= [D (0.1)/ D(0.9]*100

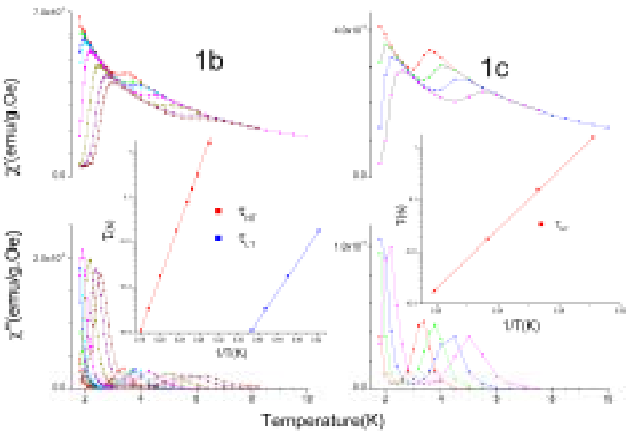

Figure 3. In-phase (χ') and out-of-phase (χ'') ac magnetic susceptibility curves versus temperature measured at several frequencies in the range 0.01 Hz to 1.4 kHz for the **1b** and **1c** samples. The inserts show the fit of the relaxation time to the Arrhenius law for the fast (red) and slow relaxing species (blue).

Variations on U_{eff} may be attributed to the morphological differences shown in Figure 1, although polymorphism could not be neglected at this point.[10] Indeed, as can be seen in Figure 2, the X-ray powder diffractograms of both samples are different, confirming that a new crystallographic phase is obtained by the GAS method.[11] Therefore, to give more insight into the origin of such magnetic divergences, two new samples (**1c** and **1d),** were obtained by increasing the solvent CO_2 molar fraction (X_w) used during the GAS crystallization. The characteristics of crystalline particles resulting from the GAS process can be tuned varying only one operational parameter. For samples **1c-d**, the same supersaturation ratios, stirring rates, CO_2 flow rates, working temperature and pressures, were used. The only different operational parameter was X_W. Since the CO_2 is acting as anti-solvent, an increase of X_w will induce an increase of the maximum supersaturation attained in the solution, enhancing nucleation over crystal growth, and therefore, the obtaining of smaller particles with a narrower size distriution. This is indeed what happens. As expected, data summarized in Table 1 indicate that samples **1c** and **1d** have a smaller average particle diameter and a higher U.I. Moreover, the powder X-ray diffractograms of the GAS processed samples **1c** and **1d** are in perfect agreement with that obtained for sample **1b**, confirming that the same polymorph has been obtained (for comparison purposes, the powder X-ray diffractogram of sample **1c** is also shown in Figure 2). Therefore, samples **1b-d** are excellent candidates to study particle size influence on the magnetization relaxation of Mn_{12} clusters.

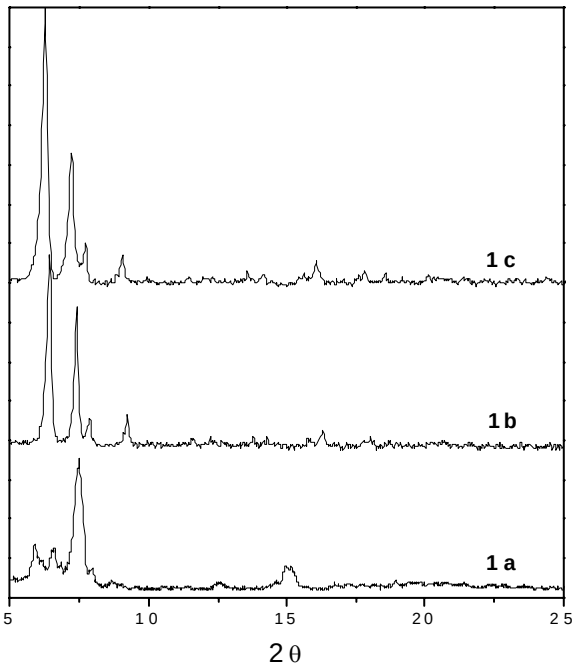

Figure 2. Low angle part of the XR diffraction patterns taken at room temperature for the compounds 1a-c.

Ac magnetic susceptibility curves for samples **1c-d** were obtained and studied. For each sample, the two peaks in χ_M'', associated with the presence of the fast and slow relaxing species, are also observed. However, a deeper ananlysis and comparison of the χ_M'' curves for samples **1b-d**, reveals variations on the ratio of both species and considerable temperature shifts on the maximum of the ac peaks. As an example, the plot of the in-phase and out-of-phase ac susceptibility (χ_M' and χ_M'') signals versus temperature taken at different frequencies for samples **1b** and **1c** are shown in Figure 3. Moreover, considerable differences on U_{eff} for the slow relaxing species were observed. Such effective energy barrier was found to be 65.4 K and 68.9 K for, **1c** and **1d**, respectively, differing by almost 5 K with respect to that found for sample **1b** (63.7 K).[12] Considering that samples **1b-d** have been shown to exhibit the same crystallographic phase (X-Ray) and morphology (SEM), such differences on the effective energy barier most likely arise from differences on the particle size.

In summary, we have reported the use of dense gases for the obtaining of a new crystalline phase of Mn_{12} complex **1** with control on its particle size, dispersivity and polymorphic purity.

This can be extended to the crystallization of several other functional molecular materials where control of a given property is highly desired. Moreover, comparison of the magnetic properties of the three samples crystallized by the GAS method, which differ on their average particle size distribution, reveals significant differences on the effective energy barrier for the magnetic interconversion. Such differences may arise both, from variations on the molecular anisotropy (variations of the D value) and/or modifications on the tunneling behavior along the miniaturization process. Further work is currently underway to shed more light on this origin, due to its importance for understanding the magnetization relaxation of SMMs and their potential technological implications.

This work was supported by DGI (Spain) under projects MAT2002-0043 and by the European Commission under the NoE MAGMANET (Contract NMP3-CT-2005-515767) and QUEMOLNA Marie Curie RTN (Contract MRTN-CT-2003-5044880).

María Muntó,[a] Jordi Gómez-Segura,[a] Javier Campo,[b] Nora Ventosa,[a] Jaume Veciana[a] and Daniel Ruiz-Molina*[a]

[a] *Institut de Ciència de Materials de Barcelona (CSIC), Campus Universitari, 08193 Bellaterra, Catalonia, Spain. Fax: 34 93 580 57 29; Tel: 34 93 580 18 53; E-mail: dani@icmab.es*

[b] *Instituto de Ciencia de Materiales de Aragón, CSIC-Universidad de Zaragoza, C/ Pedro Cerbuna 12, 50009 Zaragoza (Spain); Fax: 34 93 976 76 12 29; Tel: 34 34 976 76 27 42*

Notes and references

† The GAS crystallization procedure used for the crystallization of complex **1** comprises four steps: 1) dissolution of the complex **1** in $CHCl_3$ at 298 K and atmospheric pressure to form a solution with a supersaturation ratio of β_i=C/Cs =0.9, where C stands for the initial concentration of complex **1** and C_s stands for the saturation limit, 2) addition of CO_2 at flow rate, Q = 0.45 Kg/h, over the mixture $CHCl_3$/**1** solution to obtain a volumetric expanded liquid solution, at 298 K and a pressure of 10 MPa, containing a given molar fraction CO_2 molar fraction, X_W. During the addition of CO_2 the solution is vigorously stirred. *Sample Characterization*. Scanning Electron Microscopy (SEM) was done on a Hitachi S-570 and a Hitachi 2300 Scanning electron Microscope. Volumetric particle size distributions were measured by the Light Laser Scattering technique on a Beckman- Coulter LS 13 320 following the International Standard ISO 13320-1:1999(E). X-Ray powder spectra were obtained by placing the sample into a 300 micron-diameter-capillar and recording the spectra from 2Q=2 to 60 with a diffractometer (INEL CPS-120) working in Debye-Sherrer geometry. Alternating current (ac) magnetic susceptibility experiments were carried out on a Quantum Design SQUID magnetometer. Ac magnetic susceptibility curves were studied for samples of complex **1a-c** in the 1.8-10 K range with a 1 Oe ac oscillating field in the frequency range of 0.01-1400 Hz while the external magnetic field was held at zero. The magnetization relaxation times (τ) were obtained from the relationship $\omega\tau$=1 at the maxima of the χ_M'' vs. temperature curves. The χ_M'' peak positions were determined by fitting the χ_M'' vs. temperature data to, one or two, Lorentzian functions. Then the inverse of each peak position versus τ are fitted, by least-squares procedures, to the Arrhenius law.

1 (a) G. Christou, D. Gatteschi, D. N. Hendrickson, and R. Sessoli, *MRS Bull*. 2000, **25**, 56. (b) D. Gatteschi and R. Sessoli, *Angew. Chem. Int. Ed*. 2003, **42**, 268.

2. (a) R. Sessoli, D. Gatteschi, A. Caneschi, A. Novak, *Nature* 1993, **365**, 141. (b) D. Gatteschi, A. Caneschi, L. Pardi, R. Sessoli, *Science* 1994, **265**, 1054.

3. (a) J. R. Friedman, M. P. Sarachik, J. Tejada, and R. Ziolo, *Phys. Rev. Lett*. 1996, **76**, 3830. (b) J.M. Hernández, X.X. Zhang, F. Luis, J. Bartolomé, J. Tejada, R. Ziolo, *Europhys. Lett*. 1996, **35**, 301. (c) L. Thomas, F. Lionti, R. Ballou, D. Gatteschi, R. Sessoli, B. Barbara, *Nature* 1996, **383**, 145.

4. J. M. Hernandez, F. Torres, J. Tejada, E. Molins, *Phys. Rev. B*. 2002, **16,** 1407

5. D. Ruiz-Molina, G. Christou, D. N. Hendrickson, Mol. Cryst. Liq. Cryst. 2000, 343, 335.

6. M. Soler, W. Wernsdorfer, Z. M. Sun, J. C. Huffman, D. N. Hendrickson, G. Christou, *Chem. Commun*. 2003, 2672.

7. (a) J. Jung, M. Perrut, *J. Supercrit. Fluids*, 2001, **20**, 179. (b) D.W. Matson, J.L. Fulton, R.C. Petersen, R.D. Smith, *Ind. Eng. Chem. Res.*, 1987, **26**, 2298. (c) R.Thiering, F. Dehgani, N.R. Foster, *J. Supercrit. Fluids*, 2001, **21**, 159. (d) N. Ventosa, S. Sala, J. Veciana, J. Llibre, J. Torres, *Cryst. Growth & Design*, 2001, **1**, 299.

8. In the GAS process, a volume of liquid solution of the compound to crystallize is expanded several-fold by mixing it with compressed CO_2. This expansion produces a solvating power decrease of the mixture, which becomes supersaturated and then the solute precipitates as a finely divided powder. For more information see: P.M. Gallagher, M.P. Coffey, V.J. Krukonis, N. Klasutis, *Supercritical Fluids Science and Technology*, ACS Symp. Ser., 1989, **406**,334.

9. (a) D. Ruiz, Z. S. Sun, B. Albela, K. Folting, J. Ribas, G. Christou, D. N. Hendrickson, *Angew. Chem. Int. Ed. Engl*. 1998, **37**, 300. (b) Z. M. Sun, D. Ruiz, E. Rumberger. C. D. Incarvito, K. Folting, A. L. Rheingold, G. Christou, D. N. Hendrickson, *Inorg. Chem*. 1998, **37**, 4758.

10. This is a common situation for crystalline materials obtained by supercritical fluids. Indeed, crystallization takes place far from stable thermodynamic situations, enhancing the obtaining of kinetically favored polymorphic forms, non achievable by thermodynamically controlled methods.

11. The X-ray diffractogram of sample **1a** is in agreement with that simulated for a structure of **1** already publsihed. See: R. Sessoli, H. – L. Tsai, A. R. Schake, S. Wang, J. B. Vincent, K. Folting, D. Gatteschi, D. N. Hendrickson, *J. Am. Chem. Soc*. 1993, **115**, 1805.

12. On the same frequency range the χ_M'' peaks for **1c-d** appear out of the temperature working range. This was another evidence for the particle size influence on the magnetization relaxation of Mn_{12} SMMs.

Artículo H

Título:
Observation of a quantum phase transition in a crystal of interacting nanomagnets

Autores:
F. Luis, J. Campo, J. Gómez, G. J. McIntyre, J. Luzón, D. Ruiz.

Revista:
Physical Review Letters

Observation of a Quantum Phase Transition in a Crystal of Interacting Nanomagnets

F. Luis*,[1], J. Campo[1], J. Gómez[2], G. J. McIntyre[3], J. Luzón[1], and D. Ruiz[2]
[1] *Instituto de Ciencia de Materiales de Aragón, CSIC-Universidad de Zaragoza, 50009 Zaragoza, Spain.*
[2] *Institut de Ciencia de Materials de Barcelona, Campus de la UAB, Bellaterra 08193, Spain.*
[3] *Institut Laue Langevin, 6 rue Jules Horowitz, 38042 Grenoble, France.*

We use neutron diffraction to probe the magnetization of a crystal of Mn_{12} single-molecule magnets. Each of these behaves, at low temperatures, as a nanomagnet with spin $S = 10$ and strong anisotropy along the crystallographic c axis. Application of a magnetic field $B_\perp$ perpendicular to c induces quantum tunneling between opposite spin orientations, enabling the spins to attain thermal equilibrium. Below 0.9 K dipolar intermolecular interactions turn this equilibrium state into a ferromagnetically ordered phase. However, if $B_\perp > 5.5$ T the magnetic state of each molecule becomes a superposition of states with spin pointing up and down along c, which destroys the long range ferromagnetic correlations.

PACS numbers: 75.45.+j, 75.50.Xx

Magnetic nanostructured materials have opened new frontiers for both, basic science and practical applications, due to their unique size-dependent properties [1]. Several fundamental problems remain, however, to be understood. Of particular interest are the observation of phase transitions and the study of collective magnetic behavior in dense arrays of nanoscopic magnets. In conventional magnets, *classical* phase transitions [2] take place when the temperature is raised to a certain critical value T_c. Alternatively, a quantum phase transition can occur even at $T = 0$, if a parameter controlling magnetic interactions attains a critical threshold [3]. Quantum phase transitions differ fundamentally from their classical counterparts since they are brought about by zero-point fluctuations and imply a change of the system's ground state. Such a quantum critical behavior has been observed for 3-D model Ising ferromagnets [4]. It however remains an unresolved issue for arrays of magnetic nanoparticles, which, for their size, are intermediate (mesoscopic) between the domains of validity of quantum and classical Physics. Near a quantum phase transition a system combines quantum dynamics and entanglement [5], which can be important for applications of these arrays in ultra-high density magnetic recording and quantum computation. In this letter, we report experimental data that point to the existence of a quantum phase transition, driven by an external magnetic field, in a crystal of dipolar-coupled molecular nanomagnets.

Single-molecule magnets offer a unique opportunity for these studies [6, 7]. Clusters containing 12 manganese atoms linked via oxygen atoms (Mn_{12}), with a sharply-defined and monodisperse size, organize to form tetragonal molecular crystals. Each molecule exhibits interesting magnetic properties, such as slow magnetic relaxation and magnetization hysteresis loops, due to the combination of an $S = 10$ magnetic ground state with appreciable magnetic anisotropy. Below 10 K, the spins point either up or down along the c crystallographic axis, flipping between these orientations via quantum tunneling processes [8–11]. Since molecular spins couple via dipolar interactions, these crystals are therefore nearly perfect realizations, with magnetic units of mesoscopic size, of the Ising quantum model, the simplest one showing a quantum phase transition. Magnetic order has however not been observed for Mn_{12} yet. The reason is that tunneling times, which govern relaxation towards equilibrium at very low temperatures, are extremely long (of order two months at $T = 2$ K). For the time scales $\tau_e \sim 10^2 - 10^4$ s of a typical experiment, the spins are unable to attain thermal equilibrium below a blocking temperature $T_B \sim 3$ K, which is higher than the ordering temperature $T_c \sim 0.5$ K predicted by Monte Carlo calculations [12]. Here we circumvent this problem by the application of a transverse magnetic field $B_\perp$ that promotes quantum tunneling. Magnetic diffraction of thermal neutrons is a suitable tool for these studies because neutrons can probe the magnetization along the anisotropy axis, i.e. the order parameter, and provide a very accurate determination of the crystal's orientation with respect to the applied magnetic field.

The $\sim 0.5 \times 0.5 \times 1.5$ mm^3 single crystal of deuterated Mn_{12} acetate, $[Mn_{12}\ (CD_3COO)_{16}\ (D_2O)_4O_{12}]\cdot 2\ CD_3\ COOD{\cdot}4D_2O$, was prepared following the original method of Lis [13]. It was glued to a copper rod in good thermal contact with the mixing chamber of a ^{3}He-^{4}He dilution refrigerator, which gives access to the temperature range 45 mK $< T <$ 4 K. The c axis was carefully oriented to be perpendicular to the vertical field $0 < B_\perp < 6$ T applied by a superconducting magnet. From the orientation matrix measured at zero field and $T = 4$ K, we estimate that the crystallographic $(\bar{1}10)$ direction lay within 0.1 degrees of the magnet axis.

At a given temperature $T \leq 4$ K, we measured a series of Bragg diffraction reflections as a function of $B_\perp$ [14]. Each reflection (hkl) contains a nuclear (non-magnetic) I_N contribution and a magnetic I_m contribution. The former contains information about the atomic order, whereas the latter is proportional to the square of

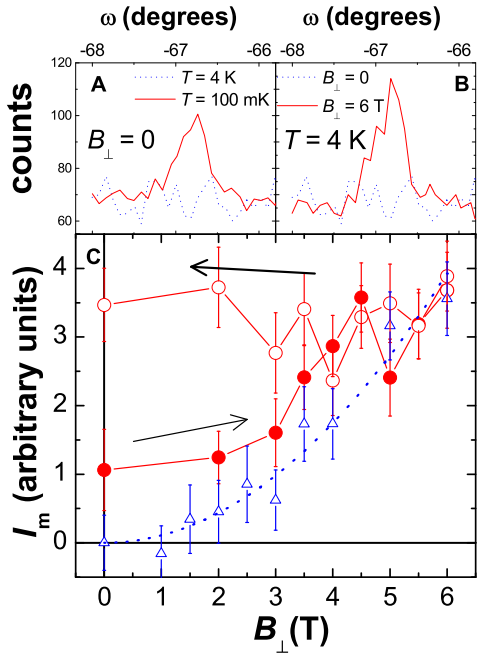

FIG. 1: (Color online) (**A**) and (**B**) Rocking curves for the $(\bar{2}\bar{2}0)$ reflection at different temperatures and magnetic fields. The counting statistics are typical for such a small crystal under these conditions. (**C**) Variation of the magnetic diffraction intensity I_m with the transverse magnetic field for the same diffraction line: △, $T = 4$ K; • and ○, $T = 100$ mK measured while increasing and then decreasing $B_\perp$, respectively. The dotted line is a least squares fit to a parabola $AB_\perp^2$.

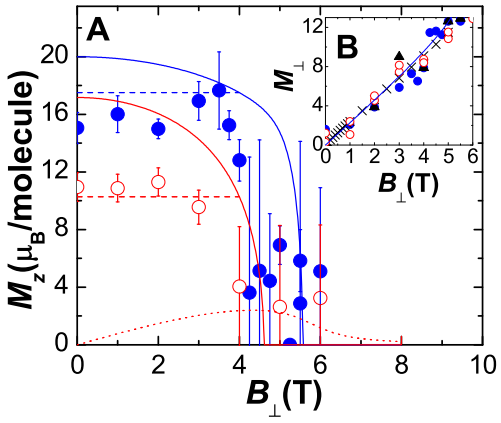

FIG. 2: (Color online) **A** Longitudinal magnetization M_z of Mn_{12} acetate measured while decreasing the transverse magnetic field from 6 T. • and ○ are for $T = 47$ mK and 600 mK, respectively. Solid lines are calculated using the mean-field Hamiltonian given by Eq. (1) and the parameters given in the text. Horizontal dashed lines indicate the magnetization, calculated at $B_\perp = 4$ T, that would become frozen below the irreversibility field. The dotted line shows M_z induced at $T = 600$ mK by the small misalignment of the crystal from the perpendicular orientation in the case of no interactions ($J_{\rm eff} = 0$ in Eq. (1)). **B** × perpendicular magnetization $M_\perp$ obtained at $T = 4$ K with a SQUID magnetometer. Data obtained from neutron diffraction are also shown: •, $T = 47$ mK; ○, $T = 600$ mK; ▲, $T = 4$ K.

the magnetization components perpendicular to the (hkl) direction. The nuclear contribution can be obtained by measuring the intensity at zero field in the paramagnetic phase. By subtracting this, $I_{\rm m}$ can be estimated at any field and temperature.

Given the strong anisotropy of Mn_{12}, the magnetization must be confined in the plane defined by the anisotropy axis c and the magnetic field, with respective components M_z and $M_\perp$. We illustrate the experimental protocol in Fig. 1 with results obtained for the $(\bar{2}\bar{2}0)$, which is sensitive to both M_z and $M_\perp$ components, and has a very small nuclear contribution. At 4 K, $I_{\rm m} \propto B_\perp^2$, as expected, since $M_z = 0$ in the superparamagnetic state and $M_\perp$ is proportional to $B_\perp$. At 100 mK, by contrast, a rather large additional contribution to $I_{\rm m}$ shows up in the low-field region (for $B_\perp < 5$ T) of Fig. 1. Since $M_\perp$ is nearly independent of T (see the inset of Fig. 2), this additional $I_{\rm m}$ reflects the onset of a non-zero M_z. Furthermore, this low-T contribution shows hysteresis. Indeed, $I_{\rm m}$ data measured while *increasing* $B_\perp$ after the sample was cooled at zero field from $T \simeq 1$ K, lie clearly below those measured while *decreasing* it, merging approximately at $B_\perp = 4$ T. The hysteresis means that spins can attain equilibrium within the experimental time $\tau_{\rm e} \simeq 7 \times 10^3$ s only above $B_\perp = 4$ T.The fact that this field-induced "jump to equilibrium" happens at approximately the same field for $T = 100$ mK and $T = 600$ mK confirms that relaxation to equilibrium proceeds via temperature-independent tunneling processes [15, 16].

Neutron diffraction data were calibrated against SQUID magnetization measurements performed at 4 K to obtain M_z and $M_\perp$ as a function of magnetic field (Fig. 2) and temperature (Fig. 3). At our minimum temperature $T = 47$ mK, M_z is nearly zero for $B > 5.5$ T and then it increases when decreasing $B_\perp$, reaching a rather large value at zero field. The temperature dependence of this zero-field M_z is shown in Fig. 3. It is approximately constant until it begins decreasing sharply for $T \gtrsim 0.6$ K. Above 1 K, as at 4 K, the fit gives $M_z \sim 0$.

These experiments show without ambiguity the existence of a net magnetization along the anisotropy axis and that it vanishes at sufficiently high temperatures and perpendicular magnetic fields. The qualitative resemblance between M_z vs $B_\perp$ and M_z vs T curves is typical of magnetic systems showing a quantum phase transition [4]. It is therefore tempting to identify M_z with the spontaneous magnetization of a ferromagnetically

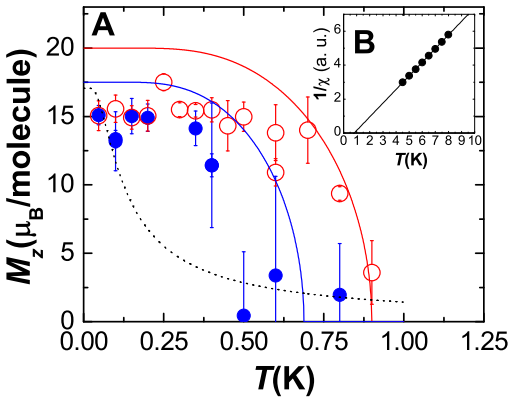

FIG. 3: (Color online) (**A**) Temperature-dependent longitudinal magnetization M_z obtained from neutron diffraction data measured at $B_\perp = 0$ (○) and 4 T (●) after performing a 'quantum annealing' at $B_\perp = 6$ T. The dotted line shows the magnetization arising from the crystal's misalignment at $B_\perp = 4$ T and solid lines are calculations (for perfect orientation) that include interactions via the mean-field Hamiltonian (1). (**B**) Reciprocal equilibrium susceptibility measured at $T > 4.5$ K along the c axis. The line is a least squares linear fit, giving $T_c = 0.8(1)$ K.

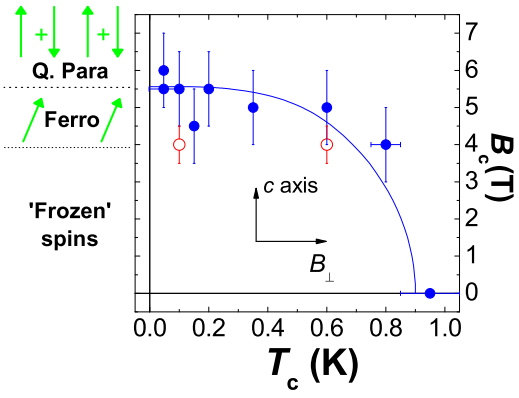

FIG. 4: (Color online) Magnetic phase diagram of Mn_{12} acetate. The solid dots show the critical magnetic field B_c at which the longitudinal magnetization is observed to vanish at each temperature. The open dots give the irreversibility field, below which the spins are no longer able to attain equilibrium within the experimental time. The solid line was obtained from magnetization curves calculated in a mean-field approximation (Eq. (1)).

ordered phase. However, for such strongly anisotropic spins, any deviation of the crystal from the perpendicular orientation can induce, at $B_\perp > 4$ T, some magnetic polarization along the anisotropy axis [16] that would then remain frozen below the irreversibility field (4 T). In our case, this deviation is known from "high"-temperature diffraction data to be smaller than 0.1 degrees, which actually agrees fully with the small M_z values measured at $B_\perp = 4$ T and above 0.5 K. In Figs. 2 and 3 we show that such a small misalignment cannot account, by itself, for M_z observed at $T > 0.1$ K. In addition, for $T > 0.4$ K (as at $T = 0.6$ K, Fig. 2), M_z increases significantly as the field is reduced to zero from $B_\perp = 4$ T, showing that, even at zero field, the spins tend to become polarized as they approach equilibrium. The existence of long-range magnetic order is also supported by the finite temperature intercept (0.8(1) K) of the reciprocal paramagnetic susceptibility shown in the inset of Fig. 3. We therefore conclude that a ferromagnetic transition takes place at either $T_c \sim 0.9(1)$ K or at $B_c \sim 5.5$ T. The ferromagnetic nature of the ordered phase agrees with theoretical predictions [12], which however predict $T_c \sim 0.45$ K, lower than observed. In our view, the discrepancy arises from the fact that Monte Carlo calculations were performed for point-like spins, whereas Mn_{12} molecules are extended nanoscopic objects. This affects the interaction energies for neighbor molecules [18] and therefore can modify the predictions for T_c.

These qualitative ideas can be put on a more solid basis with the help of theoretical calculations. A simple way to introduce interactions in the analysis is by making use of a mean-field approximation

$$\mathcal{H} = -DS_z^2 + C(S_+^4 + S_-^4) - g\mu_B\,(B_xS_x + B_yS_y) - J_{\rm eff}\langle S_z\rangle S_z \qquad (1)$$

where D and C are the uniaxial and in-plane anisotropy constants, $g = 2$ the gyromagnetic ratio, B_x and B_y are the magnetic field components along a and b, and $J_{\rm eff}$ is a mean-field interaction parameter. We estimated $D = 0.62k_B$ by fitting the perpendicular magnetization measured at 4 K, while C has been set to 2.5×10^{-4} K in order to fit the critical field $B_c = 5.5$ T. These are of the same order as the values obtained by spectroscopic techniques [19]. We also set $J_{\rm eff} \simeq 4.5\times10^{-3}k_B$ to account for the experimental $T_c \simeq 0.9$ K.

Using Eq. (1), we have calculated M_z and $M_\perp$ self-consistently. Field- and temperature-dependent calculations account reasonably well for both components, predicting in particular the vanishing of M_z at either B_c or T_c. The non complete saturation of M_z at zero field arises probably from 'down' spins that remain frozen below $B_\perp = 4$ T because the quantum tunneling rates become too slow at such low fields. We have here the curious situation that quantum fluctuations, which eventually break the magnetic order at B_c, are nevertheless necessary to attain equilibrium. In Figure 4, we show the magnetic phase diagram of Mn_{12} acetate obtained from our experiments. Application of a perpendicular field tends to shift T_c significantly towards lower temperatures. As before, the mean-field calculations reproduce reasonably well the overall features.

Summing up, our experiments on Mn_{12} nanomagnets show the existence of a ferromagnetic phase below $T_c \simeq 0.9$ K that can be destroyed by the application of an external magnetic field. Deciding, at any finite temperature, to which extent this field-induced phase transition is driven by quantum fluctuations requires measuring the critical behavior of M_z [3], which is clearly beyond the sensitivity of the present experiments. What we do see is that, above $B_c = 5.5$ T, the order parameter M_z vanishes even at the lowest accessible temperatures ($T > 47$ mK in our case). We note that B_c is about one half of the anisotropy field $2SD/g\mu_B \sim 9$ T that would be required to saturate the Mn_{12} spins along a hard axis if they were *classical* spins. In fact, as shown in the inset of Fig. 2, $M_\perp$ is still much smaller than saturation at B_c. This is a clear indication that the transition is of quantum nature. In addition, the quantum tunnel splitting Δ calculated at $B_\perp = 6$ T is of order 1.4 K. Therefore, at $T = 47$ mK almost all molecular spins should be in their ground state. In the quantum paramagnetic phase, it becomes a symmetric superposition of 'spin-up' and 'spin-down' states, a kind of mesoscopic magnetic "Schrödinger's cat" [20]. Previously, the existence of quantum superpositions of spin states was derived from the detection of Δ [15, 21, 22], while here we have directly monitored the vanishing how the z spin component vanishes.

Similar collective magnetic phenomena could, in principle, be present in arrays of larger nanomagnets, like magnetic nanoparticles, provided they are sufficiently ordered and monodisperse, requirements that appear to be within the reach of modern synthetic procedures [1]. The existence of "super-ferromagnetic" materials was predicted more than ten years ago, and shown to be of interest for applications in magnetic refrigeration [23]. However, besides indications that point to the collective, spin-glass-like, nature of the magnetic relaxation [24], no clear-cut experimental evidence for ordered magnetic phases in systems of nanoparticles has been found yet. The present and some other recent results [25] show that bottom-up synthesis can provide physical realizations of these super-ferromagnets albeit on a smaller size scale. Furthermore, quantum dynamics can be used to overcome the slow relaxation and to switch between the ordered and paramagnetic phases. The appeal of these superstructures is that they might combine any properties of the magnetic unit with any behavior for the whole array (e.g. a ferromagnet made of tiny antiferromagnetic particles or viceversa). By changing either the size of the nanomagnets or the lattice geometry, both the magnetic interaction strength (thus T_c) as well as the nature of the ground state could be tailored [12, 18].

The authors are grateful to J. L. Ragazzoni and D. Culebras for their technical assistance. We acknowledge useful comments on this work by J. F. Fernández. This work is part of the research project MAT02-433 funded by Spanish MCyT. This work was partly supported by the European Commission under project IST-NANOMAGIQC. The authors would also like to acknowledge the financial support of the ILL for the preparation of the samples.

[1] S. Sun, C. B. Murray, D. Weller, L. Folks, and A. Moser, Science **287**, 1989 (2000).
[2] K. G. Wilson, Rev. Mod. Phys. **55**, 583 (1983).
[3] S. L. Sondhi, S. M. Girvin, J. P. Carini, and D. Sahar, Rev. Mod. Phys. **69**, 315 (1997).
[4] D. Bitko, T. F. Rosenbaum, and G. Aeppli, Phys. Rev. Lett. **77**, 940 (1996).
[5] A. Osterloh, L. Amico, G. Falci, and R. Fazio, Nature **416**, 608 (2002).
[6] G. Christou, D. Gatteschi, D. N. Hendrickson, and R. Sessoli, MRS Bull. **25**, 56 (2000).
[7] D. Gatteschi and R. Sessoli, Angew. Chem. Int. Ed. **42**, 268, (2003).
[8] J. R. Friedman, M. P. Sarachik, J. Tejada, and R. Ziolo, Phys. Rev. Lett. **76**, 3830 (1996).
[9] J. M. Hernández, et al., Europhys. Lett. **35**, 301 (1996).
[10] L. Thomas, et al., Nature **383**, 145 (1996).
[11] L. Thomas, A. Caneschi, and B. Barbara, Phys. Rev. Lett. **83** 2398 (1999).
[12] J. F. Fernández and J. J. Alonso, *Phys. Rev. B* **62**, 53 (2000).
[13] T. Lis, Acta Crystallogr. B **36**, 2042 (1980).
[14] Neutron diffraction experiments were carried out on the diffractometer D10 at the Institut Laue Langevin. We worked in a two-axis normal-beam configuration at a neutron wavelength of 2.36 Å.
[15] F. Luis, F. L .Mettes, J. Tejada, D. Gatteschi, and L. J. de Jongh, Phys. Rev. Lett. **85**, 4377 (2000).
[16] I. Chiorescu, R. Giraud, A. Jansen, A. Caneschi, and B. Barbara, Phys. Rev. Lett. **85**, 4807 (2000).
[17] J. Brooke, D. Bitko, T. F. Rosenbaum, and G. Aeppli, Science **284**, 779 (1999).
[18] A point-like approximation for Mn_{12} spins gives interaction energies within 2 % of the exact result only when the intermolecular distances exceed 5 lattice parameters. For shorter distances, the flat shape of the Mn_{12} molecule reinforces interactions with molecules situated along the a or b axes with respect to interactions along c. Following simple arguments [12], this should lead to an enhancement of T_c. The size and shape of the nanostructure, in this case the molecule of Mn_{12}, appears then as an additional factor to determine (and eventually tailor) the physical behavior of the array.
[19] A. L. Barra, D. Gatteschi, and R. Sessoli, Phys. Rev. B **56** 8192 (1997).
[20] E. Schrödinger, Naturwissenschaften **23**, 807 (1935). English translation in *Quantum Mechanics and Measurement*, edited by Wheeler and Zurek, Princeton University Press (Princeton, 1981).
[21] E. Del Barco, et al., Europhys. Lett. **47**, 722 (1999).
[22] G. Bellessa, N. Vernier, B. Barbara, and D. Gatteschi, hys. Rev. Lett. **83**, 416 (1999).
[23] S. Mørup, Hyp. Interact. **90**, 171 (1994).
[24] T. Jonsson et al., Phys. Rev. Lett. **75**, 4138 (1995).
[25] M. Evangelisti et al., Phys. Rev. Lett. **93**, 117202 (2004).

Capítulo 3

Estructuración de Mn_{12} en matrices poliméricas

3.1. Introducción

Los materiales compuestos constituidos por partículas magnéticas dispersas en el interior han despertado un gran interés en los últimos años gracias a su potencialidad para reemplazar los materiales magnéticos convencionales en una amplia variedad de aplicaciones, ya sea como sistemas de almacenamiento de información a escala submicrométrica, refrigeración magnética, y aplicaciones biomédicas entre otras.[1-3] De todos ellos, el uso de polímeros como matrices es probablemente el más extendido, dado que añade flexibilidad y asegura una buena procesabilidad del sistema gracias a sus propiedades mecánicas y reológicas. Además, se pueden combinar las propiedades magnéticas de las nanopartículas con interesantes propiedades ópticas, conductoras y/o electrónicas de los polímeros. Hasta la fecha, el método más utilizado para la incorporación de nanopartículas en matrices poliméricas se basa en la mezcla de las especies inorgánicas, tales como partículas metálicas, con los polímeros orgánicos, bien en disolución o fundido por encima de la temperatura de transición vítrea.[4] Una aproximación más reciente corresponde a la combinación de los componentes inorgánicos con las matrices poliméricas mediante enlaces covalentes.[5] En estos sistemas, las partículas magnéticas están convenientemente funcionalizadas de forma que actúan como unidades repetitivas para crear redes conectadas covalentemente. En cualquier caso, la nanoestructura resultante, grado de organización y propiedades depende de la naturaleza de los componentes así como del posible sinergismo entre ellos.

Siguiendo la segunda de las aproximaciones anteriormente descritas, Larionova y col., ya han descrito la síntesis y caracterización de materiales compuestos magnéticos orgánicos-inorgánicos basados en complejos de Mn_{12}.[6] Para ello, los autores sintetizaron un nuevo complejo de Mn_{12} funcionalizado con ligandos carboxilatos tipo metacrilato para obtener copolímeros híbridos. De esta forma, además de mejorar la estabilidad química y térmica del Mn_{12}, mantienen las propiedades magnéticas de los imanes unimoleculares.

Los trabajos de esta Tesis, por el contrario, se encaminaron más a la obtención de películas delgadas compuestas de Mn_{12} en una matriz polimérica mediante la mezcla de ambos constituyentes en un disolvente orgánico. Tal y como se demostrará a lo largo del presente capítulo, en la película delgada resultante se produce una separación de fases entre el Mn_{12} y el policarbonato, resultando un material de baja periodicidad. En base a estos resultados, y con la finalidad de estructurar de forma ordenada sus componentes sólidos, se desarrolló una segunda etapa adicional correspondiente a la aplicación del método conocido como “breath-figures”. Teniendo en cuenta que los procedimientos de fabricación de estructuras porosas son elaborados y requieren de propiedades específicas en los materiales,[7-12] el fenómeno de *breath-figures* corresponde a un método general y simple aplicado para generar estructuras porosas inducidas mediante la condensación de gotas de agua sobre la superficie de una disolución polimérica *(vide infra)*. El ordenamiento resultante de poros estructurados y funcionalizados en superficie ofrece una vía potencial de fabricación con interesantes aplicaciones tecnológicas como son las membranas de separación y los procesos catalíticos.[13,14] Además, estos métodos permiten modular de forma simple y rápida, las propiedades del material en base a las correlaciones estructurales y la distribución controlada de las moléculas.

3.2. Materiales compuestos basados en imanes unimoleculares de Mn_{12} dispersos en matrices poliméricas

3.2.1. Películas delgadas de policarbonato

Inicialmente, a efectos comparativos, para entender mejor el comportamiento de la matriz polimérica, así como su influencia en los fenómenos de agregación y cristalización del Mn_{12}, se prepararon películas delgadas poliméricas exentas de Mn_{12} mediante deposición directa en superficie de una mezcla de policarbonato puro disuelto en *o*-diclobenceno y se caracterizaron mediante las técnicas de microscopia confocal y de fuerzas atómicas.

Microscopia confocal. Una de las herramientas claves en la caracterización de las películas delgadas que se presentara en el presente capítulo ha sido la microscopia óptica confocal. Mediante el uso de esta técnica se reconocen estructuras en las que la emisión por fluorescencia o bien la reflexión de la luz blanca se concentra en un único plano focal de la muestra que se superpone a toda luz que no proceda de dicho plano. En un barrido puntual, las lentes del microscopio enfocan la luz láser sobre un solo punto de la muestra *(el punto focal)*. A continuación, el láser explora la muestra por barrido puntual y genera una imagen conjugada o confocal detectada mediante un fotomultiplicador. Como ejemplo, las imágenes ópticas confocal en la sección vertical xz de una película delgada de policarbonato se muestran en la Figura 3.1.

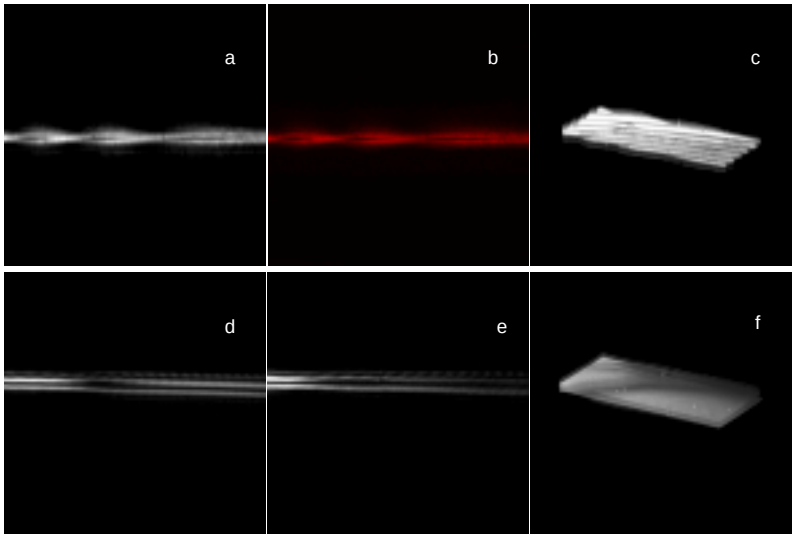

Fig. 3.1. Micrografías ópticas confocal en la sección xz de películas delgadas de policarbonato y su reconstrucción 3D *(c y f)*. Las imágenes *(a)* y *(b)* muestran la estructura helicoidal de la matriz polimérica por reflexión de luz blanca y por emisión de luz mediante su tinción con naranja de acridina, respectivamente. Las imágenes *(d)* y *(e)* muestran cambios en la longitud de onda de las fluctuaciones en superficie.

Tal y como se puede observar, tras la evaporación del disolvente en ausencia de soluto, el polímero se ordena dando lugar a estructuras fibrilares que se ordenan periódicamente en el interior de la matriz polimérica. Estas fibras corresponden a zonas de mayor

cristalinidad y por consiguiente detectables por microscopia óptica confocal a partir de la reflexión de la luz blanca. Mediante secciones transversales *(xz)*, la matriz polimérica de policarbonato muestra que las fibras se estructuran en forma de hélices levógiras a lo largo del eje preferencial de cada fibra. Puesto que la velocidad de cristalización depende de los movimientos cooperativos inducidos a lo largo de la cadena,[15,16] las oscilaciones térmicas durante el proceso de evaporación pueden desempeñar un papel importante en la estructuración final de la matriz polimérica. Así, la periodicidad de las hélices se va perdiendo paulatinamente para originar otras zonas dentro de la misma película, donde las hebras se separan para dar lugar a dos dominios paralelos con contraste óptico diferenciado *(ver Fig. 3d y 3e)*.* Este tipo de estructuración, observada en las películas delgadas, es conocido a nivel cristalino entre capas organizadas poliméricas.[17]

Microscopia de fuerzas atómicas (AFM). Además de la microscopia óptica confocal, la caracterización de la película delgada de policarbonato también se realizó mediante la técnica de AFM.

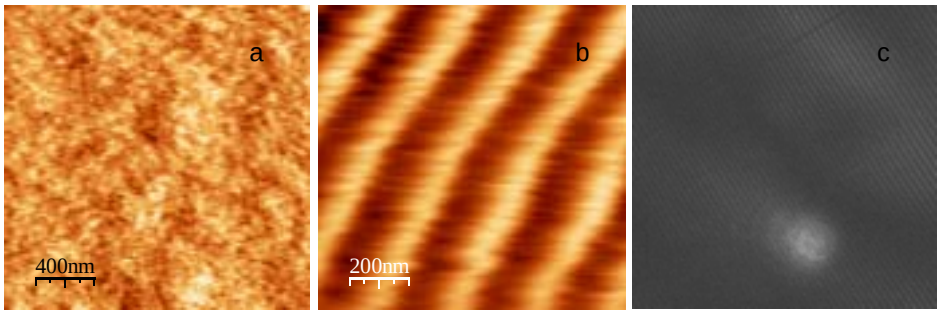

Fig. 3.2. a) Imagen AFM adquirida por contacto intermitente o semicontacto sobre la superficie de una película delgada de policarbonato; b) imagen topográfica en capas internas obtenida por contacto; c) imagen óptica confocal paralela al plano de la superficie *(xy)*.

Los estudios topográficos se realizaron inicialmente por contacto intermitente o semicontacto entre la punta del AFM y la superficie de la muestra, revelando la existencia de una capa externa amorfa que impide la observación topográfica de las fibras en superficie. No obstante, dicha estructura puede ser detectada aumentando la presión en superficie operando por contacto. De esta manera, incrementando la fuerza efectiva que ejerce la punta sobre la superficie, es posible detectar las diferentes subcapas en el interior de la matriz polimérica. Por contacto, a su vez, se aumenta la fuerza lateral por fricción pudiendo eliminar parte del material amorfo en las capas superficiales. Si se mantiene constante la fuerza a cierta profundidad, es posible detectar durante el barrido topográfico en superficie, la arquitectura cristalina de mayor rigidez *(ver Fig. 3.2)*.

*Aquellas zonas de las películas poliméricas que presentan cierto ordenamiento o cristalinidad dan lugar a estructuras birrefringentes que permiten ser detectadas por contraste óptico.

3.2.2. Películas delgadas de Mn_{12}-policarbonato

Una vez estudiado el comportamiento de las películas delgadas de policarbonato, se prepararon películas delgadas poliméricas mediante deposición directa en superficie de una mezcla de policarbonato y Mn_{12} al 12% en peso, disueltos en *o*-diclobenceno. El elevado punto de ebullición del disolvente utilizado *(180 ºC)*, permite alcanzar temperaturas relativamente elevadas *(~120 ºC)* durante el proceso de solidificación por evaporación. Las películas resultantes se estudiaron mediante microscopia óptica confocal, técnicas calorimétricas y medidas magnéticas.

Microscopia confocal. En la Figura 3.3 se muestran las micrografías ópticas obtenidas por reflexión de la luz blanca en la película delgada, observándose la presencia de microcristales de Mn_{12} intercalados en la matriz polimérica. Esta organización se ve alterada por la segregación de fase posterior del Mn_{12}, siendo éste el componente minoritario y de mayor solubilidad en *o*-diclorobenceno. Así, y teniendo en cuenta el estrecho margen de solubilidad que existe entre ambos componentes sólidos, se produce una reorganización del policarbonato en el seno de la disolución polimérica dando lugar a la fragmentación de las dos estructuras laminares en núcleos densos de policarbonato. Estos núcleos se unen formando secuencias lineales[18] que muestran una mayor reflexión de la luz blanca y se deben a la interacción entre las partes cristalizables de la cadena polimérica. Las partes no cristalizables forman una fase amorfa externa a los núcleos y se presentan exentas de reflexión debido al mayor desorden. Sin embargo, la estructuración de los núcleos de cristalización en forma de bicapa ordenada no siempre se ha obtenido, resultando altamente sensible a variaciones en el espesor inicial de la película líquida polimérica y las fluctuaciones térmicas durante la etapa de evaporación del disolvente y solidificación.

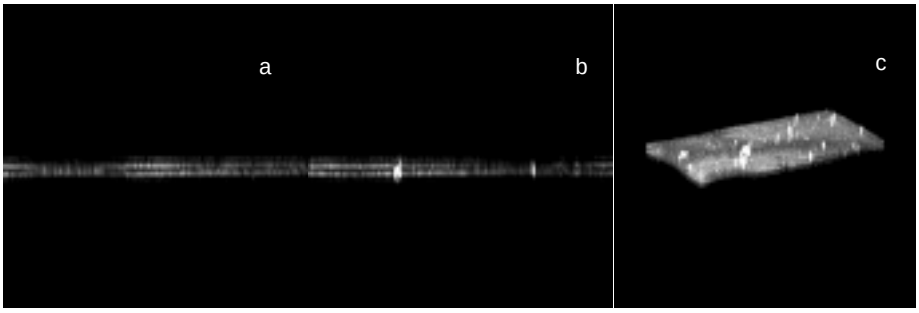

Fig. 3.3. a) Sección óptica vertical *(xz)* por reflexión de la luz blanca en película delgada de policarbonato-Mn_{12}; b) crecimiento normal a la superficie de microcristales de Mn_{12} intercalados en la matriz polimérica; c) imagen 3D a través de planos focales recogidos a intervalos de 0.2 μm en el eje z.

Adicionalmente, para confirmar la inclusión de la fase cristalina de Mn_{12} en el interior de la matriz cristalizada de policarbonato, se compararon la imagen óptica confocal por reflexión en uno de los planos focales paralelos a la superficie y la correspondiente a la transmisión de la luz blanca. La imagen de transmisión muestra una distribución aleatoria de los microcristales de Mn_{12} cuya coloración contrasta claramente con la matriz transparente de policarbonato. Sin embargo, por reflexión, ambas fases son

detectables, pudiéndose diferenciar las fases en relación a la transmisión en un mismo plano focal xy paralelo a la superficie de la muestra *(ver Fig. 3.4).*

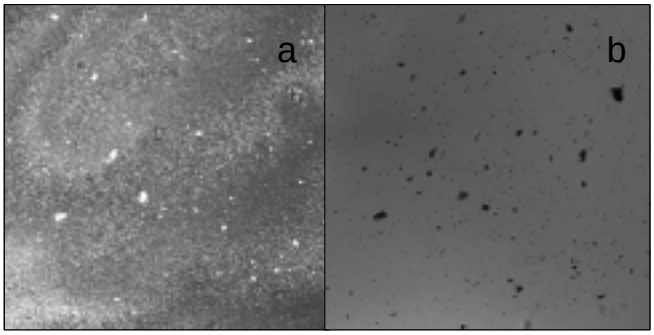

Fig. 3.4. a) Sección óptica confocal *(xy)* por reflexión de la luz blanca en película delgada de policarbonato-Mn_{12}; b) imagen obtenida por transmisión en el mismo plano focal.

Un ejemplo claro de esta separación de fases lo constituyen las mezclas poliméricas, las cuales pueden generar estructuras ordenadas que influirán en el conjunto global de las propiedades del sistema. Cuando se disuelven mezclas de polímeros o copolímeros en bloque, tras la evaporación del disolvente, existe una tendencia de las microfases segregadas a ordenarse. Adicionalmente, la eliminación selectiva del componente minoritario transforma el material en una organización estructurada de poros ordenados.[19] La existencia de este orden mesoscópico, así como la generación de interfases, tendrán una gran influencia en las propiedades dinámicas de estos materiales, ya que contribuyen a restricciones geométricas que pueden impedir algunos de los movimientos moleculares.

Magnetismo. Las películas poliméricas de policarbonato-Mn_{12} mostradas en la Figura 3.3 se apilaron entre sí y fueron alineadas respecto a un campo magnético externo aplicado de forma paralela o perpendicular a la superficie.

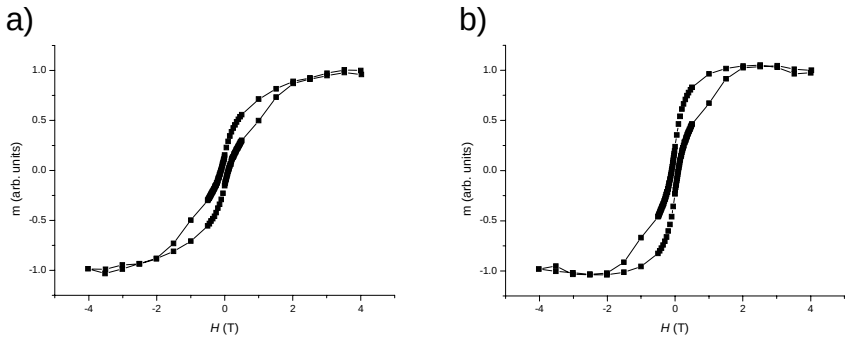

Fig. 3.5. Curvas de histéresis a 1.9 K al aplicar un campo magnético externo. a) paralelo y b) perpendicular a la superficie.

Cuando la muestra se orienta de forma que el campo queda perpendicular a la superficie, la curva de magnetización, además de fenómenos de histéresis, muestra una saturación rápida característica de unas medidas de imanes unimoleculares ordenados con el eje fácil paralelo al campo magnético *(Fig. 3.5b)*. Además, la forma de la curva de magnetización en presencia de un salto elevado a 0 T, es característica de muestras de Mn_{12} con un predominio del proceso de relajación magnética rápido. Por el contrario, cuando las mismas muestras se miden con el campo magnético externo aplicado paralelo a la superficie, la curva de magnetización refleja una menor saturación acorde

con un menor grado de orientación, demostrando que existe una cierta tendencia de los cristales de Mn_{12} a orientarse dentro de la película *(Fig. 3.5a)*. Las moléculas de Mn_{12} se empaquetan íntimamente con las de policarbonato en la fase amorfa. Sin embargo, dicha fase se encuentra confinada entre núcleos cristalinos adyacentes, dando lugar a mayor grado de ordenamiento a medida que aumenta la cristalinidad en las proximidades de los núcleos densos de cristalización. De esta manera, se generan zonas con mayor constricción que no sólo ordenan las moléculas de Mn_{12} a su alrededor, sino que favorecen el crecimiento lateral de monocristales intercalados de Mn_{12}.

Exposición a disolvente. Para obtener un control posicional en la segregación de moléculas de soluto en películas de policarbonato es necesario evitar al máximo los procesos de separación de fase inducidos por fenómenos de cristalización en la matriz polimérica. Por ello, en una segunda etapa se expusieron las películas delgadas anteriormente obtenidas, en contacto con vapores de disolvente. Los disolventes orgánicos de bajo peso molecular tales como el CH_2Cl_2 difunden en el interior de la matriz de policarbonato provocando un hinchamiento de la red polimérica, además de incrementar la solubilidad de ambos componentes sólidos por solvatación. De esta forma, se pretende minimizar la cristalización del policarbonato y por consiguiente la separación de fases con el Mn_{12}. De esta manera, tras exponer una película delgada de policarbonato puro a vapores de disolvente orgánico CH_2Cl_2, la matriz polimérica pierde la estructuración en su forma helicoidal originaria para dar lugar a un mayor contenido en fase amorfa. Estos estudios se comprobaron mediante estudios calorimétricos por DSC. Así, para el caso particular de una película de policarbonato puro estructurada en fibras helicoidales se observa la existencia de dos picos endotérmicos a 145 y 228 °C correspondientes a la evolución de dos procesos, la transición vítrea y fusión de las fases amorfa y cristalina, respectivamente. En cambio, tras el tratamiento prolongado a vapores de disolvente, únicamente se obtiene el pico endotérmico a 144 °C característico del material amorfo.

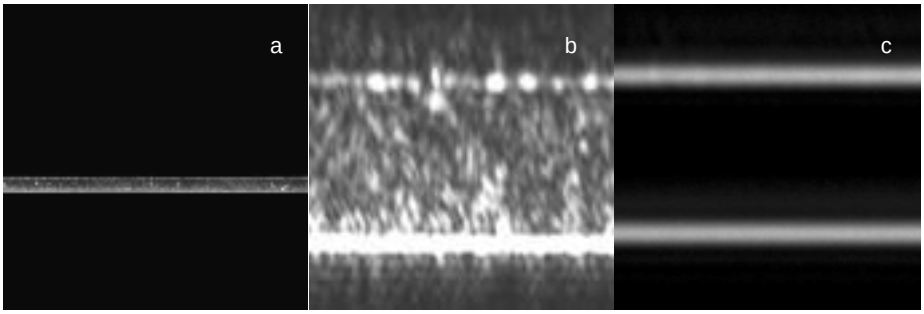

Fig. 3.6. a) Película delgada de Mn_{12}-policarbonato tras exposición a vapores de disolvente; b) corresponde a una mayor magnificación de *(a)*; c) película delgada de policarbonato puro tras exposición prolongada a vapores.

De igual manera, las películas delgadas de Mn_{12}-policarbonato fueron expuestas a vapores de disolvente. Tal y como se muestra en la Figura 3.6, las secuencias lineales de núcleos densos de cristalización originales *(ver Fig. 3.3)* pierden su estructuración secuencial en láminas originando una dispersión de núcleos cuya reducción en tamaño es considerable, fenómeno que se acentúa con el tiempo de exposición.

3.3. Estructuración de imanes unimoleculares de Mn_{12} en matrices poliméricas: "Breath-Figures"

Dadas las dificultades anteriormente mencionadas en el estudio de estructuración de complejos de Mn_{12} en policarbonato, se desarrollaron vías alternativas. Estos trabajos se realizaron en colaboración con el Dr. Fabio Biscarini del *Institute for Nanostructured Materials Studies* de Bolonia.

Un método para la estructuración de los polímeros se basa en los observaciones realizadas por Lord Rayleigh,[20] quien estudió por primera vez en 1879 la formación de estructuras ordenadas correspondientes a núcleos de vapor de agua condensados en superficie. Dicho fenómeno, denominado en la bibliografía como *breath-figures,* ha sido utilizado en los últimos años como método simple para generar estructuras porosas 2-D y 3-D organizadas en sistemas poliméricos.[21] El uso de disolventes orgánicos que presenten una presión de vapor elevada, como es el CH_2Cl_2, dan lugar al enfriamiento de la superficie de la disolución polimérica durante el proceso de evaporación, alcanzándose temperaturas entorno a los 0°C. En presencia de una atmósfera húmeda, la nucleación de gotas de agua, inmiscibles en el medio orgánico, presentarán una mayor temperatura que la superficie de la disolución polimérica debido al calor latente de condensación. Esta diferencia de temperatura conlleva a convecciones termocapilares mientras existe un gradiente de temperatura definido, estabilizando las gotas de agua y suprimiendo los fenómenos de coalescencia. De esta manera, las gotas son susceptibles a chocar elásticamente entre sí, resultando en una distribución de tamaños monodispersa y ordenada en superficie. Tras la evaporación del disolvente, la temperatura asciende a las condiciones ambientales iniciales y la matriz polimérica resultante solidifica. Durante la transición, el agua condensada y el disolvente residual se evaporan dando lugar a cavidades porosas ordenadas de forma hexagonal compacta sobre la superficie, tal y como muestra la secuencia presentada en el Esquema 1.

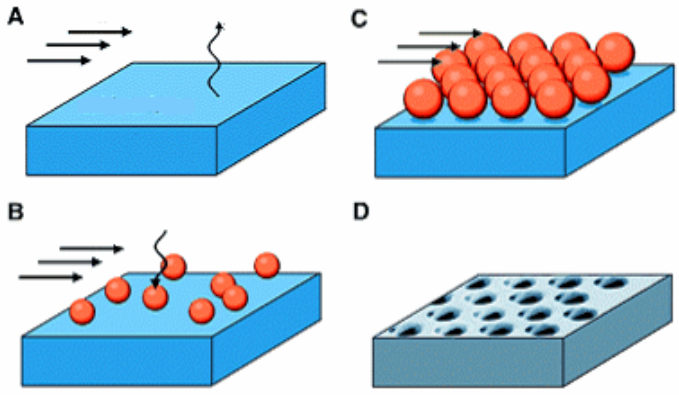

Esquema 1

3.3.1. Películas estructuradas de Mn_{12}-policarbonato

Las películas delgadas poliméricas se prepararon mediante deposición directa en superficie a través de una mezcla de policarbonato y Mn_{12} ≤3% disuelta en CH_2Cl_2. Durante el proceso de evaporación del disolvente, la humedad de la atmósfera fue

controlada en una cámara alimentada mediante el burbujeo de un flujo constante de N_2 a través de agua, dando lugar al fenómeno de *breath-figures* anteriormente comentado. Las películas resultantes se estudiaron mediante perfilometría de barrido, microscopia confocal y Raman.

Perfilometría. Previamente al estudio óptico de la matriz polimérica, las películas de Mn_{12}-policarbonato fueron analizadas en superficie por perfilometría *(Fig. 3.7)*. La imagen topográfica muestra la formación de cavidades totalmente organizadas cuyo perfil describe una morfología cónica del poro con diámetro medio 4.20 μm, distancia de separación entre perímetros 2.40 μm y 840 nm de profundidad. El tamaño obtenido es sensible a cambios en la humedad relativa durante el proceso de condensación mientras que no se han observado cambios en la morfología de las cavidades en presencia de Mn_{12} respecto al polímero puro estructurado bajo las mismas condiciones.

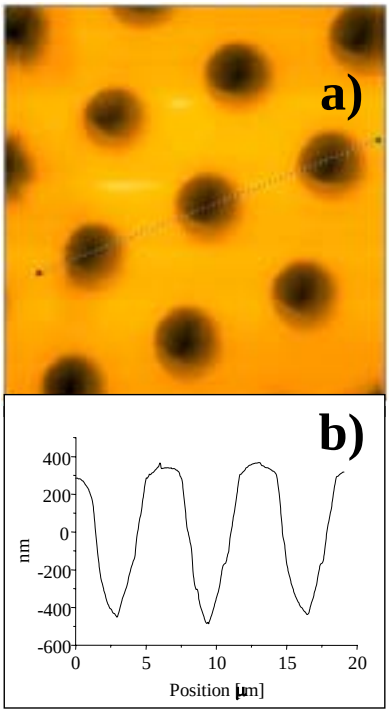

Fig. 3.7. a) Imagen topográfica adquirida sobre la superficie de una película de policarbonato-Mn_{12} estructurada en poros ordenados; b) perfil de alturas correspondiente a la línea trazada en *(a)*.

Espectroscopia Raman. Los análisis por espectroscopia Raman fueron realizados inicialmente en la superficie de películas de policarbonato puro. La distribución mayoritaria de polímero se sitúa alrededor del perímetro de los poros, resultando en zonas con una mayor densidad de moléculas de policarbonato acumuladas. Sin embargo, las zonas de menor densidad corresponden a la superficie central de cada cavidad porosa. La pérdida aproximada de intensidad fue calculada alrededor de un 50 % en comparación a la señal adquirida en la superficie externa. Las moléculas de Mn_{12} en películas compuestas siguen la misma tendencia que las de policarbonato puro. Sin embargo, algunas heterogeneidades son observadas a medida que aumenta la proporción de Mn_{12} disperso, fenómeno atribuible a los procesos de separación de fase y en consecuencia, a la pérdida de uniformidad en la posición y tamaño de las cavidades porosas.

Microscopia Confocal. Las imágenes por microscopia confocal adquiridas por reflexión de la luz blanca corroboran las medidas de caracterización por Raman y perfilometría. La Figura 3.8 muestra un contraste de intensidad de los poros invertida respecto a la matriz polimérica, mostrando claramente la presencia de interfases. La morfología de los poros en la sección transversal de la reconstrucción óptica 3-D *(d)* muestra que cada poro consiste en una doble cavidad simétrica de tipo cónica que se invierte a través de constricciones. A pesar de las diferentes técnicas utilizadas para la caracterización de las películas porosas, todavía permanecían dudas respecto de la estructura interna de los poros. Por ello, una película de policarbonato puro fue estructurada con poros mediante el fenómeno de *breath-figures* y posteriormente depositada por contacto sobre una gota de disolución acuosa compuesta de naranja de acridina al 1%. Tras su aclarado en agua ultrapura y secado a temperatura ambiente la imagen se reveló captando la emisión por fluorescencia *(Fig. 3.9)*.

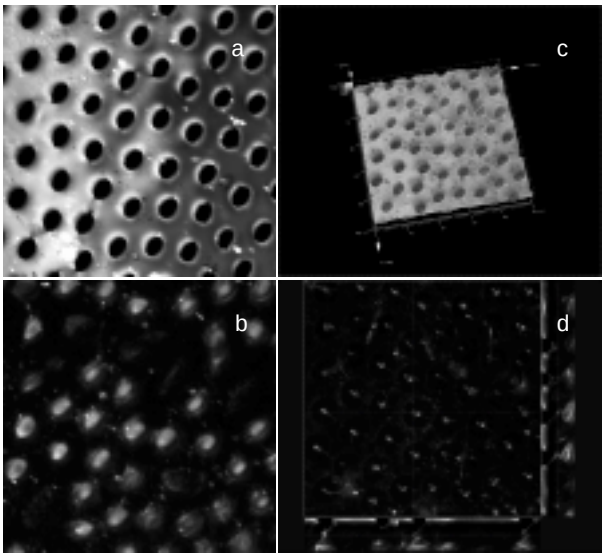

Fig. 3.8. Imágenes por microscopia óptica confocal captadas en superficie *(a)* y en profundidad *(b)*; *(c)* corresponde a la imagen 3-D; d) es la proyección de la imagen 3-D sobre el plano. Lateralmente se muestra la disposición invertida de los poros. En el plano focal central se muestran las constricciones.

En la Figura 3.9 las cavidades porosas muestran la presencia de naranja de acridina depositada en su interior. Así, la emisión fluorescente en *(c)* indica el mismo ordenamiento obtenido en correspondencia con las zonas vacías en *(a)*. En la parte superior a las constricciones, su distribución es completamente aislada e independiente hasta alcanzar planos focales situados a mayor profundidad en z *(planos xy)*, donde se demuestra la existencia de amplios dominios huecos *(d)*. Si bien las constricciones internas de los poros favorecen el aislamiento de las cavidades cercanas a la superficie, la uniformidad de tamaños observada se ve progresivamente alterada tras la formación de una red interna de interconexión entre los poros.[22] El aislamiento lateral de las cavidades porosas cercanas a la superficie no se ha observado con anterioridad en otros polímeros y abre una vía de deposición controlada de moléculas de soluto cuyas propiedades dependan de correlaciones espaciales tales como son la distancia y el tamaño.[†]

[†] Para más información ver artículo I

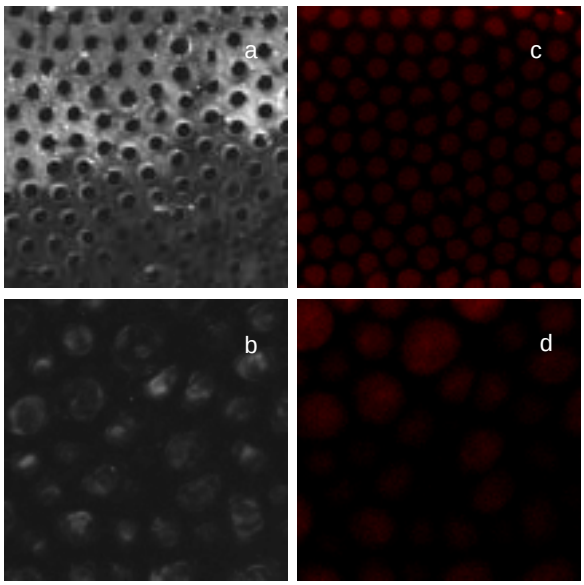

Fig. 3.9. Micrografías ópticas confocal en la sección xy. a) estructuración porosa ordenada en superficie por reflexión; b) cara opuesta a la superficie; c-d) emisión fluorescente en *(a-b)* respectivamente tras la tinción con naranja de acridina.

Posible mecanismo. Supuestamente, la condensación de gotas de agua insolubles en la superficie obstruye localmente la evaporación del disolvente orgánico a través de las interfases agua-disolución polimérica. La evaporación heterogénea resultante origina un flujo capilar más o menos radial entre las zonas internas de la matriz y las zonas de mayor velocidad de evaporación correspondientes a las regiones interfásicas de mayor curvatura[23] situadas alrededor de las gotas de agua. Dicho flujo capilar transporta consigo las moléculas de soluto disueltas y policarbonato mientras existe un déficit en el volumen de disolvente evaporado en superficie *(Fig. 3.10)*. Sin embargo, las regiones internas abastecen las pérdidas externas de fluido dando lugar a fases pobres en polímero y por consiguiente ricas en disolvente cuya evaporación final dará lugar a la formación de una red desordenada de poros interconectados.

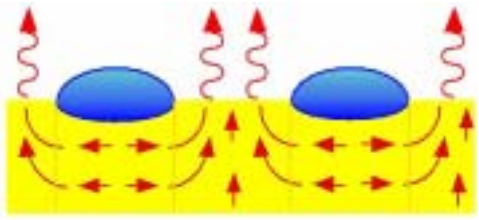

Fig. 3.10. Representación esquemática del proceso de evaporación del disolvente orgánico volátil a través de la matriz polimérica en presencia de la condensación de gotas de agua en la superficie.

3.3.2. Películas estructuradas de sistemas moleculares ópticamente activos

Independientemente de la naturaleza de la molécula, bien sea Alq_3 *(q=8-hidroxiquinoleína)* o perclorato de rodamina, se observa que éstas se disponen mayoritariamente por capilaridad alrededor de las interfases porosas, fenómeno también observado en la segregación de nanopartículas de CdSe inicialmente dispersas en una disolución polimérica.[24] A modo de ejemplo, la Figura 3.11 muestra en *(a)* la emisión por fluorescencia obtenida tras iluminar la muestra mediante una lámpara de Hg. El espectro registrado dentro y fuera del poro presenta una relación de intensidades 1:5 en *(c)*. Las imágenes por microscopia óptica confocal fueron captadas en los planos xy *(serie z)* paralelos a la superficie *(b)* y en sección transversal xz *(d)*, mostrando el

gradiente de concentración de soluto en las inmediaciones del poro cercanas a la superficie. Este último hecho corrobora a priori el mecanismo mostrado en la Figura 3.10.

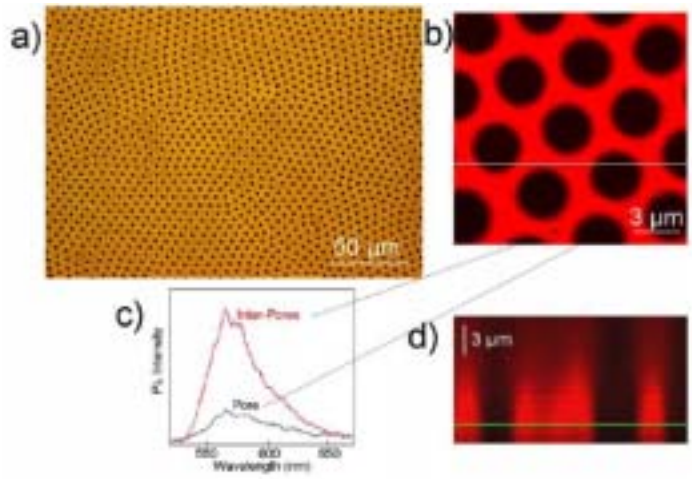

Fig. 3.11. a) Emisión fluorescente tras la excitación de la película polimérica rodamina/policarbonato por iluminación con lámpara de Hg; b) imagen óptica confocal en el plano xy; c) espectro de emisión por fluorescencia registrado dentro y fuera del poro; d) imagen óptica confocal en la sección transversal xz correspondiente a la línea blanca trazada en *(b)*. La línea verde en *(d)* indica el plano de la superficie.

Adicionalmente, la reconstrucción 3-D de la Figura 3.12 muestra la acumulación preferencial de moléculas óptimamente activas alrededor de cada poro, cuya imagen corresponde a la acumulación de los distintos planos focales captados paralelos a la superficie de la película polimérica porosa.

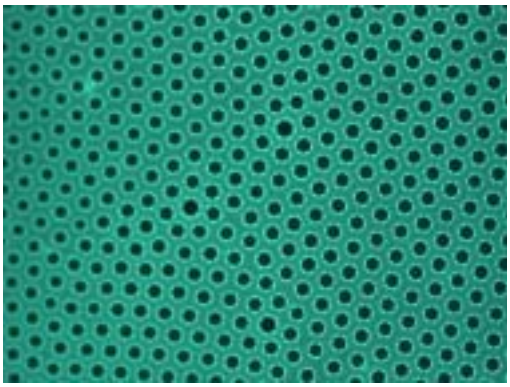

Fig. 3.12. Reconstrucción óptica 3-D obtenida por en películas de Alq_3/policarbonato por microscopia óptica confocal.

Sin embargo, y a pesar que dicho mecanismo es independiente del tipo de soluto, agente transportador y substrato utilizado, no debemos olvidarnos que únicamente es válido en aquellos casos donde existe un amplio intervalo de miscibilidad entre los componentes sólidos, actuando el sistema como una película líquida de disolución. Para el caso particular del Mn_{12} los procesos de separación de fases son altamente favorecidos por su escasa miscibilidad. No obstante, estos procesos son detectables fácilmente por microscopia óptica confocal. Así, las películas de Mn_{12}-policarbonato fueron estructuradas con poros en la superficie mediante el método de *breath-figures* y posteriormente tratadas con vapores de disolvente orgánico de CH_2Cl_2. Estos estudios demuestran que es posible controlar los procesos de segregación de fase a partir de la estructuración ordenada de poros en la superficie.[‡]

[‡] Para más información ver artículo J

3.4. Referencias

1. F. Shir, L. Yanik, L.H. Bennett, E. Della Torre, R.D. Shull, *J. Appl. Phys.*, **2003**, 8295.
2. C. Wang, N.T. Flynn, R. Langer, *Adv. Mater.*, **2004**, *16*, 1074.
3. K.A. Malini, M.R. Anantharaman, S. Sindhu, C.N. Chinnasamy, N. Ponpandian, A. Narayanasamy, M. Balachandran, V.N.S. Pillai, *J. Mater. Sci.*, **2001**, *36*, 821.
4. H.-L. Tasi, J.L. Schindler, C.R. Kannewurf, M.G. Kanatzidis, *Chem. Mater.*, **1997**, *9*, 875.
5. C. Sanchez, G.J. de, A.A. Soler-Illia, F. Ribot, T. Lalot, C.R. Mayer, V. Cabuil, *Chem. Mater.*, **2001**, *13*, 3061.
6. S. Willemin, B. Donnadieu, L. Lecren, B. Henner, R. Clérac, C. Guérin, A. Meyer, A.V. Pokrovskii, J. Larionova, *New. J. Chem.*, **2004**, *28*, 919.
7. M. Campbell, D.N. Sharp, M.T. Harrison, R.G. Denning, A.J. Turberfield, *Nature*, **2000**, *404*, 53.
8. H. Míguez, S.M.Yang, N. Tétreault, G.A. Ozin, *Adv. Mater.*, **2002**, *14*, 1805.
9. B. Xu, F. Arias, G.M. Whitesides, *Adv. Mater.*, **1999**, *11*, 492.
10. A. Blanco, E. Chomski, S. Grabtchak, M. Ibisate, S. John, S.W. Leonard, C. Lopez, F. Meseguer, H. Miguez, J.P. Mondia, G.A. Ozin, O. Toader, H.M. Van Driel, *Nature*, **2000**, *405*, 437.
11. A. Imhof, D.J. Pine, *Nature*, **1997**, *389*, 948.
12. S.A. Davis, S.L. Burkett, N.H. Mendelson, S. Mann, *Nature*, **1997**, *385*, 420.
13. J.-M. Nam, C.S. Thaxton, C.A. Mirkin, *Science*, **2003**, *301*, 1884.
14. J.M. Perez, T. O'Loughin, F.J. Simeone, R. Weissleder, L. Josephson, *J. Am. Chem. Soc.*, **2002**, *124*, 2856.
15. J.M. Jonza, R.S. Porter, *J. Polym. Sci, Polym. Phys.*, **1986**, *24*, 2459.
16. H.R. Harron, R.G. Pritchard, B.C. Cope, D.T. Goddart, *J. Polym. Sci, Polym. Phys.*, **1996**, *34*, 173.
17. Y. Matsushita, N. Torikai, Y. Mogi, I. Noda, C.C. Han, *Macromolecules*, **1993**, *26*, 6346.
18. R.L. Morgan, M.J. Hill, P.J. Barham, *Polymer*, **1999**, *40*, 337.
19. T. Thurn-Albrecht, R. Steiner, J. DeRouchey, C.M. Stafford, E. Huang, M. Bal, M. Tuominen, C.J. Hawker, T. P. Russell, *Adv. Mater.*, **2000**, *12*, 787.
20. L. Rayleigh, *Nature*, **1911**, *86*, 416.
21. M. Srinivasarao, D. Collings, A. Phillips, S. Patel, *Science*, **2001**, *292*, 79.
22. B. Erdogan, L. Song, J.N. Wilson, J.O. Park, M. Srinivasarao, U.H.F. Bunz, *J. Am. Chem. Soc.*,**2004**, *126*, 3678.
23. R.D. Deegan, O. Bakajin, T.F. Dupont, G. Huber, S.R. Nagel, T.A. Witten, *Nature*, **1997**, *389*, 827.
24. A. Böker, Y. Lin, K. Chiapperini, R. Horowitz, M. Thompson, V. Carreon, T. Xu, C. Abetz, H. Skaff, A.D. Dinsmore, T. Emrick, T.P. Russell, *Nat. Mat.*, **2004**, *3*, 302.

Artículos relacionados: Capítulo 3

Estructuración de Mn_{12} en matrices poliméricas

Artículo I

Título:
Self-organization of luminescent molecules embedded into ordered macroporous polycarbonate films by templating breath-figures

Autores:
J. Gómez-Segura, M. Cavallini, M.A. Loi, E. Da Como, G. Ruani, M. Massi, M. Muccini, D. Ruiz-Molina, J. Veciana, R. Kshirsag, F. Biscarini

Revista:
Journal of American Chemical Society (en evaluación)

Self-organization of luminescent molecules embedded into ordered macroporous polycarbonate films by templating breath-figures

Jordi Gómez-Segura,[†] Massimiliano Cavallini,[,‡] Maria Antonietta Loi,[‡] Enrico Da Como,[‡] Giampiero Ruani,[‡] Massimiliano Massi,[‡] Michele Muccini,[‡] Daniel Ruiz-Molina,[†] Jaume Veciana,[†] Rajendra Kshirsag,[‡] and Fabio Biscarini[‡]*

Institut de Ciència de Materials de Barcelona (CSIC), Campus Universitari, Bellaterra 08193, Catalonia, Spain, and Istituto per lo Studio dei Materiali Nanostrutturati, Sez. Di Bologna, Via P. Gobetti 101, I-40129 Bologna, Italy.

RECEIVED DATE (to be automatically inserted after your manuscript is accepted if required according to the journal that you are submitting your paper to)

TITLE RUNNING HEAD. Self-organization of luminescent molecules.

[*] To whom correspondence should be addressed. E-mail: m.cavallini@ism.bo.cnr.it. Fax: +39 051 639 8539. Tel: +39 051 639 8523.

[†] Institut de Ciència de Materials de Barcelona (CSIC).

[‡] Istituto per lo Studio dei Materiali Nanostrutturati (CNR).

ABSTRACT. The study and characterization of macroporous polycarbonate films induced by templating breath figures is discussed. The polymeric solution, consisting of a volatile organic solvent (CH_2Cl_2) and dye molecules, i.e., *tris*-(8-hydroxyquinoline)-Al(III) (Alq_3) or rhodamine perchlorate,

was allowed to evaporate in a moist atmosphere. By the evaporative cooling, condensation of micrometre-sized water droplets that locally cap the surface, induces a non-homogeneous solvent evaporation. As a consequence, the drying solvent acts as a carrier fluid that is responsible for solute transport to compensate the evaporative losses. The resulting capillary flow, combined with water droplets that self-assemble into a well-ordered array, yield spatially-correlated patterns of dye molecules that migrate to the polymer solution-water interfase. The control of surface segregation with concentration gradients of solute molecules opens a new approach to tailoring physical properties based on the principle of length scales. The combination of self-assembly processes of both luminescent molecules and regular cavities into ordered arrays occur on two different length scales, which offers their prospective use in optical or opto-electronics applications.

INTRODUCTION. Phase segregation in polymer blends, block copolymers and polymer-dispersed solutes are a convenient approach to tailoring material properties that are based on the emergence of self-organization processes on characteristic length scales. However, our motivating work has been focused on the study of polymer-dispersed solutes that show intense photoluminescence (PL) response. The molecule of choice Alq_3 is a well-known electroluminescent material, potentially useful in organic opto-electronics applications,[1, 2] whereas rhodamine is commonly used as a dye for lasing. The polymer under study, poly(bisphenol-A-carbonate) (PC), possesses remarkable mechanical properties[3] with high impact strength below its glass transition temperture (ca. 150 °C), transparency and flexibility. Self-assemblies of dye molecules and micrometre-sized pores induced by the so-called breath figures phenomenon occur simultaneously on different length scales. As a consequence, the formation of ordered arrays of pores in thin polycarbonate films allows spatially correlated patterns of luminescent molecules that are initially embedded in a polymeric solution.

2-D well-ordered arrays of micrometre-sized pores in polymer films are of great interest in filtration, membrane separation, interconnects and information storage. Therefore, much attention has been focused on the development of new standard and simple methods. To date, photolithography,[4] phase

separation of block copolymers,[5] inverse opals,[6] and soft lithography[7] enable the use of these arrays in technological applications. Other significative approaches involve templating colloidal particles,[8] emulsions[9] and biological materials.[10] However, these routes require specific properties of the probe materials under study as well as elaborated procedures. A simple and soft method that circumvent the above-mentioned limitations is the formation of 2D or 3D ordered macroporous materials based on polymer systems. This method, wich has been described by François et. al.[11] and more recently by Srinivasarao et. al.,[12] exploits the well-known breath figures phenomenon that was studied by Lord Rayleigh[13] as early as 1879. Based on these previous investigations, a cold surface, i.e., solid or liquid, is prone to condense water droplets in contact with moist air, giving rise to distinct patterns on the surface. Interestingly, this method allows the control over the pore size (ϕ = 0.2-20 μm) and separation distance, both by regulating the velocity of the moist air flow.[14]

The breath figures phenomenon has been observed on a wide variety of systems,[15] even condensing polar conjugated molecules on a non-polar surface in a regime of partial wetting.[16] Moreover, it has also been investigated new routes to fabricating well-ordered hexagonal arrays of bubbles in rigid-rod polymeric systems,[17] thermal cross-linking of interconnected bubbles into isolated holes with picolitre volume,[18] honeycomb-patterned polymer films[19-22] and nanoparticle thin-films.[23] Recently, straightforward routes imply the obtaining of self-organized polymer membranes of micro-porous channels[24] and the formation of hierarchically structured nanoparticle arrays by self-assembly processes.[25] In the latter case, CdSe nanoparticles were used to decorate breath figures in polymer thin-films. Motivated by these experiments, herein we report the use of the breath-figures phenomenon to arrange patterns that are spatially periodic in solute concentration.

EXPERIMENTAL SECTION.

Materials. Poly(Bisphenol-A-carbonate) (pc) in the form of pellets (average M_w ca. 64,000) and CH_2Cl_2 (HPLC grade) were used as received from Aldrich and no further purification was carried out. The synthesis and purification of Alq_3 are described elsewhere.[26]

Methods. Poly(Bisphenol-A-carbonate) (50 mg) was dissolved in CH_2Cl_2 (50 ml) under a N_2 flow passed through anhydrous $CaSO_4$ as a desiccant. Subsequently, either Alq_3 or rhodamine perchlorate 590, Exiton, INC., was added to the previously polymer solution (dye/pc: 3 wt.-%). A 50-μl drop of the resulting solution was cast onto a glass slide and exposed to moist atmosphere. For our system, a relative humidity >50% was found to be necessary to achieve an uniform droplet size on the micrometer scale. Backfilling of macroporous PC polymer scaffold was carried out by dipping a film into an aqueous solution (1 wt.-%) of acridine orange that was diluted in glacial acetic acid (1:1).

An atomic force profilometer Nanopics 2100 from KLA Tencor was operated in air at room temperature. A Wheastone bridge circuit is used to detect microdisplacement by a piezo-resistive, self-sensitive cantilever. Images were acquired scanning in contact mode (spring constant k= 3 N/m) using pyramidal-shaped Si tips (20 nm radius) integrated to nano-crystalline Si cantilevers (400-nm long). Resolution in z (height) is 3 Å.

Confocal optical micrographs were imaged with a Leica TCS 4D from Leica Microsystems (Heidelberg) equipped with a krypton-argon laser (488 nm) as a light source. Vertical optical sectioning (reflected white light, 63x NA 1.4 oil immersion lens) was acquired scanning in the xy or xz plane. 3-D view of the film was reconstructed as successive focal planes (a z series) collected at 0.2-μm intervals. Nikon Eclipse TE-2000-E laser scanning confocal microscope was used to image fluorescence. Pc-rhodamine samples were excited using a krypton-argon laser (488 nm) as a light source whereas Alq_3 samples were excited using a Ti sapphire laser (second armonic: 420 nm). Spatially-resolved photoluminescence measurements were performed by focusing the laser beam onto a selected area of the sample.[27] Wide-field fluorescence images were recorded with a digital colour camera after illuminating the sample with a Hg lamp as a light source.

Confocal micro-Raman measurements were collected on a Renishaw 1000 system equipped with a Peltier refrigerator-cooled CCD. Images were acquired according to the sample topography using auto-focus routines. An He-Ne laser (632.8 nm) was used as a source whose spot (~ 1μm diameter) was focused onto the surface through the objective lens (50x NA).

RESULTS AND DISCUSSION. Well-ordered arrays of air cavities were induced by the breath-figures phenomenon. Pure polycarbonate films and samples containing luminescent dopant agents showed indistinctively the same morphology, i.e., conical-shaped arrays of holes that were imaged by laser scanning confocal microscopy (LSCM) and profilometry measurements. Although the droplet-size distribution and separation distance are sentitive to experimental parameters such as the solvent, humidity and polymer concentration, the presence and different chemical nature of the embedded solute molecules did not influence the pore morphology. Spatially periodic patterns in solute concentration was investigated by additional fluorescence microscopy experiments and micro-Raman microscopy. Profilometry measurements were carried out to gain knowledge on the morphology corresponding to the well-ordered array of top cavities (Figure 1). The corresponding conical-shaped structures were studied in at least three different well-separated 50x50 μm^2 sites. The height profile across the surface topography shows air pockets that are approximately 840 nm in depth. The averaged diameter at the surface baseline is around 4.20 μm and separation distances between perimeters 2.40 μm.

LSCM micrographs were processed into 3D image stacks from successive focal planes collected across the film thickness. In-plane pores result depleted of dye molecules that exhibit an enhanced signal around the empty cavities, which is in correspondence to their perimeters. However, a weaker signal that is spatially periodic around the pores is detected. Therefore, intensity losses that are radially distributed may be ascribed to interference of light emitted between adjacent pores. The well-ordered hexagonal array of pores exhibits structured domains because of randomly distributed defects. For instance, the presence of oversized pores evidences the above-mentioned intensity losses such that the number of scattered light gaps is in agreement with the number of neighbouring pores in the lattice.

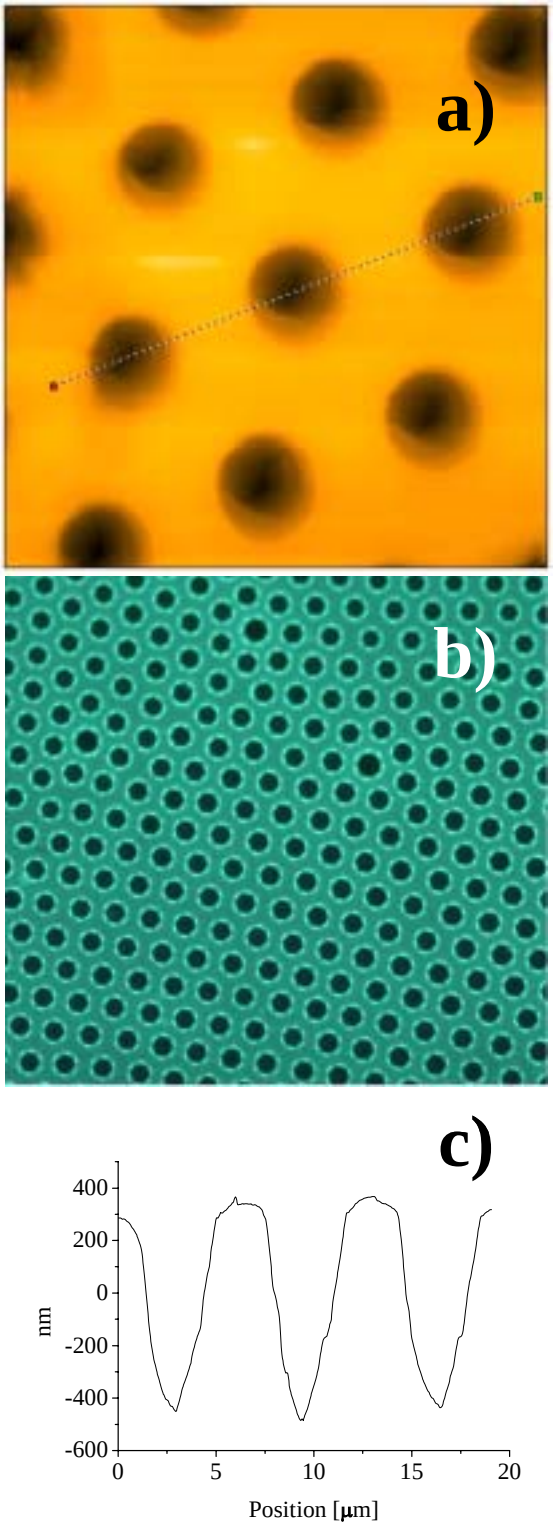

Figure 1. Micro-structured film of PC-Alq_3: a) profilometry measurements on the surface. Scan size 20 μm; b) 3D confocal optical image of successive focal planes collected at 0.2-μm intervals (z series) along the film thickness; c) height profile across the surface.

Likewise, patterned films comprising PC-rhodamine mixtures exhibit an array of pores of around 3-µm diameter that are arranged into structured domains. Figure 2 shows the corresponding wide-field fluorescence micrograph. A six-fold organized honeycomb structure coexists with smaller four-fold square lattice domains, the latter arising from disclination lines or five-fold organized point defects. Spatially resolved intensity measurements are depicted by PL spectra that were recorded from light emitted from inter-pore and subsidence regions of the pore structure. Both spectra possess identical features that are in excellent aggreement with that of pure rhodamine. However, a five-fold lower intensity is emitted by PL from the inner pore structure despite they appear dark in LSCM micrographs.

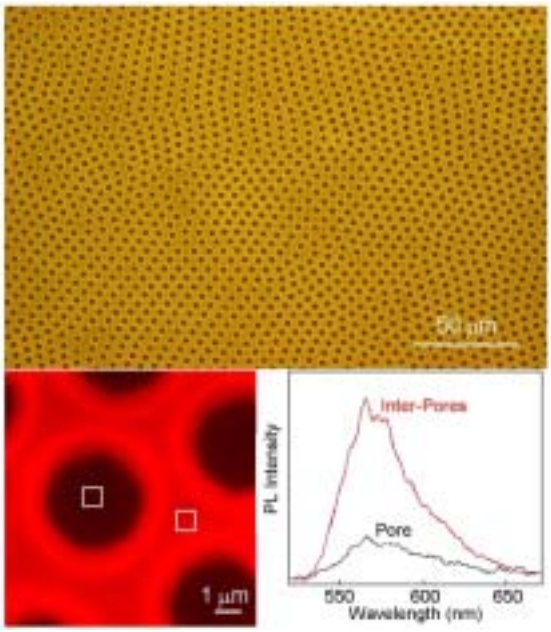

Figure 2. Micro-structured film of PC-rhodamine: Wide-field fluorescence micrograph (top image) and PL spectrum measured at the locations indicated by white squares (bottom image).Confocal optical sectioning in depth corresponding to the cross section represented by the white line in (b). The green line is representative of the focal plane in (b) that is parallel to the film surface.

To circumvent the background luminesce, confocal micro-Raman measurements were performed using a macroporous structured PC film. Independently of the position, the Raman spectra coincide with that of pure PC and no signals were attributed to either residual solvent or water in the polymeric matrix. Raman spectra were mapped on the focal plane corresponding to the surface. Thereby, the

Raman intensity recorded at the centre of the pores was half of that recorded in inter-pore regions. Moreover, Raman depth profile was acquired at different focal planes (z series) across the film thickness (Figure 3). The inset represents the depth dependence of integrate intensity corresponding to the band that arises at 890 cm^{-1}; the intensity is normalized with respect to the spectrum collected at the surface of inter-pore regions despite an enhanced intensity was around the pore edges. The measured intensity that was collected at the centre of the pore decreases progressively on account of the lesser density in depth. However, a non-zero signal remains constant at pronounced depth, fact that may be ascribed to light scattering effects.

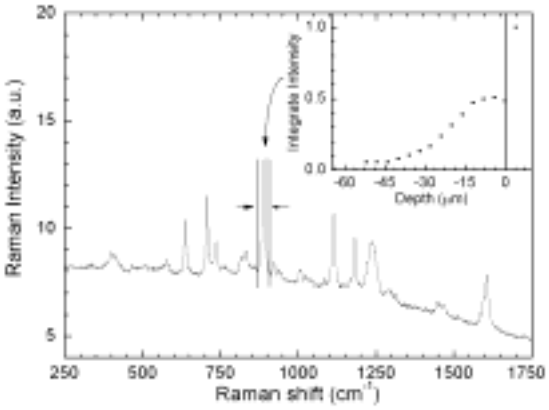

Figure 3. Raman spectrum of a micro-structured PC films (40-μm depth). The inset represents the integrate intensity of the band at 890 cm^{-1} collected in depth from the centre of the pore. The intensity is normalized with respect that recorded at the surface of inter-pore regions.

Based on these findings, confocal optical images were collected using reflected white light. The reflection mode enables the detection of contours and fringes corresponding to interfacial regions, i.e., the polymer matrix-air interface. Successive focal planes were collected at 0.2-μm intervals (z series) and the corresponding image stack was processed into the 3D reconstruction shown in Figure 4a. In-plane reflection points act as mirror centers corresponding to geometrical constraints such that each pore comprises two cavities that lie vertically inverted. The observation of unprecedented morphologies induced by breath figures is inherently ascribed to the nature of the polymer under study. A plausible

explanation arises from the physical properties of PC, potentially used in microporous anisotropic phase inversion membranes.[28]

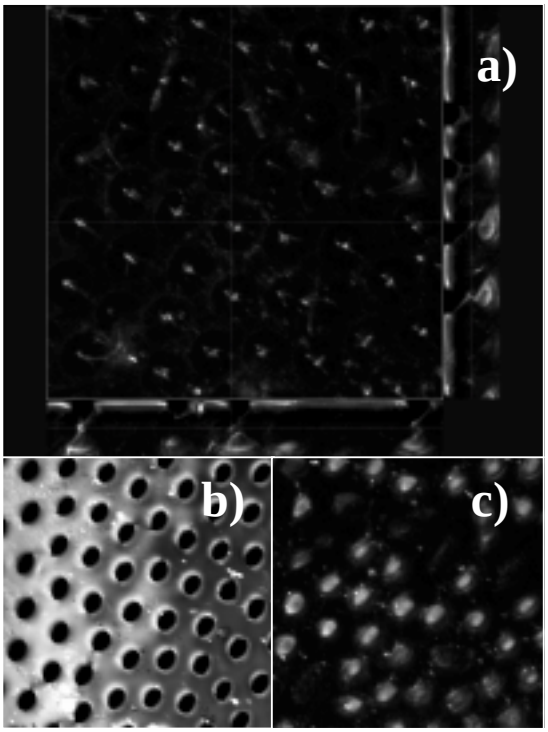

Figure 4. Confocal optical images of PC (reflected white light: a) 3D optical reconstruction showing constricted points (in-plane) and lateral sectioning across the film thickness showing the array of pores comprising inverted cavities; b) optical sectioning corresponding to the focal plane at the surface interface not included in the above 3D reconstruction; c) focal plane below geometrical constraints.

Along the evaporation pathway, the air-liquid interfacial temperature decreases. Below the dew point, water droplets from the moist air condense on the film surface. At the polymer solution-water droplet interface the precipitation rate of polycarbonate increases significantly and undergoes shrinkage by solidification. Therefore, a higher resistance to solvent evaporation is expected through the capped surface. Thus, liquid flows outwards to replenish the solvent losses along with mass transport of solute molecules.[29] The phenomenon, wich is independent of the chemical nature of their components, provide a means to concentrate the embedded dye molecules to the pore periphery close to the surface. Confocal optical sectioning of the film thickness shows a concentration gradient of solute molecules that preferentially accumulate decorating the walls of the pores.[25] Based on this effect, the greater

distribution of molecules lies close to the film surface, where the array of pores by fluorescence shows a regular shape in depth (Figure 5). By contrast, their density diminishes drastically going deeper into the film while the regular cavities undergo structural constraints as revealed by profilometry measurements and LSCM operated in reflection mode.

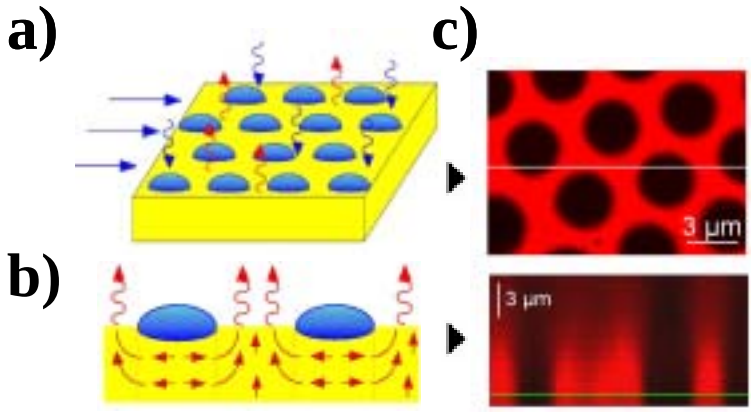

Figure 5. Micro-structured film of PC-rhodamine: a) Schematic representation of the standard breath-figures method (top image). A volatile solvent (in red) undergoes cooling evaporation on the surface. A moist air flux parallel to the surface allows condensation of water droplets (in blue) below the dew point of water into a well-ordered hexagonal array; b) proposed mechanism; c) LSCM image corresponding to the focal plane parallel to the surface (top image); confocal optical sectioning in depth corresponding to the cross section represented by the above white line (bottom image). The green line is representative of the focal plane close to the surface.

Both LSCM and micro Raman experiments revealed poor intensity signals at pronounced depth. To circumvent either the background luminescence or light scattering effects that derive from the polymer scaffold, new experiments were carried out by using pure polycarbonate films. Thereby, backfilling the cavities with aqueous acridine solution allows a thorough study of empty cavities. Figure 6 shows the confocal optical images corresponding to the film surface and sectioning in depth. Acridine was enable to dye polycarbonate material such that the surface interface shows lack of fluorescence in the regions where the pores are located (a). In contrast, focal planes recorded across the top cavities of the porous

structures invert the signals. Thereby, the polymer matrix remained unaltered by the presence of acridine with lack of fluorescence. However, the array of pores was filled in solute molecules that underwent precipitation in the empty regions above the structural constraints (b). To clarify these observations, superimposed micrographs were acquired simultaneously in both fluorescence and reflection operative mode as shown in (c). Successive focal planes collected below the constraints revealed an interconnected bubble network at pronounced depth, as shown by the 3D reconstruction (e). Therefore, constraints are supposed to prevent the lateral interconnection between the array of top cavities. However, they act as vertical channels that flow into a lean phase in polycarbonate as revealed by the above-mentioned micro Raman experiments. Evidence of vertical channels was observed in those pores that remained free of precipitated acridine (f). Evaporative cooling process drives the condensation of water droplets on the film surface. However, once the film returns to ambient temperature, water droplets evaporate leaving behind pores in the polymeric film. As a consequence, the lean phase in polycarbonate, which in turn is rich in solvent, gives rise to interconnected bubbles or macrovoids as ascribed to its lower density (d).[28] Moreover, the formation of vertical channels can be inferred to residual solvent that evaporates from the lean phase in polycarbonate or swelled phase.[30]

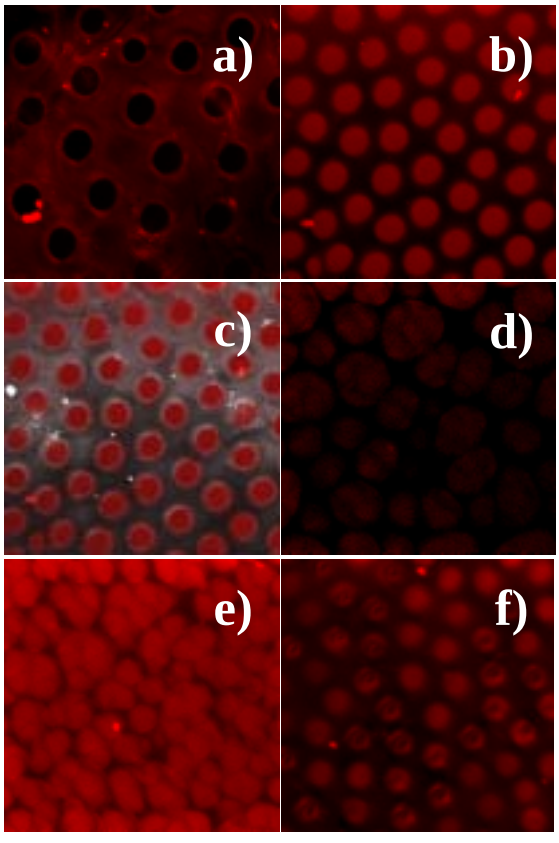

Figure 6. Backfilling of acridine solution in PC films: a) confocal optical image recorded at the film surface; b) focal plane collected across the array of top cavities; c) superposition of images collected at the same focal plane using both fluorescence and reflection mode; d) focal plane collected at pronounced depth showing an interconnected bubble array; e) 3D reconstruction of the above-mentioned focal planes; f) confocal optical image revealing vertical channel through constraints.

CONCLUSIONS. In conclusion, herein we report the self-assembly process of luminescent solute molecules into conical-shaped cavities in polycarbonate thin-films. A well-ordered hexagonal array of micrometre-sized cavities arises from condensing water droplets (breath figures) that self-assemble on the surface of a polymeric solution. The breath-figures phenomenon has previously been successfully used to generate 2D or 3D ordered macroporous materials based on polymeric systems. However, the use of polycarbonate thin-films for this purpose has never been so far reported. Unprecedentedly, the well-ordered array of pores comprises two inverted cavities that shows individually anisotropic shape. A very small gap of miscibility is attained at the polymer solution-water interface and the precipitation rate of polycarbonate is hence significantly enhanced. As a consequence, constrictions at approximately half the height suppress the formation of interconnected channels between the array of top cavities. Along the evaporation pathway, the combination of self-assembly processes allows the segregation of solute molecules according to the ordered array of cavities. The surface segregation of spatially-correlated luminescent molecules, such as Alq_3 and rhodamine perchlorate, opens their prospective use towards the application of breath figures for their patterning over large areas on two length scales, the pore size and the separation distance.

Acknowledgement. This work was supported by the Information Society Technologies Programme of the European Commission, as a part of the project NANOMAGIQC IST-2001-33186, and by EU NAIMO Integrated Project No NMP4-CT-2004-500355.

(1) Tang, C. W.; Vanslyke, S. A. *Appl. Phys. Lett.* **1987**, *51*, 913-915.

(2) Friend, R. H.; Gymer, R. W.; Holmes, A. B.; Burroughes, J. H.; Marks, R. N.; Taliani, C.; Bradley, D. D. C.; Dos Santos, D. A.; Brédas, J. L.; Lögdlund, M.; Salaneck, W. R. *Nature* **1999**, *397*, 121-128.

(3) Castro, C.; Ramos, J.; Millán, A.; González-Calbet, J.; Palacio, F. *Chem. Mater.* **2000**, *12*, 3681-3688.

(4) Campbell, M.; Sharp, D. N.; Harrison, M. T.; Denning, R. G.; Turberfield, A. J. *Nature* **2000**, *404*, 53-56.

(5) Thurn-Albrecht, T.; Steiner, R.; DeRouchey, J.; Stafford, C. M.; Huang, E.; Bal. M.; Tuominen, M.; Hawker, C. J.; Russell, T. P. *Adv. Mater.* **2000**, *12*, 787-791.

(6) Míguez, H.; Yang, S. M.; Tétreault, N.; Ozin, G. A. *Adv. Mater.* **2002**, *14*, 1805-1808.

(7) Xu, B.; Arias, F.; Whitesides, G. M. *Adv. Mater.* **1999**, *11*, 492-495.

(8) Blanco, A.; Chomski, E.; Grabtchak, S.; Ibisate, M.; John, S.; Leonard, S. W.; Lopez, C.; Meseguer, F.; Miguez, H.; Mondia, J. P.; Ozin, G. A.; Toader, O.; Van Driel, H. M. *Nature* **2000**, *405*, 437-440.

(9) Imhof, A.; Pine, D. J. *Nature* **1997**, *389*, 948-951.

(10) Davis, S. A.; Burkett, S. L.; Mendelson, N. H.; Mann, S. *Nature* **1997**, *385*, 420-423.

(11) Widawski, G.; Rawiso, M.; François, B. *Nature* **1994**, *369*, 387-389.

(12) Srinivasarao, M.; Collings, D.; Philips, A.; Patel, S. *Science* **2001**, *292*, 79-82.

(13) Rayleigh, L. *Nature* **1911**, *86*, 416-417.

(14) Peng, J.; Han, Y.; Yang, Y.; Li, B. *Polymer* **2004**, *45*, 447-452.

(15) Beysen, D.; Knobler, C. N. *Phys. Rev. Lett.* **1986**, *57*, 1433-1436.

(16) Brinkmann, M.; Graff, S.; Biscarini, F. *Phys. Rev. B* **2002**, *66*, 165430.

(17) Song, L.; Bly, R. K.; Wilson, J. N.; Bakbak, S.; Park, J. O.; Srinivasarao, M.; Bunz, U. H. F. *Adv. Mater.* **2004**, *16*, 115-118.

(18) Erdogan, B.; Song, L.; Wilson, J. N.; Park, J. O.; Srinivasarao, M.; Bunz, U. H. F. *J. Am. Chem. Soc.* **2004**, *126*, 3678-3679.

(19) Yu, C.; Zhai, J.; Gao, X.; Wan, M.; Jiang, L.; Li. T.; Li. Z. *J. Phys. Chem. B* **2004**, *108*, 4586-4589.

(20) Yabu, H.; Tanaka, M.; Ijiro, K.; Shimomura, M. *Langmuir* **2003**, *19*, 6297-6300.

(21) Karthaus, O.; Maruyama, N.; Cieren, X.; Shimomura, M.; Hasegawa, H.; Hashimoto, T. *Langmuir* **2000**, *16*, 6071-6076.

(22) Stenzel-Rosenbaum, M. H.; Davis, T. P.; Fane, A. G.; Chen, V. *Angew. Chem. Int. Ed.* **2001**, *40*, 3428-3432.

(23) Shah, P. S.; Sigman Jr., M. B.; Stowell, C. A.; Lim, K. T.; Johnston, K. P.; Korgel, B. A. *Adv. Mater.* **2003**, *15*, 971-974.

(24) Ohzono, T.; Nishikawa, T.; Shimomura, M. *J. Mat. Sci.* **2004**, *39*, 2243-2247.

(25) Böker, A.; Lin, Y.; Chiapperini, K.; Horowitz, R.; Thompson, M.; Carreon, V.; Xu, T.; Abetz, C.; Skaff, H.; Dinsmore, A. D.; Emrick, T.; Russell, T. P. *Nat, Mat.* **2004**, *3*, 302-306.

(26) Vogel, A. I. *Textbook of Quantitative Chemical Analysis*, 5th ed., Longman Scientific & Technical, New York **1989**.

(27) Loi, M. A.; Da Como, E.; Zamboni, R.; Muccini, M. *Synth. Met.* **2003**, *139*, 687-690.

(28) Di Luccio, M.; Nobrega, R.; Borges, C. P. *Polymer*, **2000**, *41*, 4309-4315.

(29) Deegan, R. D.; Bakajin, O.; Dupont, T. F.; Huber, G.; Nagel, S. R.; Witten, T. A. *Nature* **1997**, *389*, 827-829.

(30) D'Archivio, A. A.; Galantini, L.; Biffis, A.; Jerábek, K.; Corain, B. *Chem. Eur. J.* **2000**, 6, 794-799.

Artículo J

Título:
Structuring polycarbonate thin-films doped with Mn_{12} single-molecule magnets

Autores:
J. Gómez-Segura, D. Ruiz-Molina, M. Cavallini, F. Biscarini, J. Veciana.

Revista:
Chemistry of Materials (en evaluación)

Structuring Polycarbonate Thin-Films Doped with Mn_{12} Single-Molecule Magnets

Jordi Gómez-Segura,[†] *Daniel Ruiz-Molina,**[,†] *Massimiliano Cavallini,*[‡] *Fabio Biscarini*[‡] *and Jaume Veciana*[†]

Institut de Ciència dels Materials de Barcelona (CSIC), Campus UAB, Bellaterra 08193, Catalonia, Spain, and Istituto per lo Studio dei Materiali Nanostrutturati, Sez. Di Bologna, Via P. Gobetti 101, I-40129, Bologna, Italy.

RECEIVED DATE (to be automatically inserted after your manuscript is accepted if required according to the journal that you are submitting your paper to)

TITLE RUNNING HEAD: Mn_{12} doped thin-films

* To correspondence should be addressed. E-mail: dani@icmab.es. Fax: +93 580 57 29. Tel: +93 580 18 53.

† Institut de Ciència de Materials de Barcelona (CSIC)

‡ Istituto per lo Studio dei Materiali Nanostrutturati (CNR)

Nanocomposite thin-films phase separate by solvent evaporation of a Mn_{12}-polymer solution with a low miscibility gap. Phase-separation from ordered mesoporous thin-films allows the formation of hierarchically structures on a mesoscopic scale that are endowed with controlled size and separation distance. The formation of a well-ordered hexagonal array of pores, or ‘breath-figures’, which is the condensation of water droplets on the surface of a polymeric solution, is combined with the study of the swelling properties. Thereby, the polymer scaffold is exposed to organic solvent vapors. As a consequence, the array of pores is released by softening to afford the formation of mesostructured materials. Indeed, semi-globular domains phase separate selectively on the film surface according to

the array of pore sites as revealed by confocal optical microscopy and atomic force microscopy imaging. Magnetic measurements prove the nanocomposite thin-films to have single-molecule magnetic properties.

Introduction

Polymer-based nanostructures have attracted substantial research interests in the field of materials science. The ease of processing polymers at room temperature and their low cost are combined with specific mechanical, optical or conducting properties that enable the use of nanocomposite materials in technical applications, for example, as catalysts, chemical sensors and optical/electronic devices. Indeed, the incorporation of embedded nanoparticles by dispersion into polymer matrices[1] or copolymerization of functionalized inorganic nanoclusters, covalently linked to organic polymer networks,[2] can be designed by means of a simple and soft methodology based on polymer solutions or in a melt form.

Magnetic nanocomposites represent promising materials that offer potential applications as magnetic refrigerants[3] and magnetic information storage devices. Very recently, much attention has been focused on the study and preparation of hybrid cross-linked copolymers based on Mn_{12} single-molecule magnets (SMMs) containing polymerizable functionalities.[4] Earlier approaches to arranging Mn_{12} SMMs imply their dispersion into well-organized multilayered Langmuir-Blodgett films[5] and polymeric thin films.[6] The latter methodology, described previously by us, allows a reliable and simple methodology to address embedded Mn_{12} molecules onto a polymeric film surface. The choice of polycarbonate as a matrix endows the nanocomposite with flexibility, crisp-resistance and transparency, allowing to improvement of the thermal and chemical stability of the Mn_{12} SMMs as well as the overall strength of the film.[7] Moreover, these molecular magnets have a high energy barrier for the spin reversal that originates from a large-spin ground state and magnetic anisotropy. As a consequence, these complexes exhibit interesting magnetic properties characteristic of bulk ferromagnets, due to individual molecules rather than long-range ordering, such as stepwise magnetization hysteresis loops and resonant magnetization tunneling. This fact, together with their

easy preparation, reproducibility, low cost and monodispersed size, enable the use of these molecular systems as ideal candidates in quantum-computing applications.[8]

Nanocomposite thin-film preparation relied on a two-step process involving the drop-casting of a polymer solution that contains dispersed Mn_{12} SMMs and the subsequent treatment with different organic solvent vapors. Solvent treatment originates that a small fraction of the initially embedded Mn_{12} molecules migrates to the film surface with an aggregation state that can be controlled at will, fact that depends on the nature of the solvent. It has already been established that after absorption of suitable amounts of a solvent, capable of effectively solvating the polymer chains, the swollen polymer network exhibits an extensive porosity. This situation provides a valuable route for the molecular reorganization on the nanocomposite with a small fraction of Mn_{12} molecules emerging to the film surface. By this method, Mn_{12} domains are spatially isolated and enclosed with the polymeric surroundings revealing magnetic contrast by magnetic force microscopy (MFM). Based on these findings, we have developed straightforward routes to fabricating structured film patterns of SMMs on a polymer surface, thereby allowing spatially and geometrically controlled domains of Mn_{12} aggregates to be used as magnetic bits of information. Therefore, Mn_{12} complexes are patterned by molding a dispersion in a polymer solution onto a structured master (e.g., a DVD). The protrusions of the polymer replica surface are released by subsequent solvent vapor exposure, allowing the complexes to concentrate preferentially on the surface reproducing the original protrutions.[9]

Very recently, we have studied the self-assembly of Mn_{12} molecules into ring structures by templating breath-figures on a hydrophobic surface.[10] A cold surface (i.e., solid or liquid) in contact with moist air condenses water droplets giving rise to distinct patterns on the surface, the well-known breath figures phenomenon.[11] Likewise, a polymer solution that consists of a volatile organic solvent undergoes cooling evaporation coupled with condensation of water droplets in a moist atmosphere. On the basis of this, the breath figures phenomenon has recently been used as a simple, reliable and soft methodology to generate 2D or 3D ordered macroporous materials based on polymeric systems.[12] Other approaches involve microdomains of block copolymers, where elimination of the minor component transforms the material into an array of pores.[13] Ordered

mesoporous materials are hence of great importance for the obtaining of well-ordered arrays of dispersed nanocomposites with controllable size and separation distance.

Experimental Section

Materials and Sample Preparation. Poly(Bisphenol-A-carbonate) was used as purchased from Aldrich in the form of pellets (average Mw ca. 64,000) and *o*-dichlorobenzene (HPLC grade) was freshly distilled at reduced pressure. All manipulations were handed under anhydrous conditions. The complex of choice, $[Mn_{12}O_{12}(O_2CC_6H_4C_6H_5)_{16}(H_2O)_4]$ (1)**,** was prepared and purified following the methodology described elsewhere.[14]

Films were cast onto a glass surface from a 10^{-2} g/cm^3 solution of polycarbonate in *o*-dichlorobenzene; furthermore, films containing 12 wt.-% of complex **1** were prepared under the same experimental conditions. After solvent evaporation at 120 °C films were removed from the glass surface at room temperature by immersion into a water bath.

A CH_2Cl_2 solution of Mn_{12}/polycarbonate (3 wt.-%) was cast onto a glass slide in a moist atmosphere whose relative humidity (65%) was found to be necessary to achieve a monodispersed well-ordered array of micrometer sized water droplets. After complete solvent evaporation was completed, the resulting macroporous structured films were subsequently exposed to CH_2Cl_2 vapors over silica in a saturated chamber. As a consequence, the array of pores was allowed to release by softening until films become completely transparent.

Laser Scanning Confocal Microscopy. Confocal optical micrographs were imaged with a Leica TCS 4D from Leica Microsystems (Heidelberg) equipped with a krypton-argon laser (488 nm) as a light source. Optical sectioning (reflected white light, 63x NA 1.4 oil immersion lens) was acquired scanning in the xy or xz plane. 3-D view of the film was reconstructed as successive focal planes (a z series) collected at 0.2-μm intervals. Samples were placed on a slide and nail polish was used to seal the coverslip using immersion oil as a mounting medium. Film thickness was measured optically to oscillate between 4-5 μm.

Profilometry measurements. Macroporous materials were imaged in air at room temperature on an atomic force profilometer Nanopics 2100 from KLA Tencor. A Wheastone bridge circuit is used to detect microdisplacements by a piezo-resistive, self-sensitive cantilever. Images were acquired operating in contact mode using nano-crystalline Si cantilevers (400-nm long) ended by pyramidal-shaped Si tips (20 nm radius).

Atomic Force Microscopy. A commercial scanning force microscope PicoSPM from Molecular Imaging was operated in air at room temperature. Intermittent-contact, contact and friction modes were used to study the mechanical properties on the surface after swelling treatment. Microfabricated silicon cantilevers were used with characteristic spring constant 1.2-3.5 Nm^{-1} and resonance frequency 65-90 kHz.

Magnetic Measurements. DC magnetic measurements were collected on a Quantum Design MPM®XL superconducting SQUID magnetometer equipped with a 7 T magnet. The operational range of temperature corresponds to 1.8-300 K. The field-dependence of magnetization was carried out operating in hysteresis mode at 1.9 K. The samples were magnetically saturated in a 4.0 T field, then the field was cycled down to -4.0 T and back up to +4.0 T. Magnetic anisotropy was studied applying the external magnetic field either parallel or perpendicular to the surfaces of a series of stacked films containing 12 wt.-% in the Mn_{12} complex.

Results and Discussion

Nanocomposite thin-films consisting of a polycarbonate-based matrix and embedded Mn_{12} molecules were prepared from a polymer solution as previously described in the experimental section. The growth in amplitude for a given fluctuation in liquid thin-films is reached for wavelengths larger than a critical value that depends on the initial film thickness and surface tension.[15] The surface tension tends to reduce surface corrugations induced by thermal motions in order to minimize the surface Gibbs energy, whereas intermolecular forces, by contrast, favor the disproportionation of the film. Disproportionation phenomenon is ascribed to the onset of a disjoining pressure that originates from migration of molecules from thinner to thicker parts of the film. As a consequence, the mass transport minimizes the overall van der Waals energy.[16] Our

research interests are based on the study of liquid thin-films consisting of a polymer solution that undergoes thermal oscillations. Along the evaporation pathway, surface corrugations are controlled at a rate that depends on the viscosity of the liquid, therefore inducing fluctuations in composition such that one part of the system gets more concentrated at expense of another. As a consequence, the polymer solution becomes unstable and phase-separation occurs in order to minimize the free energy of mixture.

Herein, we report a simple and reliable convergent approach that is based on the condensation of micrometre-sized water droplets, or breath-figures, on the surface of a Mn_{12}-polymer solution and the subsequent swelling process induced by solvent vapor exposure. As a consequence, the well-ordered array of pores undergoes softening and release by swollen-induced surface smoothening process. This method, which allows the control of phase-separation, opens a new route to fabricating mesostructured materials of functionalized domains on the polymer surface that can be used as magnetic information storage, sensors or catalytic sites.

Complex **1** shapes an hydrophobic outer shell as well as to favour π-type interactions between the peripheral phenyl groups. Moreover, the low gap of miscibility between the binary system Mn_{12}-polycarbonate favors phase-separation of their components, which is enhanced by immiscible condensing water droplets on the surface of the polymer solution.

The resulting films were thoroughly characterized by microscopy techniques to gain knowledge on the formation of microphases by crystallization-induced phase separation.

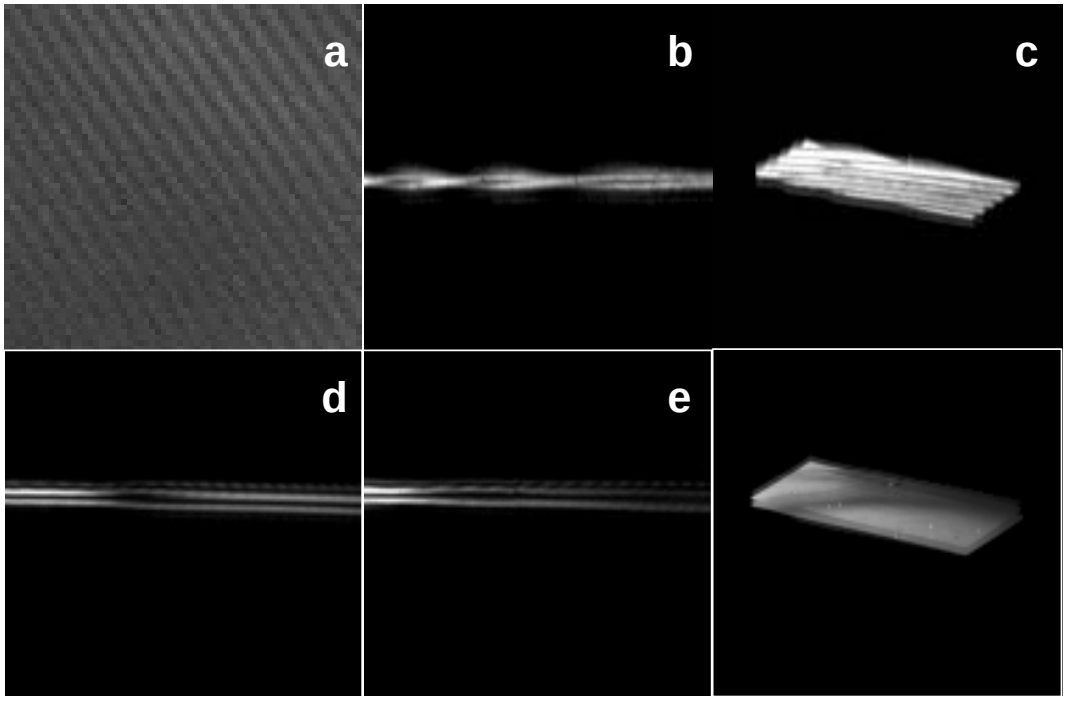

Figure 1. Confocal optical micrographs of pure polycarbonate films showing a pattern of highly oriented fibrils (top panel): (a) Zoomed image corresponding to a focal plane collected parallel to the film surface (xy); (b) Optical sectioning across the film thickness (xz); (c) 3-D image of successive focal planes collected at 0.2-μm intervals (z series). Lack of the well-ordered array of fibrils (bottom panel): (d-e) Lamellar stack domains showing correlated surface undulations that are smeared out along their propagation; (f) 3-D reconstruction.

Confocal optical images in Figure 1 correspond to pure polymer films. In-plane optical sectioning (xy) reveals a periodical pattern of highly oriented fibrils of polycarbonate, whose characteristic size and separation distance is subjected to variations of the film thickness. Moreover, optical vertical sectioning (xz) in Figure 1 shows helical coiled fibrils that twist unclockwise along their preferential axis spacing progressively their helicity. However, the lack of the well-ordered fibrillar array was confirmed after additional imaging made in distinct well-separated sites of a film sample of a 5-cm diameter. By contrast, the presence of lamellar stack domains are observed to be oriented parallel to the polymer film-air interfaces. Evidence of the periodical pattern of polycarbonate fibrils in the polymer matrix was corroborated by high-resolution atomic force microscopy (AFM). By switching the AFM mode from intermittent-contact to contact mode, the effective force that the tip exerts on the sample surface is increased. The initially featureless polycarbonate film surface (r.m.s roughness <1 nm) is depleted of magnetic domains as depicted in Figure 2. At elevated tip forces the surface layer is depressed and a periodical pattern of highly oriented polycarbonate is appreciable with a characteristic 267-nm pitch across the film surface. Therefore, the array of fibrils can be detectable by scanning confocal microscopy according to the in-plane resolution of 200 nm, which is in agreement with the confocal optical image shown in Figure 1. The topmost layer of the films can be hence understood as an amorphous polycarbonate phase bound to the rigid well-ordered subsurface layers. The apparently disordered amorphous phase is nonbirefringent[17] and therefore appearing as dark in optical confocal imaging.

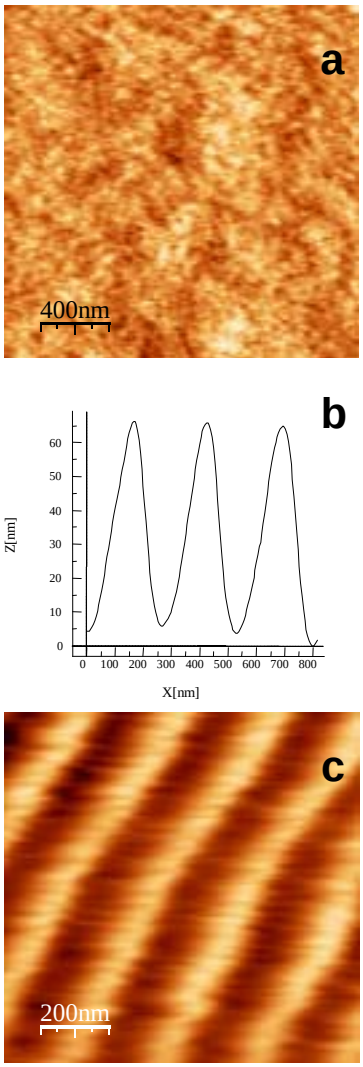

Figure 2. AFM images on the surface of pure polycarbonate films. (a) Topographical image operating in semi-contact mode; (b) height profile across the film surface in (c) showing a pattern of highly oriented fibrils of polycarbonate by switching to contact mode in (a).

Solvent-induced preparation endows the resulting polymer thin-films with an extent of crystallinity as ascribed to semicrystalline polycarbonate, thereby allowing the observation of birefringent or crystalline structures by confocal optical microscopy. The initial polymer solution is supposed to consist of solvated molecules in the form of coils. These coils, in contrast to extended polymer chains, result in a spread of chain conformation over the associated rotational energy barrier, which is driven by an increase in entropy. As the solvent evaporates, entanglements become more relevant and chains pack together side-by-side by secondary bonding network, giving rise to birefringent or crystalline entities. Conventional crystallization from dilute polymer solutions can be considered a thermodynamically controlled quasi-static process. Thus, an entropy penalty has to be compensated by a reduction in enthalpy as polymer chains adopt the energetically most favorable conformation within the crystals. However, film cast by solvent evaporation at relatively high temperature allows crystallization-induced phase separation at a rate controlled by thermal oscillations and viscosity. The rate of crystallization in polycarbonate is in turn controlled by segmental motions[18] along the polymer chains and can be sensitive to thermal fluctuations, chain length effects and the range of molar masses.[19] Thus, a cooperative movement along the polymer chains favors their conformational arrangement such that entanglements promote their aggregation in the form of well-ordered helical fibrils. As a consequence, intermolecular interactions between the carbonyl groups are accompanied by cooperative motions involving both the carbonate and the phenyl rings as previously reported for polycarbonate small-molecule analogues.[20]

From the confocal optical micrographs shown in Figure 1, an intermediate void layer less than 1 μm thick is observed between the two lamellar stack domains. This fact may be ascribed to interference of light reflected from the lamellae, as similarly occurs in black films,[21] or most likely due to ‘liquidlike’ amorphous polycarbonate as revealed on the surface by the aboved-mentioned AFM investigations. Indeed, the intermediate volume scatters light, however, because of its amorphous nature, and would not be birefringent.

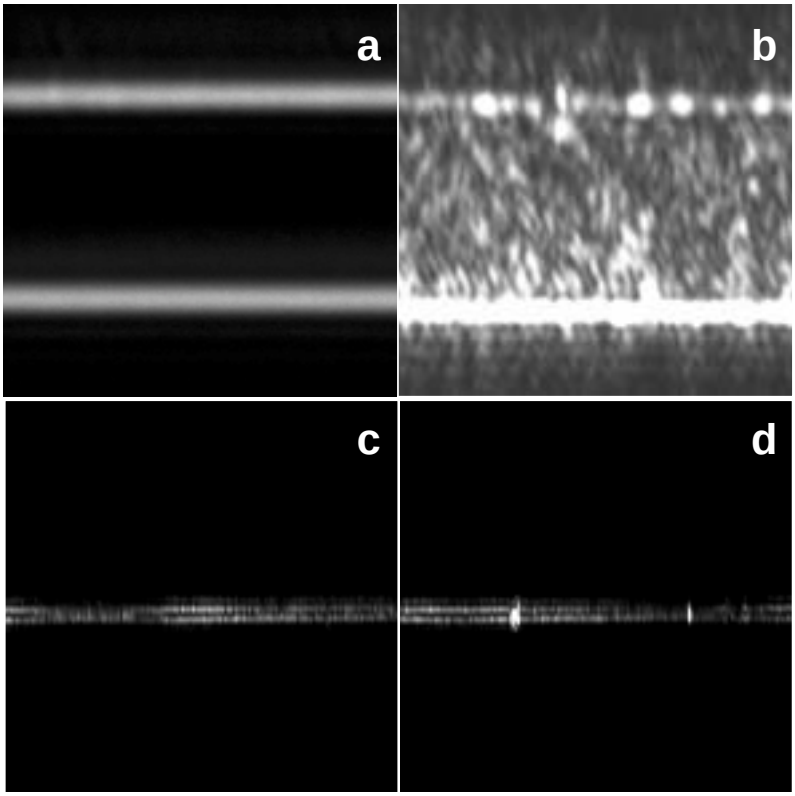

Figure 3. Confocal optical micrographs: (a) Zoomed image corresponding to the vertical sectioning of a pure polycarbonate film after solvent vapor exposure; (b) the same as in (a) performed on a Mn_{12}-polycarbonate film; (c) Vertical sectioning (xz) of polycarbonate films with 12 wt.-% of Mn_{12} complex showing linear sequences of polycarbonate crystallites; (d) The same as in (c) showing intercalated Mn_{12} micro-crystals that grow preferentially oriented normal to the film surface.

To balance both explanations, a cast film of polycarbonate was exposed to extended CH_2Cl_2 vapor exposure at room temperature. By polymer chain solvation, conformational rotation effects are reactivated by an increase of entropy and quenched after complete solvent evaporation. The vertical sectioning in Figure 3 reveals a greater content of 'liquidlike' amorphous phase, which in turn is unnoticeable by reflected white light despite the greater inter-plane distance of approximately 5 µm between both polymer film-air interfaces. However, in the presence of Mn_{12} molecules crystallization-induced phase separation enhance the onset of discrete structures.

Films containing 12 wt.-% of the Mn_{12} complex were prepared in the same experimental conditions as pure polycarbonate films. During solvent evaporation, phase separation yields at least

two liquid phases, one lean and the other rich in polymer when the system approaches the two-phase boundary.[22] The rich phase in polymer precedes the formation of the polymeric matrix and two neighbouring lamellar domains result from the nucleation and growth of crystallites.[23] These crystallites, which act as building blocks that are oriented normal to the surface, merge with each other into linear sequences.[24] Moreover, a few grooves are observed that recalls the helical structure of polycarbonate films devoid of the Mn_{12} complex. Separation of crystallisable and non crystallisable chain parts of polycarbonate leads to the lateral growth of denser cores by chain folding mechanism and a less ordered exterior. Evidence of feasible inter-crystalline-line links,[25] which are polymer chains that are shared by two neighboring crystalline entities, may be predicted in the 'twisting regions', which favors the lateral growth of crystallites into a single stack domain. However, the Mn_{12} molecules are originally dispersed into the lean phase in polymer. Phase-separation of polycarbonate crystallites evolves giving rise to constraining forces that favor the nucleation and lateral growth of randomly distributed Mn_{12} micro-crystals. These crystals are unambiguously assigned to Mn_{12} and distinguishable from the polymeric crystallites by contrast between transmitted and reflected white light (Figure 4).

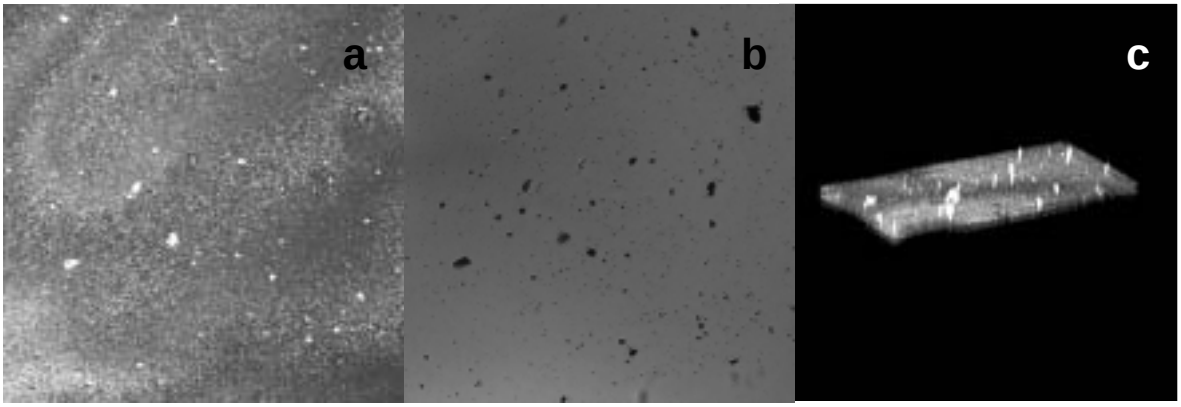

Figure 4. Confocal optical micrograph (a) of a focal plane parallel to the film surface and its corresponding image obtained by transmitted white light through the entire film thickness; (c) 3-D reconstruction of successive focal planes collected at 0.2-μm intervals (z series) showing the inclusion of randomly dispersed Mn_{12} crystals.

Therefore, swelling process force the crystalline polymer scaffold to "melt" into a single stack domain and newly formed nuclei grow as the solvent evaporates.

The first challenge to circumventing phase-separation into randomly distributed microstructures was studied by templating breath figures onto the film surface. Figure 5 shows a patterned film after condensation of micrometre-sized water droplets. The initial well-ordered hexagonal array of pores consists of conical-shaped air cavities of a 800-nm depth and a 4-μm diameter as measured by profilometry measurements in (d). After swollen-induced softening of the polymer scaffold, the array of pores is progressively released into concave shapes of less than a 200-nm depth and an average diameter of approximately a 6 μm. To assess the mechanical properties on the surface of the Mn_{12} samples the AFM microscope was initially operated in intermittent-contact mode. On switching to contact mode, the efective force that the tip exerts on the sample is increased as well as the apparent depth. Depending on the loading force the subsidence is measured to increase at least twice the depth operating in intermittent-contact mode, therefore revealing a softer material. The surface corresponding to the concave shapes was also investigated, showing no other morphology than the presence of small clusters. However, friction mode and phase imaging, which are sensitive to the local chemical composition and mechanical response of the surface, exhibit a strong contrast versus the compact polymer surroundings.

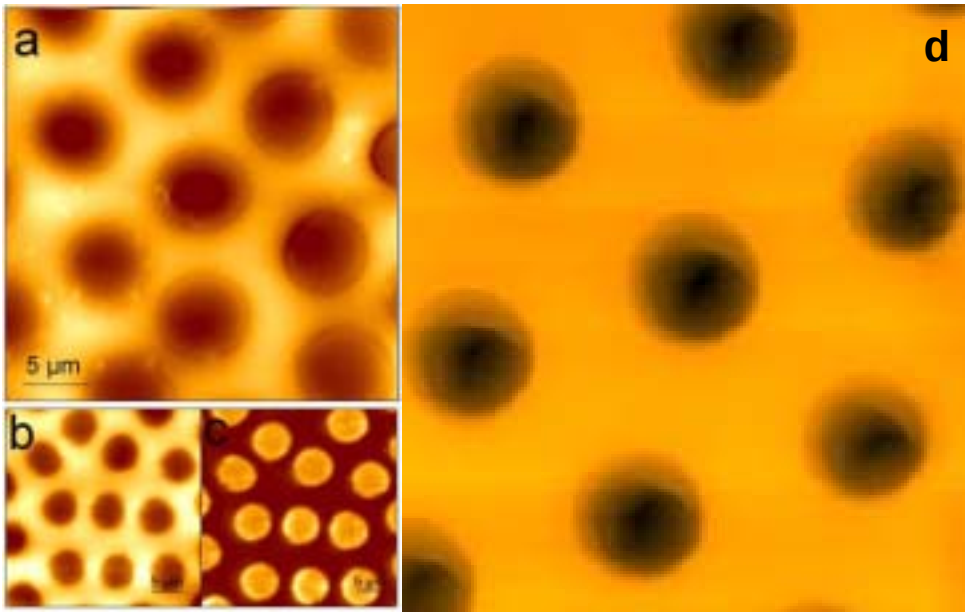

Figure 5. AFM images of microporous Mn_{12}-polycarbonate films: a) image in (d) after solvent vapor exposure acquired in semi-contact mode (z scale is 0-240 nm); b) Topography image acquired

in contact mode (z scale is 0-330 nm); c) Image in (b) measured in friction mode; (d) Hexagonal array of pores induced by breath-figures. Scan size is 20 μm.

Optical sectioning was explored on swollen-induced nanocomposite samples by laser confocal scanning microscopy. Control experiments were carried out on polycarbonate thin-films as blank samples devoid of dispersed Mn_{12} molecules. Indeed, in the latter case, the polymer sacaffold was gently swelled by exposure to CH_2Cl_2 vapors, which flow through the well-ordered array of microporous channels into a network comprising interconnected bubbles.[26] As a consequence, the polymer scaffold colapses by softening, allowing the nucleation of birefringent structures in the form of polarizing spherulites, whose diameter was measured optically to be approximately 12 μm.[27] Moreover, the radial growth of these spherulites as well as the onset of polycarbonate fibrils by solvent-induced crystallization drive the coalescence of the initially well-ordered array of pores by shrinkage (Figure 6). By contrast, in the presence of Mn_{12}, the control of phase-separation is selectively attained in the surface sublayers and not observed elsewhere across the film thickness. In-plane sectioning corroborates the formation of close-lying semiglobular microdomains that are oriented in a planar fashion parallel to the film surface. Therefore, the resulting mesostructured film surface is confirmed to result from the well-ordered array of mesoporous materials. Indeed, swollen-induced phase-separation can be controlled selectively at the pore sites, whose cavities are suited as templates for fabricating well-ordered dispersed nanocomposites.

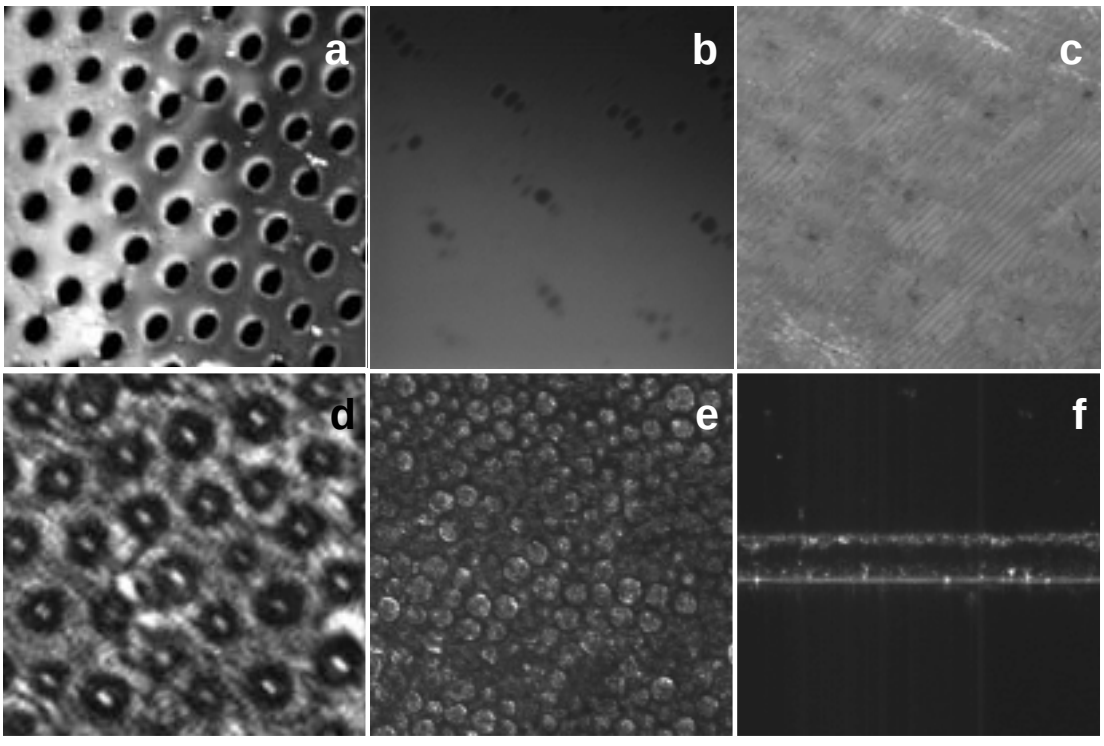

Figure 6. Confocal optical micrographs. Pure polycarbonate films (top panel): (a) Focal plane (xy) corresponding to the film surface; (b) image of (a) after swelling process showing the coalescence of the pores on the surface; (c) 3-D reconstruction showing a pattern of polycarbonate fibrils close to the surface. Spherulite nuclei are in correspondence with the pore sites in (b). Polycarbonate films with 12 wt.-% of Mn_{12} complex (bottom panel): (d) Optical sectioning across the bottom of the well-ordered array of pores; (e) Film surface after solvent vapor exposure showing microdomains that form at the expense of air cavities in (d); (f) optical sectioning across the film thickness (xz) showing the array of microdomains in (e) distributed on the film surface.

Differential interference contrast (Nomarski) microscopy[28] renders images whose contrast is obtained by refractive index gradients that are converted into amplitude changes. The initial mesoporous thin-films become transparent after swelling by solvent vapor exposure, thereby allowing the study by Nomarski imaging. When light passes through a transparent sample that comprises elements whose refractive index differ, the spatial rate of the wavefront will change because of the varying optical path-lengths. Figure 7 shows the gradient of intensities corresponding to the focal plane close to the surface. A three-dimensional profile is hence provided by refractive index inhomogeneities that enhance contours and fringes that correspond to isolated microdomains; furthermore, the topmost layer of the microstructured film surface reveals the formation of clusters in agreement with the above-mentioned AFM studies.

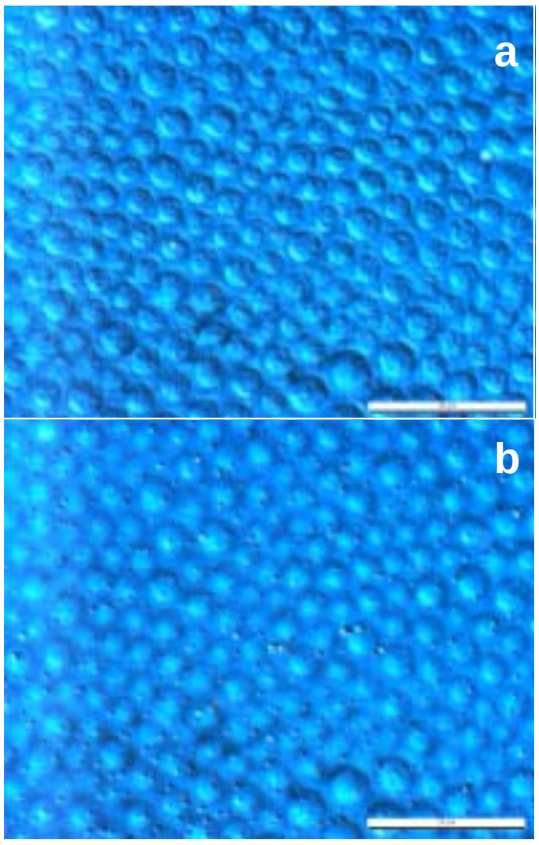

Figure 7. Differential interference contrast (Nomarski) micrographs: (a) microdomains are located in the surface close-lying sublayers as shown in (b) by the presence of clusters at the topmost layer corresponding to the surface. Scale bar is 25 μm.

Magnetic measurements were carried out to study the magnetic behavior and SMM properties. A series of stacked films corresponding to nanocomposite films were aligned parallel and perpendicular to the applied external magnetic field. Samples made up by casting and lately treated by solvent vapor exposure exhibit differencies in their magnetic behavior. Film casting evidenced a dense core of polymeric crystallites that grow in lateral dimensions as revealed by confocal optical microscopy. From the polymeric solution, chain folding mechanism is feasible and controls the crystallization process. The growth of crystalline structures imposes restrictions on the mobility of the amorphous phase with respect to the free polymeric solution. Moreover, the amorphous phase confined between neighbouring crystallites can achieve some degree of ordering by interaction with the crystal lattice. Thus, conformationally constrained chains induce a preferential alignment of the Mn_{12} molecules rather than in the liquidlike amorphous regions, where polycarbonate and Mn_{12} molecules are intimately packed together. Likewise, some Mn_{12} crystallites are observed to grow in lateral dimensions. As a consequence, hysteresis is observed when the external magnetic field is applied either parallel or perpendicular to the film surfaces. Magnetization hysteresis data (Figure 8) shows at 1.9 K a field of reversibility (point where at wich the curves obtained by scanning in each direction coincide) about 2 T and coercive field of a few hundred Oe. Remnant magnetization at zero field is 24% of the saturation value when the field is applied perpendicular, versus 15% parallel to the surface. The hysteresis loop can be understood by contribution of two-frequency-dependent peaks as observed in the ac magnetic susceptibility data. At 1.9 K the high-temperature species, i.e. higher effective potential barrier, is blocked while the low-temperature species remains

superparamagnetic and undergoes rapid relaxation near zero field. Frequency-dependent out-of-phase ac signals and hysteresis in the magnetization versus external field are seen for solid samples of complex **1**, which indicates that this complex behaves as a single-molecule magnet with a T_b value of 4–6 K and as a paramagnet at higher temperatures. A consistent magnetic behavior is observed for the same complex dispersed in thin films of polycarbonate, revealing SMM properties.

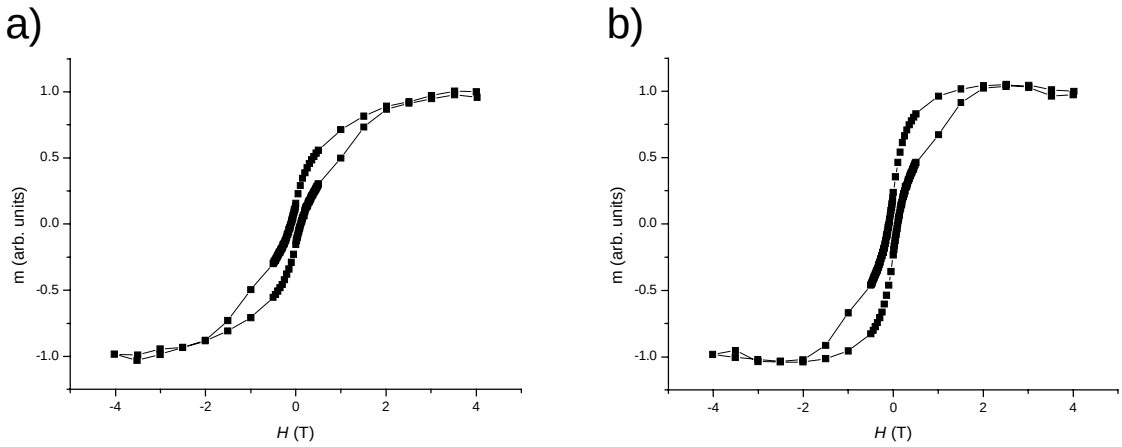

Figure 8. Hysteresis loops at 1.9 K of films containing 12 wt.-% in Mn_{12} when an external field is applied to the film surfaces, a) parallel, b) perpendicular.

Acknowledgment. This work was supported by the Information Society Technologies Programme of the European Commission, as part of the project NANOMAGIQC, and by EU NAIMO Integrated project No NMP4-CT-2004-500355.

(1) Tasi, H.-L.; Schindler, J. L.; Kannewurf, C. R.; Kanatzidis, M. G. *Chem. Mater.* **1997**, *9*, 875-878.

(2) Schubert, U. *Chem. Mater.* **2001**, *13*, 3487-3494 and references therein.

(3) Shir, F.; Yanik, L.; Bennett, L. H.; Della Torre, E.; Shull, R. D. *J. Appl. Phys.* **2003**, *93*, 8295-8297.

(4) Willemin, S.; Donnadieu, B.; Lecren, L.; Henner, B.; Clérac, R.; Guérin, C.; Meyer, A.; Pokrovskii, V.; Larionova. J. *New. J. Chem.* **2004**, *28*, 919-928.

(5) Clemente-León, M.; Soyer, H.; Coronado, E.; Mingotaud, C.; Gómez-García, C. J.; Delhaès, P. *Angew. Chem. Int. Ed.* **1998**, *37*, 2842-2845.

(6) Ruiz-Molina, D.; Mas-Torrent, M.; Gómez, J.; Balana, A. I.; Domingo, N.; Tejada, J.; Martínez, M. T.; Rovira, C.; Veciana, J. *Adv. Mater.* **2003**, *15*, 42-45.

(7) Castro, C.; Ramos, J.; Millán, A.; González-Calbet, J.; Palacio, F. *Chem. Mater.* **2000**, *12*, 3681-3688.

(8) Chudnovsky, E. M.; Tejada, J. *Macroscopic Quantum Tunneling of the Magnetic Moment*, Cambridge University Press, Cambridge **1998**. Del Barco, E.;Vernier, N.; Hernandez, J. M.; Tejada, J.; Chudnovsky, E. M.; Molins, E.; Bellesa, G. *Europhys. Lett***. 1999**, 47, 722-728.

(9) Cavallini, M.; Gómez-Segura, J.; Ruiz-Molina, D.; Massi, M.; Albonetti, C.; Rovira, C.; Veciana, J.; Biscarini, F. *Angew. Chem., Int. Ed.* **2005**, *44*, 888-892.

(10) Gómez-Segura, J.; Kazakova, O.; Davies, J.; Josephs-Franks, P.; Veciana, J.; Ruiz-Molina, D. *Chem. Commun.* (submitted).

(11) Rayleigh, L. *Nature*, **1911**, *86*, 416-417.

(12) Srinivasarao, M.; Collings, D.; Philips, A.; Patel, S. *Science* **2001**, *292*, 79-83.

(13) Thurn-Albrecht, T.; Steiner, R.; DeRouchey, J.; Stafford, C. M.; Huang, E.; Bal, M.; Tuominen, M.; Hawker, C. J.; Russell, T. P. *Adv. Mater.* **2000**, *12*, 787-791.

(14) Ruiz-Molina, D.; Gerbier, P.; Rumberger, E.; Amabilino, D. B.; Guzei, I. A.; Folting, K.; Huffman, J. C.; Rheingold, A.; Christou, G.; Veciana, J.; Hendrickson, D. N. *J. Mater. Chem.* **2002**, *12*, 1152-1161.

(15) Vrij, A.; Overbeek, J. Th. G. *J. Am. Chem. Soc.* **1968**, *90*, 3074-3078.

(16) Henn, G.; Bucknall, D. G.; Stamm, M.; Vanhoorne, P.; Jérôme, R. *Macromolecules* **1996**, *29*, 4305-4313.

(17) Song, R.; Fan, Q. *Eur. Polym. J.* **2000**, *36*, 1463-1470.

(18) Jonza, J. M.; Porter, R. S. *J. Polym. Sci, Polym. Phys.* **1986**, *24*, 2459-2472.

(19) Alizadeh, A.; Sohn, S.; Quinn, J.; Marand, H. *Macromolecules* **2001**, *34*, 4066-4078.

(20) Henrichs, P. M; Luss, H. R.; Scaringe R. P. *Macromolecules*, **1989**, *22*, 2731-2742 and references therein.

(21) Mysels, K.; Shinoda, K.; Frankel, S. *Soap films*; Pergamon: New York, **1959**. Exerowa, D.; Kruglyakov, P. M. *Foam and Foam Film: Theory, Experiment, Application*; Studies in Interface Science, V. 5; Elsevier: Amsterdam, **1998**. Toca-Herrera, J. L.; Krustev, R.; Müller, H.-J.; Möhwald, H. *Colloid Polym. Sci.* **2000**, *278*, 771-776.

(22) Di Luccio, M.; Nobrega, R.; Borges, C. P. *Polymer* **2000**, *41*, 4309-4315.

(23) Strobe, G. *The Physics of Polymers*; Springer: Heidelberg, **1997**, 188.

(24) Morgan, R. L.; Hill, M. J.; Barham, P. J. *Polymer* **1999**, *40*, 337-348.

(25) Matsushita, Y; Torikai, N; Mogi, Y.; Noda, I.; Han, C. C. *Macromolecules* **1993**, *26*, 6346-6349.

(26) Erdogan, B.; Song, L.; Wilson, J. N.; Park, J. O.; Srinivasarao, M.; Bunz, U. H. F. *J. Am. Chem. Soc.* **2004**, *126*, 3678-3679.

(27) Harron, H. R.; Pritchard, R. G.; Cope, B. C.; Goddard, D. T. *J. Polym. Sci, Polym. Phys.* **1996**, *34*, 173-180.

(28) Whitehouse, D. J. *Meas. Sci. Technol.* **1997**, *8*, 955-972.

Capítulo 4

Estudio en superficie de imanes unimoleculares

4.1. Introducción

Para poder crear sistemas de almacenamiento de información de alta densidad basados en imanes unimoleculares, así como su posible aplicación en el campo computacional cuántico, se requiere de nuevos estudios sistemáticos que permitan depositarlos de forma controlada en superficie generando bits de información magnéticos, ya sea en forma de moléculas individuales o bien agregados moleculares. Tal y como se muestra en el esquema cronológico adjunto, hasta 1998 no surge la primera aproximación referente a la deposición de clústeres de Mn_{12} en superficie.[1] Dicha metodología se basó en la denominada técnica Langmuir-Blodgett *(LB)*.[2] A pesar de que la técnica anterior había sido utilizada mayoritariamente para organizar moléculas orgánicas en superficie, su uso puede extenderse a clústeres inorgánicos[3] e incluso materiales sólidos dispuestos en capas extendidas.[4] En el caso de los imanes unimoleculares de Mn_{12}, en función de la relación composicional existente clúster:lípido, es posible la obtención de monocapas o moléculas aisladas de complejos de Mn_{12} insertadas entre las multicapas lipídicas, las cuales son transferibles a substratos hidrófobos *(Fig. 4.1)*.

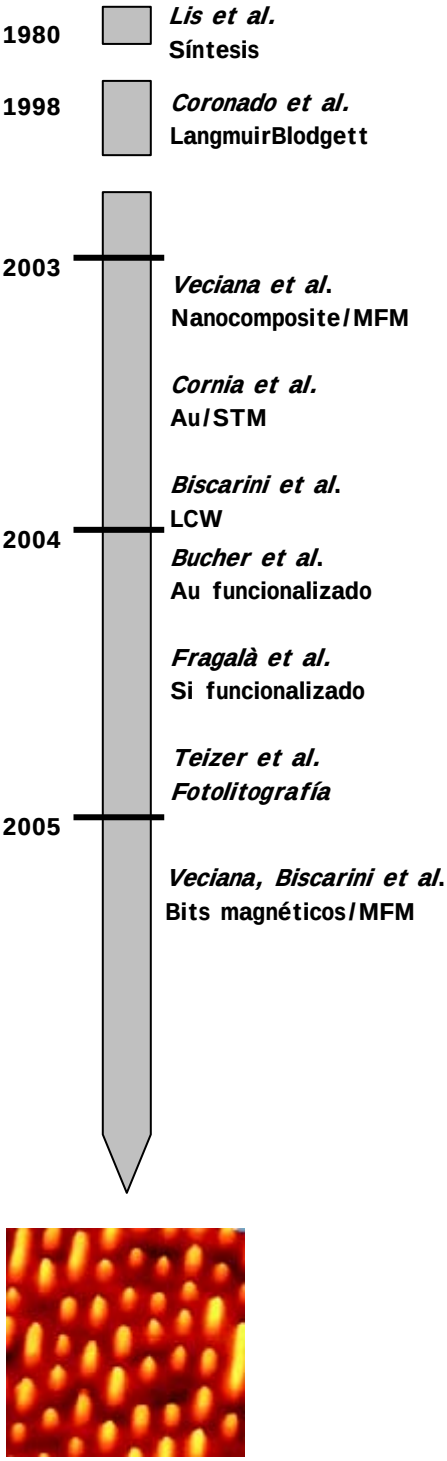

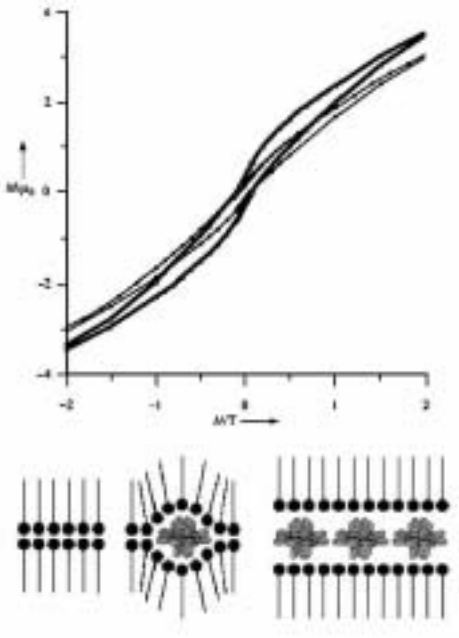

Fig. 4.1. Curvas de histéresis a 2K asociadas al aplicar un campo magnético externo *H* perpendicular o paralelo a la superficie de una película LB a elevada concentración de clústeres.

Cuando se inició la presente Tesis Doctoral, éste era el único trabajo que se había descrito en la literatura sobre el tema en cuestión, lo que demuestra la originalidad de los trabajos presentados. Después, muchas ocasiones en paralelo con los trabajos aquí presentados, se describieron otras aproximaciones en la bibliografía, todas ellas utilizando imanes unimoleculares de Mn_{12} *(ver esquema cronológico previo)*. Una gran parte de esos trabajos han implicado la deposición en substratos conductores de Au. Las moléculas de Mn_{12} no presentan a priori afinidad para adherirse a su superficie y por consiguiente es necesario funcionalizar las cadenas orgánicas periféricas con grupos afines tioles[5] o tioéteres[6] mediante el diseño de carboxilatos intercambiables en la esfera de coordinación. De esta manera, la observación directa de moléculas individuales de Mn_{12} se hace factible en superficie *(Fig. 4.2)*. Sin embargo, su detección por STM precisa trabajar con cantidades muy diluidas de material y su caracterización magnética requiere de técnicas complejas tales como espín-polarizado STM[7] o efecto Kerr magneto-óptico.[8] Posteriormente, otras estrategias de deposición situadas ya en el 2004 se han basado en la modificación directa de la superficie de Au(111)[9] o Si(100)[10] mediante una capa orgánica de moléculas doblemente funcionalizadas. De esta manera, las moléculas orgánicas actúan como puente a través de su enlace directo con el substrato *(Au-S)* y la coordinación a los complejos de Mn_{12} por intercambio de carboxilatos.

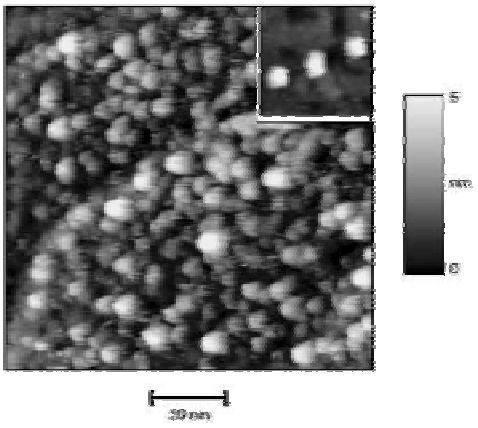

Fig. 4.2. Imagen STM de clústeres de Mn_{12} enlazadas a Au formando capas desordenadas. La imagen insertada muestra posibles moléculas aisladas en superficie.

La mayor parte de esos trabajos han implicado la funcionalización de los complejos de Mn_{12} con el carboxilato adecuado para favorece su adhesión, por ejemplo con grupos tiol, o viceversa, y funcionalización de la superficie con tioles que tengan grupos carboxilato externos capaces de actuar con los complejos de Mn_{12} *(ver Esquema 1)*. Sin embargo, en las aproximaciones utilizadas en la presente Tesis Doctoral no se han funcionalizado las moléculas de Mn_{12}. De esta manera, además de simplificar el proceso, se evita la aparición de inestabilidades químicas y térmicas en las moléculas. Para ello, en la deposición molecular nos hemos ayudado de técnicas de autoensamblaje, con un balance de interacciones hidrófilas/hidrófobas adecuado, muchas veces asistido mediante técnicas litográficas que favorecen una estructuración en la superficie. A continuación se describirán las diferentes metodologías experimentales utilizadas, prestándose especial atención al final del capítulo a la microscopia de fuerzas magnéticas *(MFM)*, que ha sido implementada para la caracterización de los sustratos moleculares.

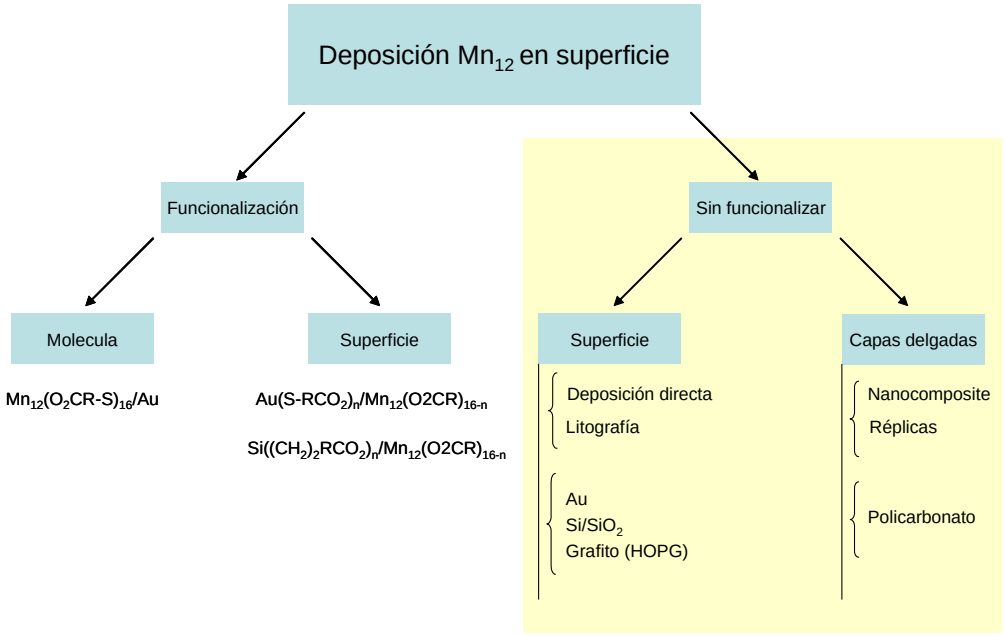

Esquema 1

4.2. Deposición controlada de imanes unimoleculares en disolución sobre diversos substratos

4.2.1. Método "Breath-Figures"

La metodología utilizada para la estructuración de imanes unimoleculares en sistemas poliméricos fue desarrollada mediante la técnica de "*breath-figures*" en el Capítulo 3. En el presente trabajo ha sido utilizada de nuevo para obtener anillos magnéticos de Mn_{12} sobre una superficie de grafito. Estos trabajos se realizaron en colaboración con el Dr. Patrick Josephs-Franks del *National Physical Laboratory (NPL)* de Londres.

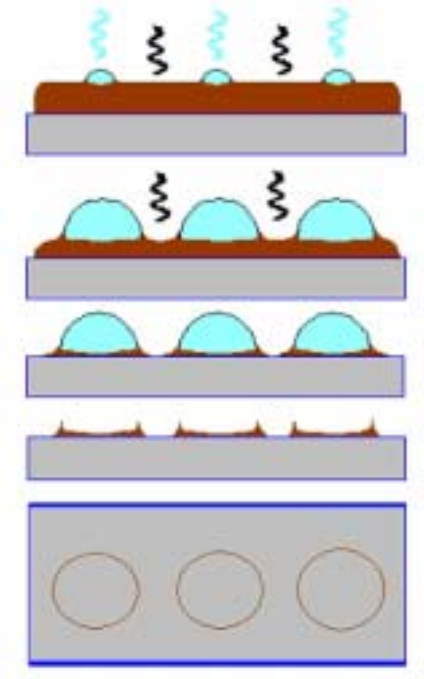

Esta aproximación, es novedosa no tan sólo en el uso de imanes unimoleculares sino también con otros sistemas moleculares orgánicos. Para ello, una disolución de $[Mn_{12}O_{12}(O_2CC_{12}H_9)_{16}(H_2O)_4]$ *(20)* es expuesta en contacto con una atmósfera húmeda *(humedad relativa>50%)*. El uso del compuesto **20** se justifica dado que presenta una alta interacción intermolecular a través de los anillos aromáticos periféricos además de conferir al entorno de la molécula un marcado comportamiento hidrófobo.

El mecanismo de formación de los anillos se representa esquemáticamente en la Figura 4.3.

Fig. 4.3. Representación esquemática del proceso de enfriamiento evaporativo en presencia de atmósfera húmeda. La disolución se confina estratégicamente en las zonas alrededor de las gotas condensadas generando depósitos sólidos.

Tal y como se describe en dicha figura, el uso de CH_2Cl_2 como disolvente orgánico, favorece la condensación y crecimiento de núcleos de agua en la superficie durante el proceso de evaporación. Si la evaporación de la disolución inicial se lleva a cabo sobre un substrato hidrófobo, como es el grafito *(HOPG)*, las gotas se mantendrán en superficie de forma que en el último estadio de evaporación del disolvente, la disolución se confina a través de la formación de meniscos, alrededor de las gotas de agua *(ver Fig. 4.3)*. La aparición de fuerzas capilares en su entorno localiza estratégicamente las moléculas de soluto dando lugar a la formación de anillos magnéticos en superficie. A diferencia del uso de disoluciones poliméricas, las moléculas de Mn_{12} se disponen de acuerdo con el perímetro de la gota en contacto con la superficie, permitiendo obtener estructuras de anillo con dimensiones a escala nanométrica, tal y como se puede obervar en las imágenes de Microscopia de Fuerzas Atómicas *(AFM)* que se muestra en la Figura 4.4. Hay que destacar que esta metodología sólo funciona en el caso de superficies hidrófobas como el caso de HOPG, y no en el caso de otras superficies polares como el SiO_x. Una posible explicación es que en el último caso las gotas de agua mojan mejor la superficie debido a su carácter hidrófilo.*

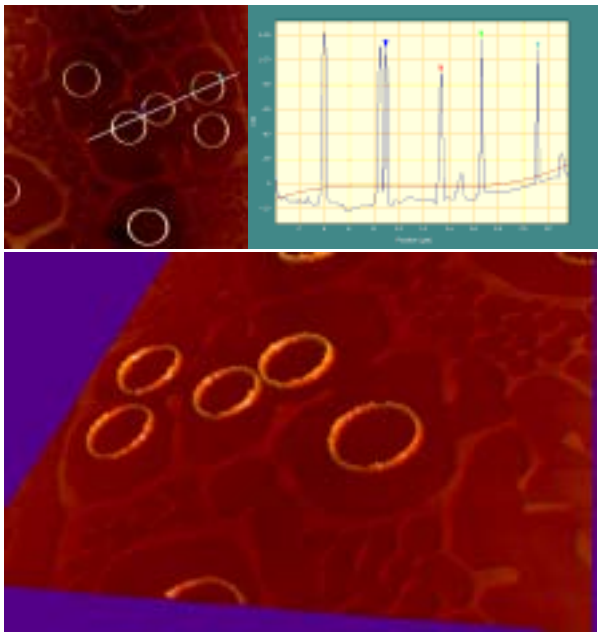

Fig. 4.4. Imagenes AFM mostrando la formación de anillos magnéticos por efecto plantilla inducidos a través de la condensación de vapor de agua en la superficie de una película líquida de disolución de Mn_{12}.

Esta técnica permite cierto control sobre el tamaño de los patrones circulares. Dependiendo del tiempo de interacción entre las gotas y el tiempo requerido por los vapores del disolvente a escapar entre los espacios intersticiales, se generará un mayor o menor grado de coalescencia entre las gotas de agua, permitiendo controlar su crecimiento. Sin embargo, la ausencia de un control posicional en superficie tienen su origen durante la etapa final de evaporación o secado. Si bien el uso de una matriz polimérica circundante permite fosilizar el proceso de condensación, en la deposición directa el frente de recesión de la capa de disolvente residual se ve perturbado en función de la rugosidad característica de la superficie y la presencia de defectos, generando heterogeneidades en su disposición espacial. Por ello se buscaron

* Para más información ver artículo K

metodologías alternativas que permitieran no tan sólo un control sobre la morfología sino también sino también su estructuración sobre la superficie.

4.2.2. Deposición asistida mediante técnicas litográficas

La formación de patrones moleculares de Mn_{12} en superficie, con control posicional y de tamaño, se consiguió mediante la deposición asistida por un sello auxiliar externo *(Fig. 4.5)*. Este trabajo se ha realizado en colaboración con el Dr. Fabio Biscarini del *Institute for Nanostructured Materials Studies* de Bolonia.

El sello, con superficie estructurada, se deposita en contacto sobre una fina película líquida de disolución previamente extendida sobre la superficie de un substrato *(1)*. A medida que el disolvente se evapora, la disolución se concentra en las protuberancias del sello por capilaridad dejando las zonas intermedia exentas de disolución *(2)*. Alcanzada la concentración crítica a una distancia sello-substrato *(d)* determinada, las moléculas de Mn_{12} comienzan a precipitar reproduciendo exactamente la replica positiva del sello. Llegado este punto, las moléculas se reorganizan según el balance competitivo entre las fuerzas de interacción molécula-superficie e intermoleculares. Dependiendo de la afinidad con la superficie dichas moléculas se disponen en forma de dominios esféricos moleculares aislados, cuando tenemos una superficie hidrófila como el SiO_X o bien hilos moleculares donde se encadenan moléculas aisladas *(Fig. 4.5, parte inferior derecha)* en el caso de una superficie hidrófoba como el grafito.[†]

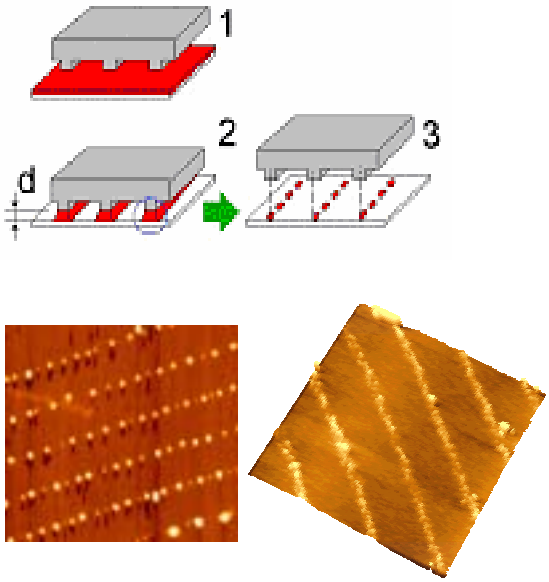

Fig. 4.5. Representación esquemática de la litografía en disolución de Mn_{12} en superficie dando lugar a dominios esféricos moleculares aislados o bien monocapas.

Dos son los posibles mecanismos para la formación de los motivos anteriores:

1) *Ruptura de una película delgada líquida*.[11] Dicha ruptura puede ser conducida mediante la nucleación y crecimiento de agujeros[12] o bien mediante fluctuaciones en la superficie de la disolución activados térmicamente *(Fig. 4.6)*.[13]

[†] Para más información ver artículo L

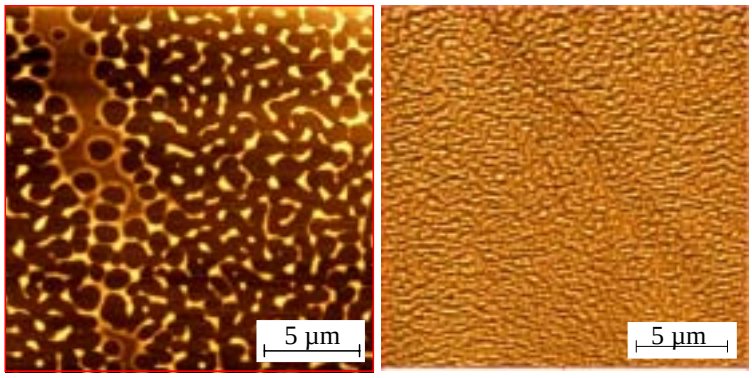

Fig. 4.6. Imágenes de AFM mostrando el resultado de una ruptura de una película delgada líquida mediante los mecanismos de nucleación de agujeros *(iz.)* y mediante fluctuaciones activadas térmicamente en superficie *(der.)*.

La energía de activación requerida para generar un agujero depende proporcionalmente de la tensión superficial y el espesor de la película. La tensión superficial tiende a mantener la superficie *(Fig. 4.7)* de la película líquida lo más plana posible *(1)*, minimizando al máximo la energía de Gibbs asociada. Sin embargo, las fuerzas intermoleculares favorecen por el contrario la desproporcionación de la película líquida originando a lo largo de la película líquida zonas de espesor variable *(2)*. Como consecuencia, se genera un flujo capilar que transporta moléculas desde zonas de menor a mayor espesor.[14] Finalmente, el resultado de su ruptura conlleva a la formación de núcleos aislados *(3)* cuyo tamaño final vendrá determinado según la distancia inicial entre el sello y el substrato. [15]

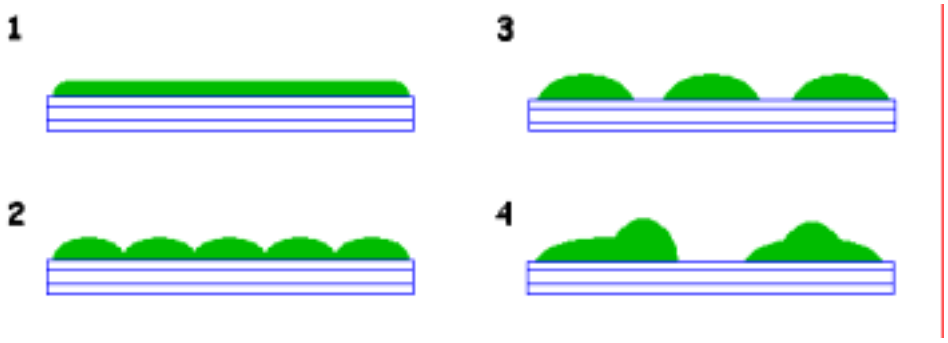

Fig. 4.7. Representación esquemática de la ruptura de una película líquida inicial en dominios aislados y posterior agregación.

2) *Nucleación y crecimiento en régimen parcial de afinidad con el substrato*.[16] Los dominios moleculares esféricos formados en superficie son el resultado de la nucleación y posterior agregación a través de zonas de captura en el entorno de interacción de cada núcleo formado. Los núcleos con mayor tamaño crecerán a expensas de los más pequeños, proceso que cesa en el momento en que los núcleos alcanzan un mismo tamaño y distancia de equilibrio.

4.3. Sistemas moleculares sobre películas delgadas poliméricas

En estos trabajos, el objetivo era conseguir la deposición controlada de los imanes unimoleculares sobre substratos poliméricos. El soporte polimérico, además de proporcionar una base flexible, manejable y con buenas propiedades mecánicas, se espera que estabilice los dominios moleculares sobre la superficie. Para ello, se

seleccionó como polímero el policarbonato, dado que sus propiedades han sido ampliamente estudiadas y de hecho ya se utiliza como soporte en muchos medios de grabación magnética comerciales. Como imán unimolecular se seleccionó una vez más el complejo **20** dada su gran estabilidad térmica y sobre todo su elevado tamaño molecular, lo que facilita su detección mediante AFM. Los trabajos se realizaron en colaboración con el Prof. Javier Tejada de la Universidad de Barcelona. La estructura molecular del compuesto **20**, donde se manifiesta sus considerables dimensiones, se muestra en la Figura. 4.8.

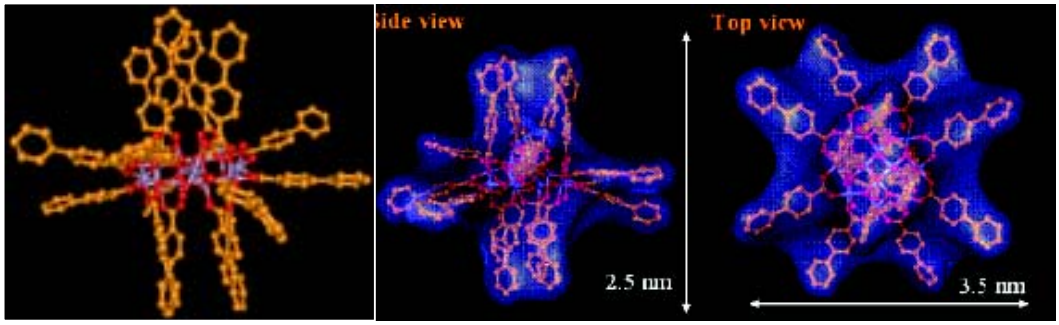

Fig. 4.8. Estructura molecular del complejo de Mn_{12} **20** mostrando el núcleo central de átomos metálicos de Mn (lila) en disposición discoidal. El eje uniaxial se sitúa normal al plano que contiene los 8 carboxilatos periféricos 4-fenil-benzoato.

La preparación de películas delgadas de nanocomposite consta de dos etapas diferenciadas *(Fig. 4.9):*

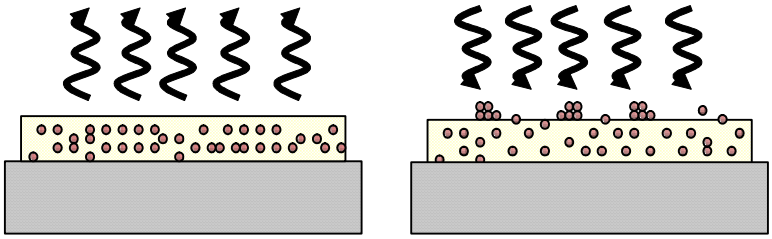

Fig. 4.9. Preparación de las películas de nanocomposite por evaporación del disolvente (etapa 1); tratamiento a vapores de disolvente y migración a superficie de moléculas (etapa 2).

1)Formación de la película polimérica con moléculas dispersas de Mn_{12}

Inicialmente se prepara una disolución del polímero con una concentración determinada de moléculas de Mn_{12} en una disolución de *o*-diclorobenceno y se deposita sobre una superficie plana. Una vez se evapora el disolvente, se forma una película delgada de unas pocas micras, donde las moléculas de Mn_{12} inicialmente están dispersas dentro de la matriz polimérica. No obstante, el estudio en superficie mediante AFM revela la formación de dominios moleculares de Mn_{12} que se encuentran aislados entre sí mediante la matriz polimérica circundante. La nucleación y crecimiento de estos dominios se produce directamente en la interfase película-gas, cuyo estado de

agregación depende de la composición inicial de la disolución polimérica. Sin embargo, el crecimiento de las alturas y anchuras medias de los dominios no muestran un mismo comportamiento. De esta manera, los dominios muestran un crecimiento en altura hasta alcanzar valores estables correspondientes a la altura topográfica de una o dos moléculas de Mn_{12}. Este fenómeno se observa incluso a bajas concentraciones de moléculas de Mn_{12} dispersas en la matriz polimérica de policarbonato *(<4% en peso)*. Sin embargo, el crecimiento progresivo mostrado, en cuanto a las anchuras medias se refiere, controla la forma final de los agregados magnéticos en superficie dando lugar a estructuras extendidas a medida que se incrementa la composición. Cabe esperar por consiguiente un compendio de interacciones afines molécula-superficie además de las interacciones intermoleculares π-π entre los ligandos fenilo periféricos. El comportamiento descrito anteriormente se muestra representado en la Figura 4.10 en forma de histogramas.

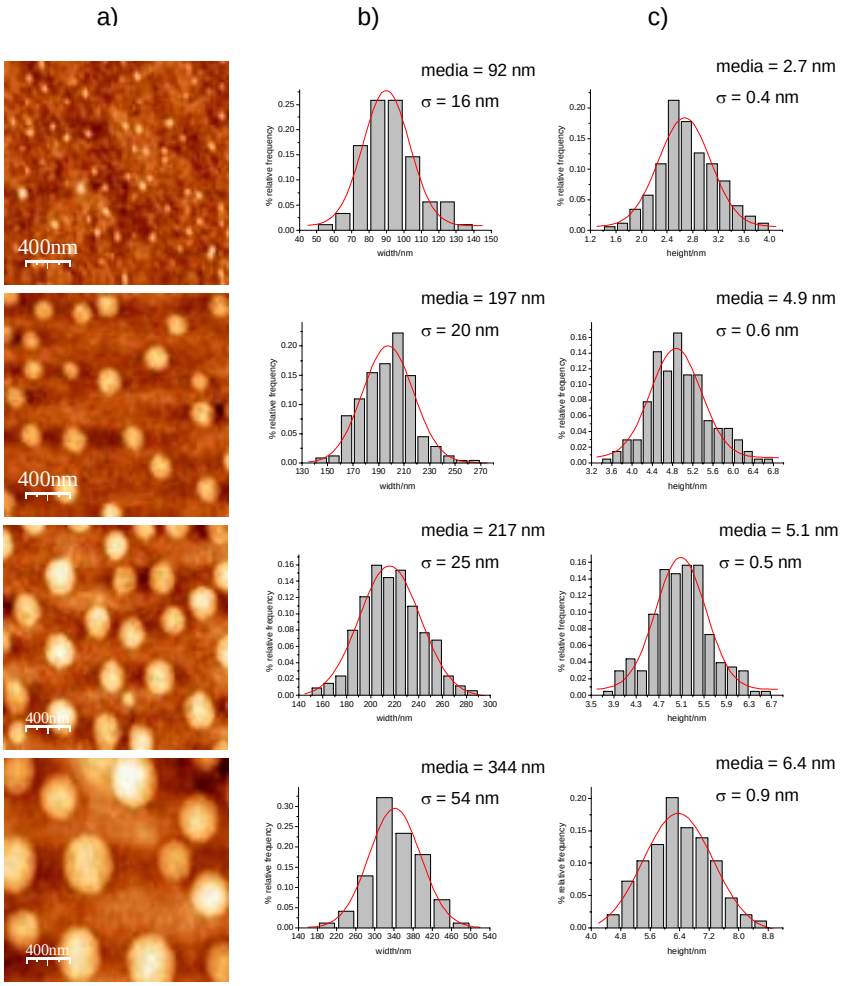

Fig. 4.10. a) Imágenes de AFM sobre una superficie de 2x2 μm en películas de policarbonato al 1, 8, 12 y 24 % en peso de Mn_{12} y sus correspondientes histogramas respecto a las anchuras (b) y alturas (c) de pico.

2)Tratamiento a vapores de disolvente orgánico

Además de esa pequeña fracción de moléculas que salen espontáneamente a la interfase polímero-gas, las moléculas también pueden ser conducidas a la superficie mediante

exposición controlada a pequeñas cantidades de vapores de disolvente. En un primer estadio, los vapores penetran a través de la matriz mediante un proceso de hinchamiento de la red polimérica. El marcado aumento de porosidad e interconexión de canales generados por el hinchamiento de la red polimérica dan lugar a una vía de migración de las moléculas hacia las capas más superficiales. De esta manera, la caracterización en superficie a través de técnicas por AFM, revela la formación de dominios moleculares aislados mediante la matriz polimérica y cuyo estado de agregación depende en gran parte de la naturaleza del disolvente utilizado *(Fig. 4.11)*.[‡] Un ejemplo básico lo componen las mezclas de hexano/CH_2Cl_2. A medida que se aumenta la proporción de CH_2Cl_2, disolvente en el que la molécula de Mn_{12} muestra elevada solubilidad, el perfil topográfico de los agregados disminuye en altura hasta alcanzar el tamaño de una única molécula aislada.

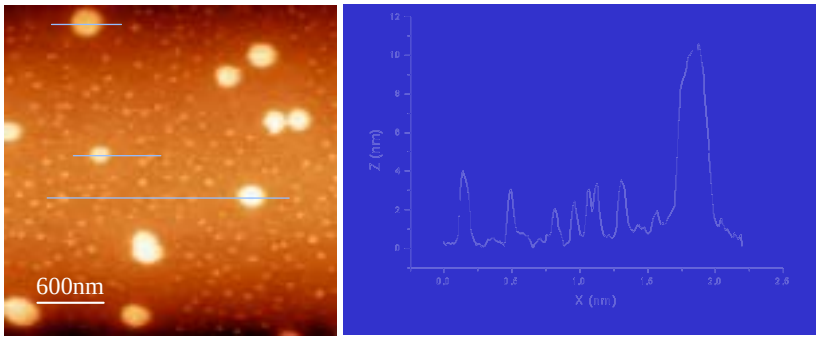

Fig. 4.11. Imágen de AFM correspondiente a películas de nanocomposite tratadas con mezcla de disolvente hexano/ CH_2Cl_2 (1:3).

Finalmente, hay que destacar que para concentraciones inferiores al 4%, la exposición a vapores genera estructuras fibrilares atribuidas a la interacciones π intermoleculares entre los grupos fenilo periféricos. A medida que aumenta el tiempo de exposición los fenómenos de coalescencia disminuyen la densidad de población en superficie *(Fig. 4.12)*, favoreciendo la agregación.

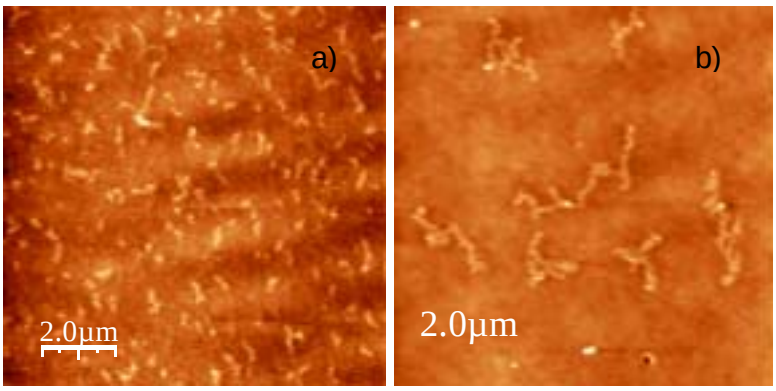

Fig. 4.12. Imágenes AFM sobre una superficie 2x2 µm correspondiente a una película delgada Mn_{12}-policarbonato al 8% en peso; a) deposición directa en superficie; b) tratamiento a vapores de disolvente puro *(CH_2Cl_2)* en *(a)* durante 3 minutos de exposición a 27±1 °C.

[‡] Para más información ver artículo M

4.4. Ordenamiento de los imanes unimoleculares en películas delgadas asistido mediante técnicas litográficas

Esta última metodología es una combinación de las descritas anteriormente, es decir, moléculas sobre películas poliméricas delgadas y técnicas litográficas en superficie *(Fig. 4.13a)*. Estos trabajos fueron realizados en colaboración con el Dr. Fabio Biscarini del *Institute for Nanostructured Materials Studies* de Bolonia.

Tal y como se muestra en la Figura 4.13, la variación consiste en depositar la disolución con la mezcla de polímero y moléculas directamente sobre un substrato estructurado. La película de nanocomposite resultante corresponderá en este caso a la réplica invertida del molde. Para evitar imperfecciones, es preciso que la superficie estructurada del nanocomposite no se vea dañada durante el proceso de separación con el molde. Para ello, el conjunto molde-réplica se sumerge en un baño de agua que actúe de no solvente. Durante la solidificación de la película polimérica en su estado líquido, el polímero se encoge sobre el substrato,[17] dando lugar a pequeñas cavidades situadas entre la interfase de contacto molde-replica.[18] La entrada progresiva de agua por capilaridad favorece así la separación de la réplica evitando el uso de técnicas agresivas.

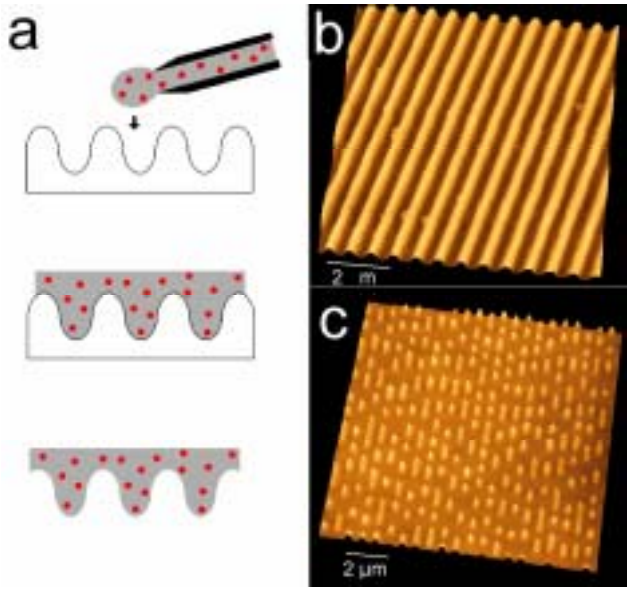

Fig. 4.13. a) Representación esquemática del proceso experimental de formación de réplicas por moldeo a partir de disoluciones poliméricas de Mn_{12}; b) Réplica de un DVD virgen; c) DVD grabado mostrando la secuencia de bits de información.

Posteriormente, la superficie estructurada de la réplica es expuesta a vapores de disolvente para facilitar la migración de moléculas de Mn_{12} hacia la superficie. La solvatación de las cadenas poliméricas y el descenso de la temperatura de transición vítrea asociada al polímero origina la erradicación progresiva de la estructuración inducida tras la etapa de moldeo. De esta manera, la energía de Gibbs asociada a la superficie se ve estabilizada a través de la disminución de área superficial. Las protuberancias iniciales en la superficie de la réplica corresponden a zonas de mayor espesor y por consiguiente contienen un mayor número de moléculas de Mn_{12} dispersas. Además, durante el proceso de relajación, las moléculas muestran una difusión lateral en el plano restringida, dando lugar a un gradiente de concentración en superficie que reproduce de forma exacta la topografía inicial de la réplica. Un esquema simbólico del proceso anteriormente descrito se muestra en la Figura 4.14 mientras que las imágenes

de AFM experimentales de una réplica de DVD expuesta a disolvente se muestra en la Figura 4.15. Los resultados de este trabajo, pioneros en el campo del magnetismo molecular, permiten controlar posicionalmente el gradiente de concentración de moléculas de Mn_{12} sobre superficies poliméricas y abre una vía hacia el desarrollo de *memoria magnética* permanente a nivel molecular.[§]

Fig. 4.14. Representación esquemática del proceso de agregación de Mn_{12} por exposición a vapores de disolvente.

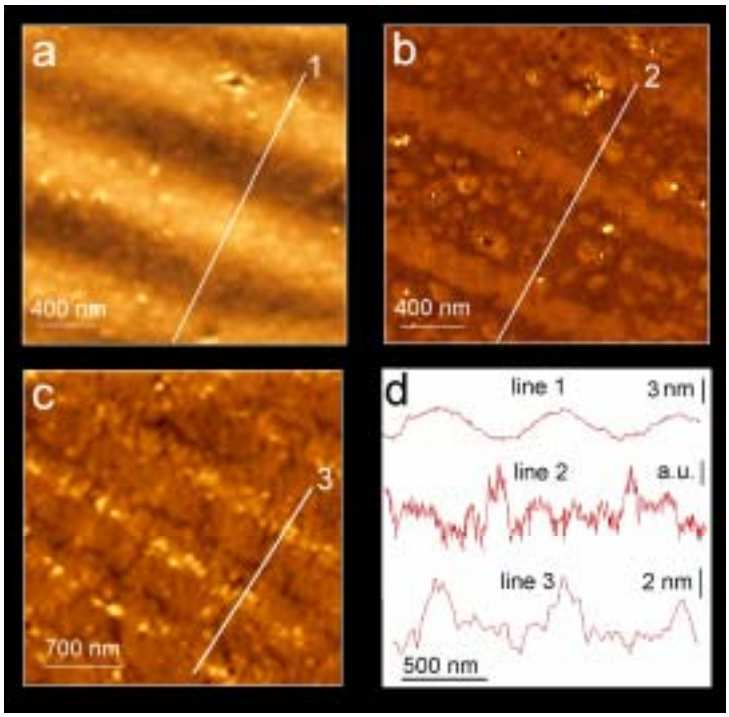

Fig. 4.15. a) Réplica de un DVD no grabado después de una exposición de 2 minutos *(a)* y 3 minutos *(c)* a vapores de CH_2Cl_2. La imagen *(b)* corresponde a los cambios de fase en la frecuencia de vibración del cantilever respecto a la topografía en *(a)*. Los perfiles 1, 2 y 3 se representan en *(d)*.

4.5. Microscopia de fuerzas magnéticas

El almacenamiento de alta densidad de información implica que la escritura de bits se corresponda con el mínimo tamaño de dominio magnético estable. En base a estas observaciones, nos proponemos por primera vez detectar magnéticamente imanes unimoleculares de Mn_{12} depositados en una superficie. Así, a continuación se describe

[§] Para más información ver artículo N

el estudio de técnicas de detección magnética de dichos sistemas moleculares mediante MFM. No obstante, hay que destacar que si bien los materiales utilizados habitualmente mediante dicha técnica muestran un comportamiento ferromagnético o ferrimagnético a temperatura ambiente, los imanes unimoleculares se comportan como un superparamagneto a temperatura ambiente, lo que a priori supone una complicación para su estudio.

La microscopia de fuerzas magnéticas se desarrolló por primera vez en el año 1987 con la idea de medir fuerzas magnéticas mediante un microscopio de fuerzas atómicas.[19-21] Desde entonces, se ha convertido en una técnica microscópica de gran utilidad en el estudio de una amplia gama de fenómenos magnéticos a nivel local, permitiendo por ejemplo la visualización directa de dominios magnéticos. La obtención de imágenes corresponde a un gradiente de campo magnético y su distribución en superficie mediante la medida de la variación de la fuerza de interacción entre la punta *(magnética gracias a un recubrimiento de cobalto)* y el campo magnético local.[22] El hecho de que dichas interacciones predominen sobre las topográficas, dependerá de la distancia entre la punta y la superficie, ya que las fuerzas magnéticas persisten a mayor distancia que las fuerzas de van der Waals. Si la punta se encuentra a una altura cercana a la superficie, en la región donde se opera de forma estándar con el AFM en modo no contacto *(fuerzas de interacción atractivas)*, la imagen será predominantemente topográfica debido a las fuerzas de van der Waals a corto alcance. Adquiriendo una serie de imágenes a diferentes distancias es posible separar los efectos topográficos hasta obtener imágenes puramente magnéticas.

Así, los estudios de MFM sobre los imanes unimoleculares de Mn_{12} depositados en superficies se realizaron en dos etapas bien diferenciadas. En primer lugar se obtiene la imagen topográfica en modo semicontacto, detectando un gradiente de fuerza que contiene información sobre la estructura de la superficie y el campo magnético local. Posteriormente, el cantilever se separa progresivamente de la superficie y se traza en altura el perfil de la topografía obtenida previamente a la misma frecuencia de resonancia. De esta manera se separan las contribuciones de la fuerza de van der Waals a corto alcance de la fuerza magnética, la cual persiste a larga distancia.

En la Figura 4.16 se muestra la imagen de topografía por AFM *(primer barrido)* y el correspondiente contraste magnético de los anillos magnéticos descritos en el apartado 4.2.1. Tal y como se puede observar, incluso a 300 nm existe un claro contraste de fase que se atribuye primordialmente a la presencia de interacciones dipolares. Aunque a temperatura ambiente y en régimen paramagnético las moléculas de Mn_{12} no poseen un ordenamiento preferencial del momento magnético en ausencia de campo magnético externo, al aproximar la punta, ésta actúa como un dipolo magnético capaz de magnetizar las moléculas individuales. Como consecuencia, las moléculas tienden a ordenar sus momentos magnéticos durante su trazado por líneas de la superficie lo que sin duda contribuye a una mejor observación y contraste magnético. Este hecho fue corroborado mediante la utilización de puntas convencionales de Si utilizadas para AFM. Tras distanciarse la punta 50 nm por encima de la topografía inicial, los efectos topográficos se desvanecen mientras que no se observa contraste de fase adicional. Sin embargo, mediante el uso de la punta de Co la imagen de la fase muestra un claro contraste entre 50-300 nm claramente atribuibles a fuerzas de largo alcance *(Fig. 4.16)*. Además, el contraste magnético se ve favorecida por el entorno diamagnético, es decir, la superficie de grafito que rodea los anillos.

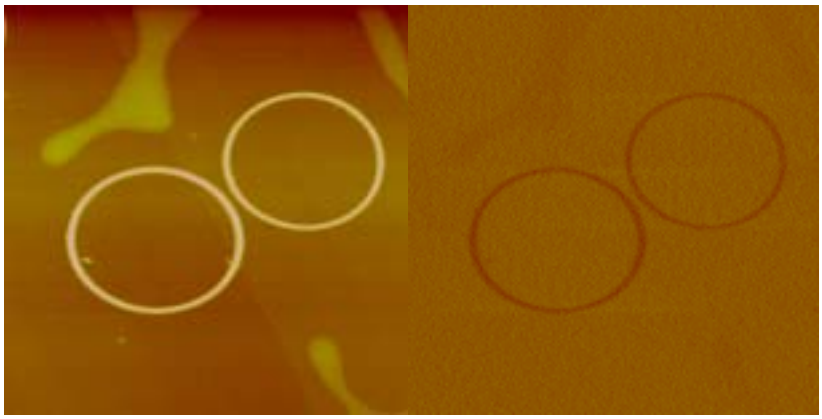

Fig. 4.16. Imagen de AFM topográfica *(iz.)* y su correspondiente contraste magnético en la fase *(der.)* a una separación de 300 nm sobre la topografía inicial en substrato de HOPG.

El estudio de caracterización magnética por MFM también se realizó sobre superficies poliméricas que contienen los complejos de Mn_{12}. En concreto se realizó el estudio sobre algunas películas poliméricas descritas en los apartados 4.3 y 4.4. Por ejemplo, la imagen de AFM y la correspondiente imagen de MFM de una superficie de una película delgada que contiene Mn_{12} al 4% se muestran en la Figura 4.17. Tal y como se demuestra una vez más, existe una muy buena concordancia entre lo que sería el perfil topográfico y el perfil magnético, lo que pone en evidencia la viabilidad de esta técnica para detectar el momento magnético de agregados moleculares. No obstante hay que enfatizar que el contraste magnético sólo se observa para agregados moleculares de tamaños considerables donde existen un gran número de moléculas, y por lo tanto, una mayor respuesta magnética.

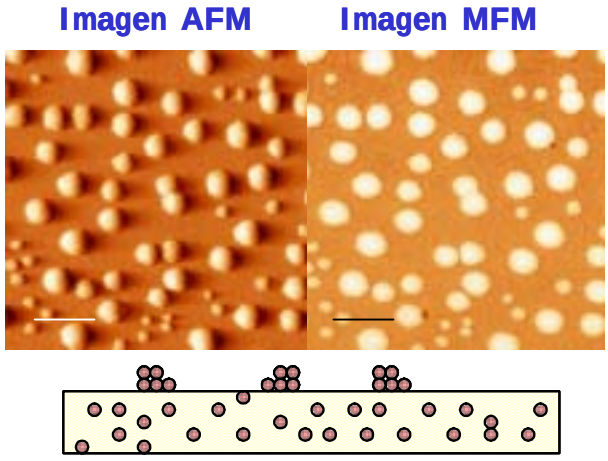

Fig. 4.17. Imágenes de AFM y MFM correspondiente a películas de nanocomposite tratadas con mezcla de disolvente CH_2Cl_2/hexano (1:1).

Finalmente y siguiendo la metodología descrita en el apartado *(4.4)*, una película de nanocomposite correspondiente a una réplica de un DVD grabado fue preparada. Dicha réplica consiste *(Fig. 4.18)* en una serie alineada de dominios topográficos de distinta

longitud *(d)* en función de la secuencia digital codificada *(c)*. La exposición a vapores de disolvente permite erradicar el perfil inicial de 125 nm de altura hasta obtener una superficie prácticamente plana *(a)* con una rugosidad media inferior al nanómetro de altura. De esta manera, los efectos topográficos se ven minimizados al máximo sin interferir posteriormente en la señal magnética detectada por MFM. Para ello, se utilizó una punta recubierta de Co separada de la superficie al menos 50 nm de altura. La imagen magnética obtenida *(b)* cuyo perfil topográfico se muestra en *(f)*, permite resolver con una relación señal ruido de 2:1 la secuencia de bits de información acorde con la topografía *(e)*. Por consiguiente, el MFM permite la detección a temperatura ambiente de agregados en superficie basados en imanes unimoleculares de Mn_{12} en forma de memoria permanente. Independientemente a su baja temperatura de bloqueo, su identificación en régimen paramagnético se atribuye al contraste magnético obtenido respecto a la naturaleza diamagnética de la matriz polimérica. La técnica es por lo tanto aplicable a otras substancias paramagnéticas tales como los radicales orgánicos libres.

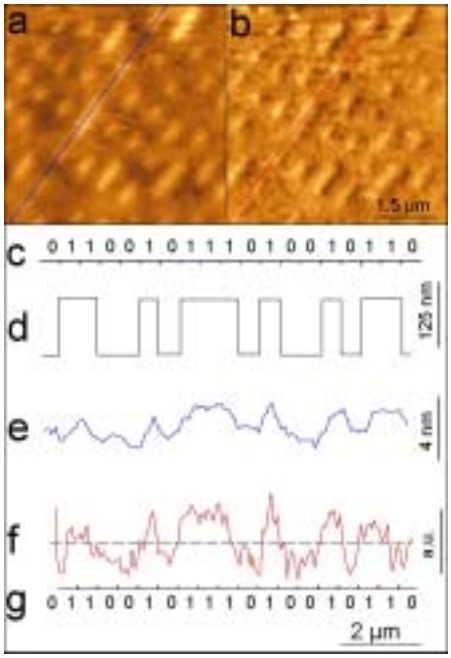

Fig. 4.18. Imágenes de AFM (a) y su correspondiente contraste magnético en la imagen de fase (b) sobre la superficie de películas delgadas de nanocomposite policarbonato-Mn_{12}.

4.6. Referencias

1. M. Clemente-León, H. Soyer, E. Coronado, C. Mingotaud, C. J. Gómez-García, P. Delhaès, *Angew. Chem. Int. Ed.*, **1998**, *37*, 2842.
2. A. Ulman, *An introduction to Ultrathin Organic Films: From Langmuir-Blodgett to Self-Assembly*, Academic Press, Boston, **1991**.
3. M. Clemente-León, C. Mingotaud, B. Agricole, C. Gómez-García, E. Coronado, P. Delahès, *Angew. Chem.*, **1997**, *109*, 1143; *Angew. Chem. Int. Ed. Engl.*, **1997**, *36*, 1114.
4. C. T. Seip, G. E. Granroth, M. W. Meisel, D. R. Talham, *J. Am. Chem. Soc.* **1997**, *119*, 7084.
5. A. Cornia, A. C. Fabretti, M. Pacchioni, L. Zobbi, D. Bonacchi, A. Caneschi, D. Gatteschi, R. Biagi, U. Del Pennino, V. De Renzi, L. Gurevich, H. S. J. Van der Zant, *Angew. Chem. Int. Ed.*, **2003**, *42*, 1645.
6. S. Phark, Z.G. Khim, B.J. Kim, B.J. Suh, S. Yoon, J. Kim, J.M. Lim, Y. Do, *Jpn. J. Appl. Phys.*, **2004**, *43*, 8273.
7. S. Heinze, M. Bode, A. Kubetzka, O. Pietzsch, X. Nie, S. Blügel, R. Wiesendanger, *Science*, **2000**, *288*, 1805.
8. W. J. Geerts, B. Donehew, V. Williams, T. Schmiedel, *Rev. Sci. Instrum.*, **2002**, *73*, 2086.
9. A. Nait Abdi, J.P. Bucher, P. Rabu, O. Toulemonde, M. Drillon, Ph. Gerbier, *J. Appl. Phys.*, **2004**, *95*, 7345.
10. G.G. Condorelli, A. Motta, I. L. Fragalà, F. Giannazzo, C. Raineri, A. Caneschi, D. Gatteschi, *Angew. Chem., Int. Ed.*, **2004**, *43*, 4081.
11. G. Reiter, *Langmuir*, **1993**, *9*, 1344.
12. R. Seemann, S. Herminghaus, K. Jacobs, *Phys. Rev. Lett.* **2001**, *86*, 5534.
13. R. Xie, A. Karim, J. F. Douglas, C. C. Han, R. A. Weiss, *Phys. Rev. Lett.* **1998**, *81*, 1251.
14. G. Henn, D. G. Bucknall, M. Stamm, P. Vanhoorne, R. Jérôme, *Macromolecules*, **1996**, *29*, 4305.
15. A. Vrij, J. Th. G. Overbeek, *J. Am. Chem. Soc.*, **1968**, *90*, 3074.
16. D. Beysens, C. M. Knobler, *Phys. Rev. Lett.*, **1986**, *57*, 1433.
17. C. Castro, J. Ramos, A. Millán, J. González-Calbet, F. Palacio, *Chem. Mater.* **2000**, *12*, 3681.
18. C. Stropnik, V. Musil, M. Brumen, *Polymer*, **2000**, *41*, 9227.
19. G. Binning, C.F. Quate, C. Gerber, *Phys. Rev. Lett.*, **1986**, *56*, 930.
20. Y. Martin, H.K. Wickramasinghe, *Appl. Phys. Lett.*, **1987**, *50*, 1455.
21. J.J. Sáenz, N. García, P. Grütter, E. Meyer, H. Heinzelmann, R. Wiesendanger, L. Rosenthaler, H.R. Hidber, H.-J. Güntherodt, *J. Appl. Phys.*, **1987**, *62*, 4293.
22. Q. Zhong, D. Inniss, K. Kjoller, V.B. Elings, *Surf. Sci. Lett.*,**1993**, *290*, L688.

Artículos relacionados: Capítulo 4

Estudio en superficie de imanes unimoleculares

Artículo K

Título:
Self-organization of Mn_{12} single-molecule magnets into ring structures induced by breath-figures as templates

Autores:
J. Gómez-Segura, O. Kazakova, J. Davies, P. Josephs-Franks, J. Veciana, D. Ruiz-Molina

Revista:
Chemical Communications

Self-organization of Mn_{12} single-molecule magnets into ring structures induced by breath-figures as templates

Jordi Gómez-Segura,[a] Olga Kazakova,[b] Julia Davies,[b] Patrick Josephs-Franks,[b] Jaume Veciana[a] and Daniel Ruiz-Molina*[a]

Receipt/Acceptance Data **[DO NOT ALTER/DELETE THIS TEXT]**
Publication data **[DO NOT ALTER/DELETE THIS TEXT]**
DOI: 10.1039/b000000x [DO NOT ALTER/DELETE THIS TEXT]

Cooling evaporation of a CH_2Cl_2 solution of Mn_{12} clusters on HOPG initiates the formation of water droplets that act as templates for the formation of self-assembled molecular magnetic rings.

Single-molecule magnets (SMMs) exhibit large spin ground states with large magnetoanisotropy, resulting in an energy barrier for the spin reversal. As a consequence, each molecule exhibits slow magnetization relaxation rates and interesting magnetic properties that are characteristic for nanoscale magnetic particles, such as out-of-phase ac magnetic susceptibility signals and stepwise magnetization hysteresis loops.[1] Therefore, SMMs represent an exciting breakthrough towards the realisation of the ultimate high-density information storage devices and quantum computing applications.[2] However, if a truly molecular computational device based on SMMs is to be achieved, new systematic studies that allow us to obtain spatially and geometrically controlled patterns of SMMs onto a given surface are essential. One of the first steps in this direction was the organization of these molecules within multilayered Langmuir-Blodgett films.[3] Since then, other approaches such as self-assembly of a thiol modified Mn_{12} complex;[4] grafting on Au(111)[5] or Si(100)[6] surfaces; and photolithography on Si/SiO_2 surfaces[7] have been reported. In our group, we have also been strongly involved in the development of new methodologies to address individual Mn_{12} molecules both, on the surface of polycarbonate thin-films by a soft lithographic technique and for the multiple length scale patterning of Mn_{12} molecules over different surfaces (HOPG and Si/SiO_2).[8]

Here, in a further step to expand the range of methodologies explored for the deposition of functional molecular materials on a surface, we report a new valuable and simple route based on the condensation of water droplets on a cold surface that act as a template for the self-organization of Mn_{12} molecules into magnetic rings. Such a methodology, based on the well-known breath-figures phenomenon,[9] has already been successfully used to generate 2D or 3D ordered macroporous materials based on polymeric systems[10] but not for ordering molecules on surfaces.

The molecule of choice was the Mn_{12} complex $[Mn_{12}O_{12}(O_2CR)_{16}(H_2O)_x]$ comprising aromatic biphenyl moieties ($R=C_6H_4C_6H_5$) (**1**).[11] In addition to being well studied, this molecule exhibits a considerable thermal and chemical stability,[12] large volume and an hydrophobic outer shell that is expected to favour molecular self-assembly through π•••π interactions between the phenyl groups. Initially, a solution of **1** in a highly volatile organic solvent (CH_2Cl_2) was cast onto freshly cleaved highly oriented pyrolitic graphite (HOPG) wafers under a moist atmosphere. Imaging of the surface by atomic force microscopy (AFM) after solvent evaporation reveals the formation of uniform ring-shaped deposits of Mn_{12} randomly distributed all over the surface. A topographic image and the corresponding height profile are shown in the top section of Figure 1. The image shows several ring-shaped structures located on the HOPG surface, a pattern that was confirmed after additional measurements were made in at least three different well-separated 50 x 50 μm^2 sites. In each of the images, rings appear to be relatively uniform in size, with an experimental averaged height that ranges from 119 to 135 nm, averaged diameters ranging from 4.2 to 4.6 μm and ring-thickness at half height of approximately 140 nm.

A feasible interpretation for the formation of the Mn_{12}-based magnetic rings is shown in Figure 2. Drop casting of a solution of complex **1** in CH_2Cl_2 results in an initially continuous thin-film. Subsequently, along the course of the evaporative cooling, water droplets condense from the moist atmosphere onto the film surface, according to the well-known breath-figures mechanism (step a). The water droplets locally cap the liquid film surface and the solvent is only allowed to evaporate in between the droplets, driven by convective motion (step b), as previously observed in polymeric matrixes.[10] In the later stages of solvent evaporation, the continuous thin-film undergoes fragmentation as ascribed to the characteristic dewetting phenomena,[14] although the spherical

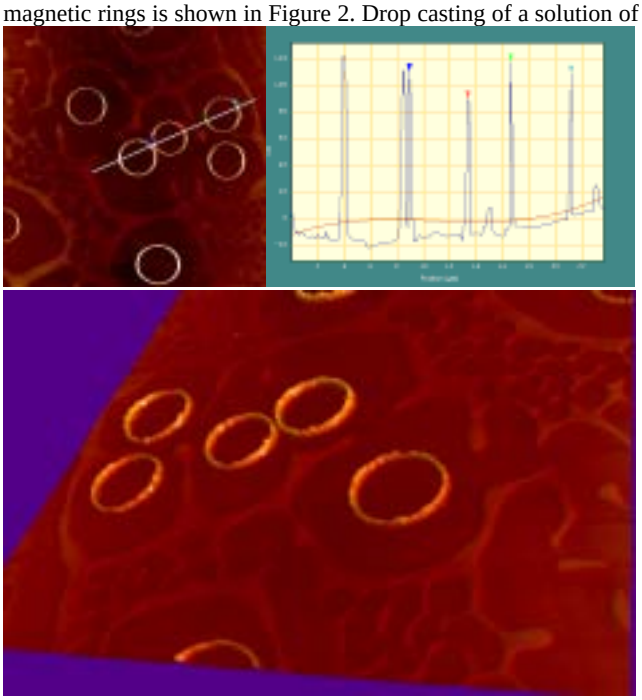

Fig. 1 Drop-casting on HOPG from a CH_2Cl_2 solution of **1** exposed to a moist atmosphere. AFM top-view topographic image (top left). Height profile (top right) across lined-up rings indicated in the top-view topographic image and the corresponding 3D image (down). Scan size is 35 μm.

* dani@icmab.es

cap water droplets remain unaltered on the surface of the HOPG. As a consequence, the residual solution is strategically confined to the constrained regions at the periphery of each droplet (step c). [15] During completion of the evaporation process, solute molecules accumulate to form solid deposits of Mn_{12} that recalls the droplet perimeter (steps d and e). The regions immediately surrounding the rings are depleted in Mn_{12} deposits because of a rapid radial shrinkage to the droplet edges, although a residual thin-film of Mn_{12} molecules remain on the surface along the film fragmentation path, showing the characteristic morphology of the dewetting patterns (see bottom of Figure 1).[14]

To give more insight into the mechanism shown in Figure 2, the same experiments were repeated onto a hydrophilic Si/SiO_2[¶] surface. As shown in Figure 3, imaging of the surface by AFM

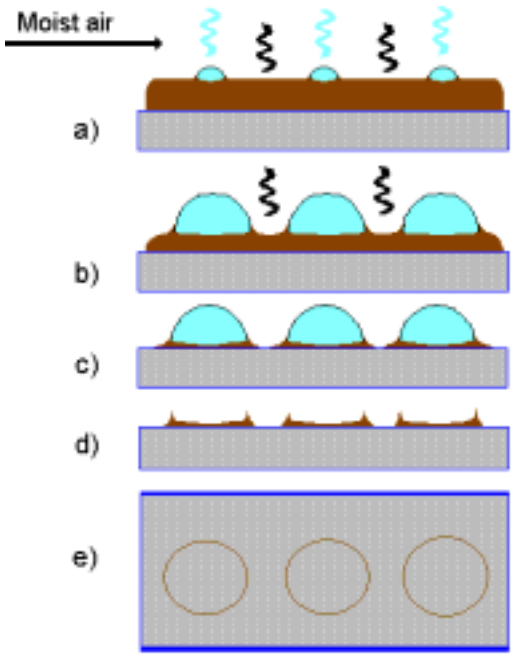

Fig. 2. Schematic stepwise representation of the solvent evaporation process. Evaporative cooling causes water droplets to condense on the surface of the thin solvent film. The edges of the water droplets pin the solution and a solid deposit of Mn_{12} is formed in the location of the concave capillary bridge.

after solvent evaporation reveals this time the lack of regular ring patterns in at least three different well-separated 50 x 50 μm^2 sites. On the contrary, the observation of an inhomogeneous distribution of amorphous features has been attributed to the enhanced hydrophilicity of the native silicon oxide compared with HOPG. The wetting characteristics of the water molecules implies a decrease in the droplet flatness ratio (i.e., the ratio of droplet height to radius). Therefore, more extended wetting areas are prone to disruption giving rise to a distribution of dispersed features.

Finally, to assign the rings shown in Figure 1 to Mn_{12} molecules rather than any solvent impurity, further characterization of Mn_{12} rings was performed using magnetic force microscopy (MFM). MFM uses a magnetic tip that allows the combination of topographic imaging of an object with the mapping of a local distribution of magnetic moments.

A first scan was acquired at a height intimately close to the sample surface (about 3-5 nm), where the short-range van der Waals' force is active, such that the obtained image is

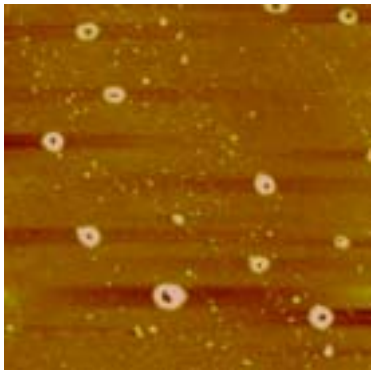

Fig. 3. Drop-casting onto hydrophilic Si/SiO_2 wafer from a CH_2Cl_2 solution of **1** exposed to a moist atmosphere. Scan size is 10 μm.

predominantly topographic. A similar pattern to that shown in Figure 1, with a poorer resolution due to the use of a thicker Co-coated tip, was observed (see Figure 4). Subsequently, the tip was retracted to a selected lift scan height in the range of 50-300 nm, where magnetic interactions become apparent at the expense of topographic effects. In all the distance range, the phase shift (MFM image) of cantilever oscillations reveals changes in the resonant frequency induced by the magnetic interaction between the tip and the sample at the position of the rings previously found by topographic imaging. For instance, Figure 3 shows the spatial variation of magnetic forces obtained with a Co-coated tip at 300 nm, at which height the interatomic van der Waals' force is suppressed and only long-range magnetic forces persist.

The MFM image shown in Figure 4 was obtained at room temperature, where Mn_{12} clusters are paramagnetic without a preferential ordering of their magnetic moment. Nevertheless,

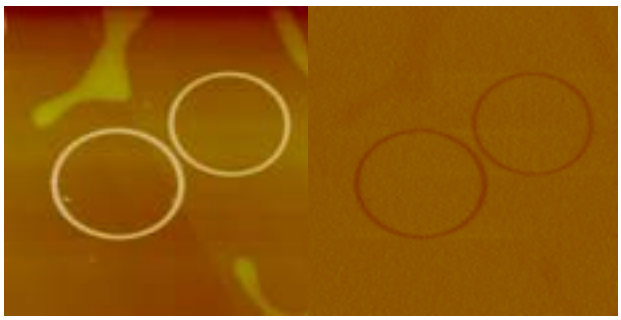

Fig. 4. AFM images of Mn_{12} rings of **1** on HOPG: topography (left) and the corresponding phase-contrast image at 300-nm lift height (right). Scan size is 12 μm.

application of a near magnetic field (i.e., the field induced by the magnetic tip, which to some extent can be considered as a magnetic dipole) is likely to magnetize the individual molecules even at room temperature. Moreover, even though small, the collection of magnetic moments of the molecules is enough to generate a magnetic contrast with the diamagnetic surrounding, detectable even at room temperature.[13] As a consequence, the magnetic moments of all molecules become observable by MFM. This fact was confirmed when a non-magnetic Si tip was used, under similar experimental conditions.[§] In this case, all traces of rings on the phase-lag image due to topographic effects decrease progressively until the scan height reaches approximately 50 nm, from where on they disappear completely.

In summary, breath figures have been used as a template method to arrange Mn_{12} SMMs into reproducible and uniform magnetic ring-shaped self-assemblies. Morever, breath figures is

a well-known phenomenon that is prone to form ordered arrays with controlled sizes under specific experimental conditions.[16] With this aim, we are currently exploring the feasibility to achieve spatially controlled patterns of self-assembled rings on surfaces not only of Mn_{12} but also of several other functional molecular systems. Studies in order to understand the influence of experimental parameters on the size of magnetic ring-shaped self-assemblies are also underway.[17]

This work was supported by the *Information Society Technologies* Programme of the European Commission, as a part of the project NANOMAGIQC IST-2001-33186, DTI NMS Quantum Metrology Programm (UK) and by a Marie Curie Research Training Network (contract QUEMOLNA, number MRTN-CT-2003-504880). Authors also acknowledge the *Programa Nacional de Materiales* of the Dirección General de Investigación (Spain), as part of project MAGMOL (MAT2003-04699).

Jordi Gómez-Segura,[a] Olga Kazakova,[b] Julia Davies,[b] Patrick Josephs-Franks,[b] Jaume Veciana and Daniel Ruiz-Molina*[a]

[a] Institut de Ciència de Materials de Barcelona (CSIC), Campus Universitari, 08193 Bellaterra, Catalonia, Spain. Fax: 34 93 580 57 29; Tel: 34 93 580 18 53; E-mail: dani@icmab.es

[b] National Physical Laboratory (NPL), Hampton Road, Teddington, Middlesex TW11 0LW, UK. Fax: 44 20 8614 0563; Tel: 44 20 8943 6654

Notes and references

† The synthesis of **1**, $[Mn_{12}O_{12}(O_2CC_6H_4C_6H_5)_{16}(H_2O)_4]$, has been described elsewhere.[11] A CH_2Cl_2 solution of **1** (10^{-4} g/cm^3) was cast onto freshly cleaved HOPG (Agar Scientific) or Si/SiO_2 in a moist atmosphere (relative humidity 65%).

¶ A Si(100) wafer was chemically etched with a 10% HF solution for 2 min and rinsed in ultrapure distilled water. Reoxidation was carried out in moist atmosphere (relative humidity 55%) for 24 h.

§ AFM/MFM measurements were performed using a commercial atomic force microscope MultiMode operating in air at room temperature. The AFM images were acquired in tapping mode using phosphorus or antimony (n) doped Si tips (spring constant= 40 N/m, resonant frequency= 300 kHz). For MFM measurements, Co/Cr-coated tips were used operating in the lift mode (spring constant= 2.8 N/m, resonant frequency= 75 kHz).

1 G. Christou, D. Gatteschi, D.N. Hendrickson and R. Sessoli, *MRS Bull.*, 2000, **25**, 66.
2 D. Gatteschi and R. Sessoli, *Angew. Chem. Int. Ed.*, 2003, **42**, 268.
3 M. Clemente-León, H. Soyer, E. Coronado, C. Mingotaud, C. J. Gómez-García and P. Delhaès, *Angew. Chem., Int. Ed.*, 1998, **37**, 2842.
4 A. Cornia, A. C. Fabretti, M. Pacchioni, L. Zobbi, D. Bonacchi, A. Caneschi, R. Biagi, U. Del Pennino, V. De Renzi, L. Gurevich and H. S. J. Van der Zant, *Angew. Chem., Int. Ed.*, 2003, **42**, 1645.
5 A. Nait Abdi, J. P. Bucher, P. Rabu, O. Toulemonde, M. Drillon and P. Gerbier, *J. Appl. Phys.*, 2004, **95**, 7345; J. S. Steckel, N. S. Persky, C. R. Martinez, C. L. Barnes, E. A. Fry, J. Kulkarni, J. D. Burgess, R. B. Pacheco and S. L. Stoll, *Nano Lett.*, 2004, **4**, 399.
6 G. G. Condorelli, A. Motta, I. L. Fragalà, F. Giannazzo, C. Raineri, A. Caneschi and D. Gatteschi, *Angew. Chem., Int. Ed.*, 2004, **43**, 4081.
7 K. Kim, D. M. Seo, J. Means, V. Meenakshi, W. Teizer, H. Zhao and K. R. Dunbar, *Appl. Phys. Lett.*, 2004, **85**, 3872.
8 D. Ruiz-Molina, M. Mas-Torrent, J. Gómez, A. I. Balana, N. Domingo, J. Tejada, M. T. Martínez, C. Rovira and J. Veciana, *Adv. Mater.*, 2003, **15**, 42; M. Cavallini, F. Biscarini, J. Gómez-Segura, D. Ruiz and J. Veciana, *Nano Lett.*, 2003, **3**, 1527; M. Cavallini, J. Gómez-Segura, D. Ruiz-Molina, M. Massi, C. Albonetti, C. Rovira and J. Veciana, *Angew. Chem. Int. Ed.*, 2005, **44**, 888.
9 Lord Rayleigh, *Nature*, 1911, **86**, 416.
10 M. Srinivasarao, D. Collings, A. Philips and S. Patel, *Science,* 2001, **292**, 79.
11 D. Ruiz-Molina, P. Gergier, E. Rumberger, D. B. Amabilino, I. A. Guzei, K. Folting, J. C. Huffman, A. Rheingold, G. Christou, J. Veciana and D. N. Hendrickson, *J. Mater. Chem.*, 2002, **12**, 1152.
12 P. Gerbier, D. Ruiz-Molina, J. Gómez, K. Wurst and J. Veciana, *Polyhedron*, 2003, **22**, 1951; J. Gómez-Segura, E. Lhotel, C. Paulsen, D. Luneau, K. Wurst, J. Veciana, D. Ruiz-Molina and P. Gerbier, *New J. Chem.*, 2005, **29**, 499.
13 Likewise, similar magnetic responses have been previously observed for other paramagnetic organic molecules on diamagnetic surfaces: H. Nishide, T. Ozawa, M. Miyasaka, E. Tsuchida, *J. Am. Chem. Soc.*, 2001, **123**, 5942.
14 G. Reiter, *Langmuir*, 1993, **9**, 1344; R. Seemann, S. Herminghaus and K. Jacobs, *Phys. Rev. Lett.*, 2001, **86**, 5534; R. Xie, A. Karim, J. F. Douglas, C. C. Han and R. A. Weiss, *Phys. Rev. Lett.*, 1998, **81**, 1251; A. Vrij and J. Th. G. Overbeek, *J. Am. Chem. Soc.*, 1968, **90**, 3074.
15 Confirmation for the formation of a concave capillary bridge (meniscus) constrained at the droplet edges was obtained by placing directly water droplets on a surface of a CH_2Cl_2 solution that had been cast onto HOPG and following the evaporation process by optical microscopy. For more information see: Z. Lin and S. Granick, *J. Am. Chem. Soc.*, 2005, **127**, 2816.
16 D. Beysens and C. M. Knobler, *Phys. Rev. Lett.*, 1986, **57**, 1433; D. Beysens, A. Steyer, P. Guenoun, D. Fritter and C. M. Knobler, *Phase Transitions*, 1991, **31**, 219.
17 J. Peng, Y. Han, Y. Yang, B. Li, *Polymer*, 2004, **45**, 447.

Artículo L

Título:
Multiple length scale patterning of single-molecule magnets

Autores:
M. Cavallini, F. Biscarini, J. Gómez-Segura, D. Ruiz, J. Veciana

Revista:
Nano Letters

NANO LETTERS

2003
Vol. 3, No. 11
1527−1530

Multiple Length Scale Patterning of Single-Molecule Magnets

Massimiliano Cavallini,[†] Fabio Biscarini,*[,†] Jordi Gomez-Segura,[‡] Daniel Ruiz,[‡] and Jaume Veciana[‡]

CNR − Istituto per lo Studio dei Materiali Nanostrutturati, Sez. di Bologna, Via P. Gobetti 101, I-40129 Bologna, Italy, and CSIC − Institut de Ciencia de Materials de Barcelona, Campus Universitari de Bellaterra, 08193 Cerdanyola, Spain

Received August 8, 2003; Revised Manuscript Received September 16, 2003

ABSTRACT

Controlling materials on multiple length scales is one of the most compelling issues in nanotechnology research today. Here we demonstrate that arrays of nanometer-sized aggregates, each made of a few hundred single-molecule magnets derived from Mn_{12} complexes, can be patterned on large areas by self-organization assisted by stamps on a surface in a dewetting regime. The large length scale is imposed by the motif of the stamp protrusions, and the smaller length scales, viz., the size and distance of the molecular aggregates, are controlled by deposition and growth phenomena occurring in a volume confined beneath the protrusions by capillary forces. The method is general to a variety of molecular materials and substrates because repulsive, as opposed to specific, interactions are required. Our result hints at the possibility of sustainable patterning of single-molecule magnets for ultra-high-density magnetic storage and quantum computing.

Single-molecule magnets (SMM) have a large-spin ground state with appreciable magnetic anisotropy, resulting in a barrier for the spin reversal. As a consequence, interesting magnetic properties such as out-of-phase ac magnetic susceptibility signals and stepwise magnetization hysteresis loops due to individual molecules rather than to long-range ordering are observed below the blocking temperature (T_B) where the magnetization relaxation rates are very slow.[1,2] Such molecules may become materials with a potential impact in ultra-high-density magnetic storage[3] and in quantum computing applications,[4] provided their T_B values can be increased to reasonable values and the molecules can be organized into addressable domains. With this aim, the possible deposition of isolated SMMs derived from Mn_{12} complexes or very small aggregates of such molecules onto a polycarbonate surface[5] has been demonstrated. Very recently, the self-assembly of thiol-substituted Mn_{12} complexes has been achieved on Au thin films.[6] In either case, no control of position and distance was shown, and although the latter method is amenable for contact printing, it may be desirable to pattern SMMs onto a variety of surfaces rather than being restricted to gold thin films. The use of microcontact printing and capillary filling to pattern the deposition of a ferrofluid on a surface with features on the order of micrometers was reported.[7]

The fabrication of ordered patterns of Mn_{12} SMMs is a crucial step in the realization of memory elements based on these materials. New approaches that allow direct fabrication of ordered patterns of SMMs, either isolated or aggregated, onto surfaces where each molecule or molecular aggregate can be used as a bit of information are required. Because Mn_{12} SMM is a paramagnetic material at room temperature, an ordered pattern of molecular aggregates is technologically more relevant than individually isolated molecules dispersed on a surface in view of developing new storage media. Arrays of domains with a characteristic size and position can indeed be addressed and read differentially by a magnetic head or by magnetic scanning probes.[5]

Here we demonstrate the patterning of aggregates of Mn_{12} SMMs with size and distance control on multiple length scales ranging from tens of nanometers to millimeters. We use a convergent approach based on the stamp-assisted deposition of molecules from a solution together with dewetting phenomena arising from competing interactions between the molecules and the substrate. Such an approach, which is suitable for a number of soluble materials[8] and nonwettable substrates, can be in principle pushed down to the limit where single-molecule magnets are patterned into ordered arrays, this process ultimately being limited only by the coarsening of the individual molecules.

The complex used in this work is $[Mn_{12}O_{12}(O_2CC_{12}H_9)_{16}(H_2O)_4]$ (**1**), whose synthesis has been previously described.[9]

Figure 1 shows the molecular structure of complex **1**, obtained by the minimization of its structure with a force field method.[10] Complex **1** exhibits a structure with a coin-shaped Mn_{12} core stabilized by an outer shell of 16 biphenyl

* Corresponding author. E-mail: f.biscarini@ism.bo.cnr.it. Tel: ++39-051-6398523. Fax: ++39-051-6398540.
[†] CNR.
[‡] CSIC.

10.1021/nl034630l CCC: $25.00
Published on Web 10/25/2003

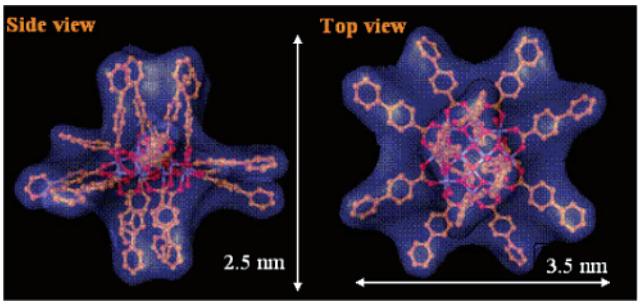

Figure 1. Molecular structure of Mn_{12} complex **1**. Side and top views of the molecular structure of complex **1** obtained by molecular modeling. Connolly surfaces around the molecule show the van der Waals shape and volume.

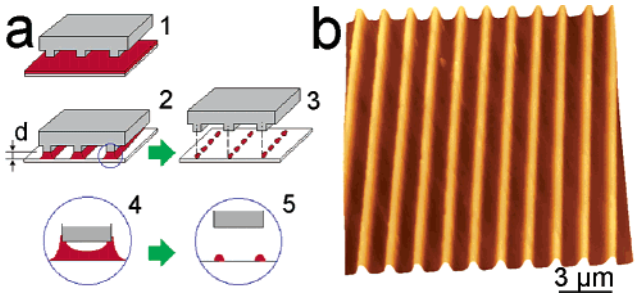

Figure 2. Schematic representation of stamp-assisted deposition. (a**)** (1) The stamp is placed in contact with a layer of solution spread on the substrate. (2) As the solvent evaporates, the onset of capillary forces pins the solution to the protrusions. Because the evaporation rate is faster in the thinner parts, the receding front between adjacent protrusions leaves dry areas in between. (3) As the critical concentration is reached in the solution confined under the protrusion, Mn_{12} clusters precipitate. The material is deposited according to the positive replica of the stamp; as the deposition is followed by dewetting, arrays of droplets with a characteristic size and distance will form. (4) Dilute solutions yield split structures pinned to the edges of the protrusions. (5) Strings of nanodroplets are obtained by dewetting the material deposited upon the regime (4). **(**b**)** AFM images of the stamp used in this experiment. It consists of parallel lines that are 500 nm wide and with 1.5 μm pitch.

carboxylate ligands. The ligands make the outer shell hydrophobic, and we expect that the deposition of **1** from a solution onto a hydrophilic surface will result in spherically capped droplets formed by aggregates of molecules. Two possible mechanisms may indeed contribute to this phenomenology: nucleation and growth in a partial wetting regime[11] or dewetting of an initially smooth film.[12] Both phenomena have been observed in thin films of molecular materials and are known to yield spontaneously spatial correlations in size and distance upon certain conditions.[13−15]

In the case of growth in the partial wetting regime, correlations arise because of intertwined nucleation and ripening, the latter being a size/distance-dependent phenomenon that stops as the ripened nuclei have reached the same size at an equilibrium distance.[13−14]

Dewetting is the rupture of an initially continuous film upon an external perturbation, which can develop via two possible mechanisms: (i) nucleation and growth of holes[16] and (ii) spinodal dewetting.[17] The latter occurs by fluctuations of the film surface with the emergence of a characteristic wavelength that, for a given material, is controlled by the film thickness. The latter is therefore a desirable mechanism, being dependent on a convenient experimental variable.[18]

Our strategy is to control the wetting/dewetting phenomena over a large area in order to control the multiscale organization of complex **1** from nanometer-sized aggregates of a few molecules to large arrays with submicrometer or nanometer length scales.

Solution casting is not suitable for multiscale patterning over a large area because surface defects pin the receding fluid front and induce a nonequilibrium flow of material.[19] Because defects are randomly distributed, the result is a spatially inhomogeneous deposition of aggregates. To overcome the problem of defining the positions on the surface where deposition will occur, we assist the deposition of the solute with stamps placed gently on top of the solution layer. The process we developed is schematically described in Figure 2.

The protrusions of the stamp act as pinning sites for the drying solution, and the critical concentration for the solute to start precipitating is reached only in the small volume of solution confined under the protrusion. The stamp imparts the large-area spatial modulation to the solution and hence to the deposited solute. Accidental defects on the surface become statistically irrelevant because the stamp features are considerably more dense and their effect is modulated through the choice of solvent and the chemical nature of the surface of the stamp. As a result, the process of droplet formation is confined under the stamp protrusions. The smaller length scales, viz., droplet size and interdroplet distances, will depend on the initial concentration of the solution and the volume under the protrusions, which is controlled by the distance between the stamp and the substrate. A remarkable outcome of our approach with respect to a printing technique with intimate contact between the stamp and substrate is the possibility to downsize the printed features with respect to the lateral size of the protrusions.[8] This is achieved by controlling the distance between the stamp and the substrate and, indirectly, the lateral size of the menisci forming under the protrusions by exploiting the process shown in Figure 2a.[8] In the case of an extremely dilute solution, it is possible to obtain ultranarrow split features because of the pinning at the sharper edges of the protrusions. In this regime, deposited structures as small as tens of nanometers wide can be obtained by using protrusions that are a few hundred nanometers wide but have sharper edges. An AFM image of the stamp that is used is shown in Figure 2b.

The result of the deposition of a solution of SMM **1**, obtained following the methodology described in Figure 2, is shown in Figure 3.

The substrates that were used were native silicon oxide deposited onto Si(100), obtained by etching a silicon wafer with a 10% HF solution for 2 min and then rinsing it in ultrapure distilled water before reoxidizing it in humid air (relative humidity 55%) for 24 h.

In Figure 3a, it is shown that patterning is effective across at least a 100 × 100 μm^2 area, the assessment of the latter

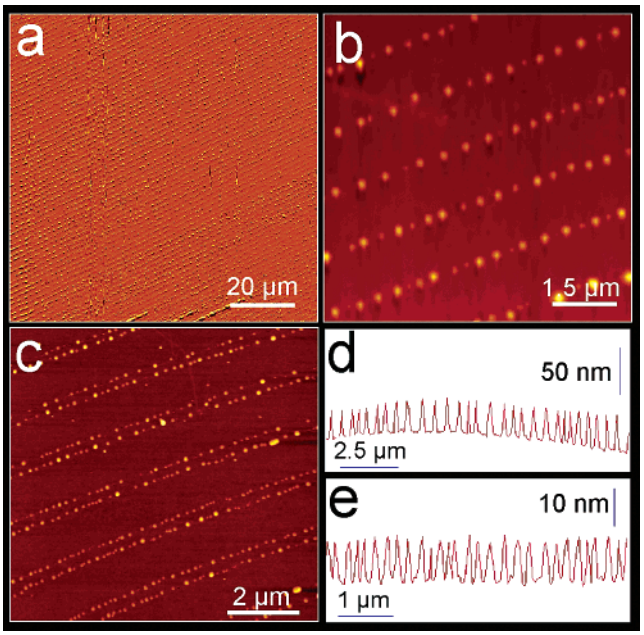

Figure 3. (a) AFM image (error signal) of patterns of **1** fabricated on a large area (100 × 100 μm^2). (b) Image of printed features using a dilute solution. (c) Image of printed features using a very dilute solution. Typical line profile along a line obtained using (d) a dilute solution (corresponding to b) and (e) a very dilute solution (corresponding to c).

being limited by the maximum scan length of the AFM piezoelectric tube. We succeeded in patterning 1 × 1 mm^2 areas on a laboratory bench. The pattern is made of parallel lines that replicate the periodicity of the stamp. At greater magnification (Figure 3b), the lines appear to consist of droplets aligned along the stretching direction: their average size is 270 ± 89 nm, and their distance is 441 ± 138 nm (Figure 3d). The remarkable result is that the arrays of complex **1** droplets are obtained by using a featureless stamp with a much larger size. By using a more dilute solution (Figure 3c), we obtain split strings of droplets, whose apparent lateral fwhm is 70 ± 15 nm; their height is 8 ± 2 nm, and their spacing is 200 ± 42 nm. Considering that complex **1** can be approximated by an oblate ellipsoid whose van der Waals axes are 2.5 and 3.5 nm, we estimate that each aggregate consists of a few hundred molecules.

The patterning mechanism is a wetting/dewetting transition that occurs after the stamp-assisted deposition of Mn_{12} stripes. The stripes, which have a hydrophobic shell, have no affinity for the hydrophilic surface, and the surface energy is the driving force for the film rupture.

Figure 4 supports the mechanism by the dewetting of initially continuous strips or lines of deposited material, as opposed to nucleation and growth in the partial wetting regime. Here the process of the formation of aggregates was stopped by removing the stamp before completion. The imaged area shows droplets of different sizes that have not completed either their coalescence or fragmentation and lines, not yet dewetted, that are breaking into droplets by bulging and narrowing on a characteristic length scale. We cannot establish details about the specific mechanism of dewetting

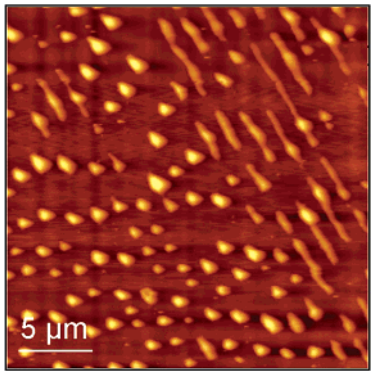

Figure 4. AFM image of a printed Mn_{12} SMM on Si(100) with native silicon oxide. The stamp was removed a few seconds before the end of the process. The formation of lines of materials and how these are rupturing into droplets to give rise to aggregates is apparent.

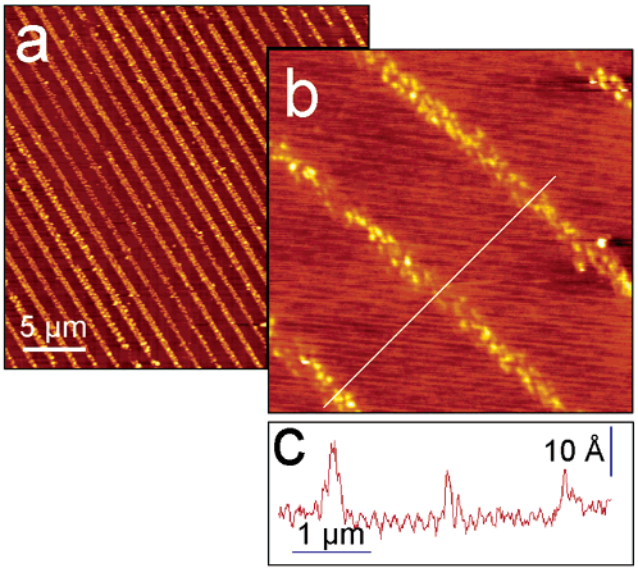

Figure 5. (a) AFM image of a printed Mn_{12} SMM line pattern using a diluted solution on a hydrophobic surface (HMDS). (b) Enlargement of a. The width of the printed features is 200 nm, and the thickness is only one molecule. (c) Topographical line profile along the white line.

because the kinetics of rupture is experimentally difficult to image in real time.

The remarkable feature of this approach is that the spatial correlations on smaller length scales are introduced by the dewetting phenomena and not by the stamp. Thus, there is no need for stamps with very fine features to define the individual positions and sizes of the nanostructures. The technological advantage consists of the ability to pattern on length scales much smaller than those of the features present in the stamp.

In Figure 5, the same experiment was performed on a hydrophobic substrate, viz., silicon oxide primed from hexamethyl disiloxane (HMDS). The silicon oxide surface is terminated with trimethylsilyl groups. Similar results were obtained on highly oriented pyrolitic graphite. In this case, the wettability of the surface by complex **1** molecules results in monolayer stripes, 3 ± 1 nm high and less than 200 nm

wide, that replicate the motifs of the protrusions. Thus, by using wetting conditions instead of dewetting, we can deposit one to two monolayer-thick stripes of finite lateral size that are amenable to STM experiments.

In conclusion, the possibility to pattern ordered arrays of nanostructures made of small Mn_{12} single-molecule magnets has been demonstrated. The approach we devised is based on stamp-assisted deposition from a solution on a substrate in a regime of partial wetting or dewetting. Our method integrates two important features into a convergent approach: (i) a large-area, parallel fabrication due to the use of the stamp and (ii) the capability of introducing multiple length scales because of the interplay of the growth phenomena of the nanostructures. It is therefore a genuine bottom-up patterning on smaller length scales, where it exploits competing interactions between the adsorbate and the substrate. These can be tuned by the design and a proper functionalization of the outer ligands of the Mn_{12} complex and of the substrate. This is particularly appealing in the case of magnetic molecules, where we could imagine, by suppressing coalescence and ripening phenomena, that single molecules could be organized into addressable memory elements at ultrahigh density.

Acknowledgment. We thank Carlo Taliani for his encouragement and discussions. This work was partially supported by EU-RTD Growth G5RD-2000-00349 MONA LISA and IST-2001-33186 NANOMAGIQC, COST Action D19/W004 “Stereochemical effects on self-assembly and switching at the nanometer scale”, and the Italian Space Agency Progetto COME-NO. This collaboration is also part of the joint CNR−CSIC initiative LAMAT.

References

(1) Sessoli, R.; Gatteschi, D.; Caneschi, A.; Novak, M. A. *Nature* **1993**, *365*, 141.
(2) Gatteschi, D.; Sessoli, R. *Angew. Chem., Int. Ed.* **2003**, *42*, 268.
(3) Krusin-Elbaum,; L., Shibauchi, T.; Argyle, B.; Gignac, L.; Weller, D. *Nature* **2001**, *410*, 444.
(4) Chudnovsky, E. M.; Tejada, J. *Macroscopic Quantum Tunneling of the Magnetic Moment*; Cambridge University Press: Cambridge, England, 1998.
(5) Ruiz-Molina, D.; Mas-Torrent, M.; Balana, A. I.; Domingo, N.; Tejada, J.; Martínez, M. T.; Rovira, C.; Veciana, J. *Adv. Mater.* **2003**, *15*, 42.
(6) Cornia, A.; Fabretti, A. C.; Pacchioni, M.; Zobbi, L.; Bonacchi, D.; Caneschi, A.; Gatteschi, D.; Biagi, R.; Del Pennino, U.; De Renzi, V.; Gurevich, L.; Van der Zant, H. S. J. *Angew. Chem., Int. Ed.* **2003**, *42*, 1645.
(7) Palacin, S.; Hidber, P. C.; Bourgoin, J.-P.; Miramond, C.; Fermon, C.; Whitesides, G. M. *Chem. Mater.* **1996**, *8*, 1316.
(8) Cavallini, M.; Biscarini, F. *Nano Lett.* **2003**, *3*, 1269.
(9) Ruiz-Molina, D.; Gerbier, Ph.; Rumberger, E.; Amabilino, D. B.; Guzei, I. A.; Folting, K.; Huffman, J. C.; Rheingold, A. L.; Christou, G.; Veciana, J.; Hendrickson, D. N. *J. Mater. Chem.* **2002**, *12*, 1152.
(10) Molecular Modelling System. *HyperChem 5.02* for Windows 95/NT.
(11) Beysens, D.; Knobler, C. M. *Phys. Rev. Lett.* **1986**, *57*, 1433.
(12) Reiter, G. *Langmuir* **1993**, *9*, 1344.
(13) Brinkmann, M.; Biscarini, F.; Taliani, C.; Aiello, I.; Ghedini, M. *Phys. Rev. B* **2000**, *61*, R16339.
(14) Brinkmann, M.; Graff, S.; Biscarini, F. *Phys. Rev. B* **2002**, *66*, 165430.
(15) Cavallini, M.; Biscarini, F.; Léon, S.; Zerbetto, F.; Bottari, G.; Leigh, D. A. *Science* **2003**, *299*, 531.
(16) Seemann, R.; Herminghaus, S.; Jacobs, K. *Phys. Rev. Lett.* **2001**, *86*, 5534.
(17) Xie, R.; Karim, A.; Douglas J. F.; Han, C. C.; Weiss, R. A. *Phys. Rev. Lett.* **1998**, *81*, 1251.
(18) Menozzi, C. Crescita e Morfologia di Film Sottili Molecolari Nanostrutturati. Thesis, Department of Physics, Università di Bologna, Bologna, Italy, A. A. 2000−2001.
(19) Deegan, R. D.; Bakajin, O.; Dupont, T. F.; Huber, G.; Nagel, S. R.; Witten, Th. A. *Nature* **1997**, *389*, 827.

NL034630L

Artículo M

Título:
Isolated single-molecule magnets on the surface of a polymeric thin film

Autores:
D. Ruiz-Molina, M. Mas-Torrent, J. Gómez-Segura, A.I. Balana, N. Domingo, J. Tejada, M.T. Martínez, C. Rovira, J. Veciana

Revista:
Advanced Materials

ADVANCED MATERIALS

[15] In order to form thin films for vitrification, it was necessary to load the grids with warm gelator solution that had not yet gelled. The solution was then allowed to cool slightly, beginning the gelation process, on the grid before blotting and plunging (see Experimental). In this way we were able to capture the initial aggregation before complete gelation made it impossible to form thin films. The use of glow-charged grids was found to facilitate the formation of uniformly thin, well-formed films.
[16] R. Oda, I. Huc, M. Schmutz, S. J. Candau, F. C. MacKintosh, *Nature* **1999**, *399*, 566.
[17] SEM images of the dried and rinsed gel of **1** indicated a fibrous structure [2].
[18] a) J. H. Fuhrhop, W. Helfrich, *Chem. Rev.* **1993**, *93*, 1565. b) E. R. Zubarev, M. U. Pralle, E. D. Sone, S. I. Stupp, *Adv. Mater.* **2002**, *14*, 198. c) J. V. Selinger, M. S. Spector, J. M. Schnur, *J. Phys. Chem. B* **2001**, *105*, 7157. d) I. Nakazawa, M. Masuda, Y. Okada, T. Hanada, K. Yase, M. Asai, T. Shimizu, *Langmuir* **1999**, *15*, 4757.
[19] J. H. Jung, H. Kobayashi, M. Masuda, T. Shimizu, S. Shinkai, *J. Am. Chem. Soc.* **2001**, *123*, 8785.
[20] As previously reported, at pH 5.9, **2** forms a gel, suggesting that its molecular aggregation is related to **1** [2].
[21] As part of the powder indexing module of Cerius^2: P. E. Werner, L. Eriksson, M. Westdahl, *J. Appl. Crystallogr.* **1985**, *18*, 367.
[22] a) K. D. M. Harris, M. Tremayne, B. M. Kariuki, *Angew. Chem. Int. Ed.* **2001**, *40*, 1626. b) P. J. Prest, R. B. Prince, J. S. Moore, *J. Am. Chem. Soc.* **1999**, *121*, 5933. c) C. W. Struijk, A. B. Sieval, J. E. J. Dakhorst, M. van Dijk, P. Kimkes, R. B. M. Koehorst, H. Donker, T. J. Schaafsma, S. J. Picken, A. M. van de Craats, J. M. Warman, H. Zuilhof, E. J. R. Sudholter, *J. Am. Chem. Soc.* **2000**, *122*, 11 057. d) S. Ito, M. Wehmeier, J. D. Brand, C. Kubel, R. Epsch, J. P. Rabe, K. Mullen, *Chem. Eur. J.* **2000**, *6*, 4327. e) M. E. Amato, R. Caminiti, G. A. Carriedo, E. J. Garcia-Alonso, J. L. Garcia-Alvarez, G. M. Lombardo, G. C. Pappalardo, *Chem. Eur. J.* **2001**, *7*, 1486.
[23] L. Leiserowitz, A. T. Hagler, *Proc. R. Soc. London, Ser. A* **1983**, *388*, 133.
[24] J. Bernstein, M. C. Etter, L. Leiserowitz, in *Structure Correlation, Vol. 2* (Eds: H.-B. Burgi, J. D. Dunitz), John Wiley & Sons, New York **1994**, p. 431.
[25] Experimentally, using the flotation technique in a carbon tetrachloride/heptane mixture, the density of the fibers is between 1.6 and 1.3 g cm^{-3}.
[26] G. H. Stout, L. H. Jensen, *X-ray Structure Determination – A Practical Guide*, 2nd ed., John Wiley & Sons, New York **1989**.
[27] S. B. Kennedy, E. R. deAzevedo, W. A. Petka, T. P. Russell, D. A. Tirrell, M. Hong, *Macromolecules* **2001**, *34*, 8675.
[28] J. Dubochet, M. Groom, S. Mueller-Neuteboom, in *Advances in Optical and Electron Microscopy, Vol. 8* (Eds: R. Barer, V. E. Cosslett), Academic Press, New York **1982**, p. 107.

Isolated Single-Molecule Magnets on the Surface of a Polymeric Thin Film**

By *Daniel Ruiz-Molina*, *Marta Mas-Torrent*, *Jordi Gómez*, *Ana I. Balana*, *Neus Domingo*, *Javier Tejada*, *María T. Martínez*, *Concepció Rovira*, and *Jaume Veciana**

Single-molecule magnets (SMMs) have a large-spin ground state with appreciable magnetic anisotropy, resulting in a barrier for spin reversal.[1] As a consequence, interesting magnetic properties such as out-of-phase ac magnetic susceptibility signals and stepwise magnetization hysteresis loops are observed. In addition to resonant magnetization tunneling[2–4] several other interesting phenomena have also been reported during the past few years.[5–9] The origin of slow magnetization relaxation rates as well as of other phenomena is due to individual molecules rather than to long-range ordering, as confirmed by magnetization relaxation and heat-capacity studies.[10] Therefore, SMMs represent nanoscale magnetic particles of a sharply defined size that offer potential access to ultimate high-density information storage devices[11] and quantum-computing applications.[12,13] However, if a truly molecular computational device based on an SMM is to be achieved, new systematic studies are required that encompass ways of addressing properly oriented individual molecules or molecular aggregates onto the surface of a thin film, where each molecule or molecular aggregate can be used as a bit of information. The first approach to arrange SMMs into well-organized multilayered films was undertaken by means of the Langmuir–Blodgett (LB) technique.[14] Although these self-assembled monolayer films are transferable to other substrates, there are limitations to their practical utilization since these LB films may become unstable especially due to incompatible surface energies.

Here we report a new soft, reliable, and simple methodology to address individual Mn_{12} complexes onto a film surface. Such a methodology is based on the preparation of polymeric thin films, made from a polycarbonate matrix and a Mn_{12} complex, and subsequent treatment with different organic solvent vapors. Solvent treatment leads to the emerging of a small fraction of the Mn_{12} molecules to the surface of the film with an aggregation state that can be controlled at will, depending on the nature of the solvent. It has already been established that after absorption of suitable amounts of a solvent that is capable of effectively solvating the polymer chains, the swollen polymer network exhibits an enhanced porosity.[15] This situation provides a valuable route for the molecular reorganization of the nanocomposite with a small fraction of Mn_{12} molecules (approximately 0.1 %) emerging to the film surface.

Imaging of the thin film prior to and after solvent treatment using scanning electron microscopy (SEM) does not provide any information on solvent effects except for a solvent-induced surface-smoothening process. Resolution of any structure at the nanometer scale without beam-induced damage proved difficult, therefore atomic force microscopy (AFM) studies were performed. Firstly, high-resolution AFM images of a thin film that was treated with the vapor of a 1:1 CH_2Cl_2/hexane mixture were obtained. The top-view topographical images and the corresponding height profiles across surface locations, which are indicated in the topographical images, are shown in Figure 1. In the same figure, the corresponding 3D-AFM topography images are also shown (Fig. 1b and 1e). The images show many semi-globular islands located on the film surface, a pattern that was confirmed after additional measurements made in a minimum of three different well-

[*] Prof. J. Veciana, Dr. D. Ruiz-Molina, Dr. M. Mas-Torrent, J. Gómez, Dr. C. Rovira
Institut de Ciència de Materials de Barcelona (CSIC)
Campus Universitari de Bellaterra, E-08193 Cerdanyola (Spain)
A. I. Balana, Dr. M. T. Martínez
Instituto de Carboquímica (CSIC)
Miguel Luesma Castan 4, E-50015 Zaragoza (Spain)
N. Domingo, Prof. J. Tejada
Facultad de Física, Universitat de Barcelona
Diagonal 647, E-08028 Barcelona (Spain)

[**] This work was supported by the *Information Society Technologies* Programme of the European Commission, as part of the project NANOMAGIQC, and the *Programa Nacional de Materiales* of the Dirección General de Investigación (Spain), as part of the project MAGMOL.

  0935-9648/03/0101-0042 $ 17.50+.50/0

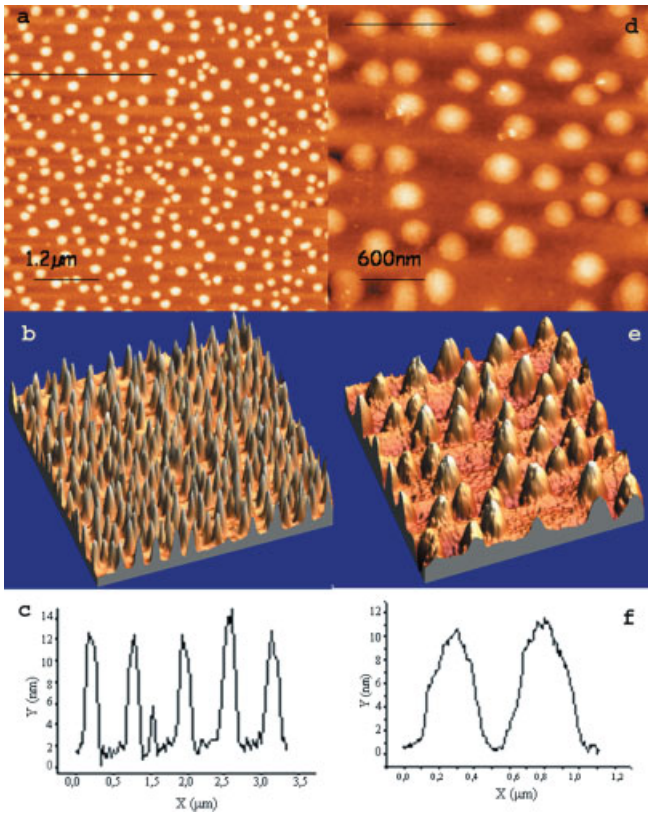

Fig. 1. AFM images of nanocomposite films, made from a polycarbonate polymeric matrix and the Mn_{12} complex, which have been treated with CH_2Cl_2/hexane (1:1). The left part of the figure shows islands on a 10×10 μm surface. a) Topographical top-view. b) 3D image of the same area. c) Height profile. The right part of the figure (d–f) shows data for a 3×3 μm surface. The height profiles in (c) and (f) are taken at the location indicated by the black lines in (a) and (d), respectively.

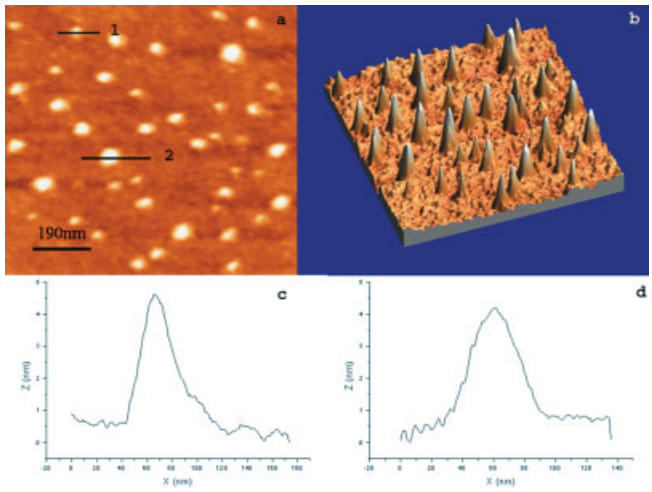

Fig. 2. AFM images of a thin nanocomposite film, made from a polycarbonate polymeric matrix and the Mn_{12} complex, which has been treated with pure CH_2Cl_2. a) Topographical top-view image. b) The corresponding 3D image of the same area. c) Height profile at location marked 1 in (a). d) Height profile at location marked 2 in (a).

separated 10×10 μm sites. In each of the images, the particles appear to be relatively uniform in size, with an experimental averaged height of 12 ± 1 nm.

A detailed study of the molecular structure of the Mn_{12} complex used in this paper showed that this complex exhibits an averaged structure with a coin-like shape with two different end-to-end distances.[16] This result was obtained by the minimization of its structure with a force-field method. The largest end-to-end distance was found to be almost 4 nm, whereas the shortest was 3 nm. Therefore, as each of the islands observed using AFM has an average height of 12 nm, it must contain at least three or four Mn_{12} molecules. On the other hand, the averaged observed full width at the baseline level, which is approximately 250 nm, is evidently larger than the expected width for four aggregated Mn_{12} molecules. The origin for such deviation may be attributed either to the presence of more than four Mn_{12} molecules at the basal plane and/or to geometrical AFM-tip convolution effects.[17] Finally, it has to be mentioned that AFM images of thin films preceding solvent treatment exhibit rather uneven and rough surfaces with the lack of any semi-globular islands.

The formation of molecular aggregates of the Mn_{12} complex in the form of islands is explained well by the large number of phenyl rings present in this complex, which may cause them to aggregate mainly due to attractive π–π interactions. The solvent mixture used favors such aggregation. Indeed, the Mn_{12} complex is highly soluble in CH_2Cl_2 but not in hexane. This situation certainly favors the formation of aggregates. For this reason, a new polymeric thin film was exclusively exposed to CH_2Cl_2 vapor to address individual molecules rather than aggregates of several molecules onto the film surface. The topographical top-view and the corresponding 3D images along with some profiles across surface locations are shown in Figure 2. In this case, the experimental averaged height of the dots observed by AFM topography turned out to oscillate between 4 and 5 nm, which is in excellent agreement with the molecular end-to-end distance of 4 nm determined for the Mn_{12} complex. Moreover, the size of the dots appears to have become substantially more monodisperse, as expected for single molecules.[18] This provides further evidence that indeed truly individual Mn_{12} molecules are imaged here.

Magnetic force microscopy (MFM) was applied to study both the molecular image and the magnetic response of nanocomposite thin films. MFM uses a tip that is magnetized by covering it with magnetic material. This unfortunately leads to images of poorer quality than those previously obtained due to the thickening of the tip. However, it offers the possibility of mapping the magnetic behavior of objects on the studied film surface. In a first sweep, the AFM tapping mode is used whereas in the second sweep, which is carried out over the same area but with the tip retracted to be out of the topographical signal, the local magnetization of the sample is monitored. The top-view topographical image and the corresponding MFM images of thin films treated either with CH_2Cl_2 and CH_2Cl_2/hexane vapor are shown in Figure 3. MFM images clearly indicate a magnetic gradient response exactly corresponding to the molecular position found by topographic im-

  0935-9648/03/0101-0043 $ 17.50+.50/0

ADVANCED MATERIALS

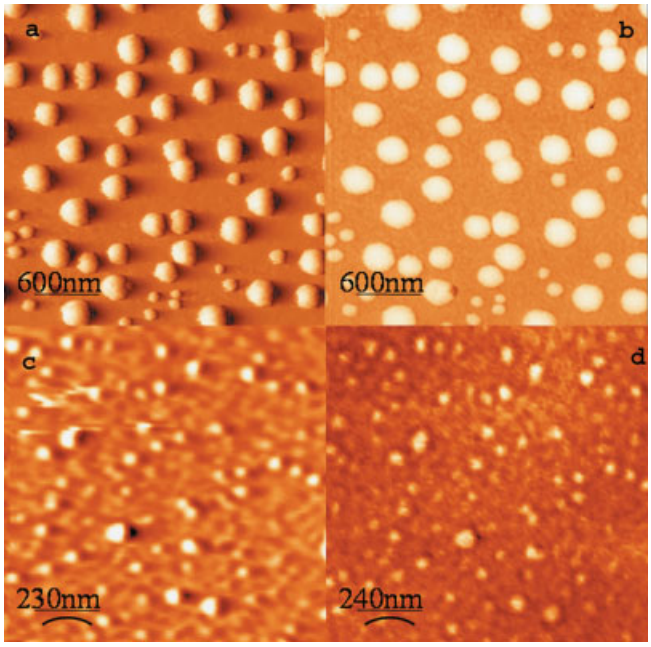

Fig. 3. MFM images of nanocomposite thin films treated with CH_2Cl_2/hexane (1:1) (a,b) and with CH_2Cl_2 (c,d). a,c) Topographical images taken with the magnetic tip. b,d) Magnetic images of the same area after retracting the tip by 30 nm.

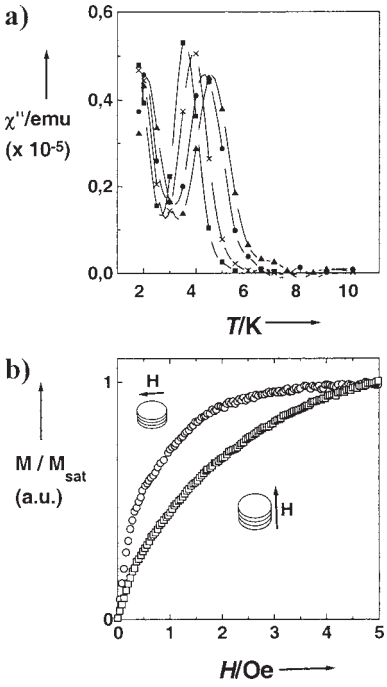

Fig. 4. a) Out-of-phase component of magnetic susceptibility for the nanocomposite thin films at four different frequencies (■ 3 Hz, × 10 Hz, ○ 50 Hz, ▲ 100 Hz). b) Field dependence of magnetization for several stacked films placed parallel (○) and perpendicular (□) to the direction of the applied magnetic field. For the parallel case saturation is achieved at 2.5 T, whereas for the perpendicular case the saturation occurs at fields larger than 5 T.

aging. This fact is the best confirmation to unequivocally assign the dots observed by high-resolution AFM images to single Mn_{12} molecules or aggregates of such molecules rather than to any impurity or small polymeric crystallites.

Magnetic characterization of the nanocomposite thin films was initially performed by means of ac magnetic susceptibility measurements at different frequencies using several wrinkled thin films compressed into the sample holder. Consequently, this sample contains a collection of randomly oriented and fixed Mn_{12} molecules inside the polymeric matrix. As shown in Figure 4a, the thin films show two out-of-phase ac frequency-dependent peaks, with an effective potential barrier (U_{eff}) of 36 K and magnetic relaxation time $\tau_0 = 10^{-9}$ s for the low-temperature peak, and 56 K and $\tau_0 = 4 \times 10^{-8}$ s for the high-temperature peak, respectively. At this point, it is important to mention that both frequency-dependent peaks exhibit the same relative intensity and values for τ_0 and U_{eff} as those observed for a polycrystalline sample of the Mn_{12} complex. To get more insight into the orientation of the molecular complexes inside the bulk polymeric matrix, several thin films were aligned and stacked together. Magnetic measurements were then performed with the magnetic field applied parallel and perpendicular to the surfaces of the stacked films. The field-dependence of magnetization shown in Figure 4b indicates that most of the molecules of the Mn_{12} complex of the thin film tend to align their easy-magnetization axis in some direction inside the plane. This fact also explains why hysteresis is only observed when the field is applied parallel to the surface, and is not detected otherwise. Such alignment may be explained by considering the internal structural reorganization of the polymeric matrix during the swelling process. Indeed, when the solvent molecules penetrate the film and cause it to swell, the glass-transition temperature is reduced to ambient temperature. As a consequence, restrictions on the rotation of the polymer chains are removed, and this therefore permits the movement of molecules that are inside the matrix. After drying the solvent, an energetically favorable polymeric conformation is readily adopted, resulting in the development of oriented microcrystalline domains under ambient laboratory conditions. In view of that, Mn_{12} molecules also tend to align during the swelling process forced by the microcrystalline polymeric environment and they remain oriented after drying the solvent. Further work to fully address this explanation is currently underway.

In summary, here we report a new, simple, and reliable methodology to address individual single-molecule magnets onto a thin film surface, which can be used as magnetic quantum bits for information storage or quantum computing.[19] The advantages of this approach are considerable. Firstly, the polymeric matrix plays a critical role in stabilizing the SMM as well as in enhancing the overall mechanical strength of the film.[20] The lack of stability of LB films or the use of rather aggressive techniques such as chemical or physical vapor deposition can thus be circumvented. Secondly, polycarbonates are commercially important and technologically interesting polymers that have a combination of properties not found in any other plastic, including very high impact strength, creep resistance, optical clarity, and a low moisture absorption. And finally, the resulting nanocomposite thin films are fully com-

  0935-9648/03/0101-0044 $ 17.50+.50/0

patible with today's magnetic and magneto-optical storage technologies, where polycarbonate resins are used as the basic support for the fabrication of disks. Therefore, the nanocomposite thin films reported here can be easily transferred or even directly prepared by a spin-coating method onto a disk support without losing continuous nanoscopic characteristics.

Experimental

The Mn_{12} complex used to prepare the nanocomposite was $[Mn_{12}O_{12}(O_2CC_6H_4C_6H_5)_{16}(H_2O)_4]$, which has recently been described [21]. Polycarbonate films with 4 wt.-% of molecularly dispersed complex were cast onto a glass surface. Spectrochemical characterization of the resulting films with a typical thickness of 10–15 μm, showed no evidence of any decomposition process and therefore gave good indications that the Mn_{12} complexes embedded in the polymeric matrix were stable. Next, the films were treated with solvent vapor of CH_2Cl_2 or 1:1 CH_2Cl_2/hexane mixtures by simply placing the film at the top of a flask containing a small amount of the organic solvent for 5 min. The films were then dried, resulting in a glassy material with no detectable porosity. AFM/MFM measurements were performed with a commercial scanning force microscope from Nanotec. The AFM images, were taken in tapping mode, with Olympus silicon cantilevers with a spring constant of 0.75 $N\,m^{-1}$ and a resonance frequency of 80 kHz. The MFM images were taken with Nanosensors silicon cantilevers (spring constant 4 $N\,m^{-1}$, 72 kHz resonance frequency) which were covered with 50 nm of cobalt. The scan lift-height for the magnetic images was 30 nm. With the magnetic cantilever, the first scan reveals the topography and after retracting a certain height; the second scan reveals the magnetic mapping of the same area. AC and DC magnetic measurements were collected with a Quantum Design MPMS2 SQUID magnetometer equipped with a 5 T magnet with operating frequencies from 3 to 1500 Hz, and temperatures from 1.8 K to 400 K.

Received: September 30, 2002

[1] R. Sessoli, D. Gatteschi, A. Caneschi, M. A. Novak, *Nature* **1993**, *365*, 141.
[2] J. R. Friedman, M. P. Sarachick, J. Tejada, R. Ziolo, *Phys. Rev. Lett.* **1996**, *76*, 3830.
[3] J. M. Hernandez, X. X. Zhang, F. Luis, J. Bartolomé, J. Tejada, R. Ziolo, *Europhys. Lett.* **1996**, *35*, 301.
[4] L. Thomas, F. Lionti, R. Ballou, D. Gatteschi, R. Sessoli, B. Barbara, *Nature* **1996**, *383*, 145.
[5] J. A. A. J. Perenboom, J. S. Brooks, S. Hill, T. Hathaway, N. S. Dalal, *Phys. Rev. B* **1998**, *58*, 330.
[6] L. Bokacheva, A. D. Kent, M. A. Walters, *Phys. Rev. Lett.* **2000**, *85*, 4803.
[7] A. D. Kent, Y. Zhong, L. Bokacheva, D. Ruiz, D. N. Hendrickson, M. P. Sarachick, *Europhys. Lett.* **2000**, *49*, 521.
[8] W. Wernsdorfer, R. Sessoli, *Science* **1999**, *284*, 133.
[9] D. Ruiz, Z. Sun, B. Albela, K. Folting, J. Ribas, G. Christou, D. N. Hendrickson, *Angew. Chem. Int. Ed.* **1998**, *37*, 300.
[10] H. J. Eppley, H.–L. Tsai, N. De Vries, K. Folting, G. Christou, D. N. Hendrickson *J. Am. Chem. Soc.* **1995**, *117*, 301.
[11] L. Krusin-Elbaum, T. Shibauchi, B. Argyle, L. Gignac, D. Weller, *Nature* **2001**, *410*, 444.
[12] E. M. Chudnovsky, J. Tejada, *Macroscopic Quantum Tunneling of the Magnetic Moment*, Cambridge University Press, Cambridge **1998**.
[13] E. Del Barco, N. Vernier, J. M. Hernandez, J. Tejada, E. M. Chudnovsky, E. Molins, G. Bellesa, *Europhys. Lett.* **1999**, *47*, 722.
[14] M. Clemente-León, H. Soyer, E. Coronado, C. Mingotaud, C. J. Gómez-García, P. Delhaès. *Angew. Chem. Int. Ed.* **1998**, *37*, 2842.
[15] A. A. D'Archivio, L. Galantini, A. Biffis, K. Jerábek, B. Corain, *Chem. Eur. J.* **2000**, *6*, 794.
[16] Molecular Modeling System. HyperChem 5.02 for Windows 95/NT, AutoDesk, Inc.
[17] K. Takada, D. J. Díaz, H. D. Abruña, I. Cuadrado, B. González, C. M. Casado, B. Alonso, M. Morán, J. Losada, *Chem. Eur. J.* **2001**, *7*, 1109.
[18] The heights of a few single molecules are smaller than the average 4–5 nm. Such a result can be ascribed to molecules that have not completely emerged to the surface of the films.
[19] J. Tejada, E. M. Chudnovsky, E. del Barco, J. M. Hernandez, T. Spiller, *Nanotechnology* **2001**, *12*, 181.
[20] C. Castro, J. Ramos, A. Millán, J. González-Calbet, F. Palacio, *Chem. Mater.* **2000**, *12*, 3681.
[21] D. Ruiz-Molina, P. Gerbier, E. Rumberger, D. B. Amabilino, I. A. Guzei, K. Folting, J. C. Huffman, A. Rheingold, G. Christou, J. Veciana, D. N. Hendrickson, *J. Mater. Chem.* **2002**, *12*, 1152.

Electrophosphorescence from a Conjugated Copolymer Doped with an Iridium Complex: High Brightness and Improved Operational Stability**

By *Xiong Gong*, *Jacek C. Ostrowski*, *Guillermo C. Bazan*,* *Daniel Moses*,* *Alan J. Heeger*, *Michelle S. Liu*, and *Alex K.-Y. Jen*

By utilizing triplet-based emitting centers in polymer and organic light-emitting diodes (PLEDs and OLEDs), and thereby capturing both singlet and triplet excited states, the internal quantum efficiency can, in principle, be increased to 100 %.[1,2] The utilization of triplet emitters to improve efficiencies was proposed by several groups.[3–8] Recently, considerable progress has been demonstrated with electrophosphorescent OLEDs (based on small molecules) and PLEDS (based on polymers) as the host materials, and heavy-metal (Pt, Ir, Os) complexes and rare-earth metal complexes as the guest.[3–13]

With the addition of the phosphorescent guest, emission takes place either by Förster energy transfer from the host to the singlet excited state of the guest complex followed by intersystem crossing to the guest triplet state, or directly by electron and hole trapping on the metal–organic complex. Dexter energy transfer can also enable direct transfer from the triplet of the host to that of the guest.

For the iridium heavy-metal complexes, the emission originates from the triplet excited state to the ground state. By using different ligands, this triplet phosphorescence can be

[*] Prof. G. C. Bazan, Dr. D. Moses, Dr. X. Gong, J. C. Ostrowski, Prof. A. J. Heeger
Institute for Polymers and Organic Solids
University of California at Santa Barbara
Santa Barbara, CA 93106-5096 (USA)
E-mail: bazan@chem.ucsb.edu; moses@ipos.ucsb.edu
Prof. G. C. Bazan
Department of Chemistry, University of California at Santa Barbara
Santa Barbara, CA 93106 (USA)
Prof. A. J. Heeger
Department of Physics and Materials Department
Universitiy of California at Santa Barbara
Santa Barbara, CA 93106 (USA)
M. S. Liu, Prof. A. K.-Y. Jen
Department of Materials Science and Engineering
University of Washington, Roberts Hall
Box 352120, Seattle, WA 98195-2120 (USA)

[**] This work was supported by the Mitsubishi Chemical Center for Advanced Materials at UCSB and the Air Force Office of Scientific Research through the MURI Center ("Polymeric Smart Skins"), Charles Lee, Program Officer. X. Gong is grateful to Dr. Gang Yu and Dr. Runguang Sun of Dupont Displays Corporation for valuable discussion. J. C. Ostrowski is a Kodak fellow and G. C. Bazan thanks the NSF for financial support (NSF CHE 0098 240). A. K-Y. Jen and M. Liu thank the Air Force Office of Scientific Research for support through the MURI Center ("Polymeric Smart Skins"). M. Liu thanks the Nanotechnology Center at the University of Washington and PNNL for the Joint Institute Nanotechnology Fellowship.

  0935-9648/03/0101-0045 $ 17.50+.50/0

Artículo N

Título:
Magnetic information storage on polymer using patterned single-molecule magnets

Autores:
M. Cavallini, J. Gómez-Segura, D. Ruiz-Molina, M. Massi, C. Albonetti, C. Rovira, J. Veciana, F. Biscarini

Revista:
Angewandte Chemie

Communications

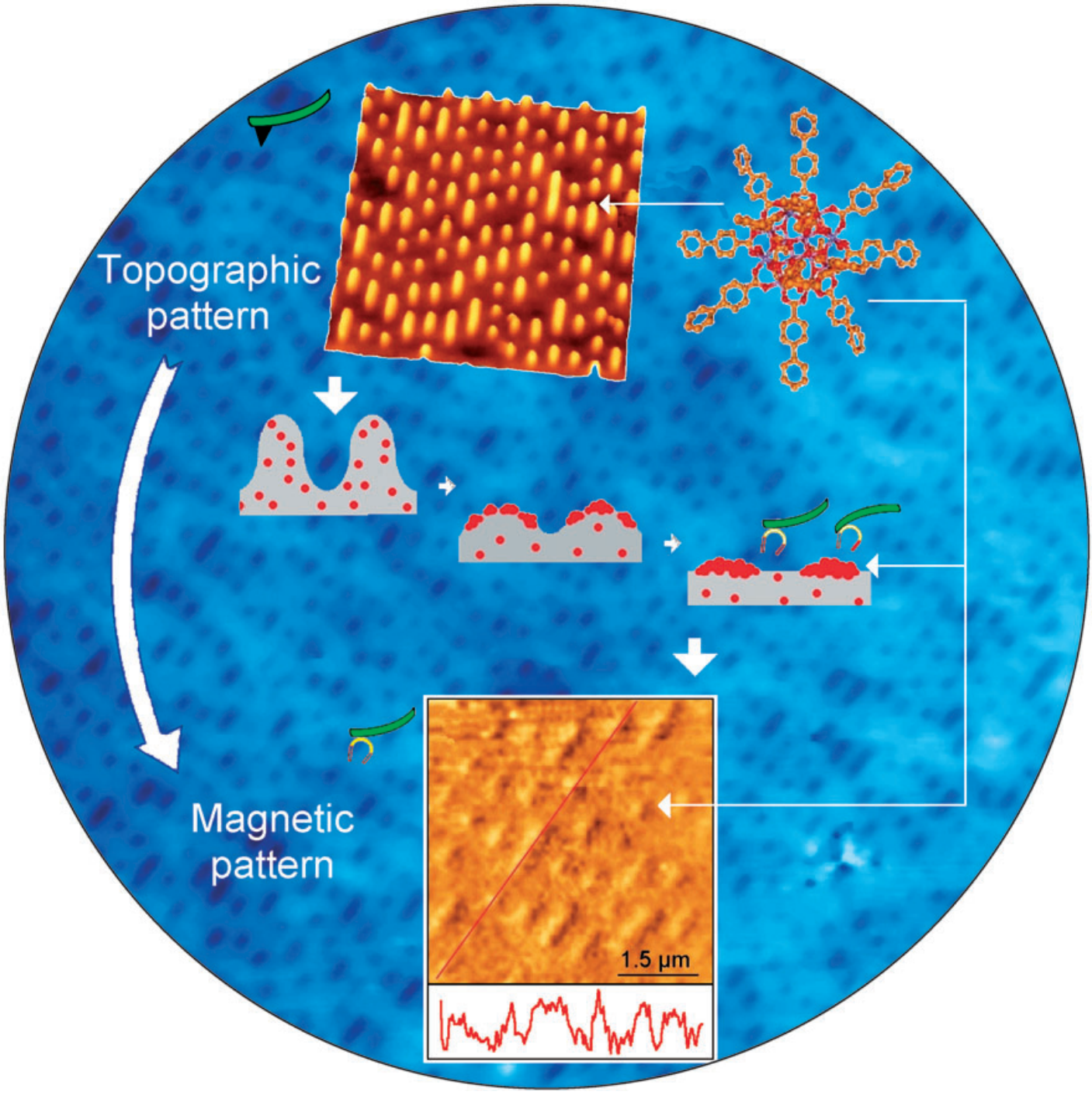

A molecule-based magnetic material with a paramagnetic response at room temperature has been used to fabricate patterns of magnetic bits on a polycarbonate surface. This system can be used effectively as a permanent information-storage medium with magnetic readout. For more information see the Communication by J. Veciana, F. Biscarini, and co-workers on the following pages.

DOI: 10.1002/anie.200461554

Nanotechnology

Magnetic Information Storage on Polymers by Using Patterned Single-Molecule Magnets**

Massimiliano Cavallini, Jordi Gomez-Segura, Daniel Ruiz-Molina, Massimiliano Massi, Cristiano Albonetti, Concepció Rovira, Jaume Veciana, and Fabio Biscarini**

Nanoscopic magnetic materials are of increasing interest because of their potential use for ultrahigh-density information storage, quantum computing, sensing, and biomedical applications.[1–3] Herein we demonstrate that, while working in the paramagnetic regime, it is possible to encode and read out information from domains of Mn_{12} molecules patterned on a polymer surface across a large area. The patterns are fabricated by molding a dispersion of Mn_{12} molecules in a polycarbonate matrix on a structured master, then exposing the polymer replica to the vapor of an organic solvent. The protrusions of the replica surface disappear upon exposure to the solvent, and the Mn_{12} molecules concentrate on the surface at the positions of the original protrusions. The distribution of Mn_{12} molecules at the polymer surface gives rise to a magnetic contrast, which can be imaged by magnetic force microscopy. Information can be transferred from a recorded digital video disk (DVD), functioning as the master, to a magnetically readable flexible medium.

The search for increasingly small, lighter, and cheaper nanoscopic magnetic materials faces the challenge of overcoming anomalies such as dipolar interactions, matrix effects, domain wall rearrangements, and percolation effects, which degrade the observable magnetic properties. Thus, there is a worldwide effort aimed at developing new and enhanced nanostructured magnetic materials. An emerging family that is being explored is molecule-based magnets, because they possess several attractive attributes: 1) they have homogeneous and precisely defined sizes; 2) their chemical and topological structure can be tailored by chemical design; 3) they are soluble in common solvents and hence can be easily processed for applications; and 4) they can be considered as the ultimate limit for storing high densities of information data.[4] Mn_{12} clusters have a large-spin ground state with appreciable magnetic anisotropy, which results in a barrier for the spin reversal.[5–8] As a consequence, interesting magnetic properties such as out-of-phase ac magnetic susceptibility signals and stepwise magnetization hysteresis loops, caused by individual molecules rather than by long-range orderings, are observed below the blocking temperature (T_B).[9] However, if a truly molecular magnetic device is to be achieved, addressing properly oriented individual magnetic molecules or their aggregates, as well as increasing their critical temperatures of such molecule-based materials, are required. The first successful attempts toward the development of functional molecule-based magnetic devices focused on the deposition and addressing of Mn_{12} clusters on different surfaces. Mn_{12} clusters have been organized into multilayered films by the Langmuir–Blodgett technique or self-assembly on functionalized surfaces.[10] Deposition of isolated or small aggregates of such molecules onto a polycarbonate surface[11] and the self-assembly of thiol-substituted Mn_{12} clusters on thin Au films[12] have also been achieved. Nevertheless, no control of the position and distance between Mn_{12} molecules was attained in either case. Recently, we used a stamp-assisted self-organization method to successfully pattern Mn_{12} molecules into 50-nm-diameter dots with a characteristic length scale less than 200 nm,[13] which demonstrates the possibility of addressing organized clusters on the surface of a silicon wafer.

Herein, we report a reliable and simple methodology to pattern magnetic Mn_{12} molecules on a polycarbonate (PC) film, and show that it is possible to map (read) the patterned domains on the film surface while working in the paramagnetic regime. We used the complex $[Mn_{12}O_{12}(O_2CC_{12}H_9)_{16}(H_2O)_4]$ (**1**), whose synthesis has been previously described.[14] Frequency-dependent out-of-phase ac signals and hysteresis in the magnetization versus external field are seen for solid samples of complex **1**, which indicates that this complex behaves as a single-molecule magnet with a T_B value of 4–6 K and as a paramagnet at higher temperatures.[14] A consistent magnetic behavior is observed for the same complex dispersed in thin films of polycarbonate.[11] In the work described herein, the films are prepared by casting a solution of complex **1** and polycarbonate in CH_2Cl_2 onto a blank DVD support that acts as a structured master (Figure 1 a).[15] On the basis of the similarity of the conditions used in the process reported in ref. [11], we infer that the magnetic behavior of complex **1** should remain unchanged.

Once the solvent is evaporated, the replica is removed from the master, which results in a stable, flexible, and transparent film of a solid solution of complex **1** in polycarbonate. The film surface, imaged by atomic force microscopy (AFM), exhibits an inverted pattern with respect to the DVD master, with parallel lines 300-nm wide and 120-nm deep and a periodicity between grooves of 740 nm (Figure 1 b). A representative topographical profile along line 1 in Figure 1 b is shown in Figure 1 d. In a second step, the film is exposed to a saturated atmosphere of CH_2Cl_2 vapor that swells the film and solvates the polymer chains, thus decreasing the glass transition temperature of the polymer below

[*] Dr. M. Cavallini, Dr. M. Massi, Dr. C. Albonetti, Dr. F. Biscarini
CNR-Istituto per lo Studio dei Materiali Nanostrutturati
Sez. di Bologna
Via P. Gobetti 101, 40129 Bologna (Italy)
Fax: (+39) 051-639-8539
E-mail: f.biscarini@ism.bo.cnr.it
J. Gomez-Segura, Dr. D. Ruiz-Molina, Prof. C. Rovira, Prof. J. Veciana
CSIC-Institut de Ciencia de Materials de Barcelona
Campus Universitari de Bellaterra
08193 Cerdanyola (Spain)
Fax: (+34) 93-580-5729
E-mail: vecianaj@icmab.es

[**] This work was supported by the European Commission under projects IST-NANOMAGIQC and NMP-IP-500355 NAIMO, the European Science Foundation under Eurocore SONS program FUNSMARTS, and the Dirección General de Investigación (Spain) under project NanoMultiFun.

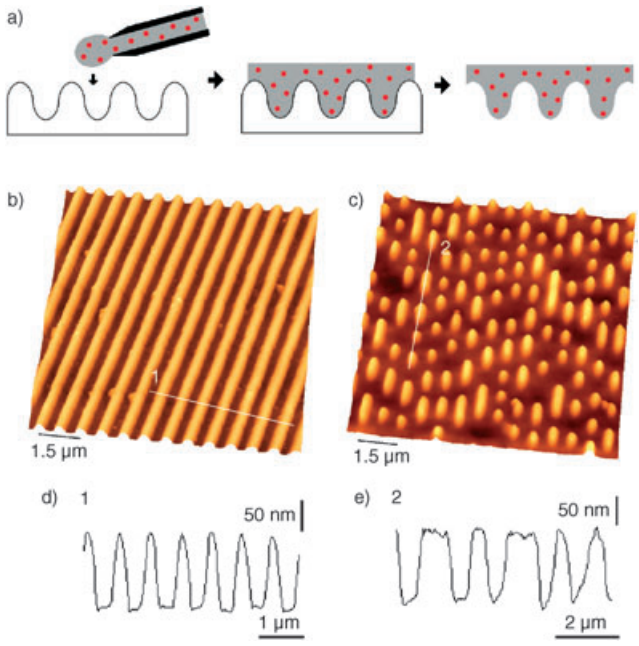

Figure 1. a) Schematic representation of the experimental process followed to obtain a DVD replica made of a solid solution of Mn_{12} complex and PC. b) AFM image of a Mn_{12}–PC replica exhibiting a sequence of grooves replicating the blank DVD master. The distance between grooves is 740 nm and their depth and width are 120 and 300 nm, respectively. c) AFM image of a Mn_{12}–PC replica of a recorded DVD, which exhibits a structured sequence of bits of information as protrusions. One bit corresponds to a protrusion 300 nm wide, 400 nm long, and 120 nm high. d) Topographical line profile along the white line 1 drawn in (b). e) Topographical line profile along the white line 2 drawn in (c).

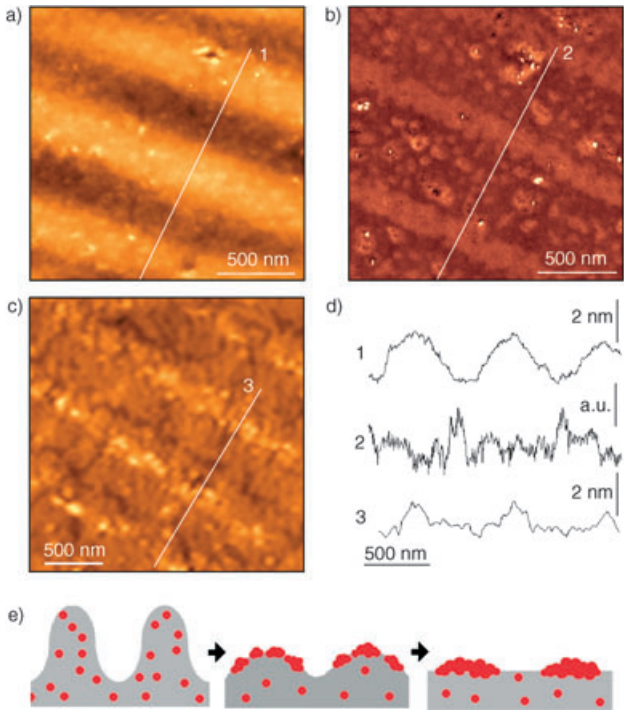

Figure 2. a) AFM topography image of a molded film of Mn_{12}–PC, as in Figure 1 b, after treatment with CH_2Cl_2 solvent vapor for 120 s. The height of the protrusions has decreased by more than 96% compared to its original value of 120 nm. b) AFM phase-contrast image of the replica surface depicted in (a) showing the inhomogeneous distribution of the Mn_{12} solute at the surface. Darker areas are solute-rich regions. c) AFM image of the film after treatment with CH_2Cl_2 vapor for 180 s. d) Profiles along the white lines shown in the topographic (lines 1 and 3) and phase-contrast (line 2) images. e) Schematic representation of the smoothening and Mn_{12} aggregation processes occurring during the CH_2Cl_2 solvent vapor treatment.

room temperature. Under these conditions, the structured film surface experiences a smoothening driven by the minimization of the surface tension, which leads to the progressive deletion of the topographic reliefs. The time needed for a complete smoothening depends on experimental parameters such as solvent nature, temperature, and initial surface roughness.

Topographic AFM images of the molded replica after exposure to CH_2Cl_2 vapor for 120 and 180 s are shown in Figure 2. The protrusions decrease from 120 nm (root-mean-square (rms) roughness 56 nm) to less than 5 nm after solvent exposure for 120 s (Figure 2 a and first profile in Figure 2 d), and by more than 99% (rms roughness <1 nm) after 180 s (Figure 2 c and third profile in Figure 2 d). An extensive film rupture occurs by nucleation and growth of nanosized pores upon longer exposure times (not shown). Interestingly, the corresponding AFM phase-contrast images show that the Mn_{12} clusters concentrate preferentially in the regions where the protrusions were originally formed, while they are absent from the grooves (Figure 2 b and second profile in Figure 2 d). This evidence shows that the lateral (in-plane) diffusion of Mn_{12} clusters, which were initially dissolved in the polymer solid solution, is marginal during the smoothening process. Other concurrent mechanisms may be linked to convective or diffusive mass transport toward the sharper protrusions, driven by a faster solvent evaporation rate at the loci with smaller curvature.[16]

These results encouraged us to further advance this approach by focusing on Mn_{12} molecular clusters patterned into domains with controlled shapes and positions on the polymer surface, since these domains of Mn_{12} molecules can be used as magnetic bits. With this aim, we molded a Mn_{12}–PC film replica of a recorded DVD. AFM imaging of the replica surface reveals an ordered array of 120-nm-thick protrusions of variable length ranging from 380 to 1500 nm, aligned along lines (tracks) with an intertrack distance of 740 nm (Figure 1 c). A representative topographical profile along a sector (line 2 in Figure 1 c) is shown in Figure 1 e.

The Mn_{12}–PC replica was then exposed to CH_2Cl_2 vapor, and the process was interrupted just before the rupture of the film surface took place. At this stage, the original protrusions that replicate the topographic indentations of the coded DVD have almost disappeared (topographic rms roughness is <1 nm), as is apparent from Figure 3 a and 3 e. The local magnetic response of the surface film was investigated by magnetic force microscopy (MFM), which revealed the formation of a spatially distributed magnetic pattern that closely follows the original topographic indentations of the recorded DVD (Figure 3 b). Again, the preferential concen-

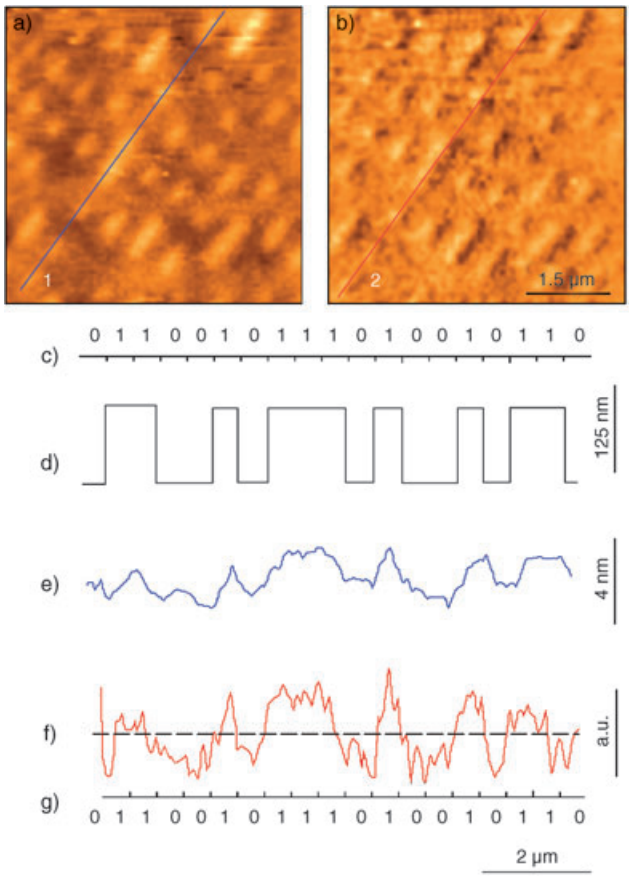

Figure 3. a) AFM topography image of a DVD replica after solvent exposure (rms roughness is 1 nm). b) Magnetic mapping of (a) with MFM. The image (phase shift during second pass) was acquired by a two-pass mode using a cobalt-coated magnetic tip. The lift height was 30 nm. c) Sequence of bits that is represented by the topographic sequence along the track marked by line 1 in (a). d) Idealized representation of the corresponding topographical line profile of the track in the replica before exposure to solvent. e) Topographical line profile of the track after exposure to solvent. f) Magnetic contrast along line 2 in (b). The mean signal line (-----) is a guide to the eye. g) Sequence of magnetic bits extracted from (f), which shows a perfect correspondence with the original sequence in (c).

tration of Mn_{12} clusters corresponding to the protrusions of the polymer film surface occurs as previously described. Each sequence of magnetic domains, composed of aggregates of Mn_{12} molecules, represents magnetically readable information that, overall, replicates the information that was originally accessible by optical readout in the DVD. The magnetic response of the domains of Mn_{12} molecules, which are paramagnetic at room temperature, to MFM can be ascribed to the strong magnetic contrast with the diamagnetic polymeric surroundings. Similar magnetic responses have been previously observed for other paramagnetic organic molecules on diamagnetic surfaces.[11,17] Figure 3d is an idealized representation of the topographical profile of the replica along the track marked by line 1 in Figure 3a before exposure to solvent. The corresponding logic sequence of bits for an optical readout is shown in Figure 3c. Figure 3f shows the line profile of the magnetic force along the same track with a signal-to-noise ratio of 2:1, which makes it possible to resolve the sequence of magnetic bits represented in Figure 3g (line 2 in Figure 3b). The sequence of magnetic bits perfectly reproduces the original sequence of optical DVD bits.

In summary, we have developed a simple process that is able to fabricate patterns of magnetic bits on a polymer surface, on the basis of a molecule-based magnetic material with a paramagnetic response at room temperature. We demonstrated that this system can be effectively used as a permanent information storage medium with magnetic readout. The patterning process can be scaled down to smaller length scales and higher densities by improving the resolution of the master, or by patterning the solute/polymer mixture by using a higher-resolution fabrication technique, for example, nanoimprint lithography. This technique may lead to the fabrication of magnetic Mn_{12} domains with features a few tens of nanometers in size,[18] which corresponds to a few molecular diameters (end-to-end distance is 4 nm). Finally, the patterning and addressing of molecular materials across multiple length scales is one of the most important issues in nanotechnology. Extension of this work could lead to the development of next-generation storage media based on a variety of molecular responses,[19] for example: charge storage; conformational, orientational, or positional shifting; phase transitions or reorganization; and optical anisotropy changes and fluorescence switching.

Experimental Section

Sample preparation: Pellets of poly(bisphenol A carbonate) (PC) with Mn_{12} single-molecule magnets (4% by weight) was dissolved in CH_2Cl_2, and the solution was cast on a master. The DVD masters were covered with a 100-nm-thick Au film. Circular samples of 1 cm diameter and 20 µm thickness were fabricated.

AFM/MFM measurements: AFM/MFM was carried out in air in intermittent-contact mode for imaging. For MFM measurements, cobalt-coated tips (MDT, Moscow, Russia) were used with the instrument operated in a two-pass mode: in the first pass the topography was measured in intermittent-contact mode; in the second pass the cantilever was lifted to a selected height with respect to the topography line, and the phase shift was measured as the tip followed the stored topography line. The magnetic signal was resolved as phase shift during the second pass. The magnetic contrast was comparable to that of MFM images reported earlier.[11,17] The typical lift height was 30 nm which, when compared to sample roughness (< 1 nm), was sufficient to avoid topographic artifacts in the magnetic signal. Imaging samples using a nonmagnetic tip did not yield any contrast in the second-pass mode, and neither did a magnetic tip on samples made of polycarbonate alone.

Received: August 5, 2004

Keywords: cluster compounds · magnetic properties · nanotechnology · polymers · single-molecule studies

[1] D. D. Awschalom, J. M. Kikkawa, *Phys. Today* **1999**, *52*, 33–38.
[2] H. Ohno, D. Chiba, F. Matsukura, T. Omiya, E. Abe, T. Dietl, Y. Ohno, K. Ohtani, *Nature* **2000**, *408*, 944–946.
[3] R. L. Edelstein, C. R. Tamanaha, P. E. Sheehan, M. M. Miller, D. R. Baselt, L. J. Whitman, R. J. Colton, *Biosens. Bioelectron.* **2000**, *14*, 805–813.
[4] J. S. Miller, A. J. Epstein, *MRS Bull.* **2000**, *11*, 21–28.

[5] D. Ruiz-Molina, G. Christou, D. N. Hendrickson, *Mol. Cryst. Liq. Cryst.* **2000**, *343*, 17 – 27.
[6] R. Sessoli, D. Gatteschi, A. Caneschi, M. A. Novak, *Nature* **1993**, *365*, 141 – 143.
[7] J. R. Friedman, M. P. Sarachick, J. Tejada, R. Ziolo, *Phys. Rev. Lett.* **1996**, *76*, 3830 – 3833.
[8] J. M. Hernandez, X. X. Zhang, F. Luis, J. Bartolomé, J. Tejada, R. Ziolo, *Europhys. Lett.* **1996**, *35*, 301 – 306.
[9] D. Gatteschi, R. Sessoli, *Angew. Chem.* **2003**, *115*, 278 – 309; *Angew. Chem. Int. Ed.* **2003**, *42*, 268 – 297.
[10] a) M. Clemente-León, H. Soyer, E. Coronado, C. Mingotaud, C. J. Gómez-García, P. Delhaes, *Angew. Chem.* **1998**, *110*, 3053 – 3056; *Angew. Chem. Int. Ed.* **1998**, *37*, 2842 – 2845; b) G. C. Condorelli, A. Motta, I. L. Fragala, F. Giannazzo, V. Rainieri, A. Caneschi, D. Gatteschi, *Angew. Chem.* **2004**, *116*, 4173 – 4176; *Angew. Chem. Int. Ed.* **2004**, *43*, 4081 – 4084; c) a. N. Abdi, J. P. Bucher, P. Rabu, O. Toulemonde, M. Drillon, P. Gerbier, *Jnl. Appl. Phys.* **2004**, *95*, 7345 – 7347; d) J. S. Steckel, N. S. Persky, C. R. Martinez, C. L. Barnes, E. A. Fry, J. Kulkarni, J. D. Burgess, R. B. Pacheco, S. L. Stoll, *Nano Lett.* **2004**, *4*, 399 – 402; correction: S. L. Stoll, *Nano. Lett.* **2004**, *4*, 1167.
[11] D. Ruiz-Molina, M. Mas-Torrent, J. Gómez, A. I. Balana, N. Domingo, J. Tejada, M. T. Martínez, C. Rovira, J. Veciana, *Adv. Mater.* **2003**, *15*, 42 – 45.
[12] A. Cornia, A. C. Fabretti, M. Pacchioni, L. Zobbi, D. Bonacchi, A. Caneschi, D. Gatteschi, R. Biagi, U. Del Pennino, V. De Renzi, L. Gurevich, H. S. J. Van der Zant, *Angew. Chem.* **2003**, *115*, 1683 – 1686; *Angew. Chem. Int. Ed.* **2003**, *42*, 1645 – 1648.
[13] M. Cavallini, F. Biscarini, J. Gómez-Segura, D. Ruiz, J. Veciana, *Nano Lett.* **2003**, *3*, 1527 – 1530.
[14] D. Ruiz-Molina, P. Gerbier, E. Rumberger, D. B. Amabilino, I. A. Guzei, K. Folting, J. C. Huffman, A. Rheingold, G. Christou, J. Veciana, D. N. Hendrickson, *J. Mater. Chem.* **2002**, *12*, 1152 – 1161.
[15] Y. Xia, E. Kim, X.-M. Zhao, J. A. Rogers, M. Prentiss, G. M. Whitesides, *Science* **1996**, *273*, 347 – 349.
[16] R. D. Deegan, O. Bakajin, T. F. Dupont, G. Huber, S. R. Nagel, T. A. Witten, *Nature* **1997**, *389*, 827 – 829.
[17] H. Nishide, T. Ozawa, M. Miyasaka, E. Tsuchida, *J. Am. Chem. Soc.* **2001**, *123*, 5942 – 5946.
[18] M. D. Austin, S. Y. Chou, *Appl. Phys. Lett.* **2002**, *81*, 4431 – 4433.
[19] M. Cavallini, F. Biscarini, S. Léon, F. Zerbetto, G. Bottari, D. A. Leigh, *Science* **2003**, *299*, 531 – 531.

Conclusiones

La presente Tesis reúne las siguientes conclusiones a destacar sobre el estudio de imanes unimoleculares basado en la preparación de complejos funcionalizados de Mn_{12}, estudio de sus propiedades, deposición en superficie y detección mediante técnicas magnéticas y/o ópticas:

- La estabilidad térmica de los clústeres de Mn_{12} es sensible a la naturaleza química de los grupos carboxilatos periféricos. Las reacciones de metátesis en presencia de carboxilatos con marcada acidez y/o elevado impedimento estérico provocan la fragmentación del núcleo central mediante mecanismos de descarboxilación oxidativa generando topologías de baja nuclearidad.

- En base a la estabilidad térmica se han preparado por substitución de ligando toda una serie de derivados de la familia del Mn_{12} multifuncionales: 1) los complejos de Mn_{12} enantioméricos, que fueron preparados a partir de ligandos óptimamente activos, muestran un efecto magneto-quiral no detectable a través del dicroísmo circular magnético bajo las condiciones de sensibilidad experimentales. No obstante, dichos estudios demuestran, al igual que para los complejos aquirales, el uso potencial de la espectroscopia óptica en la rápida lectura de la polarización del espín y mayor sensibilidad de detección que las técnicas de medición magnética convencionales por SQUID; 2) la preparación de complejos de Mn_{12} deuterados a permitido estudiar mediante difracción de neutrones la existencia de transiciones de fase cuántica en monocristales debido al ordenamiento dipolar de los espines a baja temperatura.

- El estudio de correlaciones magneto-estructurales por magnetometría SQUID: 1) se han estudiado técnicas de micro/nanoestructuración en imanes unimoleculares de Mn_{12} a través del procesado del material por técnicas de cristalización mediante fluidos comprimidos. Las propiedades magnéticas correspondientes a la relajación de la magnetización muestran una dependencia con la reducción del tamaño cristalino; 2) la variaciones en el entorno cristalino fueron estudiadas mediante la obtención de amorfos en fases cristalinas, mostrando cambios no significativos en las barreras de interconversión de la magnetización y fenómenos de relajación por efecto túnel.

- Se han desarrollado nuevas técnicas de deposición en superficie bajo control del tamaño, posición y geometría correspondientes a dominios moleculares magnéticos basados en agregados de Mn_{12}. Entre las superficies utilizadas destaca el uso de matrices poliméricas de policarbonato las cuales son compatibles con los sistemas de lectura magneto-ópticos convencionales.

- La posibilidad de uso de dominios moleculares de Mn_{12} como bits magnéticos de almacenamiento de información se ha realizado mediante técnicas de caracterización por MFM. De esta manera, es posible detectar a temperatura ambiente y por consiguiente en régimen paramagnético, dominios de Mn_{12} independientemente a la baja temperatura de bloqueo asociada. Su respuesta se basa en el contraste magnético con respecto a la naturaleza diamagnética de la superficie que actúa de soporte.